UNIVERSITY OF OKLAHOMA

GRADUATE COLLEGE

FULLY AUTONOMOUS SELF-POWERED INTELLIGENT WIRELESS SENSOR FOR REAL-TIME TRAFFIC SURVEILLANCE IN SMART CITIES

A DISSERTATION

SUBMITTED TO THE GRADUATE FACULTY

in partial fulfillment of the requirements for the

Degree of

DOCTOR OF PHILOSOPHY

In

ELECTRICAL AND COMPUTER ENGINEERING

By

WALID BALID
Norman, Oklahoma
2016

Downloaded from SHAREOK. Persistent Handle URL: https://hdl.handle.net/11244/51828

FULLY AUTONOMOUS SELF-POWERED INTELLIGENT WIRELESS SENSOR FOR REAL-TIME TRAFFIC SURVEILLANCE IN SMART CITIES

A DISSERTATION APPROVED FOR THE
SCHOOL OF ELECTRICAL AND COMPUTER ENGINEERING

BY

_____
Dr. Hazem H. Refai, Chair

_____
Dr. William Ray

_____
Dr. Thordur Runolfsson

_____
Dr. Choon Yik Tang

_____
Dr. Ali Imran

© Copyright by WALID BALID 2016
All Rights Reserved.

To my parent, Radwan and Mouna, who have always been loving and caring to me in every way, shape, and form. You have instilled in me the passion to learn, to dream, and to be the person I am today.

To my darling sisters, Bayan and Khazal, and brother, Ahmad, your love guides me across the oceans, beyond the seven seas to the kingdom of soul.

To my beloved wife, Arwa Soumakie, who has accompanied me with infinite love, unlimited patience and understanding, constant help, and never-ending encouragement. Without your caring support, it would not have been possible to accomplish this work.

To my daughter, Maria... I am blessed for having you, sweetheart. You are my heaven. You are the greatest gift from God I have ever gotten.

To my people at a geographical distance of 6,600 miles.

I dedicate this work to you all!

Walid Balid

Acknowledgements

I would like to extend my heartfelt appreciation and gratitude to my dear advisor, *Dr. Hazem H. Refai*, for the endless support and insightful guidance he has provided throughout my PhD journey at *The University of Oklahoma*.

I would also like to express my sincere gratitude to the distinguished members of my dissertation committee who have generously given their time and expertise to better my work. *Dr. William Ray, Dr. Thordur Runolfsson, Dr. Choon Yik Tang,* and *Dr. Ali Imran*, thank you all.

I must acknowledge *Asaad Kaadan* and all my other fellow students who generously provided me a great friendship, and unlimited support and help.

Special appreciation goes to the extended OU-TULSA family of professors, students, and staff, as well as to Michelle Farabough for her assistance in editing this dissertation.

My sincere appreciation to you all…

Table of Contents

Acknowledgements iv

Table of Contents v

List of Tables xi

List of Figures xiv

Abstract xx

Chapter 1: Introduction 1

1.1 Introduction 1

1.2 Intelligent Transportation Systems and Smart Cities 2

1.3 Current Traffic Surveillance Technologies 3

1.4 Wireless sensor networks 5

1.5 Magnetometer Sensors 5

1.5.1 Magnetometer Sensor Theory of Operation 6

1.6 Energy-Harvesting Solutions for WSN 10

1.7 Research Motivation 12

1.8 Proposed Research 15

1.9 Research Contributions 16

1.10 Dissertation Structure 17

Chapter 2: Background & Existing Knowledge 19

2.1 Introduction 19

2.2 Traffic Monitoring using MAG 19

2.3 Time Synchronization in WSN 26

Chapter 3: Sensor Design & System Integration 30

3.1 System Overview 30
3.2 Design Objectives and Requirements 32
3.3 Components Selection Methodology 32
3.4 iVCCS$_{G1}$ Platform Overview 33
3.4.1 Embedded Microcontroller 34
3.4.2 Magnetometer & Accelerometer Sensors 35
3.4.3 Embedded RF Engine 37
3.4.4 Real-Time Clock 38
3.4.5 Embedded GPS Module 38
3.4.6 Power Management Unit 39
3.4.7 Data Storage Unit 40
3.4.8 Road Surface Condition Sensors 41
3.4.9 Atmospheric Sensors Extension Module 41
3.5 iVCCS$_{G1}$ Power Consumption and Battery Life Analysis 42
3.6 Power Consumption Implications of Detection Algorithm 45
3.7 Towards Self-Powered Smart WSN 45
3.7.1 Characteristics of Self-Powered Applications 46
3.7.2 Enabling Device Power Self-Sustainability 47
3.8 iVCCS$_{G2}$ Platform Overview 47
3.8.1 A 32-bit Embedded Microcontroller 52
3.8.2 Magnetometer & Accelerometer Sensors 53
3.8.3 Embedded RF Engine 55
3.8.4 Real-Time Clock 57

3.8.5 Embedded GPS Modules 58
3.8.6 Data Logging Unit 59
3.8.7 Power Management System 60
3.8.8 Wireless Charging Receiver 70
3.8.9 Road Surface Condition Sensors 71
3.8.10 Passive Components Selection Does Matter 71
3.9 iVCCS$_{G2}$ Power Consumption and Battery Life Analysis 71
3.9.1 Components Parameters Assessment 72
3.9.2 iVCCS$_{G2}$ Power Consumption Assessment 78
3.9.3 Battery Life Estimation 83
3.9.4 Extending Battery Life 85
3.10 Proposed Large-scale System Architecture and Networking 88
Chapter 4: Algorithms Design & Firmware Development 92
4.1 Introduction 92
4.2 Real-Time Vehicle Detection & Counting Algorithm 94
4.2.1 An Overview on Implementation of Vehicle Detection Algorithms 94
4.2.2 Embedded Magnetometer Sensors 94
4.2.3 Detection and Counting using an iVCCS in Roadway Setup 95
4.2.4 Detection and Counting using a iVCCS in Roadside Setup 99
4.2.5 Adaptive Geomagnetic Baseline Drift Compensation 101
4.3 Vehicle Speed Estimation and Time Synchronization 104
4.3.1 Real-Time Vehicle Speed Estimation using Two Sensor Nodes 104
4.3.2 Real-Time Vehicle Speed Estimation using Single Sensor Node 105

4.4 Time Synchronization using Embedded GPS Module 108
4.4.1 Adaptive Compensation of the RTC Frequency Drift 109
4.4.2 Timestamps Matching Issues 117
4.5 Real-Time Vehicle Magnetic Length Estimation 118
4.6 Real-Time Magnetic Length-based Vehicle Classification 118
Chapter 5: Field Testing & Data Collection 121
5.1 Data Collection Methodology 121
5.1.1 Field Test 1 121
5.1.2 Field Test 2 124
5.1.3 Field Test 3 126
5.1.4 Field Test 4 128
5.1.5 Field Test 5 129
5.1.6 Field Test 6 130
5.1.7 Field Test 7 131
5.1.8 Field Test 8 132
5.2 Log Data File Format and Structure 133
5.2.1 ASCII Log File Structure 134
5.2.2 Binary Log File Structure 136
Chapter 6: Data Analysis & Performance Evaluation 140
6.1 Overview 140
6.2 Magnetometer Sensor Characterization Analysis 141
6.2.1 Sampling Rate in Active Detection 141
6.2.2 MAG Output Noise Characterization 141

6.2.3 MAG Sampling Rate Setting 142
6.2.4 Effect of MAG Rotation Around z-axis 143
6.2.5 Repeatability of VMS and MAG Sensors Output 144
6.3 Vehicle Detection 150
6.3.1 Optimal Detection Thresholds Analysis 150
6.3.2 Optimal Holdover Debounce-time Value 153
6.3.3 Adaptive Geomagnetic Baseline Drift Compensation Performance 161
6.3.4 Detection and Counting Accuracy 163
6.3.5 Detection in Stationary-state and Stop-and-go Scenarios 170
6.4 Assessment of Time Synchronization Algorithm 172
6.4.1 Evaluation of Timestamps Consistency 173
6.5 Vehicle Speed Estimation 174
6.6 Vehicle Magnetic Length Estimation 176
Chapter 7: iVCCS Applications in Traffic Surveillance 178
7.1 Overview 178
7.2 Introduction to Vehicle Classification Schemes 178
7.2.1 Axle-based Vehicle Classification Scheme 178
7.2.2 Available Length-Based Vehicle Classification Schemes 180
7.3 Development of Real-Time Length-Based Vehicle Classification 183
7.4 Introduction to Vehicle Re-Identification and Travel Time Estimation 205
7.5 Development of Vehicle Re-Identification Algorithm using MAG 207
7.5.1 Vehicle Magnetic Signature Processing 208
7.5.2 Features Extraction & Data Transformation 212

7.5.3 Matching Process 215
Chapter 8: Conclusion 228
8.1 Research Outcomes 228
8.2 Future Work Plan 233
References 235
Appendix A: iVCCS$_{G1}$ Schematic, Layout, BOM 244
Appendix B: iVCCS$_{G2}$ Schematic, Layout, BOM 254
Appendix C: iVCCS$_{G2}$ Design Process 264

List of Tables

Table 1-1 Ranges of magnetic elements at the Earth's surface [22] 9

Table 3-1 iVCCS design objective 32

Table 3-2 Top MAG candidates for $iVCCS_{G1}$ 35

Table 3-3 Power consumption for iVCCS components 43

Table 3-4 Power consumption for WSN components 44

Table 3-5 Power consumption in various operation modes using Li-Po batteries 45

Table 3-6 Comparison between two industry-leading 6-axis MAG-ACCEL sensors 54

Table 3-7 Top ZigBee Module candidates for $iVCCS_{G2}$ 56

Table 3-8 Characteristics of Energy Harvesting PMU for WSN 64

Table 3-9 Characteristics of Energy Harvesting Transducers and Sources for WSN 66

Table 3-10 Characteristics of energy storage devices for EH applications 67

Table 3-11 Cycle life as a function of depth of discharge 68

Table 3-12 Discharge cycles and capacity as a function of charge voltage limit. 69

Table 3-13 $iVCCS_{G2}$ MCU power consumption in various power modes 73

Table 3-14 STM32L071 Peripheral power consumption in active mode 73

Table 3-15 Serial Flash parameters 74

Table 3-16 GPS Module parameters 76

Table 3-17 RF Engine parameters 77

Table 3-18 Execution time and consumed current for $iVCCS_{G2}$ 78

Table 4-1 Length boundaries for 4-G_{SX} using different thresholding methods 119

Table 5-1 Log file structure in ASCII format 135

Table 5-2 Log file structure in Binary format 136

Table 6-1 Field Magnitude STD for Different Sampling Rates 142

Table 6-2 Detection zone characteristics based on Class 2 vehicle 159

Table 6-3 Detection MAPE for Roadway Setup—Field Test 1 163
Table 6-4 Detection MAPE for Roadway Setup—Field Test 2 164
Table 6-5 Detection MAPE for Roadside Setup—Field Test 2 165
Table 6-6 Detection MAPE for Roadway Setup—Field Test 3 165
Table 6-7 Number of detections In-Lane per-class—Field Test 4 168
Table 6-8 Total Detection Error—Field Test 4 168
Table 6-9 Detection MAPE—Field Test 5 169
Table 6-10 Detection MAPE—Field Test 6 170
Table 6-11 Detection MAPE—Field Test 7 170
Table 6-12 Speed Estimation Accuracy 175
Table 7-1 Three-group LBVC schemes boundaries for different states 181
Table 7-2 Four-group FHWA-LBVC scheme boundaries 182
Table 7-3 MDOT-LBVC scheme boundaries 182
Table 7-4 VML statistical measurements 184
Table 7-5 VML statistical measurements for 3-G_{SA} 187
Table 7-6 VML statistical measurements for 3-G_{SB} 187
Table 7-7 VML statistical measurements for 4-G_{Sx} 188
Table 7-8 Performance metrics used to evaluate built classification models 190
Table 7-9 LBVC Schemes performance results for MAG Dataset 192
Table 7-10 Decision boundaries for proposed LBVC Schemes—unites are in meter 193
Table 7-11 Decision boundaries found by different thresholding methods for 3G-S_B 200
Table 7-12 Classification rates and errors for different boundaries applied on 3G-S_B 200
Table 7-13 Classification rates by different thresholding methods for 3G-S_B LBVC 200
Table 7-14 Decision boundaries found by different thresholding methods for 4G-S_x 201
Table 7-15 Classification rates and errors for different decision boundaries 4G-S_x 202
Table 7-16 Classification rates by different thresholding methods for 4G-S_x 202

Table 7-17 Matching window size for different distances between detection points 217

Table 7-18 Statistical characteristics of fitted distributions 223

Table 7-19 Threshold-based re-identification evaluation results 226

Table 7-20 Voting-based re-identification evaluation results 227

List of Figures

Figure 1-1 Earth's magnetic field lines distribution [19] 6

Figure 1-2 The seven elements of the $B\gamma$vector in coordinate plane 8

Figure 1-3 Earth's magnetic field lines distorted by passing vehicle 9

Figure 1-4 Magnetic dipoles moment and direction in a three-dimensional space 9

Figure 1-5 Earth's magnetic field lines distribution 11

Figure 3-1 Conceptual diagram of developed system 31

Figure 3-2 $iVCCS_{G1}$ functional components block diagram 33

Figure 3-3 $iVCCS_{G1}$ printed circuit board with all components marked 33

Figure 3-4 ATxmega128A4 internal block diagram and pin-layout 34

Figure 3-5 Freescale FXOS8700CQ System Block Diagram 36

Figure 3-6 SM200P81 Module block diagram 38

Figure 3-7 Titan 2 Gms-g6 GPS module 39

Figure 3-8 WSM sensing components block diagram 41

Figure 3-9 WSM PCB with all sensing components marked, 25×28mm 41

Figure 3-10 Selected Atmospheric Sensors for WSM 42

Figure 3-11 $iVCCS_{G2}$ functional components block diagram 49

Figure 3-12 $iVCCS_{G2}$ PCB with all components marked 50

Figure 3-13 $iVCCS_{G2}$ functional components interconnections 51

Figure 3-14 STM32L071KB MCU block diagram 53

Figure 3-15 AW5161P0 support multi-wireless protocol stack [96] 57

Figure 3-16 SiT1552, a world's smallest 32.768KHz MEMS TCXO 58

Figure 3-17 Quectel's L76-L extremely compact GPS module 59

Figure 3-18 SanDisk SDSDQAF-008G-I, TI TPD8F003, and MX25R6435F 60

Figure 3-19 Energy Harvesting Transducers [102] 63

Figure 3-20 Energy Harvesting Transducers 65
Figure 3-21 Different energy harvesters (rectangles) and sources (ovals) 65
Figure 3-22 TI BQ27621-G1 Battery Fuel-Gauge [104] 69
Figure 3-23 TI BQ51051B chip (left) and Vishay IWAS-4832FE-50 coil (right) 71
Figure 3-24 PPS and NMEA timing for L76-M33 76
Figure 3-25 iVCCSG2 Final Prototype PCB 86
Figure 3-26 Sensor node processes and power sequence flow diagram 87
Figure 3-27 Architecture of the traffic surveillance system network 89
Figure 4-1 Hierarchal integration of hardware and software in iVCCS 93
Figure 4-2 Variations in B_y in forward and reverse driving directions 94
Figure 4-3 Variations in F_M in forward and reverse driving directions 95
Figure 4-4 Detection Algorithm Parameters applied on a Vehicle Flux Magnitude 95
Figure 4-5 Vehicles detection and counting algorithm functional block 96
Figure 4-6 State machine process for vehicle detection and counting 97
Figure 4-7 Class 2 vehicle magnetic signature sampled by iVCCS on roadside 100
Figure 4-8 Class 2 vehicle magnetic signature sampled by iVCCS on roadway 100
Figure 4-9 Adaptive Geomagnetic Baseline Drift Compensation Pseudocode 102
Figure 4-10 Flowchart for adaptive compensation of geomagnetic baseline drift 103
Figure 4-11 Speed estimation deployment setup 104
Figure 4-12 Moving median speed estimation algorithm 107
Figure 4-13 Speed estimation algorithm using sequence method 107
Figure 4-14 GPS-based RTC clock setting and phase alignment block 108
Figure 4-15 Pseudo-code for RTC setting and phase alignment using GPS-PPS 109
Figure 4-16 Frequency stability vs. Temperature characteristics for ABS07 110
Figure 4-17 RTC drift correction system block diagram 111
Figure 4-18 PPS-based RTC time drift correction system block diagram 112

Figure 4-19 PPS-based RTC frequency drift compensation algorithm 114
Figure 4-20 PPS-based RTC frequency drift compensation flowchart 115
Figure 4-21 SiT1552 MEMS TCXO block diagram 116
Figure 4-22 SiT1552 stability over temperature 116
Figure 4-23 Proposed LBVC Schemes for MAG 119
Figure 4-24 Implementation model for LBVC Scheme using MAG 120
Figure 5-1 System setup layout on roadways (S1–S12) and roadsides (S13–S16) 123
Figure 5-2 iVCCS enclosure—1st prototype 123
Figure 5-3 Field Test 1 deployment site 123
Figure 5-4 System setup layout on roadways (NA–NB) and roadsides (NC–ND) 125
Figure 5-5 iVCCS node enclosure—2nd prototype 125
Figure 5-6 Field test 2 deployment site 125
Figure 5-7 Field test 3 system setup layout 127
Figure 5-8 Field test 3 deployment site 127
Figure 5-9 System setup layout on roadways and roadsides 129
Figure 5-10 Eight iVCCS nodes deployed on an urban road 129
Figure 5-11 Field test 5 deployment site 130
Figure 5-12 Field test 6 deployment site 131
Figure 5-13 Field test 7 deployment site 132
Figure 5-14 Field test 8 deployment site 133
Figure 5-15 Example of ASCII data log file 135
Figure 5-16 Vehicles signatures, iVCCS on roadway – $B\gamma$ (left) and F_M (right) 139
Figure 6-1 Flow diagram for data validation and performance evaluation 140
Figure 6-2 Field magnitude histogram at different sampling rates 142
Figure 6-3 Orientation setup and Bx and By with θ=0° were rotated by 135° 144
Figure 6-4 Histogram of R between magnetic magnitudes of Node-A and B 146

Figure 6-5 Histogram of R between magnetic magnitudes of Node-A and C 146
Figure 6-6 Histogram of R between magnetic magnitudes of Node-B and C..... 146
Figure 6-7 CDF of correlation coefficients for all pairwise signals 147
Figure 6-8 Magnetic magnitudes for class 2 vehicle obtained from all Nodes 147
Figure 6-9 Magnetic magnitudes for class 3 vehicle driving over all sensors 148
Figure 6-10 Correlation coefficients CDFs for all pairs on x, y, and z-axis 149
Figure 6-11 Distribution of magnetic noise and signature separated using GMM 152
Figure 6-12 Miss-detection caused by two vehicle driving at close proximity..... 153
Figure 6-13 Speed estimation deployment setup..... 154
Figure 6-14 Magnetic Flux and Sections of a class 9 vehicle 154
Figure 6-15 Double detection caused by class 9 vehicle..... 155
Figure 6-16 False detection caused by a vehicle passing in adjacent lane 157
Figure 6-17 Probability distributions of Gap periods..... 157
Figure 6-18 S^2_T computation process 158
Figure 6-19 Probability distributions of Section 2 periods 158
Figure 6-20 Probability of double detection for a given H_{DT} 159
Figure 6-21 Detection zone edges was found to be symmetric..... 160
Figure 6-22 Variations in $B(\gamma)$caused by interfering (left) and detection (right) 161
Figure 6-23 The drift in F_{Mref} with and without adaptive compensation..... 162
Figure 6-24 F_{Mref} distribution over 24-hour with and without compensation 162
Figure 6-25 Class 9 truck at the edge of lane 2, detected in both lanes 166
Figure 6-26 Class 6 truck on the edge of lane 2, detected in both lanes 166
Figure 6-27 Class 3 truck with huge trailer on edge of lane 2, detected in both lanes..... 167
Figure 6-28 Class 2 hybrid car on the edge of lane 2, detected in both lanes 167
Figure 6-29 Motorcycle considered as False-detection..... 170
Figure 6-30 Go-Stop-Go detection using sensor in roadside setup 171

Figure 6-31 Go-Stop-Go detection using sensor in roadway setup 171
Figure 6-32 The FM and detection flag in Go-Stop-Go scenario 172
Figure 6-33 Histogram of T-Sync error between RTC and GPS 173
Figure 6-34 Histogram of absolute error of RTC between two nodes 173
Figure 6-35 VML by FHWA F Scheme – Highway Data 176
Figure 6-36 VML by FHWA F Scheme – Urban Data 177
Figure 6-37 VML by FHWA F Scheme – Combined 177
Figure 7-1 U.S. FHWA Classification Scheme F with 13 class 179
Figure 7-2 VML scatter plots for dataset that used to develop LBVC schemes 184
Figure 7-3 Histograms of VML by FHWA F Scheme Classes 185
Figure 7-4 Recommended Classification Schemes 186
Figure 7-5 Dataset scatter plots for 3-G_{SA}; 3-G_{SB}; and 4-G_{Sx} 186
Figure 7-6 Histograms of VML by 3-G_{SA} 187
Figure 7-7 Histograms of VML by 4-G_{Sx} 188
Figure 7-8 Confusion Matrix for RUSBoost using 4G-S/MAG dataset 194
Figure 7-9 Class distribution in Dataset collected using MAG 195
Figure 7-10 Class distribution in Dataset collected from IDL 195
Figure 7-11 Two overlapped Gaussian distributions with an unknown decision threshold α 196
Figure 7-12 Gaussian distribution and decision thresholds for the MAG 3G-S_B dataset 199
Figure 7-13 Gaussian distribution and decision thresholds for the MAG 4G-S_x dataset 201
Figure 7-14 Decision boundaries for 3G-S_B LBVC for several states 205
Figure 7-15 Decision boundaries for 4G-S_x LBVC for several states 205
Figure 7-16 VMS components before and after smoothing and normalization 211
Figure 7-17 VMS magnitude before and after smoothing and normalization 212
Figure 7-18 VMS different combinations of B^x and B^y. 212
Figure 7-19 The PIP, spacing, and PL features for Class 9 VMS 215

Figure 7-20 Field components PIP, spacing, and PL 215

Figure 7-21 Extracted features at upstream and downstream for V_8 218

Figure 7-22 Re-identification algorithm block diagram 219

Figure 7-23 Distance matrixes for $EVFVnN$, $TSFVnN$, and $PLFVnN$ 221

Figure 7-24 Distance matrix for the mean of lowest twelve first features 221

Figure 7-25 The empirical distributions and their Gaussian approximations 223

Figure 7-26 Illustration of different Errors for two overlapped distributions 224

Figure 7-27 Indices of minimum distance of 21 features for 25 vehicles 227

Abstract

Reliable, real-time traffic surveillance is an integral and crucial function of the 21st century intelligent transportation systems (ITS) network. This technology facilitates instantaneous decision-making, improves roadway efficiency, and maximizes existing transportation infrastructure capacity, making transportation systems safe, efficient, and more reliable. Given the rapidly approaching era of smart cities, the work detailed in this dissertation is timely in that it reports on the design, development, and implementation of a novel, fully-autonomous, self-powered intelligent wireless sensor for real-time traffic surveillance. Multi-disciplinary, innovative integration of state-of-the-art, ultra-low-power embedded systems, smart physical sensors, and the wireless sensor network—powered by intelligent algorithms—are the basis of the developed *Intelligent Vehicle Counting and Classification Sensor* (*i*VCCS) platform. The sensor combines an energy-harvesting subsystem to extract energy from multiple sources and enable sensor node self-powering aimed at potentially indefinite life. A wireless power receiver was also integrated to remotely charge the sensor's primary battery. Reliable and computationally efficient intelligent algorithms for vehicle detection, speed and length estimation, vehicle classification, vehicle re-identification, travel-time estimation, time-synchronization, and drift compensation were fully developed, integrated, and evaluated. Several length-based vehicle classification schemes particular to the state of Oklahoma were developed, implemented, and evaluated using machine learning algorithms and probabilistic modeling of vehicle magnetic length. A feature extraction employing different techniques was developed to determine suitable and efficient features for magnetic signature-based vehicle re-identification. Additionally,

two vehicle re-identification models based on matching vehicle magnetic signature from a single magnetometer were developed. Comprehensive system evaluation and extensive data analyses were performed to fine-tune and validate the sensor, ensuring reliable and robust operation. Several field studies were conducted under various scenarios and traffic conditions on a number of highways and urban roads and resulted in 99.98% detection accuracy, 97.4782% speed estimation accuracy, and 97.6951% classification rate when binning vehicles into four groups based on their magnetic length. Threshold-based, re-identification results revealed 65.25%~100% identification rate for a window of 25~500 vehicles. Voting-based, re-identification evaluation resulted in 90~100% identification rate for a window of 25~500 vehicles. The developed platform is portable and cost-effective. A single sensor node costs only $30 and can be installed for short-term use (e.g., work zone safety, traffic flow studies, roadway and bridge design, traffic management in atypical situations), as well as long-term use (e.g., collision avoidance at intersections, traffic monitoring) on highways, roadways, or roadside surfaces. The power consumption assessment showed that the sensor is operational for several years. The *i*VCCS platform is expected to significantly supplement other data collection methods used for traffic monitoring throughout the United States. The technology is poised to play a vital role in tomorrow's smart cities.

Chapter 1: INTRODUCTION

1.1 Introduction

The rapidly increasing growth of surface transportation—driven by an ever-growing population—and its impact on traffic safety has been a major concern for the nation's transportation agencies over the last decades. The U.S. Federal Highway Administration (FHWA) predicts a 23% increase in vehicle miles traveled by 2032 [1].

Statistical studies by the World Health Organization (WHO) reported 1.25 million people die and up to 50 million injuries occur each year on the world's roads [2]. The U.S. National Highway Traffic Safety Administration (NHTSA) reported 32,719 fatalities and 2.313 million traffic injuries in 2013, 28% of which were speed-related [3]. Annual traffic fatalities caused by trucks is reportedly 4,000 deaths, and injuries to travelers numbers 100,000. Vehicular fatalities on U.S. roadways have an annual direct economic cost of $242 billion, resulting from 24 million crashes. This figure represents 1.6% of the $14.96 trillion U.S. Gross Domestic Product (GDP) reported in 2010 [4]. The total cost increases to $836 billion when considering societal harm from vehicle crashes. Furthermore, 44% of the U.S. roadways are classified as congested. According to the 2015 Urban Mobility Scorecard report [5], traffic congestion costs the U.S. $160 billion each year as a result of 7,000,000,000,000 lost hours and 3,000,000,000,000 fuel gallons wasted. Additionally, 31% of carbon dioxide emissions come from vehicle tailpipes [6].

When compared with passenger vehicles, trucks and commercial vehicles have a significant impact on pavement service life. For example, a vehicle hailing a 40-ton load causes over 4,000 times more road damage than a five-ton loaded vehicle.

Moreover, according to [7], approximately 4,000 fatalities and more than 95,000 injuries reported in 2013 involved large trucks. Such an impact requires appropriate and distinctive traffic planning strategies to mitigate the effect of anticipated increases in truck traffic. Adequate information about freight volume and vehicle classification is needed to support geometric and structural design of roadways and bridges.

Without assertive, proactive solutions, traffic crashes are predicted to rise and roadways congestion is estimated to worsen. Annual delay in the U.S. will grow to 8.3 billion hours, resulting in an increased cost of $192 billion [5].

In spite of the fact that vehicle travel on U.S. highways increased by 39% from 1990 to 2013, new roadways increased by only 4%. To accommodate the growing demand on transportation and to prevent worsening levels of roadway congestion, the U.S. FHWA must expand current transportation infrastructure capacity by 23%. One option to achieve this goal is adding 4,200 miles of new roadway each year [8]. Another is developing intelligent transportation system (ITS) technologies that maximize existing transportation infrastructure capacity and improve efficiency, making transportation systems safe, efficient, and more reliable for the rapidly approaching era of smart cities.

1.2 Intelligent Transportation Systems and Smart Cities

ITS are an integral part of nationwide traffic management systems (TMS). ITS performance depends substantially on accuracy of reported data and spatial distribution of traffic sensors [9], which in-turn influence highway and roadway efficiency and safety. Designing/planning ITS is a complex task that requires extensive analysis of public demand for transportation. To determine transportation needs, it is important to

understand the underlying characteristics of traffic patterns, such as vehicle classifications, vehicle volume and occupancy, and travel time, among many others. This understanding is an essential aspect of assisting traffic projection studies and transportation planning [10].

Real-time traffic monitoring systems play a key role in the transition toward smart cities and more efficient ITS. Autonomous traffic sensing is at the heart of smart city infrastructures, wherein smart wireless sensors are used to measure traffic flow, predict congestion, and adaptively control traffic routes. Doing so effectively provides an awareness that enables a more efficient use of resources and infrastructure.

The Internet of Things (IoT) is reshaping the future. Experts project that by 2020 nearly four billion people, more than 25 million Apps, and 26 billion embedded devices will be connected to the internet, producing 50 trillion gigabytes of data and revenue opportunities of up to four trillion US dollar [11]. For ITS to be effective in the era of IoT, traffic surveillance systems should have sufficient spatial distribution to permit interconnected network elements, providing reliable information about traffic conditions, enabling real-time data exchange among various infrastructure components, and facilitating instantaneous decision-making. In the context of ITS for smart cities, IoT technology will allow new services aimed at greatly improving quality of life.

1.3 Current Traffic Surveillance Technologies

Vehicle detection and traffic surveillance technologies are a core component of ITS. Both functions are subject to continuous improvement toward enhancing vehicle detection, speed estimation, and vehicle classification. Traffic detection and volume prediction methods are dependent upon several factors, including current and historic

traffic measurements. Widely used traffic surveillance technologies can be classified into three groups: intrusive, non-intrusive, and off-roadway sensors.

1) Intrusive sensors include inductive loops (IDL), magnetic detectors, pneumatic road tubes, piezoelectric, and weight-in-motion (WIM) sensors, which are embedded in the road surface after saw-cutting the surface or adding roadway holes.
2) Non-intrusive sensors include vision systems, microwave radar, and infrared and ultrasonic detectors, which are installed atop roadway or roadside surfaces or mounted overhead.
3) Off-roadway sensors (e.g., remote sensing via aircraft or satellite and probe vehicles equipped with Global Positioning System (GPS) receiver) that do not require roadway installation.

A description of these technologies can be found in [8], [12]. Both intrusive and non-intrusive sensors are power-hungry, expensive, and have been known to cause installation difficulties. The sensors typically require wired infrastructures and power lines for energy supply. Other drawbacks of intrusive sensors include their large-size, short life (i.e., as short as 48h for tubes [13]), and high maintenance costs associated with lane closure and traffic disruption. Piezoelectric and WIM sensors rely on pavement geometry, meaning that pavement deterioration will result in unreliable data. Moreover, resurfacing or repairing roadways requires reinstalling sensors, making worker safety for those deploying intrusive systems a concern [13].

Although vision and radar systems are widely considered accurate and typically do not disrupt traffic, their performance is subject to weather conditions (e.g. fog, rain, snow, or wind). Off-roadway sensors provide limited traffic statistics at fixed locations;

their performance is limited due to dependence on the number of probe vehicles [8], [12]. Consequently, the associated high costs (e.g., initial cost, calibration costs, regular maintenance, among others) limit spatial distribution and large-scale integration. TMS scalability and availability are essential for efficient and reliable, real-time ITS [9].

1.4 Wireless sensor networks

Wireless sensor networks (WSN) are emerging as a promising technology and a key enabler for an enormous number of physical-world sensing applications that have not previously been possible (e.g., IoT) [14]. WSN have demonstrated exceptional features, such as flexibility, scalability, reliability, and power efficiency [15]. Network scalability is exceptionally important for ITS, particularly as systems are able to accommodate an increased number of nodes connected in an ad-hoc, self-configurable manner [16]. A comprehensive survey of WSN for ITS applications can be reviewed in [15].

Systems employing WSN consist of medium to large networks of inexpensive wireless nodes capable of sensing, processing, and collaboratively distributing data acquired from the physical-world [14].

1.5 Magnetometer Sensors

Rapid technology advancements in solid electronics, embedded computing, and wireless communication protocols have transformed magnetometer sensors (MAG) into cost-effective and energy-efficient alternatives to IDLs. Unlike other methods, MAG are immune to poor weather conditions and environmental factors. They do not require line-of-sight, and they have a longer lifetime [17]. Integrating WSN with state-of-the-art embedded MAG has enabled autonomous methods for real-time traffic surveillance

application (e.g., vehicle detection on roadways and in parking lots, vehicle speed estimation, and vehicle classification). Many credit the PATH program at the University of California [12] for initiating the use of MAG sensors in traffic surveillance applications.

1.5.1 Magnetometer Sensor Theory of Operation

The earth's magnetic or geomagnetic field ($\boldsymbol{B}_{\gamma}$) is nearly uniform at any specific place on the earth's surface and ranges between approximately 25 and 65 microtesla (μT)—0.25 to 0.65 gauss (G). Notably, however, field direction and intensity change from place-to-place and over time. For example, in Oklahoma, USA, current field intensity is $F_M \approx 51\mu T$, which is the magnitude of three geomagnetic field components: north $B_X \approx 21.95\mu T$, east $B_Y \approx 1.135\mu T$, and vertical $B_Z \approx 46\mu T$ components [18].

$\boldsymbol{B}_{\gamma}$, is a three-dimensional vector that can be approximately modeled at Earth's surface as a magnet dipole (i.e., geocentric axial dipole), as it is tilted by 11.5° along the Earth's spin axis. Its south pole points towards geomagnetic north pole (see Figure 1-1).

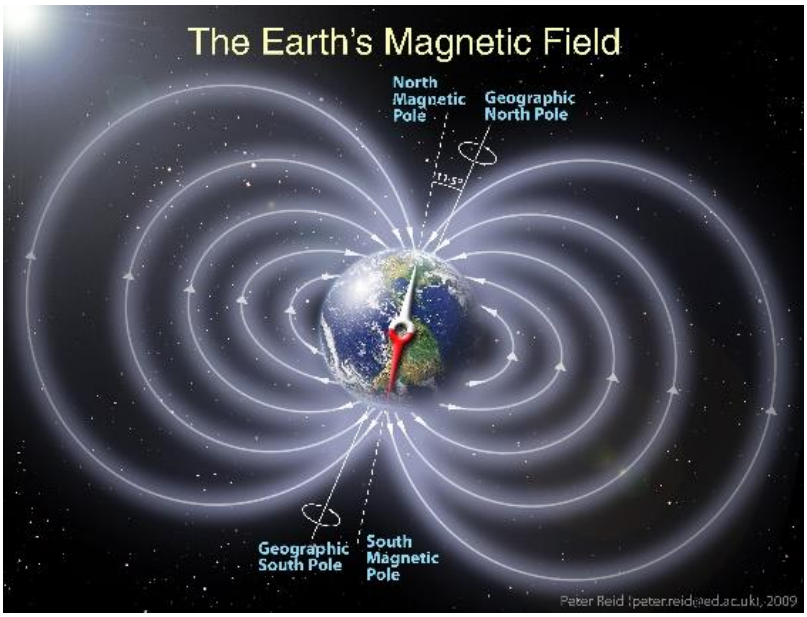


Figure 1-1 Earth's magnetic field lines distribution [19]

Geographic heading can be estimated by transferring $\boldsymbol{B}_\gamma$ to coordinate plane and knowing the declination angle. Field coordinate plane is shown in Figure 1-2. $\boldsymbol{B}_\gamma$ vector is described using seven components: 1) northerly intensity $\boldsymbol{B_x}$; 2) easterly intensity $\boldsymbol{B_y}$; 3) vertical intensity $\boldsymbol{B_z}$; 4) horizontal intensity $\boldsymbol{H}$; 5) total intensity $\boldsymbol{F_M}$; 6) inclination angle $\boldsymbol{I}$—angle between the magnetic field *B* and horizontal plane; and 7) declination (magnetic variation) angle $\boldsymbol{D}$—angle between the Geographic North and *H*. The quantities *H*, F_M, *I*, and *D*, can be determined using Eq. 1-1, Eq. 1-2, Eq. 1-3, and Eq. 1-4, respectively, from the orthogonal magnetic field components B_x, B_y, and B_z. Figure 1-2 depicts $\boldsymbol{B}_\gamma$vector elements in coordinate plane. Table 1-1 shows the range of magnetic elements at the Earth's surface.

$$H = \sqrt{B_x^2 + B_y^2} \qquad \textbf{Eq. 1-1}$$

$$F_M = \sqrt{H^2 + B_z^2} = \sqrt{B_x^2 + B_y^2 + B_z^2} \qquad \textbf{Eq. 1-2}$$

$$I = \tan^{-1}\frac{B_z}{H} = \tan^{-1}\frac{B_z}{\sqrt{B_x^2 + B_y^2}} \qquad \textbf{Eq. 1-3}$$

$$D = \tan^{-1}\frac{B_x}{B_y} \qquad \textbf{Eq. 1-4}$$

$$\Psi = \tan^{-1}\frac{B_y}{B_x} \mp D = \tan^{-1}\frac{B_y}{B_x} \mp \tan^{-1}\frac{B_x}{B_y} \qquad \textbf{Eq. 1-5}$$

Vehicles have a large mass of highly permeable ferrous materials (e.g., iron, steel, nickel, aluminum, or cobalt) that cause a small local disturbance in the Earth's magnetic field flux lines. Steel, in particular, has the capacity to concentrate flux lines, as its magnetic permeability is high relative to surrounding air. A vehicle structure with a substantial amount of steel can be detected from a significant distance (e.g., 10m). As a

vehicle passes through the Earth's magnetic field, the magnetic flux lines are absorbed in a non-uniform manner, as shown in Figure 1-3. The magnitude and direction of the disturbance depends on several factors, including speed, size, density, and permeability of vehicle structure. Different vehicles have different structures, hence, different disturbance factors relative to the geomagnetic field. This measured disturbance represents a vehicle's magnetic signature (VMS), which is unique and can be measured using MAG. VMS can be analyzed to distinguish between different types of vehicles.

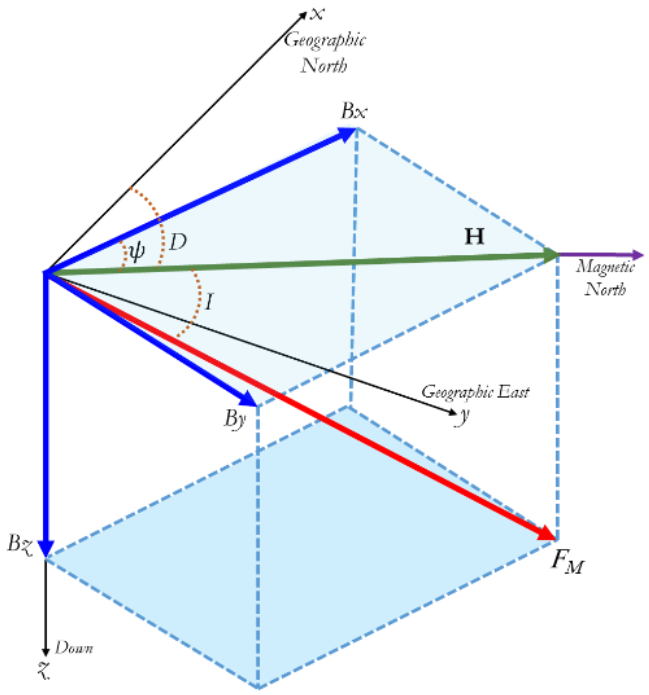


Figure 1-2 The seven elements of the B_γ vector in coordinate plane

The disturbance in magnetic field $\boldsymbol{B_\gamma}$ caused by a vehicle can be modeled as a large number of magnetic dipoles [20], each with its own moment μ and direction r in a three-dimensional space (see Figure 1-4), as given by Eq. 1-6 [21], where B_0 is the localized Earth's magnetic field vector; μ_0 is the magnetic permeability of free space given by $\mu_0 = 4\pi\times10^7\times N/A^2$; μ_i is the magnetic dipole moment of the i^{th} dipole; and r_i is the vector the i^{th} dipole moment μ_i to sensor location.

Table 1-1 Ranges of magnetic elements at the Earth's surface [22]

Element	Name	Range		Positive sense
		Min	Max	
B_x	Northerly intensity	-17μT	42μT	North
B_y	Easterly intensity	-18μT	17μT	East
B_z	Vertical intensity	-67μT	61μT	Down
H	Horizontal intensity	0μT	42μT	NA
F_M	Total intensity	22μT	67μT	NA
I	Inclination	-90°	+90°	Down
D	Declination	-180°	+180°	East/CW

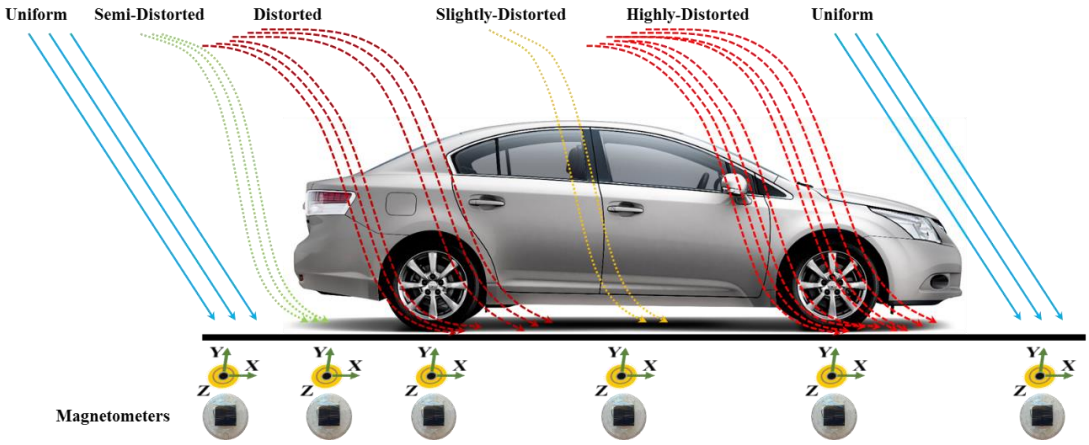


Figure 1-3 Earth's magnetic field lines distorted by passing vehicle

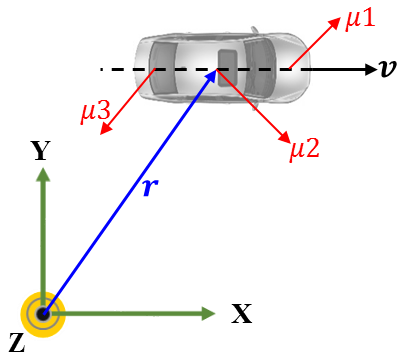


Figure 1-4 Magnetic dipoles moment and direction in a three-dimensional space

$$B_i(\overrightarrow{\mu_1}, \overrightarrow{r_1} \dots \overrightarrow{\mu_n}, \overrightarrow{r_n}) = B_0 + \frac{\mu_0}{4\pi} \sum_{i=1}^{n} \frac{3(\overrightarrow{\mu_i}.\overrightarrow{r_i})\overrightarrow{r_i} - \overrightarrow{\mu_i}|\overrightarrow{r_i}|^2}{|\overrightarrow{r_i}|^5}; \quad \textbf{Eq. 1-6}$$

$$\overrightarrow{\mu_i}, \overrightarrow{r_i} \in \mathbb{R}^3 \quad and \quad i \in \{x, y, z\}$$

A VMS can be described mathematically using a single point dipole model with a moment μ equal to the geometric sum of all dipoles and centered in the vehicle [23], as MAG measure the geometric sum of all dipoles on x, y, and z-axes. Hence, Eq. 1-6 can be written as in Eq. 1-7, where *i*=1. Given that a vehicle is moving, $\vec{B}(\vec{\mu},\vec{r})$ becomes a time-variant field and distance *r* becomes a function of time *t*, as shown in Eq. 1-8. This equation can ultimately be used to estimate the maximum magnetic field strength at distances *r* from a vehicle. It can also be used to estimate vehicle trajectory and speed [24], [25].

$$\vec{B}(\vec{\mu},\vec{r}) = B_0 + \frac{\mu_0}{4\pi}\frac{3(\vec{\mu},\vec{r})r - \vec{\mu}|\vec{r}|^2}{|\vec{r}|^5} \qquad \textbf{Eq. 1-7}$$

$$\vec{B}(t) = B_0 + \frac{\mu_0}{4\pi}\frac{3\left(\vec{\mu},\vec{r}_{(t)}\right)r_{(t)} - \vec{\mu}\left|\vec{r}_{(t)}\right|^2}{\left|\vec{r}_{(t)}\right|^5} \qquad \textbf{Eq. 1-8}$$

Assuming that background noise induced by on-board electronic components is modeled as an additive white Gaussian noise (AWGN), then data obtained from the sensors can be modeled as the sum of $\vec{B}(t)$ in Eq. 1-8 and AWGN $\emptyset$.

$$\hat{B}(t) = \vec{B}(t) + \emptyset_{\mu,\sigma} \qquad \textbf{Eq. 1-9}$$

1.6 Energy-Harvesting Solutions for WSN

Smart WSN equipped with sensors and an intelligent controller are among IoT devices. Figure 1-5 illustrates typical elements of a smart device. WSN and IoT are mostly battery-powered devices, and although these have a limited power budget, once deployed they are expected to be functional for an extended lifetime. Battery leakage, however, currently depletes the battery charge with time—merely a few years—even if rarely used [26]. The process of recharging or replacing batteries for spatially

distributed sensor nodes requires an enormous amount of time at a prohibitive cost. Even though optimizing energy and minimizing power consumption can help extend battery life, doing so is not the key to self-sustainable WSN. Notably, advances in battery capacity have not increased significantly in the last decades [27] when compared to the exponential advancement in semiconductor technology as a result of Moore's law [27]. For this reason and until there is a breakthrough in energy storage technology, research on self-sustainable WSN has redirected its focus from improving energy efficiency to introducing a micro-scale, energy-harvesting (EH) technology as the primary solution for maximizing the lifetime of WSN devices [28], [29].

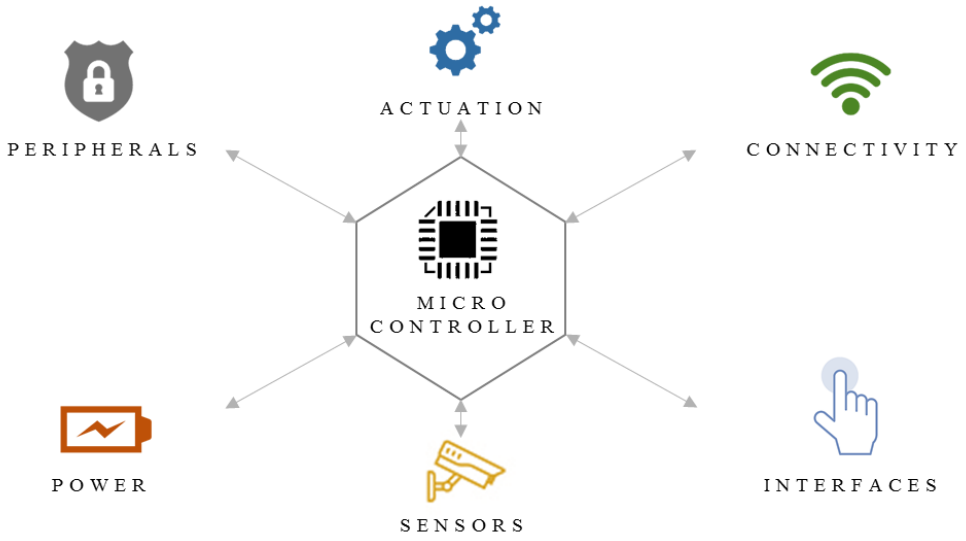


Figure 1-5 Earth's magnetic field lines distribution

Micro-scale EH, also called energy scavenging, is an eco-friendly solution based on the collection and conversion of microwatt to milliwatt energy from ambient sources, including, for example, solar (photovoltaic), vibration (piezoelectric), thermal (thermoelectric), and inductive (electromagnetic). EH have received significant attention in the last few years. Although the technology's solutions are in the initial stages, they are evolving rapidly, introducing more efficient EH and power management

chips, such as those manufactured by major semiconductor companies like Analog Devices, Texas Instruments, and Maxim Integrated, among others.

Solar energy is more widely used in EH applications, as it is inexpensive, easy to use, and has the highest power density (up to 30mW/cm^2) among other harvesters. Energy produced by photovoltaic cells is proportional to cell size and light source brightness. Piezoelectric harvesters produce energy from kinetic sources, such as vibration (e.g., motor, shoes). Piezoelectric harvesters require a predictable, consistent vibration frequency, which is one of the challenges when using Piezoelectric. Thermoelectric generator (TEG) produce energy from heat sources that have a constant temperature gradient. A comparison between various EH methods and harvesting-aware communication protocols for WSN can be reviewed in [28]–[30].

By combining all advancements in state-of-the-art ultra-low-power embedded systems, smart physical sensors, WSN, and EH will enable fully autonomous IoT devices that (ideally) will remain operational for decades without battery replacement. This technological innovation is vital for smart cities, smart homes, and smart energy.

1.7 Research Motivation

The *primary objective* for this research is designing, developing, and implementing a non-intrusive, inexpensive, and portable self-powered vehicular traffic monitoring sensor that a) accurately detects, counts, estimates speed and length, and classifies vehicles in real-time; b) can be used for short-term deployment (e.g., work zone safety, temporary roadway design studies, traffic management in an atypical situation, such as evacuations and other similar situations), as well as long-term deployment (e.g., traffic management, turn movement, and collision avoidance); and c)

is easy-to-install by simply affixing the sensor shell into the surface of highways, roadways, or roadsides without intrusive work. Such a solution will maximize existing transportation infrastructure capacity and improve efficiency, making transportation systems safe, efficient, and more reliable for the rapidly approaching era of smart cities.

A *secondary objective* is in response to the critical need of the Oklahoma Department of Transportation (ODOT) for an autonomous surveillance technology to monitor various traffic conditions. Results can be used to supplement current ITS installed throughout the state.

Because traffic volume has significant implications for highway and roadway safety, planning, and design, ODOT—like other U.S. transportation departments—is responsible for collecting permanent and temporary traffic characteristic data (e.g., vehicle count and class) from various statewide locations each year. Initially, data is used for transportation planning strategies and management processes. Unfortunately, many sites are not equipped with a vehicle counter. In this case ODOT personnel either conduct a manual count for a short period of time or hire a contracting company. The former requires intensive labor to visit hundreds of sites. Also, manual count is simply not feasible on congested highways with several lanes. Moreover, this method is usually conducted for only a few hours, which doesn't represent accurate traffic volume. Alternative methods used to collect vehicle count and class information in Oklahoma employ: 1) weight-in-motion (WIM) or automatic vehicle classifiers (AVC) deployed at permanent sites throughout the state or 2) pneumatic road tubes (PRT) installed temporarily for study proposes [31].

Currently, PRT are placed on the road surface, crossing the lanes and then fastened to the roadway. The axle of a passing vehicle causes a differential pressure in the tubes, which in turn triggers axle detection. Speed is estimated by measuring axle travel time from one tube to another. AVC, on the other hand, employ piezoelectric sensors with inductive loops that are embedded in the roadway. Although these technologies are known to be highly accurate, the systems have several drawbacks and have been known to cause installation difficulties. PRT, for instance, have a short life (e.g., as short as 48h [13]), can monitor only two lanes, and are prone to error (e.g., fake pulses or over count) due to tubes bouncing when hit by heavy vehicles traveling at high speeds [31]. Moreover, PRT installation often requires road closure and traffic disruption, making their use and the high cost of maintenance prohibitive. AVC are permanent systems deployed only at logistic locations where heavy truck volume has previously been observed. AVC have limited spatial distribution across the state because they are expensive and because recorded data is typically accurate only if maintenance and calibration is conducted every three or four months. Moreover, the safety of on-site workers deploying these system remains a major concern [13].

ODOT is in critical need of a technology that is inexpensive, nonintrusive, portable, and easy-to-install to supplement current ITS throughout the state and to collect accurate traffic information on a large-scale for extended period of time. Ideally, the system should come at a lower cost than the thousands of dollars paid every year for temporal counting studies at each AVC site.

1.8 Proposed Research

The proposed research aims at developing and implementing a novel, fully-autonomous, self-powered intelligent wireless sensor for various traffic surveillance applications. The sensor integrates state-of-the-art components, including an ultralow power, high-performance 32-bit embedded microcontroller; an energy-efficient wireless transceiver; smart embedded sensors (i.e., 3D MAG and ACCEL); a highly-accurate low-power embedded Global Positioning System (GPS) receiver; dual data storage units with ultralow power EH power management unit (PMU), maximum power point tracking (MPPT), and charge management controllers; a battery fuel gauge; a wireless power charging receiver; and atmospheric sensors. All components are managed by distinctive algorithms for implementing various traffic monitoring applications.

A 3-axis MAG sensor is used to measure magnetic disturbance to the Earth's magnetic field caused by an overpassing vehicle; a 3-axis ACCEL sensor is used to measure road surface vertical acceleration resulting from the motion of dynamic loads. Other components include a GPS module for auto-localization and global-synchronization; an RF module for wireless data transmission; and an EH for sensor self-powering and battery charging. Sensor node firmware can be upgraded over-the-air, which allows a customizable configuration to support various studies and applications. The sensor is functional in either standalone or peer-network mode wherein an intelligent access-point (*i*AP) manages WSN data transfer. Estimated cost for populating a four-lane highway in both directions is approximately $1000, which includes a 16-sensor node, a handheld wireless sensors configuration device, and an *i*AP.

1.9 Research Contributions

This dissertation introduces the design, development, and implementation of a novel, fully autonomous, battery-powered intelligent wireless sensor for traffic surveillance applications. The sensor integrates state-of-the-art embedded components, all of which are managed by distinctive algorithms for implementation of various traffic monitoring applications. All aspects and parameters necessary for design and implementation are addressed.

The developed sensor is portable, leverages primary battery-powered and solar cell energy, is inexpensive (i.e., $30 per node), and installs easily into the surface of highways, roadways, or roadsides without intrusive labor. The sensor can be used for short-term deployment (e.g., work zone safety, temporary roadway design studies, traffic management in an atypical situation such as evacuations), as well as long-term deployment (e.g., traffic management, turn movement, collision avoidance, etc.).

A novel multi-threshold-based detection algorithm is also introduced, wherein a drift in geomagnetic reference field baseline threshold (due to aging or due to variations in temperature and/or background noise relative to Earth's magnetic field over time) is adaptively auto-compensated in real-time. This method solves common problems reported in literature by keeping magnetic signal variation at a minimum, hence, providing reliable vehicle speed estimation under congested traffic, as well as low- and high-speed conditions.

A highly accurate and energy-efficient time-synchronization algorithm that utilizes GPS reference signal PPS (Pulse-Per-Second) was developed and implemented

as part of research for this dissertation, as was an algorithm for adaptive compensation of RTC Frequency Drift due to variations in temperature.

The repeatability of VMS and the consistency of MAG sensor output were investigated to determine degree of similarity between several magnetic signatures produced by multiple MAG sensors for the same vehicle under identical testing conditions. Vehicle tracking and vehicle re-identification were reported.

Several computationally efficient, real-time, length-based vehicle classification schemes developed for the state of Oklahoma were implemented and evaluated via machine learning algorithms and probabilistic modeling. Two vehicle re-identification models based on matching vehicle magnetic signatures from a single MAG were also developed.

A non-provisional patent was filed with the U.S. Patent Office on November 07, 2016 under patent application number 15/330,823; confirmation number is 7135.

1.10 Dissertation Structure

This dissertation consists of eight chapters, which are organized as follows:

- *Chapter 1*: Includes a general introduction of the scope of this dissertation, including a discussion about current technologies used in ITS; Smart cities ITS; wireless sensor networks in ITS; MAG theoretical concept and its application in traffic surveillance; the motivation for this research; and research contributions.
- *Chapter 2*: Provides a literature review of related work and focuses on relevant research contributions in vehicle surveillance using MAG, including vehicle detection, speed and length estimation, vehicle classification and re-identification, and time-synchronization in WSN, as well as EH.

- *Chapter 3*: Introduces a detailed description of the sensor system level design in its old and new generations, including design aspects, components selection, and system architecture and networking.
- *Chapter 4*: Includes information about software development and introduces various distinctive real-time algorithms developed for vehicle detection, speed and length estimation, time synchronization, drift correction, and other functions.
- *Chapter 5*: Reports field-testing and data collection studies conducted on various highways and roadways throughout the state of Oklahoma.
- *Chapter 6*: Highlights extensive data analysis and performance evaluation of the various functionalities of the developed platform.
- *Chapter 7*: Introduces two applications for *i*VCCS in traffic surveillance.
- *Chapter 8*: Presents research outcomes and makes recommendations for further research work.

Chapter 2: BACKGROUND & EXISTING KNOWLEDGE

2.1 Introduction

Vehicle-counting and classification data, in particular, play a vital role in designing roadways and bridges; predicting freight transport; scheduling maintenance operations for pavement resurfacing, reconditioning, and reconstruction; traffic planning; weight enforcement strategies; and analyzing road safety and environmental impact, among a number of other purposes [13]. Over the last decades, a vast number of methods have been proposed in literature. Each leverages various types of sensors and focuses on investigating and developing new innovative solutions for traffic surveillance. The methods aim to replace antiquated traffic surveillance technologies by implementing smart WSN. One approach for traffic surveillance that is gaining research attention is utilizing wireless MAG [32]–[58].

2.2 Traffic Monitoring using MAG

The use of magnetic sensors in vehicle detection can be traced to early 1978 [32] when a fluxgate magnetic sensor was used to actuate a lighting system as a vehicle passed the sensor. A recent study [33] proposed a 2-axis MAG for detecting vehicle driving direction. A detection rate of 99% was observed when traveling vehicles passed closely to the sensor. Performance degraded to 89% as the signal-to-noise ratio (SNR) decreased. A two-threshold, four-state machine algorithm was proposed in [34] for vehicle detection using 3-axis AMR sensor. An active magnetic detection method was introduced in [35]. Although this method solved the baseline drift problem, it was not efficient in power, cost, or size. Authors in [36] proposed a short-time transform detection-and-recognition algorithm using a MAG sampled at 2KHz. Work proposed in

[37] integrated IEEE 802.15.4 transceiver with 32-bit MCU and 1-axis AMR for a vehicle counting and collision warning application. A 3-axis MAG was used in [38] for vehicle detection in parking lots. In [39], a street parking system using a MAG was introduced, and in [40], researchers proposed a vehicle parking detection method using a normalized cross-correlation of a 3-axis MAG signal. Authors in [41] proposed a scheme for identifying the heading direction of a moving vehicle using a two-axis MAG. A wireless link budget study for intersection monitoring using MAG was proposed in [42].

Vehicle speed estimation is a key parameter for traffic surveillance applications [13]. Essential applications demanding speed estimation included length-based vehicle classification [59]; travel time estimation [60]; ramp-metering queue length estimation [61]; work zone safety [62]; curve warning [63]; vehicle emissions estimation [64]; and traffic light control, among many others. More recently, solutions based on cost- and power-efficient sensors (e.g., acoustic, MAG, and ACCEL) have become ever more popular. Each has advantages and disadvantages. For example, acoustic and ultrasound sensors are very sensitive to dirt and background noise (e.g., vehicles or wind). In this study, vehicle speed was estimated using MAG sensors.

A speed estimation algorithm using MAG was proposed in [43]–[45]. In these studies, a cross-correlation factor R was calculated via FFT by a master node from raw data received via two roadside sensor nodes. Time delay was obtained by R when the resulting signal was maximized. Although this method achieved relatively accurate estimates, it proved computationally expensive, hence, energy inefficient. A region-based approach for speed estimation was proposed in [46]. In this work, the first order

derivative was calculated on each sensor node, and a region of each signal was selected based on a threshold sent to the server for processing. Researchers in [47] claimed 90% average speed estimation accuracy by analyzing magnetic length using a single roadside node composed of an accelerometer (ACCEL) and MAG. Two magnetic sensor nodes were used in [48] to estimate speed, and a third node was used for data fusion. Actual speed was underestimated at an error rate of 20%. Authors in [49] proposed using four magnetic sensor nodes—two on each side of the lane. A 10% error in speed estimation under low speed test (e.g., 6–13m/s) was reported. Studies in [50], [51] proposed algorithms for speed estimation using a single MAG. Notably, this method was designed to estimate only average speed for the number of passing vehicles over time.

Four roadside MAG nodes were used in [43] for detection, speed estimation, and vehicle classification into four groups based on length and height ratio. Two sensor nodes were longitudinally separated by 90cm to estimate vehicle speed. A third sensor node was placed orthogonal to the first sensor node with a separation of 10cm for identifying false detection from an adjacent lane. A fourth sensor node was placed upright relative to the first sensor on a 30cm elevation for differentiating trucks from other vehicles, as height is proportional to the ratio of z-axis of both sensors. Vehicles were classified into four groups based on length and height ratio. Group 1 included sedans; Group 2 included SUVs, pickups, and vans; Group 3 included buses, as well as two and three axle trucks; and Group 4 included 4- to 6-axle trucks. Acceptable accuracy was reported. Of note is that the proposed method worked for only single lane urban roads. Furthermore, the major dataset was composed of small vehicles records; only a few trucks were included. Thus, results were inconclusive. Vehicle classification

and detection using a single-axis magnetic sensor and an improved one-against-all support vector machine (ISVM) classifier was proposed in [52]. The proposed algorithm uses concavity and convexity of magnetic signatures to distinguish among heavy tracked, tracked, and light-wheeled vehicles. A limited dataset of 93 vehicles resulted in 90% classification accuracy. In [53], a 3-axis MAG was used for detection and classification in low-speed, congested traffic. A fixed-threshold state machine algorithm was employed for vehicle detection, and a tree-based algorithm was implemented for classification. Vehicles were divided into four groups: motorcycles, saloon, buses, and SUVs. Five features —duration, energy, average energy of vehicle signature, and ratio of positive to negative energy on both X and Y axis—were extracted to distinguish between the groups. The dataset included only 253 vehicles. Although high detection and classification rates were reported, the dataset was limited to a small number of samples, and trucks and pickups were not considered. Authors in [65] proposed a vehicle classification system using two nodes installed on roadside, each combining an ACCEL and MAG. Three features, namely the integral of each of MAG magnitude, ACCEL magnitude, and magnitude distribution, were extracted and normalized to vehicle speed. Several machine-learning (ML) methods (e.g., logistic regression, neural networks, naïve based, and space vector machine) were tested. A 93.4% classification accuracy was reported for distinguishing between three groups—motorcycles, passenger cars and pickups, and heavy trucks. Notably, more than 90% of the dataset was composed of passenger cars. Moreover, class variation in the dataset was limited, and class 5 vehicles with trailers were missing. The absence of class 5 vehicles can significantly hinder classification accuracy, as these vehicles can be seen

on both urban and highway roads and can cause classification confusion due to significant variations. Furthermore, accurate clock synchronization is required for speed estimation, as all extracted features are normalized to speed. In [55], an array of MAG and ACCEL sensors was proposed for vehicle detection, speed estimation, and classification. In this study, three MAG nodes positioned longitudinally reported vehicle arrival and departure times, and six ACCEL sensors spaced six inches apart were positioned over half the lane to detect vehicle axles via a peak detection algorithm. This method was used to guarantee that at least one wheel on each axle would cross one of the ACCEL sensors. Although this method showed promising results for detecting 2-axle, 3-axle, and 5-axle vehicles, it was deemed expensive and required an enormous amount of intrusive work and high processing capability. Authors in [56] developed a features selection model for vehicle classification using a single MAG in which 17 features were initially identified and extracted, but only 10 suitable features were eventually selected. A limited dataset of 460 vehicles—mostly small cars—resulted in 92.8% average classification accuracy among four groups, including buses, small-medium cars, and large trucks. Authors in [57] proposed a detection and classification approach using a state machine detection algorithm, a shared adaptive threshold to compensate background noise, and a neuron classifier. A 2-axis AMR sensor was employed. A 90% recognition rate was reported for simulation and on-road testing. Authors in [58] integrated MAG, ACCEL, acoustic, and infrared sensors within a single sensor node for vehicle classification. Several features were extracted, including infrared signal peaks count and the minimum and maximum values of MAG and ACCEL signals. A back-propagation neural network was trained to classify vehicles

into three groups—light, medium, and heavy vehicles. Dataset was limited to only 50 vehicles. Medium vehicles were classified with acceptable accuracy. However, 25% of light vehicles and 16.7% of heavy vehicles were misclassified. Authors in [66] proposed vehicle detection algorithms based on a state-machine normalized cross-correlation between two sensors placed along the roadside. The study implemented a Gaussian filter to eliminate any interference induced by moving vehicles from adjacent lanes; a k-means clustering for setting a reference for cross-correlation detection state; and a normalized cross-correlation computation between two magnetic signals for speed estimation. A 99.65%, 99.44%, and 92% accuracy was reported for arrival detection, departure detection, and vehicle speed estimation, respectively. Although this method showed good accuracy, it required transmitting the magnetic signature from all sensors to a central access point for processing. In addition to the platforms detailed above, a number of commercial platforms based on MAG are also currently available [67]–[69].

In the aforementioned solutions, vehicles were detected using a single magnetic sensor; vehicle speed was typically estimated using two sensors at a predefined distance; length was calculated from speed and occupancy time; and vehicle classification was achieved by employing either multiple MAG or ACCEL sensors, or a combination of both. A standardized wireless protocol (e.g., IEEE 802.15.4) was considered for node-to-node and node-to-AP communications and synchronization. In most of these solutions, sensors were embedded in roadway lanes. Although the time required for installing some systems [67]–[69] into the pavement was comparatively small, the systems are relatively expensive, intrusive, and cannot be used for temporary studies or portable traffic surveillance applications (e.g., work zone safety, roadway

design studies, and managing traffic in emergency situations, like evacuations, among others). Although a variety of detection, speed estimation, and classification methods have been proposed, there has been limited evaluation of detection or classification accuracy per vehicle class over a full range of speeds. Furthermore, reported results do not reflect actual performance, as testing datasets were small and limited. Notably, classes 5 to 13 were highly underrepresented. Additionally, some proposed methods [43], [45] were energy-inefficient (i.e., computationally very expensive) and required transmission of big chunks of data to the access point for processing. These are fundamental limitations to WSN, as the sensors are battery-powered and their network operates in an unlicensed spectrum in a shared bandwidth among a vast number of different technologies and devices. Hence, high data loss is highly probable because of unstable wireless links resulting from either interfering or heavy trucks traveling over the detection zone. Other methods [47] relied on the assumption that vehicles of the same class moving at the same speed have nearly identical signatures. This assumption is misleading for the following reasons: 1) Magnetic length does not represent actual vehicle length; 2) lateral distance might change for the same vehicle; and 3) magnetic length estimation accuracy depends on the sensor's sampling rate tolerance, which normally has a ±5% error and can be affected by temperature variations. Additionally, little activity has been performed to evaluate detection and speed accuracy per vehicle class over a full range of speeds. A single method fails to encompass variances between different magnetic characteristics.

More importantly, and to the best of the author’s knowledge, no study has reported detection error types, methods for optimizing MAG for ideal performance, or

suggestions for consistency of MAG sensors output. Furthermore, limited information was provided in the literature about system design, algorithm development, and comprehensive analysis in various realistic scenarios.

2.3 Time Synchronization in WSN

Time synchronization (T-sync) is crucial in communication systems to ensure accurate functioning and data fusion, coordinated actuation, and power-efficient duty cycling. T-sync for wired communication networks has been studied thoroughly, and numerous algorithms have been developed in the last decades. Network Time Protocol (NTP) is perhaps one of the most advanced and time-tested systems [70]. Networks using NTP externally synchronize nodes to a global reference time that is injected into the network at many places via a set of master nodes synchronized using GPS. Power consumption and computational energy constraints make NTP unfeasible for WSN. Hence, maintaining a T-sync within WSN is challenging, yet still critical.

Tremendous effort has been made to implement T-sync protocols for WSN. Authors in [71] introduced *Reference Broadcast Synchronization* (RBS) protocol for WSN. In RBS, nodes broadcast reference beacons to neighbor nodes. Nodes use the beacon signal as a point of reference for their internal clock phase alignment. Authors in [72] proposed *T-sync Protocol for Wireless Sensor Networks* (TPSN). The principle behind TPSN is that a multi-level hierarchical network topology is created in which all nodes are assigned levels based on number of hops from root node (level 0). After the topology is created, a root node initiates a synchronization phase wherein every node belonging to level i synchronizes to a node in level $i-1$, and so on, until network-wide synchronization is achieved. TPSN achieves an average synchronization error equal to

$16.9\mu S$, which is a considerable improvement above the $29.13\mu S$ error in RBS. Authors in [73] introduced *Energy-Efficient Time Synchronization Protocol* (ETSP), implementing a switching mechanism between RBS and TPSN to reduce node power consumption. The switching threshold relies on the number of transmissions required to maintain synchronization, which, in turn, depend on the number of network nodes. Authors in [74] proposed *Distributed Multi-hop Low cost Time Synchronization* (DMLTS) protocol based on RBS and TPSN. DMLTS is an improved ETSP, synchronizing a group of nodes upon hearing the timing messages of a pair of nodes. This reduces the number of exchanged messages and, notably, overall energy consumption. In addition to the protocols mentioned above, *Flooding T-sync Protocol* (FTSP) [75], *Gradient T-sync Protocol* (GTSP) [76], and *Lightweight Time Synchronization* (LTS) [77] are widely used in WSN. Although such protocols have reasonable T-sync precision, several challenges remain, for example: 1) failure in wireless communication during synchronization; 2) drift error in T-sync over multi-hop (3.68μs, 20μs, and 3μs on 4 hops in RBS, TSPN, and FTSP, respectively) [78]; 3) master node requirement, 4) essential linear regression (e.g., FTSP), which is computationally demanding and power consuming; 5) TSPN-required hierarchical structure of nodes; and 6) RBS need for separate timestamp synchronization messages for which average error grows with $O(\sqrt{n})$ over multi-hops. These challenges make protocol implementation impractical for a large-scale WSN and infeasible for strict deterministic T-sync requirements. Moreover, T-synch through a periodic or frequent exchange of timing packets among network nodes imposes high power budget demand. According to [79], energy cost of 1Kbit data transmission for a 100m distance is

approximately the same as executing 3-million instructions on a 100 MIPS/Watt processor. Hence, local processing is crucial in multi-hop WSN for minimizing power consumption.

Due to rapid technology advancement and increased demand, embedded GPS modules have quickly improved in signal sensitivity, accuracy, performance, cost, size, and, more importantly, power consumption. Embedded GPS modules can now be considered the most simple and cost effective solution for high precision timing and clock synchronization. Previously, this approach was not recommended for a number of reasons, most notably energy consumption and cost. Recent studies have investigated the feasibility of using GPS for T-sync in WSN. For example, the feasibility of using a low-cost GPS receiver for T-sync of wireless smart sensors for structural health monitoring was investigated in [80]. Authors in [81] developed a GPS-based time synchronization algorithm for WSN with nanosecond accuracy. Authors in [82] claimed ±23μs T-sync accuracy of a single-hop coordinated WSN. The proposed algorithm aimed at correcting sensor node internal clock drift by transmitting a beacon from a corresponding coordinator every 245.76ms. Upon beacon packet arrival, the RF chip generates an interrupt and triggers an internal MCU timer to measure the internal clock, calculate the difference, and compensate the drift. The coordinators, on the other hand, use the PPS (Pulse-per-Second) signal from a GPS module to calculate their internal clock drift and compensate the drift error. This method, however, doesn't account for measurement uncertainties, a variety of propagation paths, or interference from other devices in the ISM band where calculated drift can be affected by jitter. Moreover, several accumulated errors are not considered (e.g., RF chip interrupt tolerance), which

renders results unrealistic. Authors in [83] used a GPS DSP platform to control the processor's RTC drift and compensate phase shift when using a 1-PPS signal. Authors reported T–sync accuracy. Details on T-sync protocols for WSN can be found in [78], [84].

Chapter 3: SENSOR DESIGN & SYSTEM INTEGRATION

The roadmap to design and implement a real-time, standalone, smart wireless sensor that exploits MAG in traffic surveillance applications requires an in-depth understanding of embedded systems hardware-software development process, including component selection, hardware design, software development, system integration, and debugging. The design process and system integration of the intelligent vehicle counting and classification sensor (*i*VCCS) are introduced in the next sections. Various algorithms developed for *i*VCCS are introduced in the next chapter.

3.1 System Overview

The multi-disciplinary, innovative integration of systems modeling—coupled with state-of-the-art smart physical sensors, wireless sensor networks, embedded systems, and intelligent algorithms—will address the components composition of the developed platform, which is purposefully designed to support various traffic surveillance applications and studies. Figure 3-1 illustrates a conceptual diagram of the various components that compose the developed system, where *i*VCCS nodes are installed into enclosures. Two enclosures are deployed in each lane on a roadway at predefined distance *d*. The system's wireless networking between *i*VCCS nodes and an intelligent access point (*i*AP) is facilitated through IEEE 802.15.4 protocol with ZigBee application layer on top. Wireless networking between *i*AP and server is managed over a cellular network that is assisted by a Quad-Band GSM/GPRS/LTE chipset with GPS module on-board.

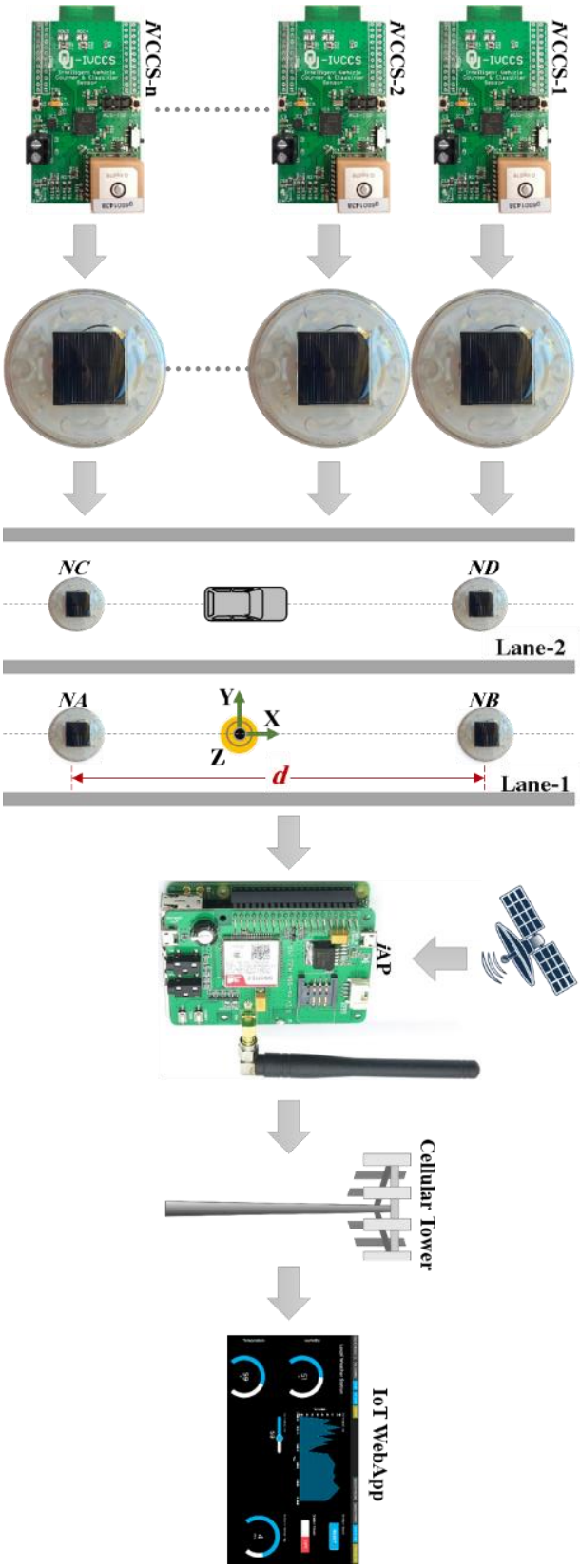


Figure 3-1 Conceptual diagram of developed system

3.2 Design Objectives and Requirements

Two prototypes—representing two generations (G1 and G2) of *i*VCCS—were designed during this research work period. The focus during the first prototype was developing and validating various algorithms and firmware to achieve highly accurate, real-time traffic monitoring using MAG. As algorithms were developed and validated, the focus in the second prototype was on finalizing sensor hardware and implementing self-powering and wireless charging features. Both prototypes share the same design objectives (See Table 3-1). A flow diagram of the design process can be found in APPENDIX C.

Table 3-1 *i*VCCS design objective

Requirement	Description
1) Cost	→ Inexpensive technology that can be deployed in mass-quantities
2) Setup	→ Nonintrusive technology that is easy-to-install and doesn't disturb traffic
3) Energy budget	→ Power-efficient technology that can run on battery for long time
4) Performance	→ High accuracy and real-time execution should not be compromised
5) Reliability	→ Should be highly reliable and able to recover from any system faults
6) Lifetime	→ Sensor components should be supported for the next 10 years
7) Portability	→ Can be used for permanents or temporary traffic monitoring studies
8) Flexibility	→ Programmable to supports various traffic monitoring studies applications
9) Scalability	→ System network can be easily expanded by adding more sensors
10) Adaptability	→ Sensor components should function in wide temperature range
11) Size/Weight	→ Should be as small as possible in size and lightweight

3.3 Components Selection Methodology

The primary objective of the selection process is identifying groups of components that should be evaluated for potential integration in the design. A selection criteria was developed to rank and evaluate each component individually based on three factors: 1) characteristics, 2) cost, and 3) size. Component characteristics can be

obtained from the component's datasheet, which defines the features and performance of the component at various conditions, including power consumption and operating temperature. The criteria and important aspects of the selection process for each component are explained in the following sections.

3.4 *i*VCCS$_{G1}$ Platform Overview

The *i*VCCS.G1 is a battery-powered, smart wireless sensor node. All components that compose the sensor, shown in Figure 3-2, were selected to achieve minimal power consumption while maintaining low cost and high-performance of the sensor. Figure 3-3 shows *i*VCCS$_{G1}$ printed circuit board (PCB) and component distribution on top and bottom layers. Board dimensions are 65(L)×36(W)×16mm(H).

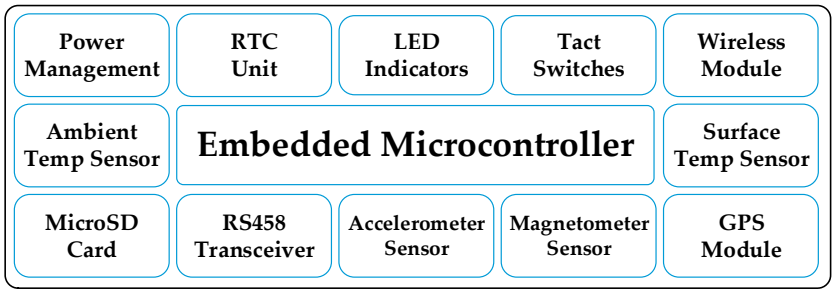


Figure 3-2 *i*VCCS$_{G1}$ functional components block diagram

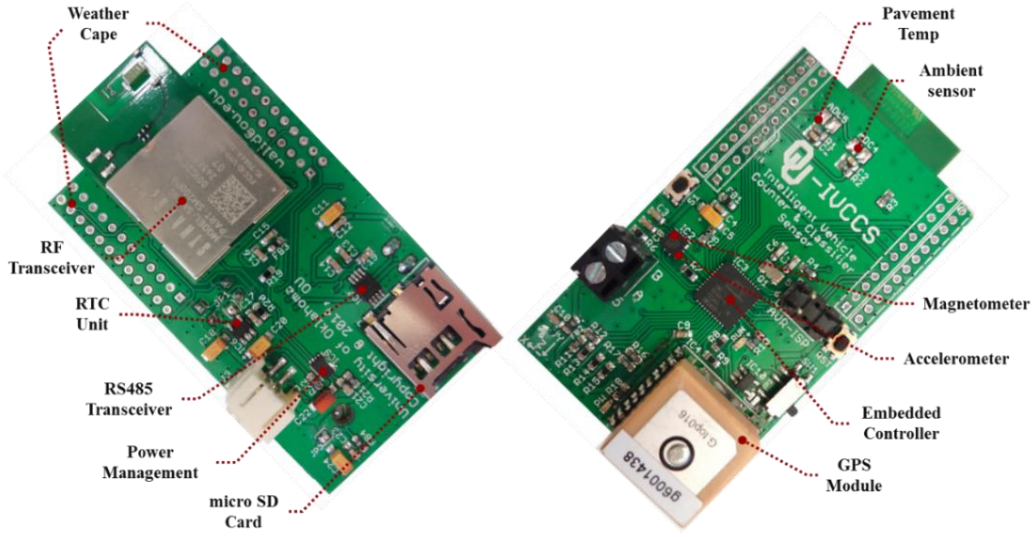


Figure 3-3 *i*VCCS$_{G1}$ printed circuit board with all components marked

3.4.1 Embedded Microcontroller

The core component of *i*VCCS$_{G1}$ is ATxmega128A4—a high-performance, pico-power, 8-bit microcontroller from Atmel [85]. Figure 3-4 illustrates the ATxmega128A4 block diagram and pin layout. ATxmega128A4 has an eight-channel event system with four-channel DMA controller that simultaneously manages eight inter-peripheral signals at 32MHz without CPU intervention. The chip also combines 128KB in-System-Programmable flash memory for developing advanced codes and algorithms for future applications. The event handler enables the system to avoid software-managed context switching and interrupt handling. Tasks are achieved with event-response time in nanoseconds. ATxmega128A4U also has a programmable multi-level interrupt controller, and 34 GPIOs, as well as rich peripherals and serial interfaces, including USART, TWI, SPI, 12-bit A/D and D/A converter, and RTC, among other on-board peripherals.

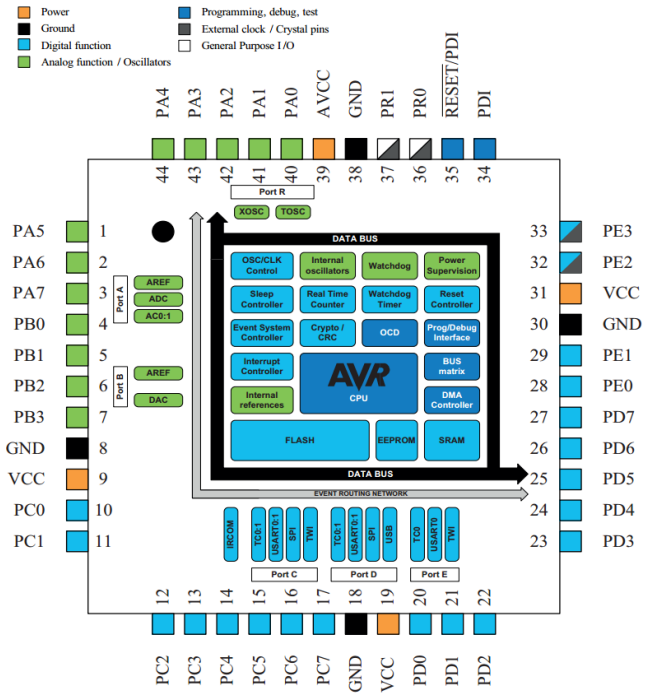


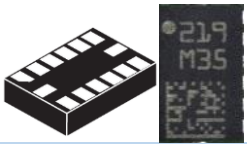
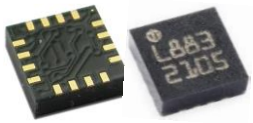
Figure 3-4 ATxmega128A4 internal block diagram and pin-layout

ATxmega128A4 has 10mA, 3.8mA, 1.4µA, and 1µA power consumption in active, idle, power-down, and power-save modes, respectively. It requires 5µs to wake-up from power-down mode and transition to active mode. These features, in addition to the fact that Atmel was confirmed in 2013 as the fastest growing among the top 10 suppliers for 8-bit MCUs, made ATxmega128A4 the best 8-bit MCU candidate.

3.4.2 Magnetometer & Accelerometer Sensors

An extensive search was conducted to find the MAG/ACCEL that best fit the selection criteria. Essential characteristics considered in the selection and evaluation process were output data rate (ODR), sensitivity, resolution, measurement range, disturbing field, power consumption, and cost. Table 3-2 lists specifications of the top three industry-leading MAG sensors available in the 2014 marketplace.

Table 3-2 Top MAG candidates for *i*VCCS$_{G1}$

	Freescale FXOS8700CQ 	**STMicroelectronics LSM303DLHC** 	**Honeywell HMC5883L** 
Interface	I^{2}C/SPI + 2-INT	I^{2}C + 2-INT	I^{2}C + 1-INT
Integration	6-axis ACCEL-MAG	6-axis ACCEL-MAG	3-axis MAG
Measurement Range	±12 Gauss	±1.3 ~ ±8.1 Gauss	±1 ~ ±8 Gauss
Update Rate (ODR)	1.563Hz ~ 800Hz	0.75Hz ~ 220Hz	0.75Hz ~ 75Hz
Measurement Period	0.64s ~ 1.25ms	1.33s ~ 4.55ms	1.33s ~ 13.33ms
Resolution	16-bit ADC	14-bit ADC	12-bit ADC
Sensitivity	1 mGauss	2 mGauss	4 mGauss
Disturbing Field	100 Gauss	20 Gauss	-
Maximum Field	1000 Gauss	10,000 Gauss	-
Power Consumption	240µA / 2µA (Idle)	110µA / 1µA (Idle)	100µA / 2µA (Idle)
Cost	US$1.25	US$3.00	US$1.75
Package	QFN-16 (3×3×1.2 mm)	LGA-14 (3×5×1 mm)	QFN-16 (3×3×1.2 mm)

FXOS8700CQ was the best fit for design requirements. FXOS8700CQ is an intelligent digital chipset, combining a 3-axis magnetic tunnel, junction-based MAG, and a 3-axis ACCEL sensor in one package [86]. The MAG has a dynamic range ±1200μT and 16-bit ADC resolution with sensitivity of 0.1μT/LSB. Power consumption is as low as 8μA and only 2μA in standby mode. FXOS8700CQ has the highest ODR among all other sensors and incorporates the industry's most advanced embedded features that enable significant system optimization for low power with substantially more savings when the application is driven by interrupt signals. In addition, the chip has a wide measurement range, high resolution (0.1μT/LSB), very low noise density (0.1μT/$\sqrt{Hz}$ at 100Hz bandwidth), high sensitivity, low output noise range (0.3–1.5μT_{RMS} for sampling rates 1.563–800Hz), ability to manage a high disturbing field, low cost, and low power consumption. Unlike other AMR sensors, FXOS8700C uses micro-electro-mechanical system (MEMS) technology with advantages in terms of cost, size, weight, and energy [87]. Figure 3-5 details the FXOS8700CQ block diagram.

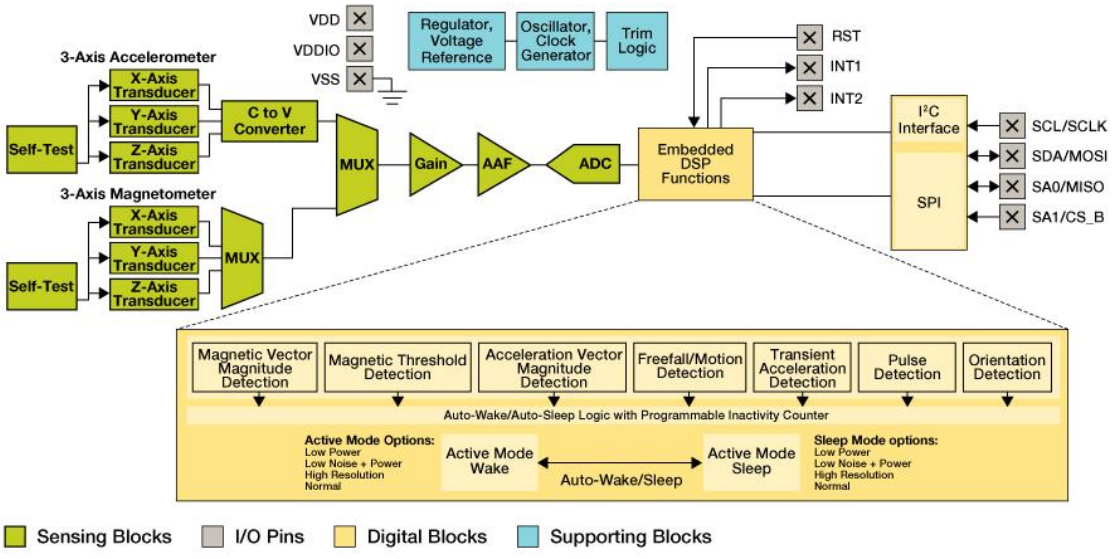


Figure 3-5 Freescale FXOS8700CQ System Block Diagram

The integration of MAG and ACCEL can be used not only for vehicle detection, but also to classify vehicles [55], such that the MAG detects presence of a vehicle by measuring disturbance to the Earth's magnetic field and ACCEL detects number of axels by measuring the vertical acceleration of a road surface due to motion of dynamic loads.

3.4.3 Embedded RF Engine

Networking between *i*AP and *i*VCCS.G1 nodes is facilitated through a low-power wireless protocol. ZigBee is one of the key enabling wireless technologies for IoT devices. This technology operates in sub-GHz and 2.4 GHz ISM (industrial, scientific and medical) radio bands based on IEEE 802.15.4 physical and MAC layers.

Among many available commercial ZigBee modules, Synapse's SM200P81 RF Engine [88] was found to be a suitable wireless interface candidate for the sensor design in all selection criteria. For example, transmit power is 3dBm with range of 1500ft and data transfer rate up to 2Mbps. More importantly, power consumption can be as low as 1.37μA with 22.5mA data transmission and 20.5mA during data receiving. Receiver sensitivity is -100dBm. Unit size is 30×19mm and costs about $17.9/1KU. Outdoor line-of-sight (LOS) range can extend up to 450 meters. SM200P81 incorporates Synapse's SNAP mesh network operating system [89], which facilitates multi-hop, instant-on, self-healing, and internet-enabled mesh networking between network devices. Figure 3-6 illustrates the SM200P81 physical module and its internal block diagram.

3.4.4 Real-Time Clock

Time-stamping is enabled by Maxim Integrated DS3231M [90], an extremely accurate, low-cost, real-time clock (RTC) unit that incorporates the industry's first temperature-compensated MEMS resonator with ±5ppm accuracy (±0.432 second/day). MEMS reduce crystal mechanical failure susceptibility. The chip has two programmable alarms and a 1Hz output (PPS), as well as a battery backup (3V) for continuous timekeeping for 10 years. In 2014, DS3231M was considered the most accurate RTC chip on the market.

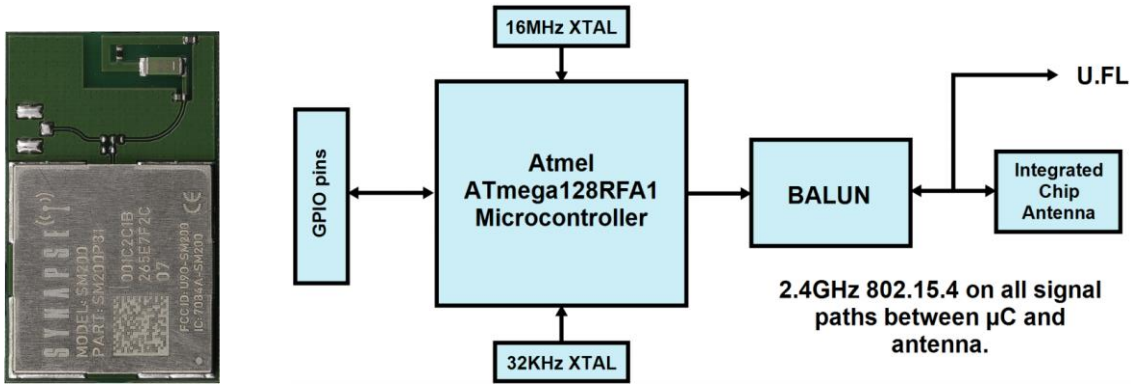


Figure 3-6 SM200P81 Module block diagram

3.4.5 Embedded GPS Module

To enable self-configuration, auto-localization, and accurate synchronization of a scalable network, a Titan 2 Gms-g6 GPS module was incorporated on *i*VCCS [91]. Titan 2 is a compact, dual-system GPS receiver module with built-in patch antenna, featuring up to 210 PRN channels, including 99 search channels and 33 simultaneous tracking channels. Titan 2 provides 2.5m positioning accuracy, ±10ns timing accuracy, and up to 10Hz update rate, as well as low-power consumption at a cost of only $16 per module. Titan 2 has a backup power mode that operates the internal RTC unit even when main power is off. This feature helps retain satellite information, locking satellites

in about 1-sec on power-up instead of performing a lengthy 30-sec cold start. Power consumption is 9μA in backup mode, 350 μA in standby mode, 23mA in tracking mode, and 25mA in accusation mode. Module size is 16×16×6.8 mm. Figure 3-7 shows the Titan 2 module.

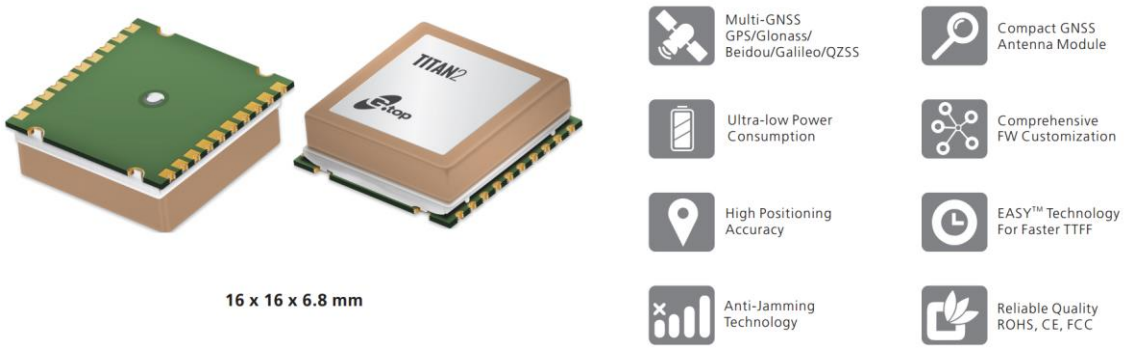


Figure 3-7 Titan 2 Gms-g6 GPS module

3.4.6 Power Management Unit

Quiescent current (Iq) is an extremely important parameter when comparing the low-power performance of various integrated chips, hence, selecting the best components for low-power design. Iq can be defined as the current drawn by a device in a load-free state (i.e., Iq represents the minimal current that supports a device's basic functionalities). Iq can be used to estimate battery run time.

The power management unit included TPS78333, an ultra-low quiescent current (i.e., Iq=500nA) with low dropout voltage (i.e., 150mV) 3.3V linear voltage regulator. TPS78333 has a thermal shutdown and overcurrent protection. Shutdown current is 18nA.

A 3.7V/2000mAh Polymer Li-Ion battery is used to supply the system. Li-Po batteries are a best fit for powering handheld and portable devices—small, lightweight, and durable. Notably, the batteries should never be discharged too low. If battery

voltage drops below approximately 3.0V per cell, the battery will no longer accept a full charge and might not hold voltage under load. As such, the load must be discounted the moment voltage drops below 3V.

MAX17043 was used to protect battery from deep-discharging [92]. MAX17043 is an ultra-compact, low-cost, host-side, fuel-gauge system for Li-Po batteries. The chip uses sophisticated algorithms to detect battery state and voltage. Shutdown current is 0.5µA. In addition to estimated capacity data sets, battery measurements can be accessed by the MCU over I^2C bus and later reported by *i*VCCS to *i*AP.

TPS78333 provided a shutdown pin controlled by MAX17043. In the event that battery voltage drops below a predetermined threshold, the MAX17043's ALT pin will shutdown regulator output.

3.4.7 Data Storage Unit

Since the sensor should support various studies and applications—which might include sampling the geomagnetic field at high sampling rate and storing raw data for an extended period—a microSD card was incorporated on board. Several microSD cards were tested. ScanDisk microSD cards were selected because compared to others, they have the lowest power consumption. Also, they support automatic switching between active and sleep mode. In general, the card will remain in sleep mode except when accessed by the host for data read or write. After completion of an operation in 5ms, the card will automatically return to and remain in sleep mode until a new command is issued by the host. Power consumption is around 20mA during a page-write operation at 10MHz rate. Buffering the data is recommended before transferring it into the card to ensure ample time in sleep mode.

3.4.8 Road Surface Condition Sensors

In addition to the aforementioned peripherals, *i*VCCS.G1 is equipped with road surface condition monitoring, including temperature and wet-dry sensors. The temperature sensor is a negative temperature coefficient (NTC) resistor (e.g., NXFT15WF104FA2B025), and the wet-dry sensor is an impedance grid resistor (IGR). Both sensors are connected through low-pass-filters (LPF) to the MUC's analog-digital-converter inputs.

3.4.9 Atmospheric Sensors Extension Module

Additional extended atmospheric measurements can be obtained from *i*VCCS by attaching a weather-sensing module (WSM), including ambient pressure, humidity, temperature, light, acoustic sound, and lightning sensors. Figure 3-8 illustrates the block diagram of WSM. Figure 3-9 shows the WSM printed circuit board (PCB).

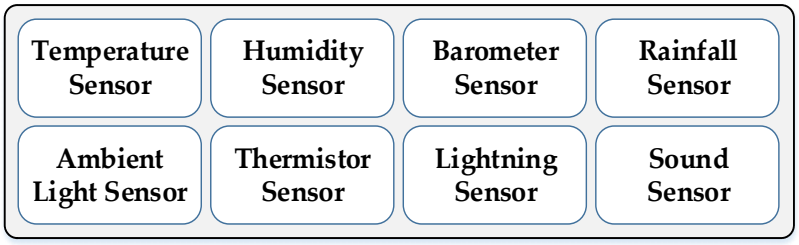


Figure 3-8 WSM sensing components block diagram

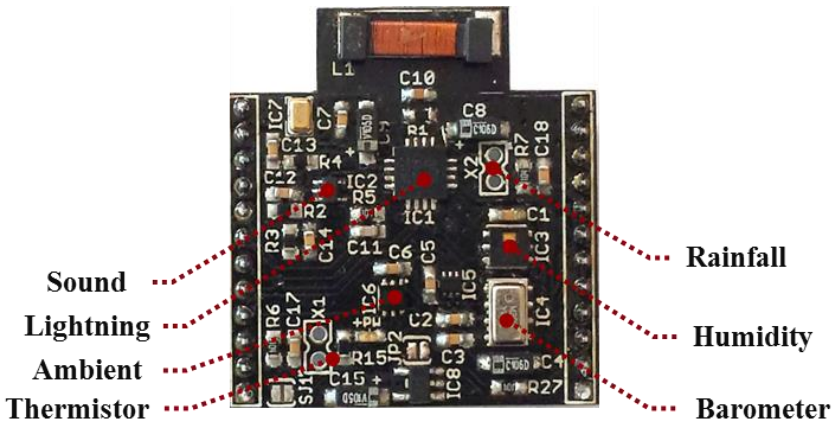


Figure 3-9 WSM PCB with all sensing components marked, 25×28mm

A comprehensive search was carried out to select the most suitable embedded sensors for weather sensing in a WSN application. Selection criterion was based on the following factors: sensitivity, accuracy, power consumption, size, cost, and communication interface (e.g., analog or digital). Selected sensors and their part numbers are shown in Figure 3-10. HTU21D is a digital Humidity Sensor; MPL3115A2 is a digital absolute xtrinsic smart pressure sensor; ADMP401 is analog omnidirectional MEMS microphone module; MAX44009 is digital ambient light sensor; TMP102 is low power digital temperature sensor; AS3935 is Franklin lightning detector with embedded algorithm that warns of lightning storm activity within a radius of 40kM; and NXFT15WF104FA2B025 is the surface temperature sensor. Additional information about particular sensors is located on their respective datasheets and application notes.



HTU21D MPL3115A2 ADMP401 MAX44009 TMP102 AS3935

Figure 3-10 Selected Atmospheric Sensors for WSM

3.5 *i*VCCS$_{G1}$ Power Consumption and Battery Life Analysis

As stated earlier, *i*VCCS is a battery-powered, wireless sensor node that uses a 3.7V/2000mAh Lithium Polymer (Li-Po) battery. *i*VCCS on-board components were carefully selected to achieve minimal power consumption.

A preliminary power consumption analysis in various operation modes showed that maximum current rates in power down, idle, and active modes are 156µA, 50nA, and 65mA, respectively. Considering 3.7V/2000mAh Li-Po Battery, battery life can be roughly estimated in each mode using Eq. 3-1, where µ is external factor allowances

that can affect battery life and T is the duty-cycle. Given that μ = 0.75 and T=1, estimated battery life in power down mode is limitless. The battery can operate *i*VCCS in idle mode for 578 days and in full active mode for 40 hours. All *i*VCCS components are operating in full active mode, including GPS, RF engine, and data logging unit. Power consumption for *i*VCCS components and WSM sensors is shown in Table 3-3 and

The most power-consuming component on *iVCCS* is the wireless transceiver engine (e.g., active current is 22mA). Power consumption is reduced, given a transition from one state to another (e.g., power-down → Idle → Active), which is driven by interrupt events. A transition from *Power Down* to *Active* mode is triggered by a vehicle arrival event wherein the MCU samples the magnetic field every *TS* (i.e., *TS* = 1.563Hz to 800Hz). A cyclic transition between *Active* ⇔ *Idle* modes occurs every TS until a transition from *Active* → *Power Down* mode is triggered by a vehicle departure event.

Table 3-4, respectively. Power consumption calculations for various operation modes using various Li-Po batteries are illustrated in Table 3-5.

$$BL_{hour} = \frac{1}{T}\left(\frac{Capacity_{mAh}}{Current_{mA}} \times \mu\right) \qquad \textbf{Eq. 3-1}$$

Table 3-3 Power consumption for *i*VCCS components

Component	Idle	Full Active
Atmel XMega A4 Microcontroller	1μA	500μA ~ 8mA
microSD Card	150uA	20mA
Voltage Regulator	500nA	8μA
Li-Po Battery Fuel Gauging	1μA	50μA
MAG Sensor	2μA	40 ~ 575μA[1]

[1] Consumption is related to sensor's sampling rate

ACCEL Sensor	2μA	40 ~ 575μA[1]
RF Module	0.37μA	20 / 22mA[2]
GPS Module	1μA	20 / 29mA[3]
Passive components	50μA	50μA
Total Current	**160μA**	**60mA ~ 80mA**

The most power-consuming component on *i*VCCS is the wireless transceiver engine (e.g., active current is 22mA). Power consumption is reduced, given a transition from one state to another (e.g., power-down → Idle → Active), which is driven by interrupt events. A transition from *Power Down* to *Active* mode is triggered by a vehicle arrival event wherein the MCU samples the magnetic field every T_S (i.e., T_S = 1.563Hz to 800Hz). A cyclic transition between *Active* ⇔ *Idle* modes occurs every T_S until a transition from *Active* → *Power Down* mode is triggered by a vehicle departure event.

Table 3-4 Power consumption for WSN components

Sensor	Power-off	Idle	Active
Digital Lightning Sensor	0	1μA	60μA
Microphone Preamplifier	0	24μA	24μA
Digital Relative Humidity sensor	0	0.1μA	480μA
Digital Pressure/Altitude sensor	0	2μA	8.5μA
Digital Temperature Sensor	0	1μA	10μA
Digital Ambient Light Sensor	0	0.65μA	1μA
MEMS Silicon Microphone	0	50μA	50μA
Voltage Regulator	500nA	500nA	8μA
Analog Impedance grid sensor	0	25μA	25μA
Analog NTC Thermistor	0	25μA	25μA
	500nA	**129μA**	**692μA**

[1] Consumption is related to sensor's sampling rate
[2] Consumption depends on the operation, read/write
[3] Consumption depends on the operation, tracking/accusation

Table 3-5 Power consumption in various operation modes using Li-Po batteries

Li-Po Battery	*i*VCCS Battery-Life (Days)			WSM Battery-Life (Days)		
	Shut-down	Idle	Active	Shut-down	Idle	Active
	500nA	156µA	60~80mA	500nA	129µA	692µA
1000mAh	83333	252	0.69	83333	323	60.21
1500mAh	125000	378	1.04	125000	484	90.32
2000mAh	166666	505	1.39	166666	646	120.42
2500mAh	208333	631	2.08	208333	807	150.53
3000mAh	250000	7578	2.08	250000	969	180.64
4000mAh	333333	1010	2.78	333333	1292	240.85

3.6 Power Consumption Implications of Detection Algorithm

MAG (e.g., FXOS8700CQ) has an active mode operation current range between 20—600µA, which is directly related to sensor ODR. MCU, on the other hand, has a slightly higher power consumption. After a detection event, *i*VCCS samples the MAG, logs and analyzes acquired data, and then sends timestamps to *i*AP. In reality, average duty-cycle of a detection system could range between 1% and 8%, meaning the system is idle more than 92% of the time. Hence, power consumption can be significantly reduced by configuring the system to automatically transition to a higher sampling rate when needed (i.e., a detection event triggered). *i*VCCS spends the majority of time in *idle* mode (i.e., no detection event), enabling the use of a very low sampling rate. This method, however, is at the expense of losing samples of vehicle signatures.

3.7 Towards Self-Powered Smart WSN

Transistor scaling is becoming exponentially smaller approximately every 18 months as a result of Moore's law, which allows twice the number of transistors per square inch of a silicon chip at lower cost and power consumption [27]. Also, with the

approaching era of IoT and smart cities, it is anticipated that the market will demand more autonomous and self-powered wireless sensors that should ideally operate for decades without service. For these reasons, it was necessary to reconsider *i*VCCS hardware design requirements first designed in 2014 before finalizing for mass production.

The reconsideration demanded the design of a new generation of sensor that is self-powered by integrating ultra-low-power (ULP) components and an advanced energy-harvesting (EH) and power management unit.

3.7.1 Characteristics of Self-Powered Applications

The essential characteristics of any self-powered application are as follows:

- Ultra-low leakage current integrated devices
- Energy-efficient components able to operate at low voltages
- Small size, lightweight, and long operating lifetime
- Primary and/or secondary power sources
- Ability to operate efficiently; consume the lowest power at low duty-cycle
- Ability to instantaneously switch between power-down and active modes
- Ability to self-sustain full operation during the device's intended lifetime
- Ability to support several operation modes (e.g., active, standby, sleep, power down)

Designing ULP applications demands an in-depth understanding of the power source side, which is as important as the power consumption side—reason being that the nature of power sources for EH systems represents a stochastic process. Notably, harvested power tends to be limited, intermittent, and unregulated, meaning that the average power and its distribution over time can be characterized. Notably, instant

power is unpredictable and subject to several non-deterministic factors. For self-sustainability of a device, the following key aspect must be considered in the design:

Average consumed power at system side must be

less than the average harvested power at source side.

3.7.2 Enabling Device Power Self-Sustainability

The most successful approach to enable self-sustainability of a device is by enabling ULP energy-efficient hardware design, as well as software development [93], meaning that system power budget must be well addressed in the design. This requires identifying the power consumption for each component in various operating modes, including Iq, transient-current, average-current, and peak-current.

Given that the sensor enclosure has limited available space, a top-down design approach can be followed to estimate the hypothetical lifetime of the device by selecting a battery that fits in space. Battery capacity represents maximum power source capability. Average power obtained for EH can be characterized based on availability, efficiency, and power levels of the ambient source. For example, given a device uses a 2800mAh Li-Po battery and has α=10% self-leakage or self-discharge over three years and a three-year lifetime, average power consumption should not exceed 106μA (See Eq. 3-2), that is assuming no other power sources are available to charge the battery.

$$I_{avg} = \frac{SOURCE_{Ah}}{TIME_{hours}} \times (1-\alpha) = \frac{2800_{Ah}}{3_{years} \times 365_{days} \times 24_{hour}} \times 0.9 = 106\mu A \qquad \textbf{Eq. 3-2}$$

3.8 *i*VCCS$_{G2}$ Platform Overview

*i*VCCS$_{G2}$ (an evolution version of *i*VCCS$_{G1}$) is a novel, fully-integrated intelligent wireless smart sensor that employs higher performance, is less expensive, and has more power efficient embedded electronics. The sensor was designed to be fully-autonomous

and self-powered with the ability to support various traffic surveillance applications and research studies.

*i*VCCS$_{G2}$ integrates single board state-of-the-art electronic components, including ultralow power, high-performance 32-bit embedded microcontroller, energy-efficient wireless transceiver, smart embedded sensors (i.e., 3D MAG and ACCEL), highly-accurate low-power embedded GPS receiver, dual-units for data storage, ULP EH power management unit (PMU) with maximum power point tracking (MPPT) and charge management controllers (CMC), battery fuel gauge, wireless power charging receiver, and atmospheric sensors. Components are managed by distinctive algorithms for implementing various traffic monitoring applications. Sensor firmware can also be upgraded over-the-air (OTA), which permits a customizable configuration to support various studies and applications. The sensor is functional in either standalone mode, wherein all data are stored on internal memory, or in peer-network, wherein *i*AP manages WSN data transfer. Figure 3-11 illustrates *i*VCCS$_{G2}$ block diagram. Figure 3-12 shows component distribution on both layers—top and bottom—on the *i*VCCS$_{G2}$ board. The sensor's PCB dimension is 45(L)×30(W)×6mm(H). Figure 3-13 depicts interconnections between on-board components. Power lines are represented in orange color; data/control busses are in green; and power switch control lines are in blue. The selection criteria and a brief description of each component are discussed in the next sections.

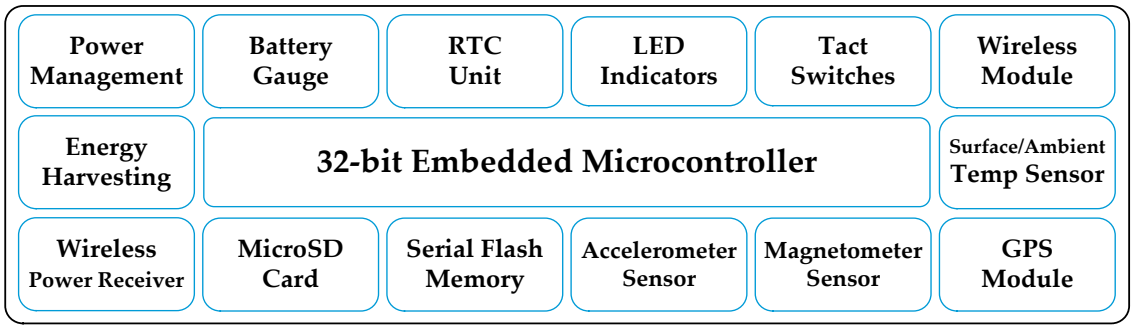


Figure 3-11 *i*VCCS$_{G2}$ functional components block diagram

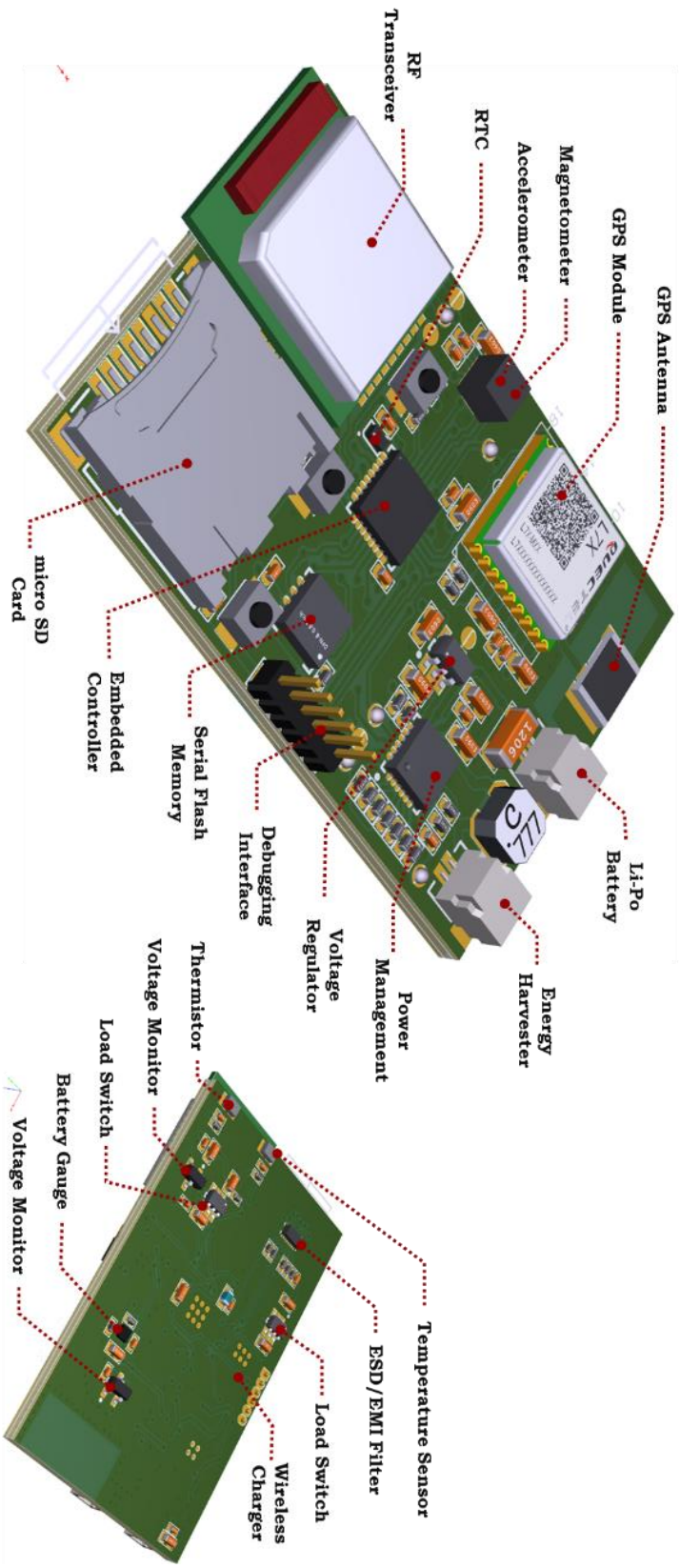


Figure 3-12 *i*VCCS$_{G2}$ PCB with all components marked

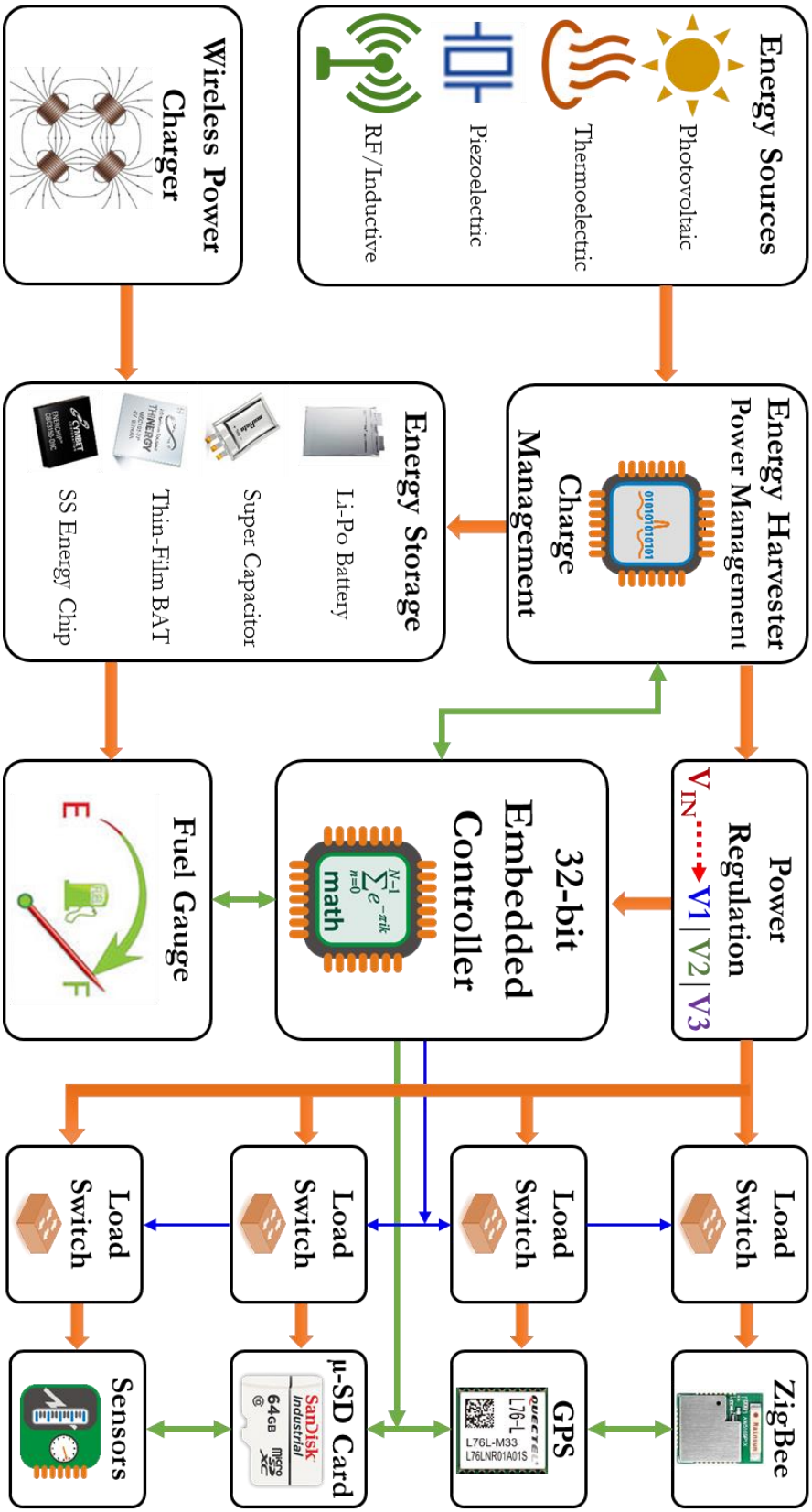


Figure 3-13 *i*VCCS$_{G2}$ functional components interconnections

3.8.1 A 32-bit Embedded Microcontroller

The selection of the right MCU is crucial for ULP embedded systems design. The criteria for MCU selection was based on the following criteria:

- Supported multiple operational power modes
- Very low power consumption in active mode
- Tremendously high and efficient processing performance
- Particularly fast wake-up time
- Ultra-low power consumption in standby mode
- Rich peripheral with autonomous operation
- Industrial grade with wide operational temperature range

From among several industry-leading ULP MCUs (e.g., TI MSP430; Freescale MKL; Renesas RL78; NXP LPC1xxx; Atmel SAM4L; Microchip XLP; and Silicon Labs EFM32), STMicroelectronics ultra-energy-efficient ARM Cortex-M0+ STM32L071xB was selected. STM32L0 MCU series is ideal for energy-sensitive applications, including wearable devices, medical implants, and smart-living devices. STM32L0 MCUs have proven class-leading, energy efficiency of 135 ULPMark™-C [94]. Moreover, STM32L0 MCUs are highly temperature-stable and have best-in-class power consumption at 125°C, combining efficiency and robustness. Figure 3-14 illustrates a circuit block diagram of the selected STM32L071KB MCU [94], which has the following energy-saving features:

→ Seven power modes, including *Run*, *Sleep*, *Stop*, *Standby*, and others
→ 139µA/MHz *Run* mode current and 76µA/MHz optimized *Run* mode
→ Energy-saving modes, including 340nA *Stop* mode with full RAM retention
→ Auto wake-up from *Stop* mode to *Run* mode (32MHz) in 3.5µs
→ Temperature operating range -40 to +125°C.
→ Optional low-power pulse counter available in ultra-low power mode

→ Low-power ADC, 41µA at 12-bit resolution and 10KSPS

→ Interconnect matrix for data handling when CPU is idle

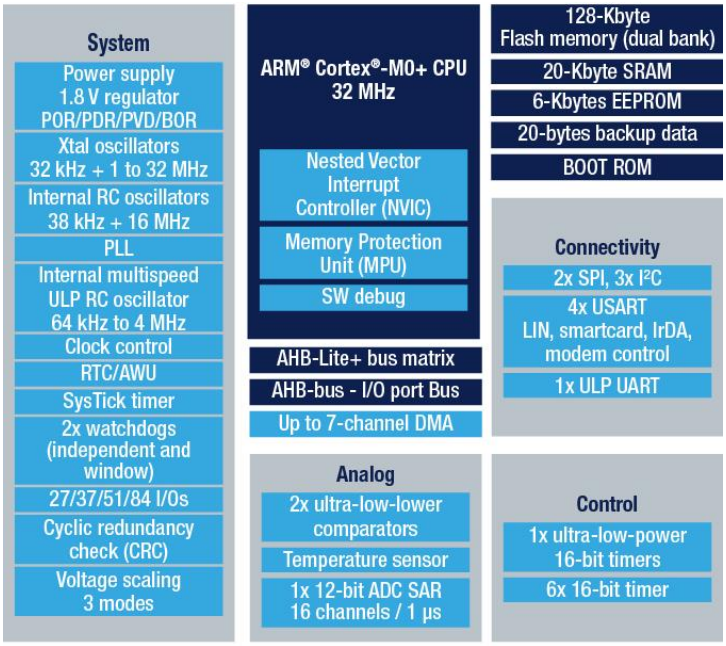


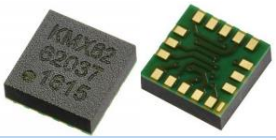
Figure 3-14 STM32L071KB MCU block diagram

Since ULP systems continually switch between *Stop* and *Run* modes, the ultra-fast wake-up time is extremely important for minimizing inefficient wake-up switching delay. The interconnect matrix allows CPU-independent, autonomous, inter-peripheral signaling and data transfer between peripherals and memory in energy-saving modes.

3.8.2 Magnetometer & Accelerometer Sensors

Kionix KMX62 is a MEMS technology-based, high-performance, low-power, inertial sensor that combines a tri-axial MAG and a tri-axial ACCEL coupled with an advanced ASIC. This sensor was released in July 2016 as best-in-class. KMX62 magnetic and acceleration sensing technique is similar to FXOS8700CQ in that acceleration is capacitance-based sensing and magnetic is impedance-based sensing. Table 3-6 shows a comparison between the two industry-leading 6-axis MAG-ACCEL sensors.

Table 3-6 Comparison between two industry-leading 6-axis MAG-ACCEL sensors

	Freescale (NXP) **FXOS8700CQ** 	**Kionix (ROHM)** **KMX62-1031** 
Control Interface	I^2C/SPI + 2-INT	I^2C + 2-INT
Dimensions	6-axis ACCEL-MAG	6-axis ACCEL-MAG
Update Rate (ODR)	1.563Hz ~ 800Hz 400Hz in hybrid mode	MAG: 0.781Hz ~ 1.60KHz ACC: 0.781Hz ~ 25.6KHz
ODR Accuracy	5% over -40°C to +85°C	2% over -40°C to +85°C
Magnetometer Range	±1200 μT	±1200 μT
Acceleration Range	±2g / ±4g / ±8g	±2g / ±4g / ±8g / ±16g
ADC Resolution	MAG: 14-bit ACC: 16-bit	MAG: 16-bit ACC: 16-bit
Measurement Period	0.64s ~ 1.25ms	MAG: 1.28s ~ 625μs ACC: 1.28s ~ 39μs
Magnetic Sensitivity	±0.1 μT/LSB	±0.0366 μT/LSB
Acceleration Sensitivity	1 Milligauss	0.366 Milligauss
Magnetic Nonlinearity	±1 $\%FS_{MAG}$	±0.5 $\%FS_{MAG}$
Acceleration Nonlinearity	±0.5 $\%FS_{ACC}$	±0.5 $\%FS_{ACC}$
Acceleration Sensitivity	±2g→ 0.244 mg/LSB ±4g→ 0.488 mg/LSB ±8g→ 0.976 mg/LSB	±2g→ 0.06mg/LSB ±4g→ 0.12mg/LSB ±8g→ 0.24mg/LSB ±16g→ 0.49mg/LSB
Magnetic Output Noise	0.3~1.5 μT-rms@1.56~800Hz	0.2~1.4 μT-rms@0.78~1600Hz
Acceleration Output Noise	126 μg/√Hz	106 μg/√Hz
Maximum Exposed Field	100,000 μT	500,000 μT
Maximum Acceleration	10,000 Gauss	50,000 Gauss
Zero-Flux Offset	±10 μT	±0 μT
Flux Offset with Temp	±0.8 μT/°C	±0.3 μT/°C
Zero-g Level Offset	±30 mg	±25 mg
g-level Offset with Temp	±0.2 mg/°C	±0.2 mg/°C
FIFO Buffer	32 Samples (ACC only)	64 Samples (ACC&MAG)
Power Consumption	Idle Mode: 2μA MAG: 40~575μA @ 12.5~400Hz ACC: 10~240μA @ 12.5~800Hz M&A: 40~440μA @ 12.5~200Hz	Idle Mode: 1μA MAG: 1.6~292μA @ ODR_{range} ACC: 1.6~156μA @ ODR_{range} M&A: 1.6~385μA @ ODR_{range}
Cost	US$1.5/1KU	US$4.00/1KU
Package	QFN-16 (3×3×1.2 mm)	QFN-16 (3×3×0.7 mm)

Since MAG/ACCEL is a core component for *i*VCCS$_{G2}$, extended selection criteria was necessary for decision-making. Table 3-6 shows that KMX62 outperforms FXOS8700CQ in every factor except cost. Because low cost is essential and because both sensors are pin-to-pin compliable, it was necessary that the final *i*VCCS$_{G2}$ design ensured its ability to adapt to either sensor. Choice is based on desired performance, as well as the application.

3.8.3 Embedded RF Engine

Among several promising IoT wireless technologies (e.g., BLE, LoRa, DASH7, 6LoWPAN, Bluetooth, and Z-Wave), ZigBee is at the forefront in terms of cost, power efficiency, distance, and throughput [95]. ZigBee has the advantage of using mesh networking topology, which eliminates single points of failure. Additionally, ZigBee is well standardized at all network levels, allowing devices from different vendors to work together seamlessly. ZigBee module selection criteria was developed to evaluate the following key characteristics:

- Support for multiple-power modes, including *idle* and *deep-sleep*
- Power consumption during *transmission*, *receiving*, *idle*, and *deep-slee*p
- Maximum distance range in LOS
- Maximum data throughput
- Size, weight, and cost

The most power-consuming component on *i*VCCS is the wireless transceiver engine (e.g., active current is 22mA). Power consumption is reduced, given a transition from one state to another (e.g., power-down $\rightarrow$ Idle $\rightarrow$ Active), which is driven by interrupt events. A transition from *Power Down* to *Active* mode is triggered by a vehicle arrival

event wherein the MCU samples the magnetic field every T_S (i.e., T_S = 1.563Hz to 800Hz). A cyclic transition between *Active* ⇔ *Idle* modes occurs every T_S until a transition from *Active* → *Power Down* mode is triggered by a vehicle departure event.

Table 3-4 details a comparison between the top four industry-leading ZigBee modules for IoT devices. All modules report comparable performance. However, AW5161P0CF serves as the best candidate in terms of cost, size, and sleep current.

Table 3-7 Top ZigBee Module candidates for *i*VCCS$_{G2}$

	ATMEL ATZB-S1-256-3-0-C	**Dresden Elektronik deRFmega128- 22M00**	**NXP JN5168-001-M00**	**ZLG AW5161P0CF**
				
Voltage Range	1.8V ~ 3.6V	1.8V ~ 3.6V	2.0V ~ 3.6V	2.2V ~ 3.6V
Controller	ATMEGA256RFR2	ATmega128RFA1	NXP JN5168	NXP JN5161
Throughput	2Mbps	2Mbps	2Mbps	2Mbps
RX Sensitivity	-97dBm	-100dBm	-95dBm	-95dBm
TX Power	+3.6dBm	+3.0dBm	+2.5dBm	+2.5dBm
Link Budget	100.6dB	103.0dB	97.5dB	97.5dB
Distance	170 – 570 meter	200 meter	200 meter	500 meter
Sleep Current	0.6μA	1μA	0.7μA	0.1μA
RX Current	17mA	18mA	17mA	19mA
TX Current	16.4mA	18mA	15.3mA	16mA
Cost	US$25/1KU	US$15/1KU	US$10/1KU	US$5/1KU
Package	30×20×5 mm	23.7×13.2×3 mm	30×16×3 mm	16.5×13.5×3 mm
Supported Protocols	ZigBit	6LoWPAN, Zigbee	ZigBee Light Link, Smart Energy, RF4CE	FastZigBee + All Low-Power

AW5161P0 [96] is a low power, high performance, surface-mount ZigBee module based on NXP JN5168. The sensor supports several protocol stacks, including IEEE 802.15.4, JenNet-IP, ZigBee Light Link, ZigBee Smart Energy, and RF4CE (See Figure 3-15). AW5161P0 has proven superior in all aspects of performance. For

example, transmit power is +2.5dBm with range of 500 meter and data transfer rate up to 2Mbps. More importantly, power consumption can be as low as 100nA in deep sleep. AW5161P0 can be configured as an *End-device*, *Router*, or *Gateway*. Size is 16.5×13.5mm, and cost is less than $5, compared to $17.76 for SM200P81 installed in *i*VCCS$_{G1}$.

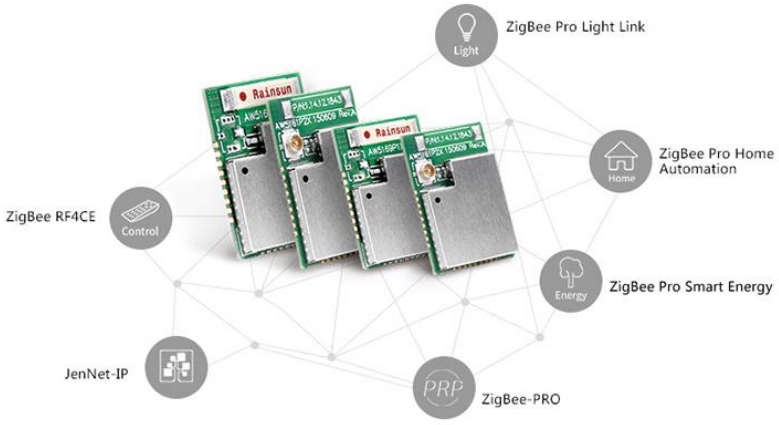


Figure 3-15 AW5161P0 support multi-wireless protocol stack [96]

3.8.4 Real-Time Clock

STM32L071KB combines an advanced internal RTC unit for providing a full-feature calendar, alarm, periodic wakeup, digital calibration, timestamp, and synchronization. The unit has a separate, accurate low speed external (LSE) oscillator with the advantage of providing a low power yet highly accurate clock source for RTC timing functions. LSE incorporates OSC32_IN and OSC32_OUT pins for crystal connection.

To provide a highly accurate, external clock source for timestamping, SiT1552 (an ULP 32.768KHz MEMS TCXO [temperature compensated crystal oscillator]) was routed directly to the OSC32_IN pin. SiT1552 is currently the smallest precision 32KHz TCXO [97] available (See Figure 3-16). SiT1552 has ±5ppm frequency stability

over a temperature range with ULP consumption of 990nA. According to SiTime Corp., SiT1552's silicon is qualified for use at 105ºC. SiT1552 was also selected due to its resistance to shock and vibration, as larger TCXOs are extremely susceptible to mechanical disturbances. In fact, each truck driving by or over the TCXO sensor is known to negatively impact timing accuracy.



Figure 3-16 SiT1552, a world's smallest 32.768KHz MEMS TCXO

3.8.5 Embedded GPS Modules

Selection criteria for a ULP GPS module included the following characteristics:

- Multiple-system support, including *GPS* and *GLONASS*
- Power consumption during *tracking*, *acquisition*, *standby*, and *backup* modes
- Number of available *PNR*, *tracking*, and *acquisition* channels
- Sensitivity, positioning accuracy, and timing accuracy
- Size, weight, and cost

Quectel's L76L-M33 GPS module [98] was selected among many commercially available GPS modules. L76L-M33 is a ULP, extremely compact (10.1×9.7×2.5mm) GNSS module, featuring <2.5m positioning accuracy, ±10ns timing accuracy, and up to

10Hz update rate at a cost of only $7.80. The module can monitor up to 210 channels, 99 of which are searchable, while simultaneously tracking another 33. L76L-M33 backup power mode consumes only 9µA for supplying the internal RTC when main power is off. This feature aids in retaining satellite constellation information and locking with satellites in less than 1-sec on power-up rather than performing a lengthy cold-start satellite search. Power consumption is 19mA for tracking; 25mA for acquisition; 2.8mA for locating; and 500µA in standby mode. Figure 3-17 illustrates Quectel's L76L-M33 GPS module.

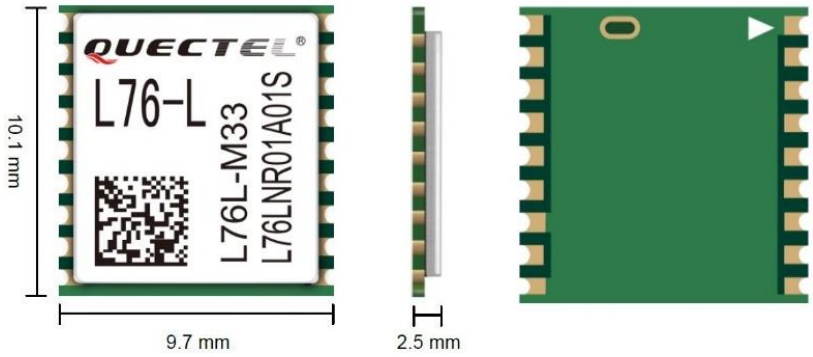


Figure 3-17 Quectel's L76-L extremely compact GPS module

3.8.6 Data Logging Unit

*i*VCCS$_{G2}$ integrates a micro-SD card and serial NOR flash for data logging. SanDisk has the best industrial-grade microSD card for applications requiring reliability, durability, and high intensity data logging, such as industrial IoT getaways and transportation [99]. SDSDQAF-008G-I Class 10 8GB microSD card was selected.

To protect the card from electrostatic discharge (ESD), electromagnetic interference (EMI), and transient voltage and current, TI TPD8F003 was added to the design. TPD8F003 [100] is a highly integrated, eight-channel EMI filter with ESD

protection (up to ±20-kV air gap discharge). The chip is ultra-small (3.30×1.35 mm) and has an ultra-low leakage current of 10nA per channel. Cost is US$0.25/1KU.

The purpose of adding a microSD card was to support raw data collection (e.g., flux magnitude and vertical acceleration), which is useful for research studies. Advantages of microSD cards include its portability and large capacity. Disadvantages include the fact that the cards are energy inefficient, large sized, and expensive.

Ultimately, only detection timestamps are necessary for essential traffic monitoring (i.e., vehicle counting, speed estimation, or length-based classification). At this point and for such applications, a more energy efficient, cheaper, and smaller solution is crucial for *i*VCCS$_{G2}$ design.

Serial NOR Flash memories are currently the best solution for logging detection timestamps. The Macronix's MX25R NOR Flash memories family [101] is specifically designed for next-generation IoT consumer wearables. These devices feature a ULP mode and density to 512Mbit. Active power consumption is 3.1mA for write and 1.9mA for read, which are 70% lower than other solutions. Deep-power-down mode consumption is only 0.1µA, which is 90% lower than other available solutions. Cost for MX25R6435F is US$1.0; size is 4×4mm.

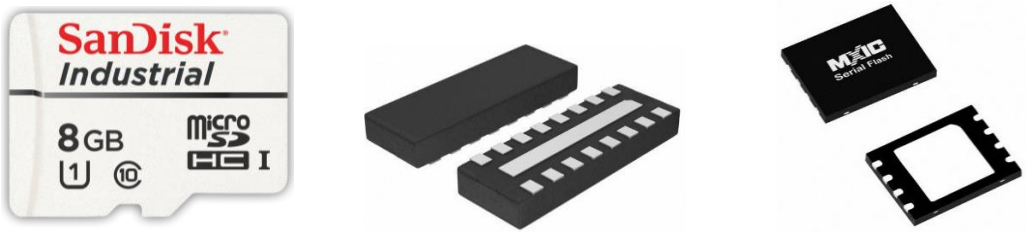


Figure 3-18 SanDisk SDSDQAF-008G-I, TI TPD8F003, and MX25R6435F

3.8.7 Power Management System

Power management system (PMU) is the core of any modern EH system. The *i*VCCS$_{G2}$ PMS was designed to incorporate the most energy-efficient components available in the market. The system is composed of 1) an EH for converting external ambient energy sources to electricity; 2) EH management unit (PMU) with maximum power point tracking (MPPT) and charge management controllers for collecting electrical energy from the harvester, and then charging an energy storage device and/or supplies other system components; 3) energy storage device for conserving harvested energy; 4) voltage regulator for conditioning the system voltage and supplying sensor components with appropriate operation voltage; 5) load switches for activating or deactivating subsystems; and 6) battery fuel gauge for providing information about the battery state. The sensor MCU has access to all PMS units, ensuring that PMU energy use is minimized when energy is not available at the input. The following subsections will discuss design aspects and selection criteria for each unit in the PMS.

3.8.7.1 Energy Harvesting Power Management Solutions

Several major semiconductor vendors, including Analog Devices, Texas Instruments, Maxim Integrated, and STMicroelectronics, offer energy-harvesting power-management (EHPM) devices with different capabilities and features. The selection process for the EHPM device was based on 19 criterions (See).

Of the aforementioned devices, ADP5091 [102] was found suitable to the sensor design in all aspects. The chip was released in late July 2016 as a ULP EHPM unit with MPPT for thermoelectric and photovoltaic sources. ADP5091 has an optimized on-chip boost-converter that can cold-start with only 380mV input, and then run from 80mV to 3.3V. Power can be harvested from sources with a 16μW to 600mW range. Internal

150mA regulated output can be programmed by an external resistor. MPPT extracts the maximum possible energy from the harvester, which has a varying impedance dependent on physical parameter changes. MPPT maintains input voltage ripple in a fixed range to maintain stable DC-DC boost conversion. A minimum operation threshold can be programmed to enable boost shutdown during a low input voltage condition (e.g., at night). Quiescent current is 450nA during DC-DC boost and 360nA when the boost is in shutdown mode.

ADP5091 also has a charging control function to protect rechargeable energy storage by monitoring battery voltage via the programmable charging termination voltage and the shutdown discharging voltage. More importantly, ADP5091 can turn off the DC-DC inverter, preventing interference with the RF engine during data transmission. The chip costs only US$2.49 and is available in a 3×3mm 24-lead LFCSP package; it is rated for a −40°C to +125°C temperature range. Figure 3-19 illustrates the ADP5091/2 internal detailed functional block diagram.

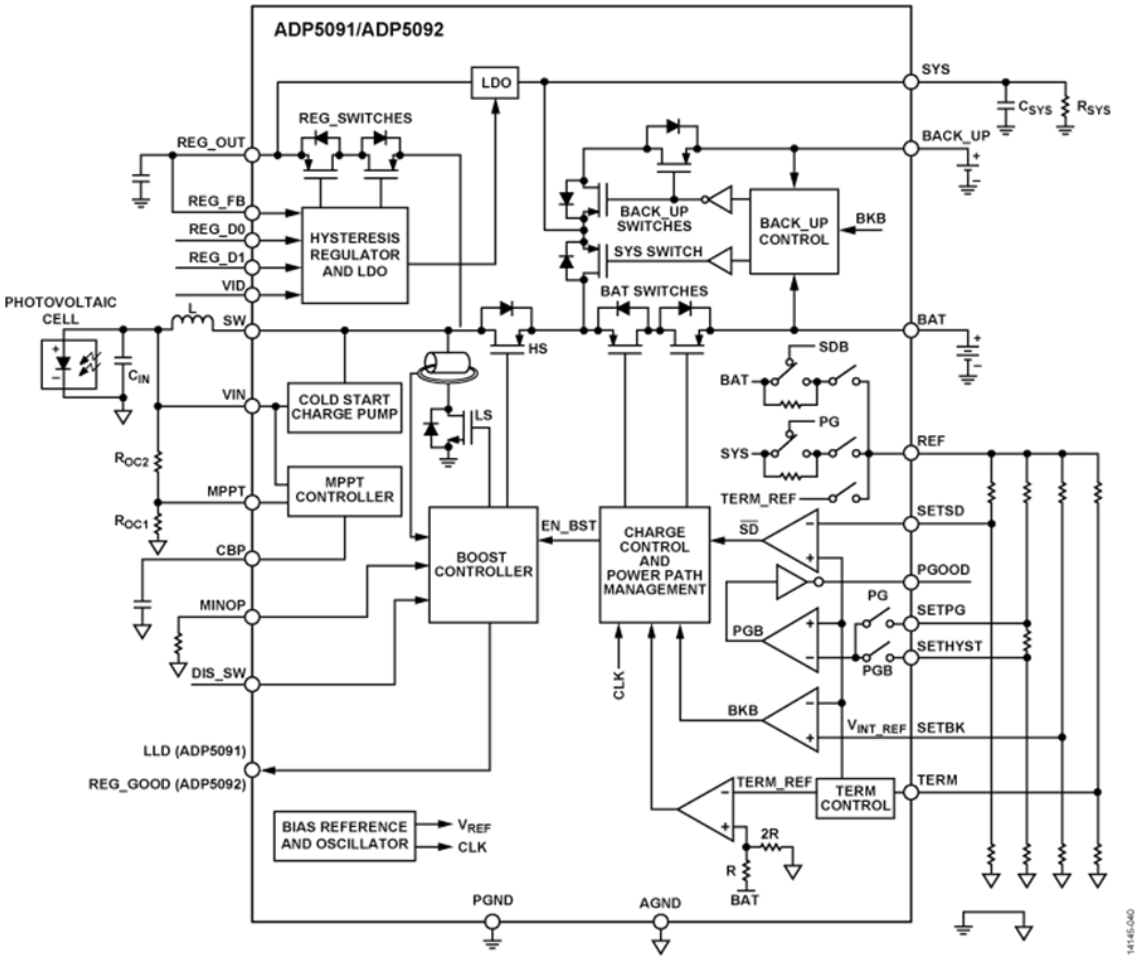
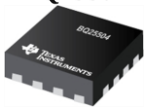
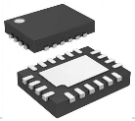


Figure 3-19 Energy Harvesting Transducers [102]

Table 3-5 Characteristics of Energy Harvesting PMU for WSN

	MAX17710	BQ25504	BQ25570	SPV1050	ADP5091/2	LTC3106	LTC3331
							
Price	$7.87 @ 1KU	$2.10 @ 1KU	$3.20 @ 1KU	$1.15 @ 1KU	$2.49 @ 1KU	3.57 @ 1KU	4.31 @ 1KU
Manufacturer	MAXIM	TI	TI	ST	AD	LT	LT
Packages	12-UTDFN 3×3 MM	16-VQFN 3×3 MM	20-VQFN 3.5×3.5MM	20-VFQFPN 3×3 MM	24-LFCSP 4x4 MM	16-QFN 3x4 MM 20-Pin TSSOP	32-QFN 5x5 MM
MPPT	NONE	Programmable	Programmable	Hardware Set	Hardware Set	Hardware Set	NONE
Iq	625nA	330nA	488nA	800nA	260nA	1.6μA	950nA
Input Voltage Range	0.75V to 5.3V	80 MV to 3 V	100 mV to 5.5 V	75 mV to 18 V	80 mV to 3.3 V	660 mV to 5.5 V	3.0V to 19V
Harvesters	PV, TEG	PV, TEG	PV, TEG	PV, TEG	ALL	PV, TEG	Vibration, PV
External Components	1×DIODE 1×INDUCTOR 2×RESITOR 3×CAPACITOR	1×INDUCTOR 9×RESISTOR 4×CAPACITOR	2×INDUCTOR 6×RESISTOR 5×CAPACITOR	1×INDUCTOR 6×RESISTOR 4×CAPACITOR	1×INDUCTOR 13×RESISTOR 4×CAPACITOR	1×INDUCTOR 3×RESISTOR 6×CAPACITOR	1×DIODE 2×INDUCTOR 1×RESISTOR 7×CAPACITOR
Dc-Dc	NONE	NONE	BOOST/BUCK	BOOST/BUCK	BOOST	Buck-Boost	Buck-Boost
LDO	1.8/2.3/3.3V (75 MA)	NONE	NONE	1.8V (100 MA) 3.3V (100 MA)	1.5~3.6V (150mA)	1.8/2.2/3.3/5V (90/300 MA)	1.8V ~ 5V 50mA
Min Solar Voltage	220 MV	100 MV	100 MV	150 MV	80 MV	300 MV	-
Max Charge Cur.	100 MA	110 MA	110 MA	70 MA	100 MA	100 MA	10 MA
Cold Start	750 MV	330 MV	330 MV	500 MV	380 MV	300mV	-
Charge Efficiency	~95%	~95%	~93%	~95%	~97%	~93%	~93%
Temperature Range	-40 to 85	-40 to 85	-40 to 85	-40°C to 125°C	-40°C to 125°C	–40°C to 125°C	–40°C to 125°C
Input Power	1 μW to 100 mW	400 mW	5 μW to 510 mW	up to 400 mW	16 μW to 600 mW	10μW to 160mW	10μW to 50mW
VBAT	2.2 V to 4.3 V	2.5 V to 5.25 V	2 V to 5.5 V	2.6 V to 5.3 V	2.2 V to 5.2 V	2.1 V to 4.3 V	4.2V
Switching Frequency	1 MHZ	1 MHZ	1 MHZ	1 MHZ	1 MHZ	-	-
Energy Storage	Battery	Battery	Battery	Supercap/Battery	Supercap/Battery	Supercap/Battery	Supercap/Battery

3.8.7.2 Energy Harvesting Transducers

EH transducers are used to collect ambient energy before converting it into electrical power. The most promising and commonly used transducers are described in [28]–[30]:

- *Photovoltaic*: converts light into energy using solar cells
- *Piezoelectric*: produces energy from kinetic sources, such as vibration
- *Electromagnetic*: converts inductive/RF radiation into power
- *Thermoelectric*: thermal-gradients energy from heat sources

Figure 3-20 shows commercially available energy transducers. A mind-map for various types of energy harvesters and sources is illustrated in Figure 3-21 [30].



Figure 3-20 Energy Harvesting Transducers

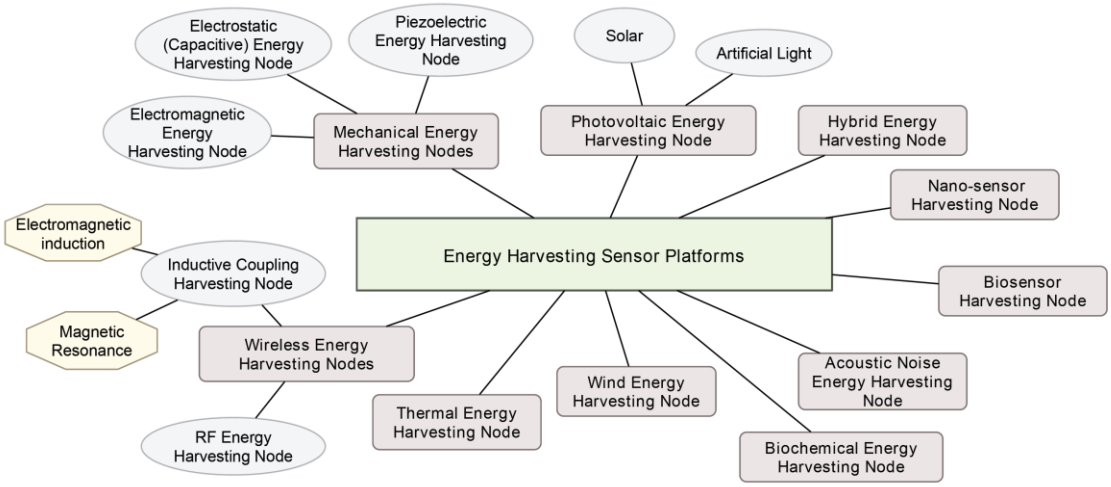


Figure 3-21 Different energy harvesters (rectangles) and sources (ovals)

A comparison between power density and efficiency for various EH transducers is shown in Table 3-9 [30]. Energy conversion *Efficiency* is defined as the ratio of harvested energy at the harvester output to available energy at the harvester input.

Table 3-9 Characteristics of Energy Harvesting Transducers and Sources for WSN

Energy Harvester	Power Density	Efficiency
Photovoltaic	Outdoors (direct sun): 15-30 mW/cm^2 Outdoors (cloudy day): 0.15 mW/cm^2 Indoors: 5-30 µW/cm^2	Highest: 32 ± 1.5% Typical: 25 ± 1.5%
Thermoelectric	Wearable: 50 µW/cm^2 Industrial: 1 to 10 mW/cm^2	±0:1% ±3%
Pyroelectric	8.64 µW/cm^2 at temperature rate of ΔT = 5°C/s	3.5%
Piezoelectric	Human: 4 µW/cm^3 Industrial: 1 mW/cm^3	source dependent
Electromagnetic	Human motion: 1 to 4 µW/cm^3 Industrial: 306 µW/cm^3 to 800 µW/cm^3	source dependent
Electrostatic	50 to 100 µW/cm^3	source dependent
RF	GSM 900/1800 MHz: 0.1µW/cm^2 WiFi 2.4 GHz: 0.01 µW/cm^2	50%
Wind	380 µW/cm^3 at the speed of 5 m/s	5%
Acoustic noise	0.96 µW/cm^3 at 100 dB 0.003 µW/cm^3 at 75 dB	-

Solar energy is more widely used in EH applications, as it is most prolific and capable among other energy sources. It is inexpensive, easy-to-use, and has the highest power density—up to 30mW/cm^2. In general, monocrystalline solar cells are preferred for outdoor applications, and amorphous solar cells are the best option in low-light levels for indoor applications.

3.8.7.3 Energy Storage Devices

The most commonly used EH energy storage for WSN are rechargeable batteries, supercapacitors, Thin-Film batteries, and Solid-State chips. Each technology has a

unique advantage. The following criteria should be considered when selecting rechargeable devices for energy-storage applications.

- Energy capacity
- Peak and continuous current
- Operation temperature (chemistries perform poorly at low temperature)
- Self-discharge
- Charge time
- Cycle life (number of discharge/charge before capacity drops to 70%)
- Cost, weight, size, shape

Table 3-10 presents a comparison between the essential characteristics of various energy storage devices.

Table 3-10 Characteristics of energy storage devices for EH applications

	Li-Po Batteries 	**Thin-Film Batteries** 	**Super Capacitors** 	**Solid-State Energy Storage** 
Energy Capacity	up to 10 Ah	up to 3 mAh	up to 1.5 mAh	up to 50 µAh
Peak Current	very high	small	high	very small
Self-discharge	5% per month	2% per year	10% per minute	negligible
Charge Time	Hours	15 minutes	Seconds	30 minutes
Cycle Life	See Table 3-12	100,000	1,000,000	5000

Li-Po batteries were chosen primarily because they have superior chemistry for small, self-powered devices. Also, they are a highly reliable power source for devices that create a relatively high-peak, steep transient current (e.g., GPS module and wireless transceiver). When compared with other technologies, Li-Po batteries have a relatively

low self-discharge current—approximately 5% per month—and limited number of cycles.

To maximize Li-Po battery cycle, especially in EH applications with daily charge-discharge cycles, a battery with higher storage capacity could help reduce depth of discharge (DoD), which is proportional to battery lifecycles. A battery with higher capacity will have lower internal resistance, which allows more peak current to supply the load. Reducing DoD to a partial discharge and avoiding over-charge can significantly reduce stress and prolong the life of Li-Po batteries. Table 3-11 illustrates a comparison between DoD level and corresponding numbers of discharge-charge cycles before Li-Po battery capacity is diminished by 20%.

Table 3-11 Cycle life as a function of depth of discharge

Depth of discharge	Discharge cycles
100%	300–500
50%	1200–1500
25%	2000–2500
10%	3750–4700

Most Li-Po batteries charge to 4.2V per cell; however, reducing peak charge voltage by 0.10V per cell would double the battery cycle life [103]. Consequently, a lower peak charge voltage will reduce the nominal capacity a battery can handle. For example, a 70mV reduction in charge voltage would reduce overall capacity by 10%, as shown in Table 3-12.

For battery longevity, it is recommended to set charge voltage to 3.92V per cell, eliminating voltage-related stress [103].

Table 3-12 Discharge cycles and capacity as a function of charge voltage limit.

Charge level (V/cell)	Discharge cycles	Capacity at full charge
4.30	150 – 250	~114%
4.20	300 – 500	100%
4.10	600 – 1000	~86%
4.00	1200 – 2000	~72%
3.92	**2400 – 4000**	**~58%**

3.8.7.4 Smart Battery Gauge

Protecting Li-Po battery from deep-discharging and over-charging is crucial for battery longevity. BQ27621-G1 [104], a system-side fuel gauging device for single-cell Li-Po batteries, was integrated into the design. This smart chip uses sophisticated algorithms to calculate remaining battery capacity, state-of-charge, battery voltage, and temperature. Data can be accessed by a MCU over serial interface (See Figure 3-22).

BQ27621-G1 is tiny (1.62×1.58×0.5 mm), inexpensive (US$1.25), power-efficient (0.6μA in shutdown mode), and requires minimal configuration and firmware development.

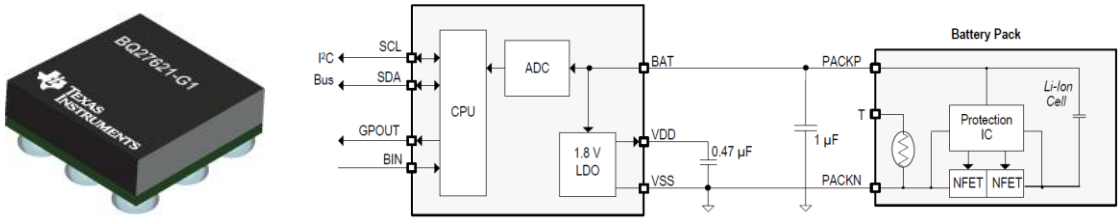


Figure 3-22 TI BQ27621-G1 Battery Fuel-Gauge [104]

3.8.7.5 Voltage Conditioning Unit

ADP165 was used to provide a regulated voltage—from the unregulated source at ADP5092 system output to the system components and modules. ADP165 [105] is an extremely low, quiescent-current, 150 mA voltage regulator. ADP165 has a shutdown

current 50nA and operating temperature range from -40 to 125°C. The chip is very small and costs only US$0.35/1KU.

3.8.7.6 Nano-Power Load Switches

For a more energy-efficient design, several TPS22860 [106]—small, ultra-low leakage current load switch—were used to control the power supply to each ZigBee module, GPS module, and microSD card. TPS22860 has a 12nA total leakage current and can support 200mA maximum continuous current. Switch cost is US$0.22/1KU.

3.8.8 Wireless Charging Receiver

Wireless charging is an essential element in powering wearable devices and IoT. Functionality is based on utilizing electromagnetic energy transmitted from a primary coil of energy transmitter in the near-field across a gap to a secondary coil of an energy receiver such that both coils are tuned to resonate at the same frequency [107]. The receiver converts inductive current into energy that can be used to charge the battery or power the device.

To enable wireless charging for *i*VCCS$_{G2}$, a BQ51051B [108] high-efficient, Qi-compliant wireless power receiver with an integrated Li-Po battery charge controller from TI was included in the design. Qi is an international charging standard developed by the Wireless Power Consortium (WPC). BQ51051B supports charging current up to 1.5A with 93% charging efficiency. The chip comes in 3.0×1.9mm package and costs US$1.9/1KU. Vishay IWAS-4832FE-50 [109] was considered for the 10W shielded receiver coil. The coil has a dimension of only 48×32×1.22mm. Figure 3-23 shows the receiver chip and coil.



Figure 3-23 TI BQ51051B chip (left) and Vishay IWAS-4832FE-50 coil (right)

3.8.9 Road Surface Condition Sensors

Road surface temperature can rise to 200ºC on a hot summer day. A cost-effective method for measuring road surface temperature is using NTC glass-based Thermistors. These sensors feature an extremely fast response time, high reliability, and an operating temperature range between -50°C and +300°C. Note that the sensor glass should be coated to ensure moisture-proof robustness. For *i*VCCS$_{G2}$, an NTC with at least 100kΩ rated resistance at 25°C (e.g., Semitec's 104NT-4-R025H43G [110] costing US$0.7 /1KU) is recommended to guarantee minimal power dissipation.

3.8.10 Passive Components Selection Does Matter

ULP design should consider leakage current from both active and passive components (e.g., capacitors). It is also imperative to understand and evaluate the effect of DC bias, temperature variation, and tolerance of the bypass capacitor, as well as the technology of the selected capacitor.

TMJ S1gma™ SMD tantalum capacitors from AVX were used in *i*VCCS$_{G2}$. This product has an extremely low DC leakage current (i.e., 0.001CV) and high stability over an operation temperature ranging between -55 and +125°C [111].

3.9 *i*VCCS$_{G2}$ Power Consumption and Battery Life Analysis

*i*VCCS$_{G2}$ was designed as an autonomous sensor to harvest, buffer, and consume available buffered energy in a highly efficient manner, especially when generated and consumed energy profiles are completely different.

Average power consumption of the sensor (i.e., $P_{avg} = I_{avg}.V_{DD}$) depends primarily on system supply voltage (V_{DD}) and average consumed current (I_{avg}), the latter being the sum of average current in active (I_{active}) and stop (I_{stop}) modes. By knowing time spent in active (T_{active}) and stop (T_{stop}) modes, battery life (BAT_{life}) can be estimated using Eq. 3-3, where α is the battery self-discharge rate.

$$\mathrm{BAT_{life}}[hours] = \frac{BAT_{Capacity}}{\frac{I_{active} \times T_{active} + I_{stop} \times T_{stop}}{T_{active} + T_{stop}}} \times \alpha \qquad \textbf{Eq. 3-3}$$

Accurately estimating battery life requires a sufficient characterization of all components parameters that have a significant influence on the system's power consumption. These are discussed in the next sections and might vary for various components.

3.9.1 Components Parameters Assessment

A comprehensive assessment for all components was performed to characterize power consumption of each component under a variety of operating modes. Component datasheets, application notes, user manual, Yokogawa DL9140 digital oscilloscope, true RMS multi-meter, and NI vector signal analyser were analysed during the assessment process.

1) Embedded MCU

MCU parameters with significant influence on power consumption are system clock, core voltage, start-up and wake-up times, analog peripherals, and processing efficiency. Table 3-13 shows power consumption and wake-up time for STM32L071 in all supported modes [94]. RTC unit is enabled in all modes, and V_{DD} is 3.3V. Table

3-14 shows the power consumption in active mode for all STM32L071 peripherals essential for *i*VCCS$_{G2}$ functions and other on-board components.

*i*VCCS$_{G2}$ MCU control the power source of all power-hungry components (i.e., RF engine, GPS, and data logging units) via ultra-low power switches. MCU spends most of its time in stop mode waiting for an event or interrupt to wake-up—for a short period—and process a pre-specified computational task. MCU power consumption in stop mode is 1µA and requires 3.5µs to switch from stop to active state. The internal system clock is set at 8MHz.

Table 3-13 *i*VCCS$_{G2}$ MCU power consumption in various power modes

	Active	Sleep	LP-Active	LP-Sleep	Stop	Standby
Wakeup Time	0µs	0.36µs	3µs	32µs	3.5µs	50µs
Consumption	175µA/MHz	35µA/MHz	8.55µA	4.65µA	1µA	655nA

Table 3-14 STM32L071 Peripheral power consumption in active mode

DMA	UART1/2	TIM6/7	RTC	I2C1	SPI	GPIO
8µA/MHz	11.5µA/MHz	3µA/MHz	300nA	9.5µA/MHz	3µA/MHz	3µA/MHz

2) Serial Flash Memory (MX25R6435F - SFM)

Essential characterization parameters for MX25R6435F [112] are listed in Table 3-15. t_{DPDD} is the delay time for release from deep power-down mode; t_{DP} is the time CS# pin should be held high to enter deep-power down mode; t_{pp} is self-timed page (i.e., 256 bytes) program cycle time; t_{RDP} is recovery time for release from deep power down mode; t_{CRDP} is CS# toggling time delay before release from deep power-down mode; I_{SB1} is standby current; I_{SB2} is deep power-down current; I_{CC1} is read current; and I_{CC1} is page-program current.

Table 3-15 Serial Flash parameters

t_{DPDD}	t_{DP}	t_{PP}	t_{RDP}	t_{CRDP}	I_{SB1}	I_{SB2}	I_{CC1}	I_{CC2}
30µs	10µs	3.2ms	35µs	20ns	24µA	0.5µA	1.9mA	3.5mA

3) Magnetometer Sensor (KMX62)

KMX62 [113] MAG has four resolution modes to support various over-sampling rates. Mode *RES<0,0>* was selected, as it has a standby current of 1µA and sampling rate (*fs*) of 5µA and 30µA active current at 50Hz and 400Hz, respectively. *fs* is set to 50Hz when MCU in stop mode and to 400Hz given that *MAG motion interrupt* occurred (i.e., vehicle in detection zone). Startup time is 1ms.

4) Voltage Supervisor (TPS3839)

TPS3839 [114] typically consumes only 100nA. However, this current rises to 15µA after power-up for 200µs where TPS3839 samples the input voltage. Power-up delay is 200ms, meaning that the power-up for any device connected with TPS3839's REST pin (i.e., RF Engine and GPS module) will be delayed for 200ms. The bypass capacitor connected with the VDD pin maintains average current at 150nA.

5) 32.768KHz MEMS TCXO (SiT1552)

The SiT1552 active oscillator has 300ms start-up time at power-up, during which time peak supply current reaches 28µA for 200ms before dropping to 0.99µA steady-state core current. SiT1552 [97] total current (I_{osc}) is the sum of core current in steady-state, load current at 10pF load capacitance, and output driver current at 3.5pF drive capacitance (i.e., $I_{osc} = (0.99) + (0.23) + (0.08) = 1.3\mu A$).

6) Load Switch (TPS22860)

Two load switches control power supply to the ZigBee module and data storage unit. TPS22860 [106] has only *10nA* quiescent current and *12nA* shutdown leakage current. Switching time is *4ns* for turn-on and *9ns* for turn-off.

7) 8-Channel EMI Filter (TPD8F003)

The *TPD8F003* chip consists of passive components (i.e., resistors and diodes). Leakage current on each channel is 10nA [100]. Only seven channels are used in *i*VCCS$_{G2}$ design.

8) Low-Dropout Linear Regulator (TPS782)

TPS782 [115] features 18nA shutdown current and 500nA quiescent current. The chip has an enable pin that consumes 0.4nA. Startup time t_{STR} or shutdown time t_{SHDN} is 500µs. Output power dissipation is calculated as $PD = (V_{in} - V_{out})I_{out}$.

9) Battery Fuel Gauge (bq27621-G1)

The bq27621-G1 [104] has four operating modes. Power consumption in normal mode is 27µA, 21µA in sleep, 9µA in hibernate, and 600nA in shutdown mode. Input leakage current is 100nA. The chip requires 125ms to produce one conversion. Data read time from the bus is 1ms.

10) Energy Harvesting PMU (ADP5092)

ADP5092 [116] is mainly comprised of two sides: one supplied directly from the harvester input (i.e., solar cell) and the other relative to the output side (i.e., SYS and BAT pins). The SYS pin has 650nA quiescent current in active state and 390nA in sleep mode. In addition to 20nA for input pins, the BAT pin has a 3.5nA leakage current.

11) GPS Module

Table 3-16 lists GPS module L76-M33 [98] essential parameters for power consumption characterization. BAUS is the data baud rate for UART interface between MCU and GPS; $I_{V_{BCKP}}$ is the supply current for backup power supply to constantly maintain GPS RTC domain running and achieve fast *Time to First Fix* (e.g., <1sec); $\boldsymbol{f_{UR}}$ is GPS NEMA date update rate; $T_{PW_{on}}$ is start-up time at power-up; and I_{acq} and I_{trk} are current consumption during acquisition and trancing, respectively. L76-M33 has 465ms~ 485ms latency range after the rising edge of PPS (See Figure 3-24 [98]). PPS duty-cycle is 1/10. A 200ms power-up delay generated by the voltage supervisor (TPS3839) should be considered only when GPS load switch was in shutdown state.

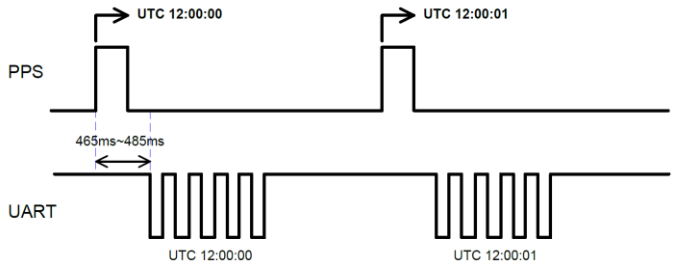


Figure 3-24 PPS and NMEA timing for L76-M33

Table 3-16 GPS Module parameters

$\boldsymbol{BAUD}$	$\boldsymbol{I_{V_{BCKP}}}$	$\boldsymbol{I_{standby}}$	$\boldsymbol{I_{acq}}$	$\boldsymbol{I_{trk}}$	$\boldsymbol{f_{UR}}$	$\boldsymbol{T_{PW_{on}}}$
115200bps	7μA	500μA	25mA	19mA	1Hz	2ms

12) RF Engine (AW5161P0CF)

AW5161P0CF [96] power-related parameters are shown in Table 3-17. Current consumption during transmission, receiving, in-sleep mode, and deep-sleep (stop) mode are denoted as I_{TX}, I_{RX}, I_{sleep}, and I_{stop}, respectively. $T_{PW_{on}}$ is the time delay required for local oscillator to stabilize during power-on before radio activities can start. T_{wakeup}

is time delay wake-up from stop or sleep modes to active mode. During power-on, only *4.98mA* is consumed because RF front-end is not operating. A 200ms power-up delay generated by the voltage supervisor (TPS3839) should be considered only when RF engine load switch is in shutdown.

Table 3-17 RF Engine parameters

$\boldsymbol{BAUD}$	$\boldsymbol{I_{TX}}$	$\boldsymbol{I_{RX}}$	$\boldsymbol{I_{sleep}}$	$\boldsymbol{I_{stop}}$	$\boldsymbol{T_{wakeup}}$	$\boldsymbol{T_{PW_{on}}}$
57600bps	18mA	21mA	700nA	120nA	180µs	1ms

Data frame transmission period (T_{Trans}) is an important parameter that should also be calculated. T_{Fram} depends on two factors: 1) configurations of RF engine and 2) size of payload frame.

AW5161P0CF operates in the 2.4GHz band, which allows 250kbps over-the-air data rate (i.e., 62500 symbols per second—each comprising 4bits). The MAC (medium access control) layer header size (H_{MAC}) is set to 25 bytes for 64-bit source and destination addresses. The physical layer header size (H_{PYH}) is fixed and equal to 6 bytes. Payload frame ($F_{Payload}$) size depends on the amount of data to be transmitted; it can be loaded up to 114 bytes. Total time required to transmit a single data frame can be calculated as in Eq. 3-4. Given that $F_{Payload} = 1$, then $T_{Trans} = 1.024ms$. For $F_{Payload} = 114$, $T_{Trans} = 4.64ms$.

$$T_{Trans} = \frac{H_{MAC} + H_{PYH} + F_{Payload}}{250kbps} \times 8bit \qquad \textbf{Eq. 3-4}$$

$4.64ms$ represents the amount of time RF engine consumes I_{TX}. This figure will be used to calculate energy required to send a radio message. Notably, this amount was determined under the assumption of an ideal scenario (i.e., interference-free and single-hop).

In a real world scenario, RF engine performs a *Clear Channel Assessment* (CCA) before data transmission to determine an available channel. AW5161P0CF implements an unslotted CSMA/CA (carrier sense multiple access with collision avoidance) algorithm instead of regular beacons. Two variables are set during configuration: 1) number of back-offs ($N_{backoff}$) allowed to attempt a single radio message transmission—one back-off period is $T_{backoff}$ 320µs (i.e., 20 symbols, each 16µs) and 2) Retry interval (T_{retry}), which is how many back-off periods the engine should wait before attempting another channel assess. Both $N_{backoff}$ and T_{retry} were set to 3.

3.9.2 iVCCS$_{G2}$ Power Consumption Assessment

Power consumption assessment was performed based-on the process and power sequence flow diagram depicted in Figure 3-26, which represents an optimized operation of *i*VCCS$_{G2}$ for vehicle detection applications. Component state and power consumption during initialization sequence and process execution are shown in Table 3-18.

Table 3-18 Execution time and consumed current for *i*VCCS$_{G2}$

Process		$I_{avg(mA)}$	$T_{(ms)}$
1.	*i*VCCS$_{G2}$ Power-up – MCU only	1.456	300
2.	Report node status, ID, and transfer data to access point	8.927	26.058
3.	Set and calibrate RTC using GPS	11.129	3765
4.	Run MAG @ 50Hz, Enable MAG EXIT, and set MCU in Stop mode	0.0347	T_{stop}
5.	Motion interrupt → MAG @ 400Hz → set MCU in Stop mode	0.0597	T_{idle}
6.	Read MAG Data and check for a vehicle departure	0.2785	T_{active}
7.	Transfer Timestamps from SRAM to Flash	3.5587	3.3
8.	Read Battery Status from the Fuel Gauge	1.5387	126

The longest process time T is considered when two tasks occur simultaneously. Total average leakage current for MCU decoupling capacitors (I_{dcap}) is 500nA.

In process No. 1, I_{avg} and T are calculated as follows:

→ $I_{avg} = [175\mu A \times 8\ (MCU \mid Active)] + [28\mu A\ (TCXO \mid Startup)] + 0.5\mu A\ (SFM \mid I_{SB2}) + [12nA \times 2\ (Load\ Switch \mid shutdown)] + [1\mu A\ (MAG \mid standby)] + [500nA + 0.4nA\ (LDO \mid Enabled)] + [600nA + 100nA\ (Gauge \mid shutdown)] + [500nA\ (I_{dcap})] + [650nA + 3.5nA + 20nA\ (Harvester \mid Active)]$.

→ $I_{leakage} \sim 4.7\mu A$

→ $T = 300ms\ (TCXO \mid Startup)$.

Assuming $F_{Payload} = 114$ bytes, process No. 2 is executed as follows:

- Enable Load Switch (U5, see *i*VCCS$_{G2}$ schematic diagram in appendix B) > *4ns* switching time and *10nA* quiescent current.
- Wakeup AW5161P0CF > T_{wakeup} + $T_{PW_{on}}$ @ $I_{idle} = 4.98mA$.
- Enable UART1 > 11.5μA×8 = 92μA (See Table 3-14)
- Send data MCU → RF engine over UART > $I_{idle} = 5.04mA$ and $T_{UART} = \left[\left(114_{Bytes} \times 8_{bit}\right) + 114_{startbit} + 114_{stopbit}\right]/57600bps = 19.79ms$
- RF engine perform CCA > Assuming $N_{backoff} = 1$ and the channel is free, then $T_{backoff} = 320\mu s$ @ 5.16mA and $T_{CCA} = 128\mu s$ @ $I_{TX} = 18mA$.
- RF engine transmits data over-the-air > $T_{Trans} = 4.64ms$ @ $I_{TX} = 18mA$.
- Disable Load Switch (U5) > *9ns* turn-off time
- Disable UART1>Total run-time $19.79ms + 320\mu s + 128\mu s + 4.64ms = 24.878ms$

→ $I_{avg} = \left[(10nA \times 4ns) + (4.98mA \times 1180\mu s) + (92\mu A \times 24.878ms) + (5.04mA \times 19.79ms) + (5.16mA \times 320\mu s) + (18mA \times 128\mu s) + \left(I_{leakage} \times\right.\right.$

$26.058ms\big) + (18mA{\times}4.64ms)\big]/(4ns + 1180\mu s + 19.79ms + 320\mu s +$

$128\mu s + 4.64ms) = 7.499mA$

$\rightarrow\ T = 4ns + 1180\mu s + 19.79ms + 320\mu s + 128\mu s + 4.64ms = 26.058ms$

Average current in process No. 2 is the sum of RF engine average current and MCU current in steady-state, active mode (i.e., subtract 28µ$A\ TCXO$ during startup).

Process No. 3 is executed in the following manner:

- Enable External Interrupt 1PPS > 3µA×8 = 24µA
- Enable Load Switch (U3/DIS_SW, see *i*VCCS$_{G2}$ schematic diagram in appendix B) > 200ms voltage supervisor delay 15µA×200µs + 150nA + 25$mA\ \left(I_{acq}\right)_{after200ms}$
- Set MCU in Stop mode > 1µA.
- Wait until 1PPS rising edge wakeups the MCU > 1sec.
- Enable TIM6 > 3µA×8 = 24µA
- Set MCU in Stop mode > 1µA.
- Wait until 1PPS falling edge wakeups the MCU > 100ms.
- Disable TIM6 > TIM6 total runtime is 100ms
- Disable External Interrupt 1PPS > Total runtime is 1.3s
- Enable UART2 with Rx Interrupt > 11.5µA×8 = 92µA
- Set MCU in Stop mode > 1µA.
- Wait (~365ms as shown in Figure 3-24) until UART2 Rx interrupt wakeups the MCU
- Search for $GPRMC (recommended minimum specific GPS/Transit data) > 100ms
- Disable Load Switch (U3/DIS_SW) > Total runtime is 1.665s for GPS and 1.865s for Load Switch.
- Disable UART2 > Total runtime for UART2 is ~465ms

- Set RTC time and date registers
- Set MCU in Stop mode > 1μA.
- Wait for RTC interrupt > 1sec
- Enable TIM6 > 3μA×8 = 24μA
- Set MCU in Stop mode > 1μA.
- Wait for another RTC interrupt > 1sec
- Disable TIM6 > TIM6 total runtime is 1000ms
- Calculate the difference of RTC and PPS pulse duration and calibrate RTC
- Set MCU in Stop mode > 1μA. Total MCU active time is 120ms@1.428mA

→ $I_{avg} = \big[(24\mu A \times 1.3s) + (15\mu A \times 200\mu s) + (150nA \times 1.865s) + (25mA \times 1.665s) + (1\mu A \times 1s) + (24\mu A \times 100ms) + (1\mu A \times 100ms) + (92\mu A \times 465ms) + (1\mu A \times 365ms) + (1\mu A \times 1s) + (24\mu A \times 1s) + (1\mu A \times 1s) + (1.428mA \times 120ms) + \big(I_{leakage} \times 3.765s\big)\big]/(3.765s) = 11.129mA$

→ $T = 3765ms$

Process No. 4 is executed as follows:

- Run MAG @ 50Hz > 5μA
- Enable External Interrupts > 24μA
- Set MCU in Stop mode > 1μA

→ $I_{avg} = \big[1\mu A + 5\mu A + 24\mu A + I_{leakage}\big] = 34.7\mu A$

→ $T = T_{stop}$ (T_{stop} can be found based on the number of vehicles per day)

Process No. 5 is executed as follows:

- If MAG Motion interrupt triggered → Run MAG @ 400Hz > 30μA
- Store Timestamp in SRAM
- Set MCU in Stop mode > 1μA

→ $I_{avg} = 59.7\mu A$

→ $T = T_{idle}$ (T_{idle} can be found based on the number of vehicles per day)

Process No. 6 is executed as described below:

- If MAG Watermark interrupt triggered → Enable I2C1 > 76µA
- **L1**: Set MCU in Stop mode > 1µA
- Wait for MAG Data-ready interrupt (DRI) > 1/400Hz = 2.5ms
- DRI? → Read MAG *x*, *y*, and *z* registers (16-bit × 3) > 180µs
- Compute magnetite → Vehicle departure? NO → go to **L1**
- Vehicle departure → Store Timestamp in SRAM → Disable I2C1
- Go to Process No. 4

→ $I_{avg} = (135.7\mu A \times 0.9) + (1.5637mA \times 0.1) = 0.2785mA$

→ $T = T_{active}$ (T_{active} can be found based on the number of vehicles per day)

Process No. 7 is executed once every 64 vehicle detections as follows:

- Enable SPI1 Interface > 24µA @ 4Mbps
- Send wakeup command to serial flash > 65µs delay
- Write data (Page Program command) from SRAM to SPI > 3.2ms / 3.5mA
- Disable SPI Interface and Set MCU in Stop mode > 1µA

→ $I_{avg} = 3.5587mA$

→ $T = 3.3ms$

Process No. 8 is executed once each day:

- Enable I2C1 > 76µA
- Send conversion command to the Fuel Gauge > 27µA / 125ms for one conversion
- Read battery status data > 280µs
- Disable I2C1 Interface and Store Data in SRAM to be sent to the access point

- Set MCU in Stop mode > 1μA

→ $I_{avg} = 1.5387mA$

→ $T = 126ms$

3.9.3 Battery Life Estimation

Battery life depends on the amount of time the sensor spends in active state compared to stop state. This primarily depends on the number of vehicles at a designated detection point. When using 4000mAh Li-Po battery to power the sensor, battery life can be calculated using Eq. 3-3 based on power consumption and time delay assessment in Table 3-18. The following assumptions were made:

1) Traffic volume at a highway designated detection point is 10,000 vehicles/day
2) Average vehicle speed is 60mph (i.e., 26.8224m/s).
3) Average vehicle length is 7m.
4) Battery state is checked once each hour.
5) Data is transmitted from *i*VCCS$_{G2}$ to *i*AP once every 15min because traffic volume data is reported in 15min bins.
6) RTC drift correction is performed once every 60min, guaranteeing microsecond synchronization accuracy.
7) Per-vehicle data is uploaded from *i*VCCS$_{G2}$ to *i*AP at midnight.

Based on these assumptions, average occupancy time is 7/26.8224 = 0.261s. Hence, active time is 2610 second/day or 3% of total time. Stop time is 97% of total time.

At 400Hz during 0.261s, MAG will sample approximately 105 data points. Watermark interrupt occurs after 50 data points, during which time current consumption is 0.0597mA and $T = T_{idle}$. Hence, $T_{idle} = 0.4762\, T_{active}$. Watermark interrupt

conserves 47.6% of the current consumed in active mode. A data point value of 50 was determined statistically based on data collected from highways and urban roads. Given a motorcycle traveling at 70mph , minimum number of data points should be greater than 70.

To estimate the battery life, the following processes (See below) should be calculated: hourly duty-cycle (DC), average current during RF transmission, RTC calibration using GPS, data transfer from SRAM to serial Flash, and battery status check processes should be calculated.

$$DC_{RF}^{[hour]} = \frac{(0.026058_{sec} \times 4_{runs})}{3600_{sec}} = 0.0289\% \rightarrow I_{avg-RF}^{[hour]} = 8.927_{mA} \times DC_{RF}^{[hour]} = 0.259\mu A$$

$$DC_{GPS}^{[hour]} = \frac{(3.765_{sec} \times 1_{run})}{3600_{sec}} = 0.1046\% \rightarrow I_{avg-GPS}^{[hour]} = 11.129_{mA} \times DC_{GPS}^{[hour]} = 11.641\mu A$$

$$DC_{SFM}^{[hour]} = \frac{(0.0033_{sec} \times 157_{run})}{3600_{sec}} = 0.0144\% \rightarrow I_{avg-GPS}^{[hour]} = 3.5587_{mA} \times DC_{GPS}^{[hour]} = 0.51\mu A$$

$$DC_{Gauge}^{[hour]} = \frac{(0.126_{sec} \times 1_{run})}{3600_{sec}} = 0.0035\% \rightarrow I_{avg-GPS}^{[hour]} = 1.5387_{mA} \times DC_{GPS}^{[hour]} = 0.054\mu A$$

Next, average current in stop, idle, and active modes should be calculated.

$$DC_{idle} = 1.4385\% \rightarrow I_{avg-idle} = 0.0597_{mA} \times DC_{idle} = 0.859\mu A$$

$$DC_{active} = 1.5823\% \rightarrow I_{avg-active} = 0.2785_{mA} \times DC_{active} = 4.4067\mu A$$

$$DC_{stop} = 97\% \rightarrow I_{avg-stop} = 0.0347_{mA} \times DC_{stop} = 33.659\mu A$$

Total average current is $51.3887\mu Ah$.

$$\text{BAT}_{\text{life}} = \frac{4000mAh}{51.3887\mu Ah} \times 0.8 = 62{,}270.499\ [hour] = 7.1\ [year]$$

As such, the sensor should operate for over 7 years when powered by a 4000-mAh battery with up to an 80% derating factor.

3.9.4 Extending Battery Life

Note that estimated battery life detailed in previous section did not consider energy generated by harvesting PMU, which is based on a highly efficiency solar-cell (i.e., SLMD121H04) utilized to charge the battery.

SLMD121H04 [117] has 2V typical voltage, 44.6mA typical current, and 89.2mW maximum power point (MPP). Cell size is 43×14×2mm, and cell efficiency is approximately 22%. Performance is acceptable in even low light conditions. SLMD121H04, *i*VCCSG2 final prototype, and the wireless charging receiver boards are shown in Figure 3-25.

The process flow diagram depicted in Figure 3-26 demonstrates how the energy harvesting PMU is operational from sunrise to sunset. Given that total run time is 8 hours and average harvested and converted energy is 18mWh (i.e., worst case scenario), average generated energy—1.5mAh—should be sufficient to compensate for consumed energy at output and to maintain longer battery life, thus sensor operations.

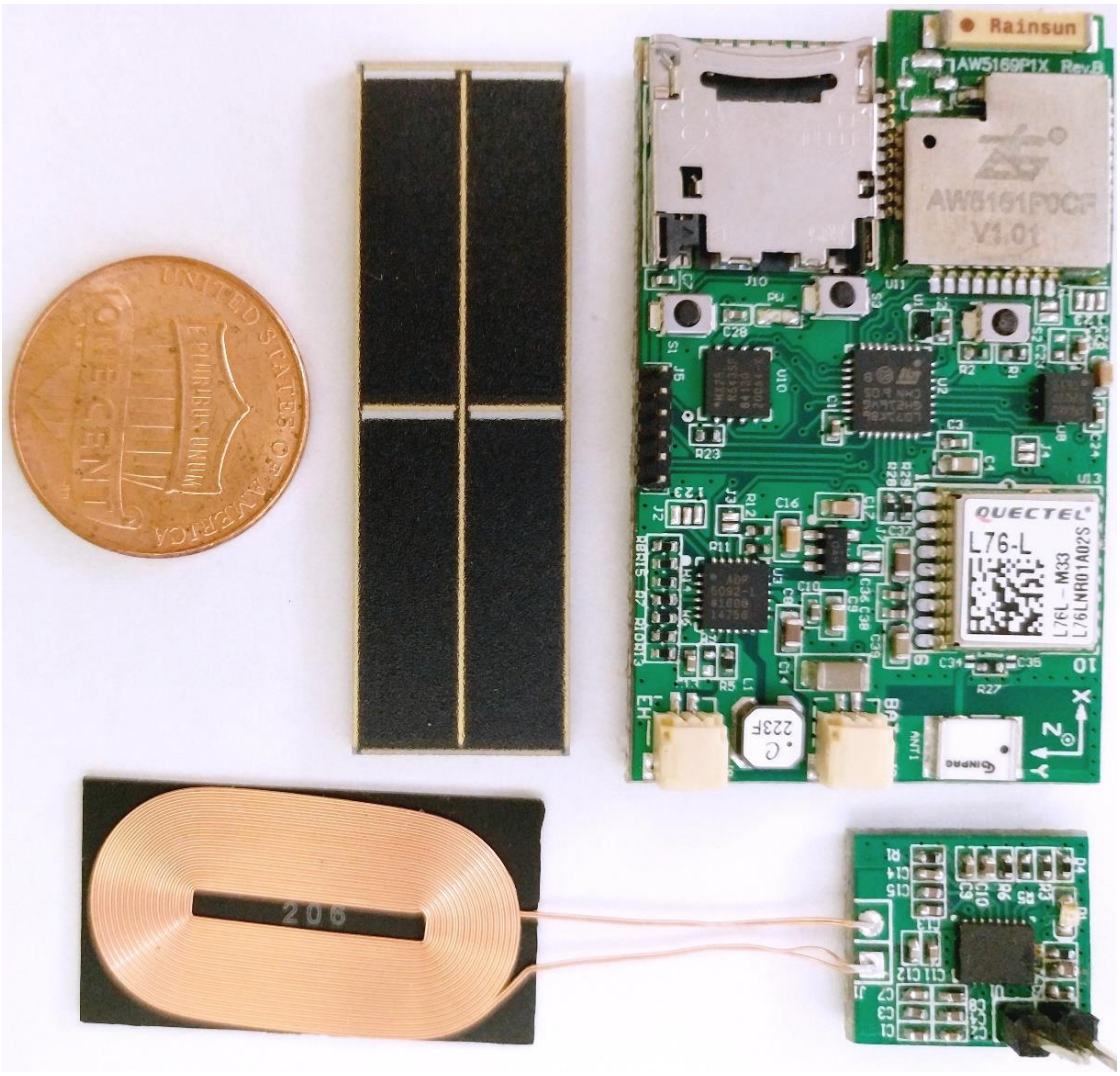


Figure 3-25 iVCCSG2 Final Prototype PCB

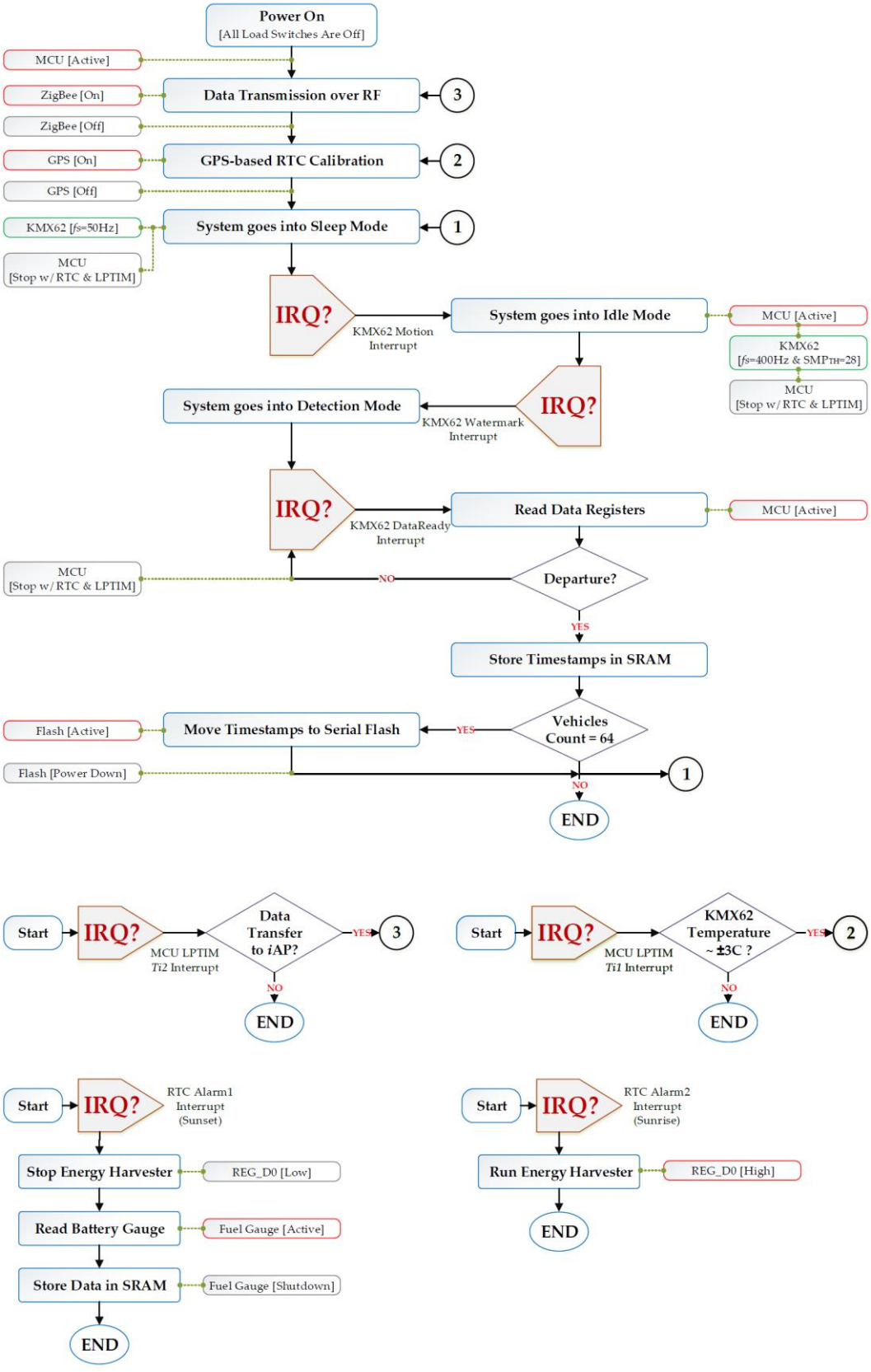


Figure 3-26 Sensor node processes and power sequence flow diagram

3.10 Proposed Large-scale System Architecture and Networking

*i*VCCS nodes can operate in either online or offline modes. In offline mode, traffic measurements, events, and magnetic signatures are logged into an on-board data logging unit. Data can be accessed anytime via an available wireless link or be retrieved by replacing the microSD card. In online mode, data are reported upon request to either *i*AP or collaborative nodes. To conserve power, the data-logging unit remains in sleep mode except when accessed by the host (i.e., MCU).

The network is organized in three tiers—*i*VCCS nodes, *i*APs, and IoT cloud server, as illustrated in Figure 3-27. At the lowest tier lies the *i*VCCS nodes, each equipped with a ZigBee RF module and a unique ID. The unique ID is reported with node coordination—obtained from an on-board GPS module—to a corresponding *i*AP for mapping purposes. *i*APs are located in the second tier, each equipped with a long-range ZigBee transceiver and an embedded industrial GPRS module [118]. *i*AP has a 10MB data cache and a powerful operation system for facilitating rapid connection timing to maximize traffic savings and minimize the cost of communication. Data can be accessed via dynamic DNS or public IP.

System wireless networking between *i*VCCS nodes and *i*AP is facilitated through IEEE 802.15.4 protocol with ZigBee on top. Wireless networking between *i*AP and the server is managed over a cellular network assisted by a Quad-Band GSM/GPRS chipset with an on-board GPS module.

Each *i*AP was set to manage up to 12 subordinate *i*VCCS nodes. Upon *i*VCCS node startup, multicast remote procedure calls (RPCs) were sent to inquire about an *i*AP

address to manage an identical channel and network. Only one *i*AP responded to the call by sending its address to the originating *i*VCCS node.

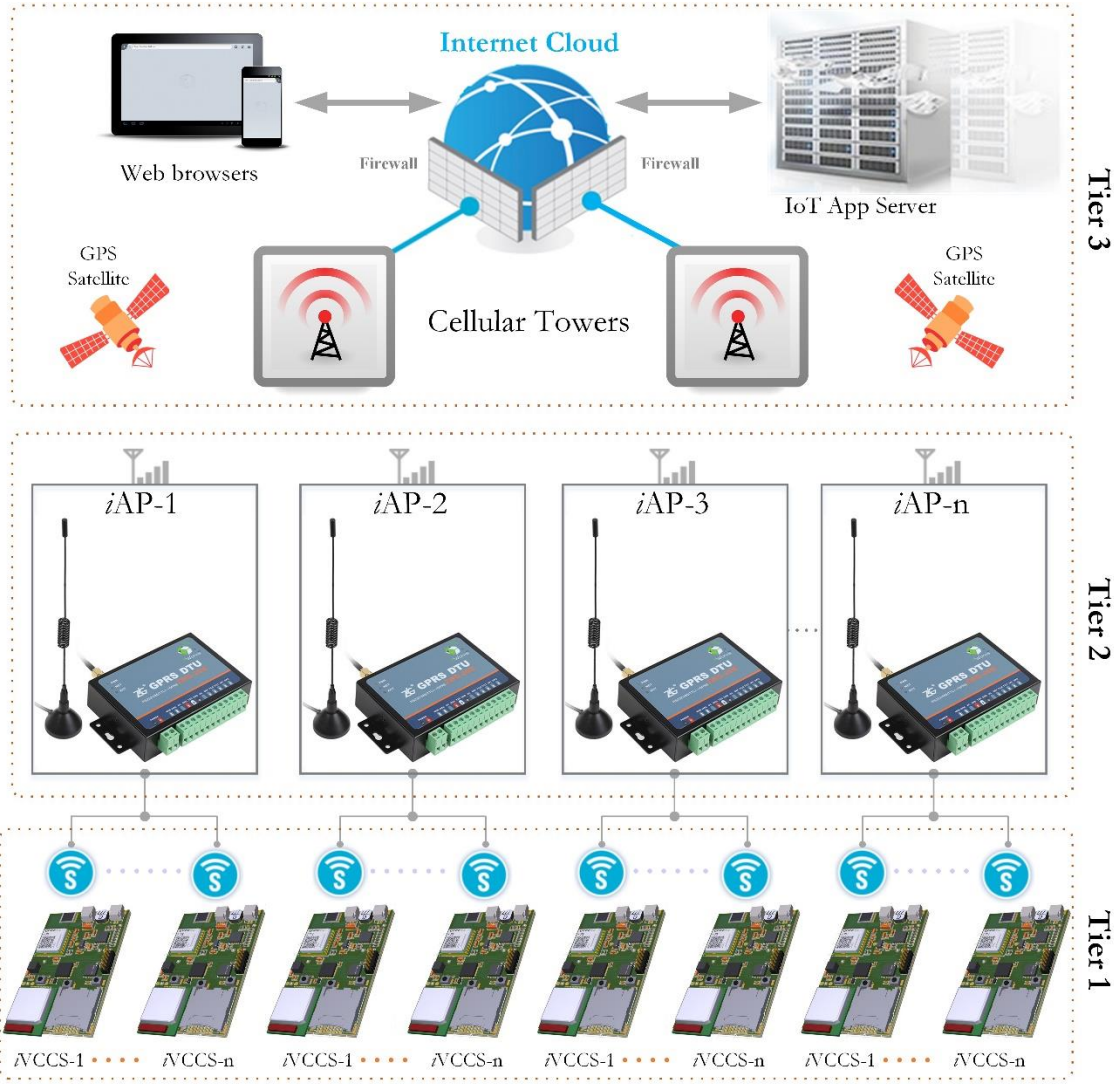


Figure 3-27 Architecture of the traffic surveillance system network

In the event that *i*AP fails to send a response after a number of inquiries within a defined period, *i*VCCS node switches to offline mode. Given that a connection is established, *i*VCCS node switches to online mode wherein, upon request, data is exchanged with the designated *i*AP. Data received by any *i*AP will be processed, analyzed, and logged on a local memory. If there is an established connection, processed data will be moved to an IoT cloud server over a cellular network. If not, data

can be forcibly retrieved by the server at any time. The IoT cloud server lies in the third tier wherein traffic data can be monitored anywhere in real-time. The cloud server can also manage and control the network configuration, as well as facilitate a system's over-the-air firmware upgrade. This hierarchical topology allows a fully scalable, self-configurable, and robust system network [119].

Once the connection is established (and upon request), *i*VCCS nodes exchange data with designated *i*AP. The request is managed by serial inquiry frames and commands.

*i*AP uses *Inquiry Frame* '*IQF*' to send an inquiry to either a specific node (unicast) or all nodes (multicast) requesting information (e.g., battery health; memory status; number of counted vehicles; time and date; sensor status, raw data, and temperature). The corresponding node responds with *Inquiry Response Frame* '*IQRF.'*

*i*AP also uses *Command Frame* '*CMDF'* to send a command to either a single node (unicast) or all nodes (multicast) asking for a specific task to be executed by the node (e.g., 'configure magnetometer', 'do recalibration'). The corresponding node responds with *Command Confirmation Frame* '*CCF*' to confirm the task by writing the binary value '10101010' in the CMD byte or deny it by writing the binary value '01010101.' Note that Sender/Receiver ID is software-coded and is not related to the MAC address.

Inquiry Frame (IQF)

1-byte	*1-byte*	*1-byte*	*1-byte*
S_{ID}	R_{ID}	***IQ***	***CRC***

Inquiry Response Frame (IQRF)

1-byte	*1-byte*	*1-byte*	*1-byte*	*1-250 byte*	*1-byte*
S_{ID}	R_{ID}	***IQ***	***CNT***	***DATA***	***CRC***

Command Frame (CMDF) / Command Confirmation Frame (CCF)

1-byte	*1-byte*	*1-byte*	*1-byte*
S_{ID}	R_{ID}	***CMD***	***CRC***

Field	***Discerption***
S_{ID}	*Sender ID (software)*
R_{ID}	*Receiver ID (software)*
IQ	*Inquiry*
CMD	*Command*
CNT	*Data bytes count*
DATA	*Data stream*
CRC	*8-bit Cyclic Redundancy Check*

Chapter 4: ALGORITHMS DESIGN & FIRMWARE DEVELOPMENT

4.1 Introduction

Providing reliable traffic-monitoring data requires precise vehicle detection and highly accurate speed estimation. Precise detection necessitates a consistent baseline (i.e., maintain static localized geomagnetic field) and coherent sampling rate. Speed estimation relies on precise time-stamping of vehicle arrival and departure, which is dependent on the accuracy of the time-synchronization (T-Sync) algorithm. In this chapter, the development and implementation of various distinctive algorithms for real-time traffic monitoring will be discussed in detail. These include vehicle detection, speed estimation, geomagnetic field baseline drift compensation, T-Sync, RTC drift correction, and other functions. Figure 4-1 illustrates a block diagram of relationships among various developed algorithms and associated interconnection with the system's hardware interfaces and physical components. Hieratical implementation shows three levels. Peripheral algorithms and drivers, namely "*Embedded Firmware,"* are implemented in the third level and interact with various "*Physical World"* components and sensors in the first level through "*Embedded Hardware"* peripherals in the second level.

All algorithms discussed in this chapter are hardware independent, meaning they perform the same intended objectives. Notably, execution performance is hardware dependent (e.g., *i*VCCS$_{G2}$ has an advance performance MCU and more energy efficient components than *i*VCCS$_{G1}$). Firmware development experience also plays a major role in algorithm efficiency during implementation. Pseudo-codes and flowcharts will be provided to maintain efficient implementation of algorithms on various platforms.

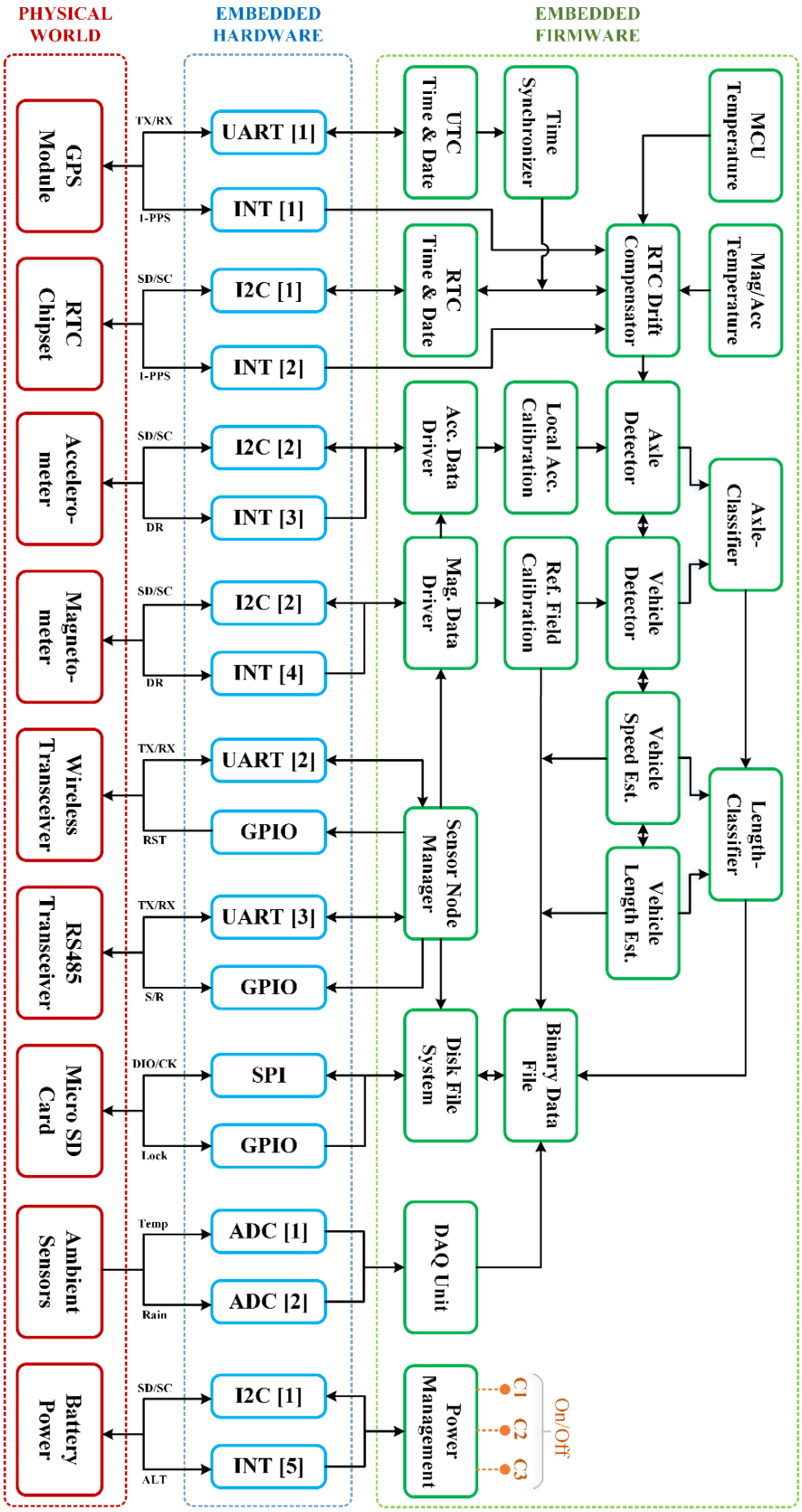


Figure 4-1 Hierarchal integration of hardware and software in *i*VCCS

4.2 Real-Time Vehicle Detection & Counting Algorithm

4.2.1 An Overview on Implementation of Vehicle Detection Algorithms

In literature, fixed [43] or adaptive [57] thresholds have been proposed for vehicle-detection algorithms. Adaptive algorithms are aimed at maintaining a detection threshold above a reference level that could drift due to variations in temperature, background noise, vibrations, aging, or relative earth magnetic field over time.

In this work, a multi-threshold-based detection algorithm was developed. Drift in geomagnetic field baseline is adaptively auto-calibrated in real-time. This method aids in solving problems reported in [53] by keeping magnetic signal variation at a minimum, hence, providing reliable vehicle-speed estimation in low-speed, as well as high speed, congested traffic.

4.2.2 Embedded Magnetometer Sensors

This work features a single MAG for measuring variations in geomagnetic field components (B_X, B_Y, and B_Z) caused by an overpassing vehicle. Figure 4-2 and Figure 4-3 illustrate variations in three geomagnetic field components and the corresponding flux magnitude (F_M): square-root of B_X, B_Y, and B_Z for the Honda Accord 2004 EX-V6, sampled at 200Hz; y-axis is the direction of the traffic.

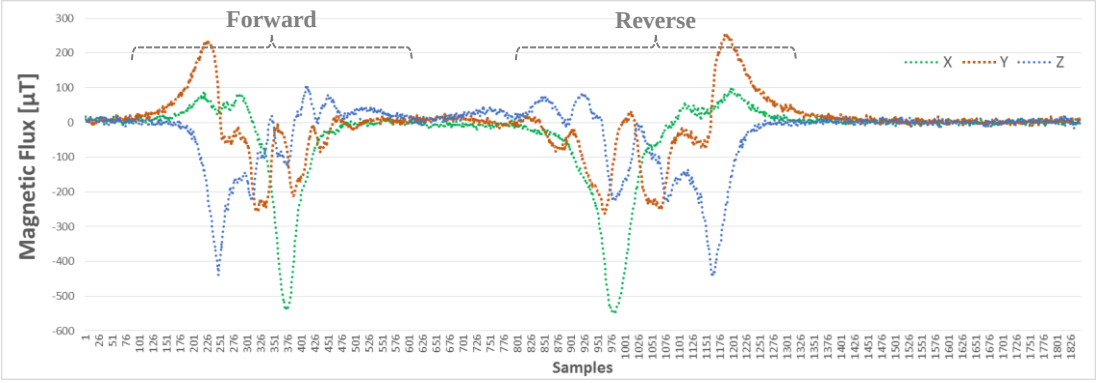


Figure 4-2 Variations in B_Y in forward and reverse driving directions

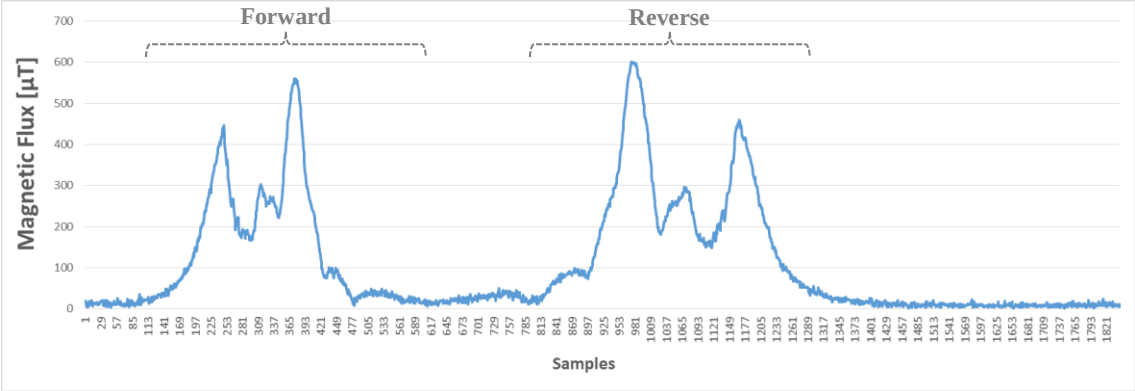


Figure 4-3 Variations in F_M in forward and reverse driving directions

4.2.3 Detection and Counting using an iVCCS in Roadway Setup

A five-state machine process algorithm was developed for real-time vehicle detection and counting, utilizing a single *i*VCCS node. The algorithm acts as an observer for disturbance in the Earth's magnetic field instigated by a passing vehicle. Localized flux lines pull away from the sensor as a vehicle passes the sensor zone and push back toward the sensor as the vehicle drives away (see Figure 1-3), creating fluctuations in F_M. The five-state machine process analyzes fluctuations for valid vehicle detection by leveraging three adaptive thresholds (TH) and three adaptive debounce timers (DT), as shown in Figure 4-4.

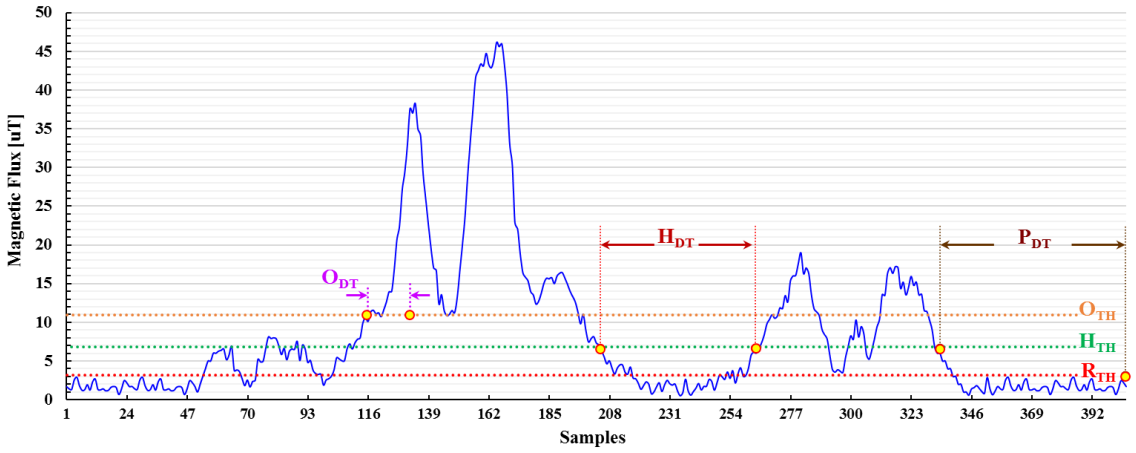


Figure 4-4 Detection Algorithm Parameters applied on a Vehicle Flux Magnitude

Detection Thresholds are defined as follows:

1) *Onset threshold* (O_{TH}): vehicle arrival
2) *Holdover threshold* (H_{TH}): vehicle departure
3) *Baseline threshold* (R_{TH}): re-calibration call

Debounce timers are defined as follows:

1) *Onset debounce timer* (O_{DT}): minimizes misdetection and false events due to a glitch or transient state
2) *Holdover debounce timer* (H_{DT}): minimizes misdetection due to fluctuations in F_M given that the vehicle has relatively small magnetic density (e.g., long trucks)
3) *Detection period debounce timer* (P_{DT}): indicates stationary detection

The algorithm was developed based on MCU interrupts (INT) and an event system to ensure real-time performance and CPU offloading to prolong battery life. Figure 4-5 details a functional block diagram for the detection and counting algorithm. Figure 4-6 illustrates a finite state machine (FSM) diagram for the five-state machine process detection algorithm.

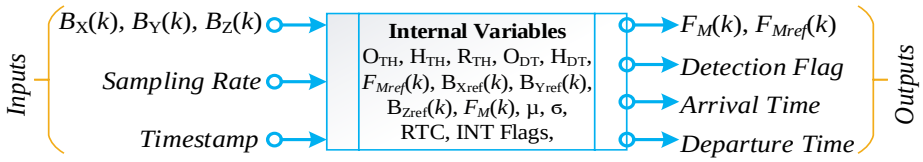


Figure 4-5 Vehicles detection and counting algorithm functional block

Upon system power up, an initialization process triggers a *calibration state* wherein MAG samples localized reference magnetic field components (e.g., B_{Xref}, B_{Yref}, and B_{Zref}) for a period T_S in the absence of vehicles. During this time the reference magnetic field flux magnitude F_{Mref} is calculated using Eq. 4-1.

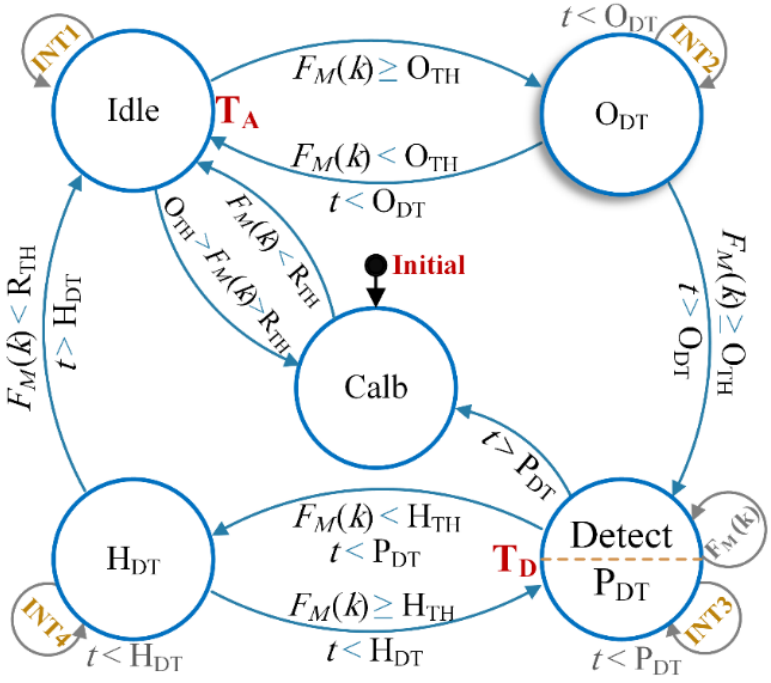


Figure 4-6 State machine process for vehicle detection and counting

$$F_{Mref}(k) = \sqrt{B_{Xref}(k)^2 + B_{Yref}(k)^2 + B_{Zref}(k)^2} \qquad \textbf{Eq. 4-1}$$

F_{Mref} is normally distributed with a mean μ and STD σ such that $F_{Mref} \propto \mathcal{N}(\mu, \sigma)$. After statistically analyzing F_{Mref}, *baseline threshold* R_{TH} is estimated using Eq. 4-2. Consequently, *onset threshold* O_{TH} and *holdover threshold* H_{TH} are calculated according to Eq. 4-3 and Eq. 4-4, respectively; α and β are experimentally defined coefficients according to the detection zone and signal-to-noise ratio (SNR), and $\alpha > \beta$ provides a hysteresis property in detection. F_{Mref} should be unilaterally and adaptively tracked and compensated, as described below in section 0.

$$R_{TH} = \mu + 2\sigma \qquad \textbf{Eq. 4-2}$$

$$O_{TH} = \mu + \alpha \times \sigma \qquad \textbf{Eq. 4-3}$$

$$H_{TH} = \mu + \beta \times \sigma \qquad \textbf{Eq. 4-4}$$

After calibration is complete, the node remains in *idle state* until MAG data-ready interrupt (*INT1*) triggers *onset debounce timer* O_{DT}, given that the state condition $F_M(k) \geq O_{TH}$ (i.e., vehicle in detection zone) is true. $F_M(k)$ is found using Eq. 4-5.

$$F_M(k) = \sqrt{\left(B_X(k) - B_{Xref}\right)^2 + \left(B_Y(k) - B_{Yref}\right)^2 + \left(B_Z(k) - B_{Zref}\right)^2} \qquad \textbf{Eq. 4-5}$$

This function simply compares the magnitude defined by O_{TH} vector with the difference of two vectors, namely sampled magnetic field $F_M(k)$ and localized magnetic field reference $F_{Mref}(k)$. If the former is greater than the latter for a minimum duration of time specified by O_{DT}, then a true detection event is raised.

This event can be expressed using vectors, as in Eq. 4-6. MAG sample is denoted by $\vec{M}$, and $\overrightarrow{M_{ref}}$ is programmable offset. Eq. 4-6 can be rewritten as Eq. 4-7, where F_M and F_{Mref} are magnitudes of $\vec{M}$ and $\overrightarrow{M_{ref}}$, and α is the angle between vectors.

$$\left|\vec{M} - \overrightarrow{M_{ref}}\right| = \sqrt{\left(\vec{M} - \overrightarrow{M_{ref}}\right).\left(\vec{M} - \overrightarrow{M_{ref}}\right)} > O_{TH} \qquad \textbf{Eq. 4-6}$$

$$\sqrt{\vec{M}.\vec{M} - 2.\vec{M}.\overrightarrow{M_{ref}} + \overrightarrow{M_{ref}}.\overrightarrow{M_{ref}}} = \sqrt{{F_M}^2 + {F_{Mref}}^2 - 2F_M F_{Mref}\cos\alpha} > O_{TH} \qquad \textbf{Eq. 4-7}$$

A transition into *detect* state occurs after O_{DT} is elapsed and the state condition $F_M(k) \geq O_{TH}$ is still true. In *detect* state, the sensor samples the magnetic field, calculates $F_M(k)$, and logs $B_X(k)$, $B_Y(k)$ and $B_Z(k)$ into a storage memory.

To minimize double-detection errors resulting from fluctuations in F_M that could possibly occur between O_{TH} and H_{TH}—given that part of the vehicle has relatively small magnetic flux density (e.g., long combination trucks), a *holdover debounce-timer* H_{DT} is utilized. H_{DT} plays a significant role in reducing detection errors.

A transition from *detect* state to H_{DT} state occurs when $F_M(k) < H_{TH}$ (i.e., vehicle departed the detection zone). A transition into *idle* state occurs when *INT4* triggers after H_{DT} is elapsed and $F_M(k) < H_{TH}$. Vehicle counter will then be incremented by one, and vehicle arrival time (T_A) and departure time (T_D) will be logged. T_A and T_D are accurately captured in exactly 12 CPU cycles when *INT1* and *INT3* triggers, respectively. The system remains in *idle* state until *INT1* is triggered again or $F_M(k) \geq R_{TH}$ (i.e., a drift in the localized magnetic field baseline).

Detection period debounce-timer P_{DT} can be configured according to the intended application. For example, P_{DT} can be used as a watch-dog-time on highways to clear errors resulting from an accidental change in field baseline during a detection event (e.g., high speed loaded truck hitting a sensor) and to trigger recalibration. P_{DT} can also be configured as a stationary detection timer for parking lot applications.

4.2.4 Detection and Counting using a iVCCS in Roadside Setup

*i*VCCS can be deployed on roadsides adjacent to the lane, in favor of a roadway setup in the center of a lane. The system uses the algorithm indicated in Figure 4-6 for vehicle detection. However, for a motorcycle or small vehicle driving on the far side of the lane opposite the sensor side, SNR could be significantly low, causing misdetection. Figure 4-7 shows variations in geomagnetic field components and magnitude caused by the Honda Accord 2004 EX-V6 when passing *adjacent* to the sensor at a distance of 1 meter. Y-axis is the traffic direction. When compared with *roadway* setup in Figure 4-8, it is clear that the magnitude in *roadside* setup is three times weaker. Moreover, signal variations in *roadside* setup are relatively uniform when compared with roadway setup.

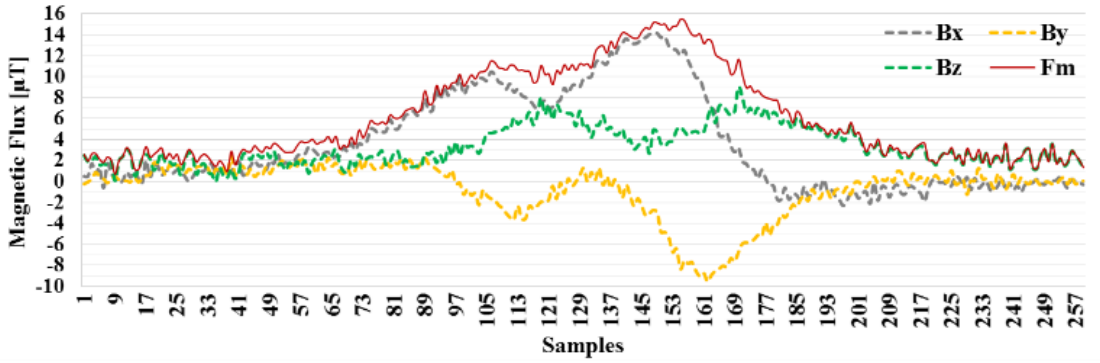


Figure 4-7 Class 2 vehicle magnetic signature sampled by *i*VCCS on roadside

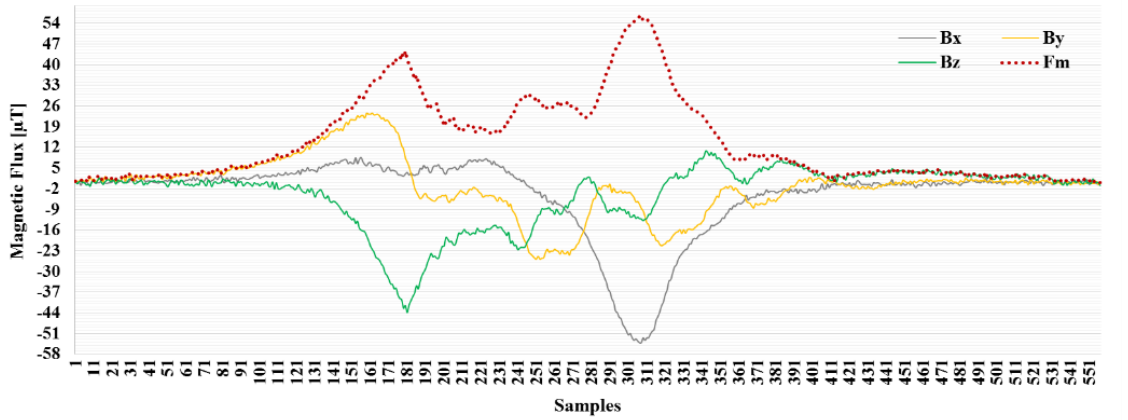


Figure 4-8 Class 2 vehicle magnetic signature sampled by *i*VCCS on roadway

To mitigate this issue, a moving average filter (MAF) with gain coefficient *w* can be employed to reduce signal fluctuations and detect the trend of the $F_{M_{gain}}(k)$, calculated using Eq. 4-8 and Eq. 4-9, which is the input of detection algorithm in Figure 4-6. One drawback of roadside setup is that it only works for roads with no more than two lanes.

$$F_{M_{gain}}(k) = \frac{w}{N}\sum_{i=0}^{N-1} F_M(k-i)\,; \qquad w = 4,\ \ N = 5 \qquad \textbf{Eq. 4-8}$$

$$F_{M_{gain}}(k) = \begin{cases} w\times \dfrac{F_M(k) + F_M(k-1) + \cdots + F_M(k)}{k}; & k < N \\ w\times \dfrac{F_M(k) + F_M(k-1) + \cdots + F_M(k-N+1)}{N}; & k \geq N \end{cases} \qquad \textbf{Eq. 4-9}$$

4.2.5 Adaptive Geomagnetic Baseline Drift Compensation

Variations in temperature, vibrations, and aging will cause a considerable drift in the mean value of $F_{Mref}(k)$, which causes detection errors and unreliable speed and length estimation. Thus, $F_{Mref}(k)$ should be tracked so that B_{Xre}, B_{Yref}, and B_{Zref} are compensated for any drift. Tracking $F_{Mref}(k)$ is achieved using a MAF when $F_M(k) < O_{TH}$. The algorithm computes new B_{Xref}, B_{Yref}, and B_{Zref} values, as in Eq. 4-10, when Eq. 4-11 is satisfied.

$$B_{ref}^{(\gamma)} = \frac{1}{M}\sum_{i=0}^{M-1} B^{(\gamma)}(k-i)\,; \quad \gamma = \{X, Y, Z\} \in \mathbb{R}^3 \qquad \textbf{Eq. 4-10}$$

$$\frac{1}{M}\sum_{i=0}^{M-1}\left[F_{M_{ref}}(k-i) - F_{M_{ref}}(k)\right] \geq R_{TH} \qquad \textbf{Eq. 4-11}$$

A high-level description of the baseline drift compensation algorithm is shown in Figure 4-9. A flowchart is detailed in Figure 4-10.

The drift compensation algorithm simply tracks geomagnetic field over time to maintain reference magnetic signal variations at a minimum. The function stores $B_X(k), B_Y(k)\ and\ B_Z(k)$, and calculates $F_M(k)$ when MAG data ready interrupt (INT1) triggers. $F_M(k)$ MAF output is compared to *baseline threshold* R_{TH}. New geomagnetic field reference level components $B_{ref}^{(\gamma)}$ are calculated and set using MAF when $F_{MAvg}(k) > R_{TH}$.

MAF, although simple, was able to detect magnetic field disturbances caused by factors not related to vehicle presence including temperature, road structure, surrounding objects, etc. This work didn't attempt to discover or model all possible drift

causing disturbances that may occur at various locations besides those field testing during this research.

Inputs: $B_X(k)$, $B_Y(k)$, $B_Z(k)$

Outputs: B_{Xref}, B_{Yref}, B_{Zref}

1: **WHILE** $F_M(k) < O_{TH}$

2: **WAITFOR** Magnetometer *Data-Ready INT*

3: BUFFER ← COMPUTE $F_M(k)$ ← READ $B_X(k)$, $B_Y(k)$, $B_Z(k)$

4: $Idx \leftarrow Idx + 1$

5: **IF** $Idx = M$ **THEN**

6: $F_{M.Avg} \leftarrow \frac{1}{M}\sum_{j=0}^{M-1} F_M[k-j]$

7: **IF** $O_{TH} > F_{M\text{-}Avg} \geq R_{TH}$ **THEN**

8: $B_{Xref}, B_{Yref}, B_{Zref} \leftarrow \frac{1}{M}\sum_{i=0}^{M-1} B^{(\gamma)}[k-i]$

9: **ENDIF**

10: $Idx \leftarrow 0$: BUFFER ← 0

11: **ENDIF**

12: **LOOP**

13: $Idx \leftarrow 0$: BUFFER ← 0

Figure 4-9 Adaptive Geomagnetic Baseline Drift Compensation Pseudocode

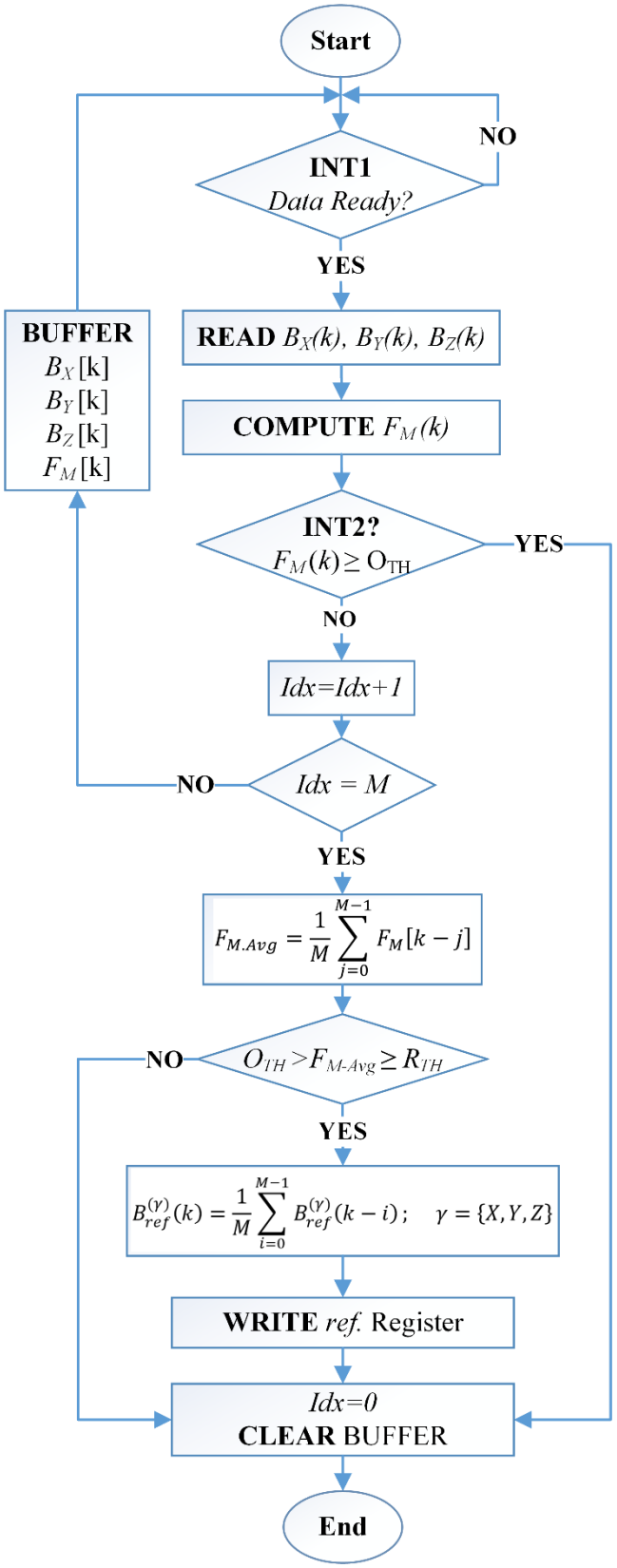


Figure 4-10 Flowchart for adaptive compensation of geomagnetic baseline drift

4.3 Vehicle Speed Estimation and Time Synchronization

In this section, the development and implementation of various algorithms for real-time vehicle speed estimation and time synchronization are discussed.

4.3.1 Real-Time Vehicle Speed Estimation using Two Sensor Nodes

The most accurate method to measure vehicle speed is by calculating travel time between two longitudinally positioned sensor nodes ($N_A \rightarrow N_B$) separated by distance *d*, as shown in Figure 4-11.

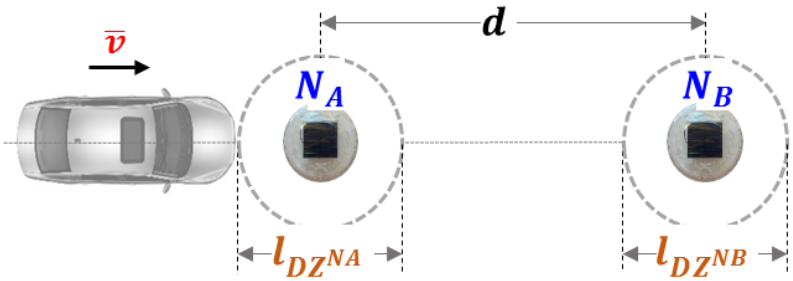


Figure 4-11 Speed estimation deployment setup

Two measures of speed can be identified: 1) per-vehicle or instantaneous speed ($\bar{v}_i$), which is the attained speed of a vehicle at time instant *t*, and 2) aggregated or time-mean speed ($\bar{v}_t$), which is the average speed of *n* vehicles *v* over time period *t* at a specific location. $\bar{v}_i$ and $\bar{v}_t$ are calculated using Eq. 4-12 and Eq. 4-13, respectively. $T_A^{(N_i)}$is vehicle arrival time; $T_D^{(N_i)}$ is the departure time; and q is number of vehicles traveling at the same speed.

$$\bar{v}_i \approx \frac{d^{(N_A \rightarrow N_B)}}{T_A^{(N_B)} - T_A^{(N_A)}} \approx \frac{d^{(N_A \rightarrow N_B)}}{T_D^{(N_B)} - T_D^{(N_A)}} \approx 2\frac{d^{(N_A \rightarrow N_B)}}{T_A^{(N_B)} - T_A^{(N_A)} + T_D^{(N_B)} - T_D^{(N_A)}} \quad \textbf{Eq. 4-12}$$

$$\bar{v}_t = \frac{1}{n}\sum_{i=1}^{n} \bar{v}_i = \frac{\sum_{i=1}^{n} q_i . \bar{v}_i}{\sum_{i=1}^{n} q_i} = \frac{\sum_{i=1}^{n} q_i . d}{\sum_{i=1}^{n} q_i . t_i} = \frac{\sum_{i=1}^{n} q_i . d^{(N_A \rightarrow N_B)}}{\sum_{i=1}^{n} q_i \, (T_i^{(N_B)} - T_i^{(N_A)})} \quad \textbf{Eq. 4-13}$$

Timestamps $T_A^{(N_i)}$ and $T_D^{(N_i)}$ are sent by sensor nodes and received by an iAP, which in turn process speed and length estimation and classification.

For reliable, accurate vehicle speed and length estimation, a high-precision time synchronization must be considered. Failing to synchronize all sensor nodes within a network will cause inaccurate measurements and confuse decision-making in the intelligent controller. Such circumstances might lead to an unsafe condition as a consequence of a false alarm. For instance, consider a vehicle travelling 90 mph on a highway on which two sensor nodes are deployed on a single lane 6 meters apart. If a required speed estimation error is anticipated to be less than ε=±1%, maximum timing error $T_{sync-err}$ should be less than 1.5ms, as indicated by Eq. 4-14 (1mph=0.44704m/s). Separation distance between sensors depends on speed range. Increasing d would reduce error. [120] recommends d=3.1—3.7 meter for arterial setup and d=6.1—7.3 meter for freeway setup.

$$T_{sync-err} = \frac{d}{v} \times \varepsilon = \frac{6}{90 \times 0.44704} \times 0.01 \approx 1.5\, ms \qquad \textbf{Eq. 4-14}$$

4.3.2 Real-Time Vehicle Speed Estimation using Single Sensor Node

Three interrelated parameters, namely vehicle magnetic length (VML), speed (v), and occupancy time ($T_{Occ}^{(N_i)}$), can be directly estimated or measured for each passing vehicle when two sensor nodes are used per lane, as in Eq. 4-15. However, when using a single sensor node, only $T_{Occ}^{(N_i)}$ can be directly calculated, as in Eq. 4-16.

$$\overline{VML} = \bar{v} \times T_{Occ}^{(N_i)} \qquad \textbf{Eq. 4-15}$$

$$T_{Occ}^{(N_i)} = T_D^{(N_i)} - T_A^{(N_i)} \qquad \textbf{Eq. 4-16}$$

Several studies have reported different techniques for estimating vehicle speed using a single IDL detector. One technique depends on assuming an average length and aggregating a large number of estimated speed samples within a time window to reduce estimation error resulting from uncorrelated length and speed measurements. However, this method is prone to error when mean length deviates (i.e., too many long vehicles).

In this work, an improved speed estimation method developed in [121] for a single IDL detector was adopted using single MAG. The first method employs a moving median, as in Eq. 4-17.

$$v_{median} = \frac{VML_{average}}{median\left(T_D^{(N_x)} - T_A^{(N_x)}\right)} \qquad \textbf{Eq. 4-17}$$

The moving median method uses a fixed window of *n* samples (i.e., vehicle speed values) centered on the current sample. The window moves one vehicle for each sample and calculates median speed for the current vehicle, and so on. Sample buffer should be selected with size enough to ensure minimal speed estimation error. Based on statistical data collected using MAG, a fixed window of 37 samples and average length of 7.2m was selected. A high-level description for moving median algorithm is shown in Figure 4-12.

Given that the ratio of short to long vehicle fluctuates, the sequence method can be applied to further improve speed estimation. Because the sensor's occupancy time ratio between two successive vehicles should be proportional to their length, it is possible to statistically determine a ratio threshold between the mean of long vehicles (LV) and short (SV) vehicles based only on occupancy time, as in Eq. 4-18. Authors in [121] suggested a ratio 3.5:1 for IDL. The statistical analysis conducted in Chapter 6 revealed a ratio 3.7:1, LV for MAG. Given multiple sequences within the sample

window, the algorithm estimates speed for each sequence and then assigns median speed from all individual estimates to the sample. Otherwise, given no such sequences within the sample window, the algorithm falls back to the moving median method. A high-level description for the sequence method algorithm is shown in Figure 4-13.

$$\hat{v}_{SV} = \frac{L_{SV}^{A}}{\left(T_{D}^{(N_x)} - T_{A}^{(N_x)}\right)_{SV}}; \qquad \hat{v}_{LV} = \frac{L_{LV}^{A}}{\left(T_{D}^{(N_x)} - T_{A}^{(N_x)}\right)_{LV}} \qquad \textbf{Eq. 4-18}$$

Inputs: window_size = 37, $VML_{average} = 7.2m$

Outputs: v_{median}

1: **WHILE (1)**

2: *Computer occupancy of each vehicle in the window of current vehicle*

3: *Search for median value within all values in the window*

4: $v_{median} \leftarrow VML_{average}$*/ median occupancy*

5: *Shift the window index to the right by 1*

6: **LOOP**

Figure 4-12 Moving median speed estimation algorithm

Inputs: $L_{SV}^{A} = 6.6m$, $L_{LV}^{A} = 15m$, $Occ_{Ratio} = 3.7m$

Outputs: $\hat{v}_{LV}$, $\hat{v}_{SV}$

1: **WHILE (1)**

2: *Occ(i) ← Computer occupancy of vehicle i in the sample window*

3: *Occ(i+1) ← Computer occupancy of vehicle i+1 in the sample window*

4: **IF** *Occ(i+1) / Occ(i) >* Occ_{Ratio} **THEN**

5: $\hat{v}_{SV} \leftarrow L_{SV}^{A}$*/ Occ(i)* : $\hat{v}_{LV} \leftarrow L_{LV}^{A}$*/ Occ(i+1)*

6: **ELSE**

7: *Compute moving median speed*

8: **END IF**

9: *Shift the window index to the right by 1*

10: **LOOP**

Figure 4-13 Speed estimation algorithm using sequence method

4.4 Time Synchronization using Embedded GPS Module

Each sensor node relies on an onboard GPS module and RTC unit to maintain an independent local clock that is globally synchronized to the GPS pulse-pre-second (PPS) signal. Therefore, wireless connectivity is not necessary for accurate functioning of *i*VCCS nodes. Time stamping, timekeeping, and failure recovery functions are enabled by the MCU's internal RTC unit, which is calibrated and aligned using the PPS signal.

Upon *i*VCCS node power-up, the embedded MCU enables the GPS module via an ultra-low, quiescent-current load switch. Once the GPS receiver is successfully locked to available satellites, the Coordinated Universal Time (UTC) information packet is used to set RTC time and date. The rising edge of PPS signal, which is globally synchronized with ±10ns timing accuracy, is used to align RTC clock phase and independently synchronize all WSN-node RTC clocks to the same reference signal (i.e., PPS) on a global scale without exchanging messages over the wireless network.

Once RTC is synchronized, MCU sets the GPS module in backup mode. Location coordination of the sensor node and its ID will be reported to the corresponding *i*AP for mapping purposes. Procedure inputs and outputs are depicted in Figure 4-14. Time zone is denoted by TZ, and daylight saving time is DST. A high-level description of RTC settings and phase alignment using a GPS module is illustrated in Figure 4-15.

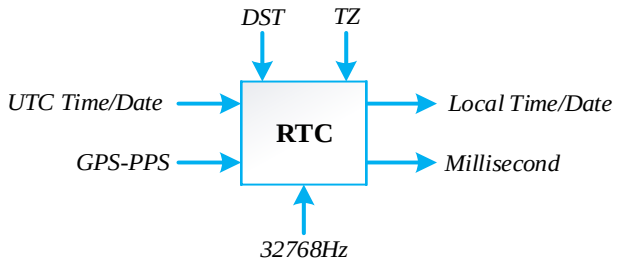


Figure 4-14 GPS-based RTC clock setting and phase alignment block

The method detailed above provides extremely accurate T-Sync, although RTC phase alignment error calculated using Eq. 4-21 is subject to frequency tolerance $f_{osc\text{-}tol}$ of the MCU oscillator. For *i*VCCS, $f_{osc\text{-}tol} = \pm 5ppm$ and f_{osc} = 32MHz. Another factor affecting T-Sync accuracy is RTC frequency drift [122], [123], which is discussed in the next section.

$$RTC_{phaseErr} = \frac{f_{osc-tol}^{(MCU)}}{10^6} = \frac{\pm 5_{ppm}}{10^6} \approx \pm 5\mu s \qquad \textbf{Eq. 4-19}$$

Inputs: Time Zone, DST,

Outputs: Local Time/Date, Geographic coordinates,

1: DISABLE *RTC clock*, INITIALIZE *GPS Module*

2: **WHILE** *GPS-3D-Fix* **IS** *BUSY* **LOOP**

3: **WHILE** *GPS-PPS* **IS** *INACTIVE* **LOOP**

4: **WHILE** *NMEA* <> *$GPRMC | $GNRMC* **LOOP**

5: **{***UTC Time, Date, Coordinates***}** ← **READ** $GPRMC|$GNRMC

6: COMPUTE *Local Time/Date, Sec* ← *Sec+1, DST, Leap Year*

7: **WAIT FOR** *GPS-PPS Rising Edge Interrupt*

8: SET *RTC(Time/Date)* ← *GPS(Time/Date)*

9: ENABLE *RTC clock*, SET *GPS Module into Power Saving mode*

Figure 4-15 Pseudo-code for RTC setting and phase alignment using GPS-PPS

4.4.1 Adaptive Compensation of the RTC Frequency Drift

RTC accuracy is dependent on a 32.768KHz crystal oscillator ($32KHz_{osc}$) with maximum resolution of 30.517μs (i.e., 1/32769 = 30.517μs). $32KHz_{osc}$ accuracy is subject to several factors, including manufacturing tolerances in the $32KHz_{osc}$, passive PCB components, temperature excursions, and aging. The primary T-Sync error when using RTC is caused by the $32KHz_{osc}$ uncompensated frequency drift.

*i*VCCS$_{G1}$ uses ABS07-32.768KHZ-T—a 32.768KHz SMD low profile crystal—which has an extended temperature operation from -55°C to +125°C for industrial applications. Output of 32KHz$_{osc}$ has parabolic frequency dependence over temperature, as depicted in Figure 4-16. Frequency drift at temperature *T* is expressed in Eq. 4-20, where β is a temperature coefficient given in ppm/T^2, which is always negative (i.e., RTC oscillator slows down at cold or hot temperatures around T_0). T_0 is a turnover temperature—25°C±5°C. If β=-0.036ppm/T^2±15% and T_0 = 25°C±5°C, the corresponding frequency drift at T=50°C, for example, is found using Eq. 4-20.

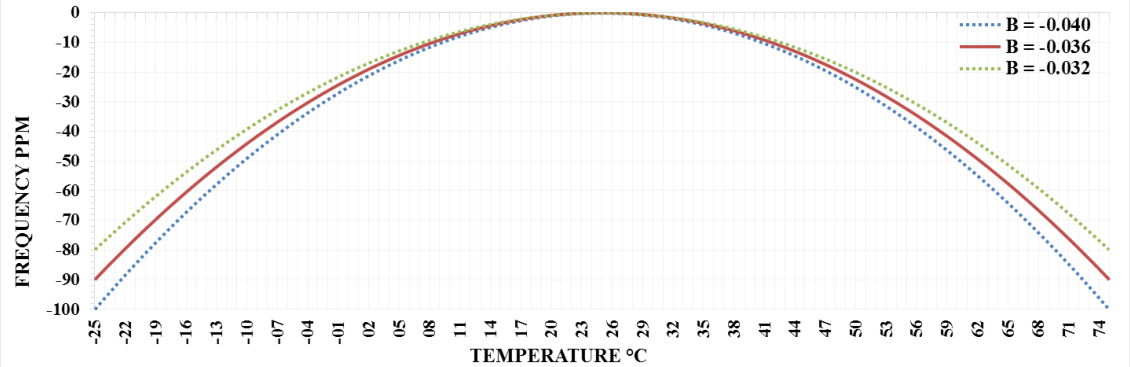


Figure 4-16 Frequency stability vs. Temperature characteristics for ABS07

$$\frac{\Delta f}{f_0} = \boldsymbol{\beta}(\boldsymbol{T} - \boldsymbol{T_0})^{\boldsymbol{2}} = -0.036\times(50-25)^2 = -22.5\,ppm \qquad \textbf{Eq. 4-20}$$

A -22.5ppm with respect to time is equal to:

$$-\frac{22.5}{10^6}\times 60\times 60\times 24 = -1.944\frac{sec}{day} = -81\frac{msec}{hour} = -1.35\frac{msec}{min} = -22.5\frac{\mu sec}{sec}$$

The 32KHz$_{osc}$ drift ε_{RTC} at constant *T* has a slope *m*=1, meaning that change in ε_{RTC} is constant over time at constant temperature. Measuring ε_{RTC} at 26°C for one hour showed a constant drift of 15µs (i.e., 54ms/hour), which can be modeled as a linear equation in Eq. 4-21, where current RTC time is denoted by t_{RTC}; corrected RTC time

is $\hat{t}_{RTC}$; GPS time at calibration moment is t_{GPS}; and $\xi_{RTC}^{(T_{osc})}$ is the accumulated error at T_{osc}. T_{RTC} is the compensated RTC time.

$$\hat{t}_{RTC} = m \times t_{RTC} \pm \xi_{RTC}^{(T_{osc})} \;\; ; \qquad \xi_{RTC}^{(T_{osc})} = \varepsilon_{RTC}^{(T_{osc})}(\hat{t}_{RTC} - t_{GPS}) \, , m = 1 \qquad \textbf{Eq. 4-21}$$

Temperature variations will cause drift in $32KHz_{osc}$ output. To maintain T-Sync error in Eq. 4-14 within an intended range, RTC drift should be tracked for compensation, meaning it is possible to correct t_{RTC} drift by knowing T_{OSC}. Corresponding frequency drift can then be calculated, with respect to time, using Eq. 4-20; $\hat{t}_{RTC}$ value can be then found using Eq. 4-21.

The objective of this method is rejecting the disturbance (i.e., variations in T_{OSC}). Measuring T_{OSC} is not possible, because oscillator does not have a built-in temperature sensor. Nevertheless, and to a greater extent, under steady-state conditions T_{OSC} can be assumed equal to the temperature of surrounding components. In addition to an on-board thermistor, MAG has an on-die temperature sensor that can be used to extrapolate T_{OSC}. This approach is appropriate, given that $32KHz_{osc}$ output has a frequency tolerance $\leq \pm 5\mu s$ and aging factor of $\leq \pm 1°C@25°C/year$. It is important to realign RTC phase when temperature changes approximately 3°C. A re-synchronization using GPS is also required every few hours to correct residual errors. Figure 4-17 illustrates the RTC drift correction process.

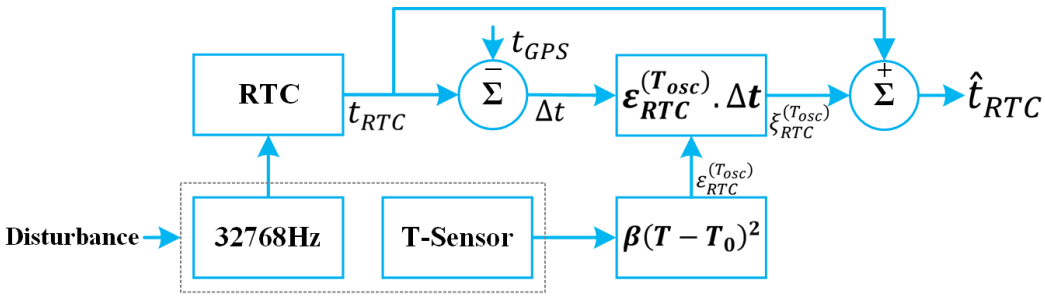


Figure 4-17 RTC drift correction system block diagram

A second approach to correcting $32KHz_{osc}$ output drift was developed. RTC-1Hz signal frequency $f_{RTC}^{(MCU)}$ was compared to an accurate reference frequency $f_{PPS}^{(GPS)}$, PPS signal frequency. In this scheme, both clocks are sampled using high frequency clock $f_{TCLK}^{(MCU)}$, driven from the MCU's 32MHz oscillator. $f_{TCLK}^{(MCU)}$has a tolerance ±5*ppm*; however, since both signals are measured using the same clock at the same time, tolerance error is canceled out. If T_{osc} changes approximately 3°C, the algorithm awakens the GPS module, aligns the RTC phase, and computes a new time correction coefficient $\xi_{RTC}^{(T_{osc})}$. Figure 4-18 illustrates the RTC phase correction system.

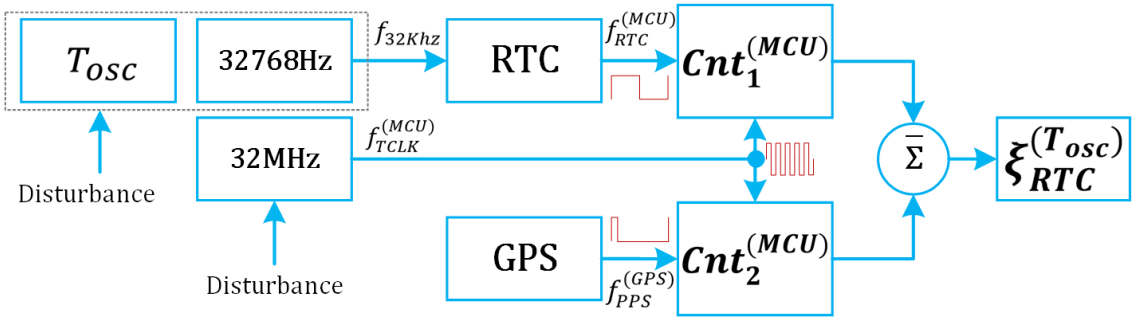


Figure 4-18 PPS-based RTC time drift correction system block diagram

Once RTC phase is aligned, the algorithm configures two 16-bit MCU counters (*Cnt₁* and *Cnt₂*) in an overflow interrupt (OVI) mode. *Cnt₁* is triggered by an external interrupt, generated on the rising edge of GPS-PPS signal. *Cnt₂* is triggered by 1-sec RTC timer interrupt, which is generated each time MCU's RTC timer reaches the top value 32,768 and then transitions to zero. Elapsed time at *Cnt₁* or *Cnt₂* overflow interrupt is calculated (See Eq. 4-22), where D_v is a clock divider and N is timer precision.

$$Cnt_{Tmax}^{(i)} = \frac{2^N \times D_v}{f_{TCLK}^{(MCU)}} = \frac{65536 \times 1}{32 \times 10^6} = 2.048\ msec \qquad \textbf{Eq. 4-22}$$

Because 2.048ms is maximum count time for Cnt_1 or Cnt_2, 488.28125 OVIs is required to count 1-sec, as evident in Eq. 4-23. OVI fraction value is equal to 0.28125/65536=18432 count. Total number of counts, calculated in Eq. 4-24, is the number of OVI multiplied by counter precision plus the residual value in the counter register. A new time correction coefficient $\xi_{RTC}^{(T_{osc})}$ is calculated, as in Eq. 4-25, where $Cnt_{avg}^{(i)}$ is the average count of *n* measurements (i.e., *n*-sec).

$$OVI_{1s}^{(Cnt^{(i)})} = \frac{t_{target}}{Cnt_{Tmax}^{(i)}} = \frac{1sec}{2.048ms} = 488.28125 \qquad \textbf{Eq. 4-23}$$

$$Cnt_{Total}^{(i)} = \left[2^N \times OVI^{(Cnt^{(i)})}\right] + Cnt^{(i)} \qquad \textbf{Eq. 4-24}$$

$$\boldsymbol{\xi_{RTC}^{(T_{osc})}} = \frac{Cnt_{avg}^{(2)} - Cnt_{avg}^{(1)}}{f_{TCLK}^{(MCU)}}; \qquad Cnt_{avg}^{(i)} = \frac{1}{n}\sum_{k=1}^{n} Cnt_{Total}^{(i)}(k) \qquad \textbf{Eq. 4-25}$$

$\xi_{RTC}^{(T_{osc})}$ value represents timing error (i.e., drift) or, in other words, time difference between measured periods of GPS-PPS-1Hz reference signal and RTC-1Hz signal.

Once the correction process is complete, GPS module is set to power-down mode. Corrected timestamp is the instantaneous RTC value plus the accumulated correction coefficient value over time.

Measurement resolution is one-cycle of $f_{TCLK}^{(MCU)}$, which is equal to 31.25ns. The correction algorithm should be executed at regular intervals (e.g., every hour) to adjust and realign the RTC phase and keep nodes synchronized. A high-level description of RTC frequency drift compensation using GPS-PPS signal is presented in Figure 4-19. A flowchart representation is depicted in Figure 4-20.

Inputs: Sec, 60minCnt

Outputs: $\xi_{RTC}^{(T_{osc})}$, RTC-CNT

1: **IF** Sec = 0 **THEN**

2: $T(k) \leftarrow \frac{1}{M}\sum_{i=0}^{M-1} T(k-i) \leftarrow$ READ Temperature

3: **IF** $T(k) \geq T(k-i) + 3$ or $T(k) \leq T(k-i) - 3$ or 60minCnt **THEN**

4: INITIALIZE GPS in Tracking Mode

5: **WHILE** GPS-3D-Fix **IS** BUSY **LOOP**

6: **WAITFOR** *GPS-PPS Rising Edge Interrupt*

7: RTC-CNT$\leftarrow$1{*Realign RTC Phase, Reinitialize RTC Reg.*}

8: $OVI^{(Cnt^{(i)})} \leftarrow 0$, $Cnt^{(i)} \leftarrow 0$, START $Cnt^{(i)}$; $i = \{1,2\}$

9: **WHILE** n < 2

10: **WAITFOR** *GPS-PPS Rising Edge Interrupt, RTC-1sec Interrupt*

11: $Cnt_{Total}^{(i)}(n) = \left[2^N \times OVI^{(Cnt^{(i)})}\right] + Cnt^{(i)}$; $i = \{1,2\}$

12: **LOOP**

13: GPS Module $\leftarrow$ Power Saving mode, 60minCnt $\leftarrow$ 0

14: $Cnt_{avg}^{(i)} = \frac{1}{n}\sum_{k=1}^{n} Cnt_{Total}^{(i)}(k)$; $i = \{1,2\}$

15: $\xi_{RTC}^{(T_{osc})} = \frac{Cnt_{avg}^{(2)} - Cnt_{avg}^{(1)}}{f_{TCLK}^{(MCU)}}$

16: **ENDIF**

17: **ENDIF**

Figure 4-19 PPS-based RTC frequency drift compensation algorithm

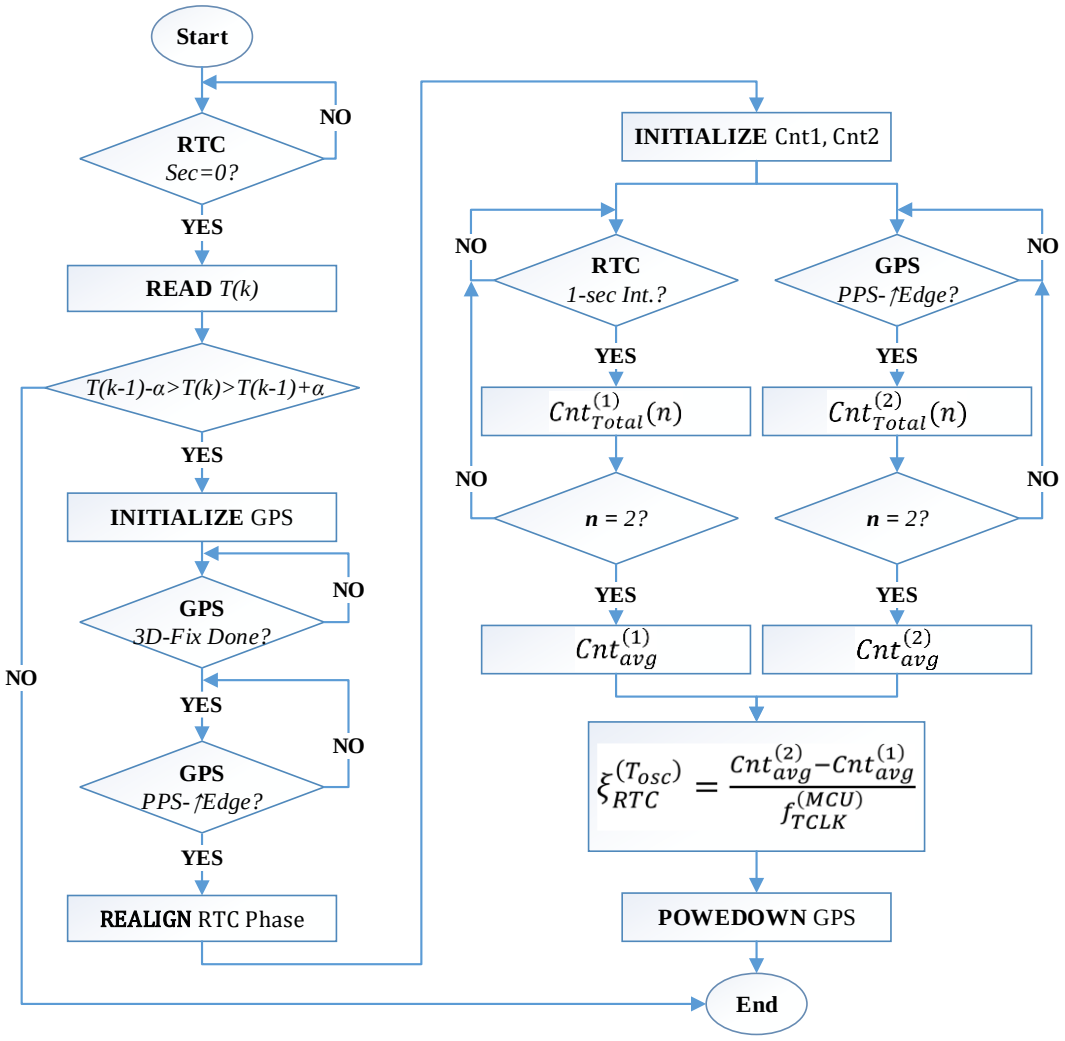


Figure 4-20 PPS-based RTC frequency drift compensation flowchart

A third approach to overcome $32KHz_{osc}$ output drift was implemented in *i*VCCS$_{G2}$. *i*VCCS$_{G2}$ uses SiT1552 [97]—an ULP 32.768KHz MEMS TCXO—to provide highly accurate clock source to the MCU's RTC unit. SiT1552 consists of MEMS resonator and a programmable analog circuit, as depicted in Figure 4-21. Unlike quartz crystals that have a classic tuning fork parabola temperature curve with a 25°C turnover point, SiT1552 temperature coefficient is factory calibrated and corrected over multiple temperature points using an active temperature correction circuit to ensure

extremely tight frequency variation (i.e., ±5ppm) throughout the -40°C to +85°C temperature range (See Figure 4-22).

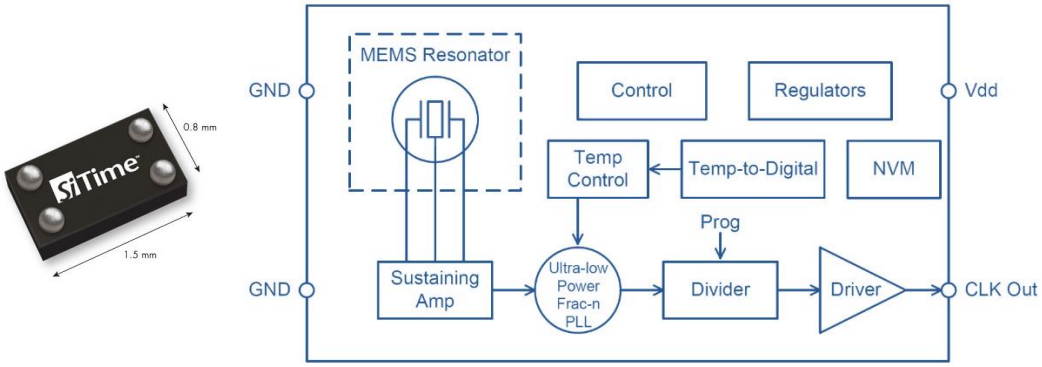


Figure 4-21 SiT1552 MEMS TCXO block diagram

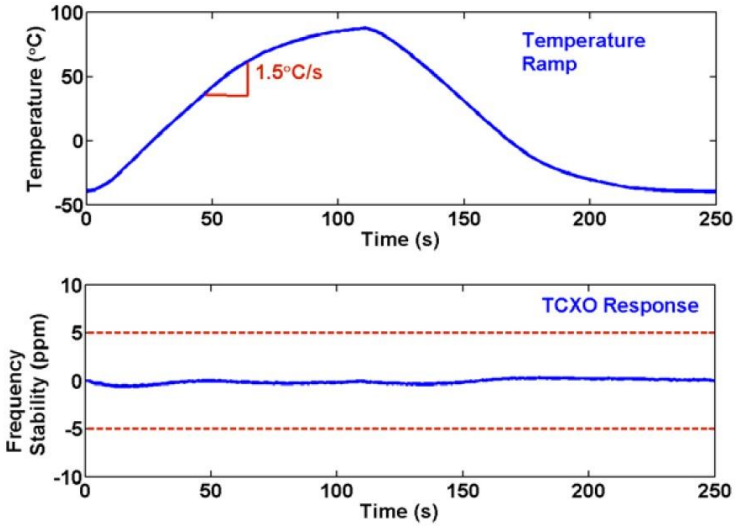


Figure 4-22 SiT1552 stability over temperature

Using SiT1552 will significantly improve $32KHz_{osc}$ output stability with ±5ppm frequency tolerance throughout the -40°C to +85°C temperature range. Notably, ±5ppm can be reduced to 0.9537ppm by employing the STM32L0 MCU *Digital Smooth Calibration* feature in *i*$VCCS_{G2}$.

The STM32L0 MCU series implements an RTC calibration register (i.e., CALP-CALM) that can be used to increase or decrease the RTC clock (i.e., 32768Hz) with a fine resolution of 0.954ppm. An offset ranging from -511 to +512 RTC clock cycles can

be added within a 32-second cycle (i.e., 2^{22}) calibration window (i.e., -487.1ppm to +488.5ppm calibration range). Hence, after RTC phase is aligned using GPS, all nodes can be kept synchronized by calculating RTC clock error when temperature changes, and then adjusting RTC calibration registers as opposed to accumulating $\xi_{RTC}^{(T_{osc})}$ to the timestamp itself. For a given $f_{CLK_IN}^{(RTC)}$ RTC input clock, Eq. 4-26 can be used to calculate effective calibrated frequency $f_{CAL}^{(RTC)}$.

$$f_{CAL}^{(RTC)} = f_{CLK_IN}^{(RTC)} 1 + \frac{(CALP \times 512) - CALM}{2^{20} + (CALM - CALP) \times 512} \qquad \textbf{Eq. 4-26}$$

4.4.2 Timestamps Matching Issues

As reported earlier, vehicle arrival and departure timestamps ($T_A^{(N_i)}$and $T_D^{(N_i)}$) are sent by each sensor node to an associated *i*AP for vehicle speed and length estimation, as well as, classification. In some cases—as a result of interference from other technologies operating in the ISM band or from a large truck passing the sensor's detection zone—the radio channel might be degraded, resulting in delayed events (i.e., $T_A^{(N_i)}$and/or $T_D^{(N_i)}$).

Furthermore, a miscalibration in MAG baseline might cause a missing, delayed, or wrong $T_D^{(N_i)}$event. This issue was solved by assigning a unique ID for each sensor node, and then combining $T_A^{(N_i)}$and $T_D^{(N_i)}$ timestamps with identification characters sent to the *i*AP at each event. Also, since sensor nodes *N1* and *N2* are placed at close proximity (6~10 meter apart), the probability of error due to a delayed event is slim to none. Given a missing $T_A^{(N_i)}$or $T_D^{(N_i)}$ timestamp, the corresponding $T_A^{(N_i)}$or $T_D^{(N_i)}$ event will be dropped.

4.5 Real-Time Vehicle Magnetic Length Estimation

Vehicle length is important for vehicle classification [12]. Vehicle magnetic length (VML) is defined as a disturbance in the Earth's magnetic field caused by the ferrous material structure of a vehicle. VML is estimated from the product of vehicle speed and sensor occupancy time $T_{Occ}^{(N_i)}$, as shown in Eq. 4-27. A $T_{Occ}^{(N_i)}$ is defined as the difference between vehicle departure and arrival times at a designated detection point; both are influenced by magnetic field detection threshold.

$$\begin{aligned}\overline{VML} &= \bar{v}\times T_{Occ}^{(N_i)} = \bar{v}\times\left(T_D^{(N_i)} - T_A^{(N_i)}\right) \\ &= \bar{v}\times\frac{T_D^{(N_A)} - T_A^{(N_A)} + T_D^{(N_B)} - T_A^{(N_B)}}{2}\end{aligned} \qquad \textbf{Eq. 4-27}$$

Because disturbance level to the Earth's magnetic field depends on vehicle composition of ferrous materials, VML can theoretically be longer than its actual physical length (i.e., bumper-to-bumper length).

Nevertheless, under the assumption that 1) symmetrical detection zone and 2) sensor sensitivity are independent of vehicle structure, vehicle physical length can be estimated using Eq. 4-28, where l_{DZ} is the estimated length of sensor's detection zone (See Figure 4-11).

$$\bar{l_V} = l_M - \bar{l_{DZ}^{(Ni)}}; \qquad \widehat{l_{DZ}^{(Ni)}} \approx \bar{v_i}\left[T_D^{(N_B)} - T_A^{(N_A)}\right] - d^{N_A\to N_B} \qquad \textbf{Eq. 4-28}$$

4.6 Real-Time Magnetic Length-based Vehicle Classification

In this section, the implementation algorithm for several LBVC schemes for MAG will be discussed. However, scheme development, including field testing and data collection, as well as extensive data analysis, will be introduced in Chapter 5 and 6.

Three distinctive LVBC schemes were developed, as illustrated in Figure 4-23. Vehicles were grouped in each bin based on structural similarity and statistical data, which are discussed in Chapter 6. The PV group includes passenger cars, pickups, and SUVs. The short-trailer (ST) group includes busses, light-trucks, and single-unit-trucks. The long vehicle (L/LT) group includes single-trailer and multi-trailer trucks. Length decision boundaries for 4-G_{SX} using different thresholding methods (i.e., τ, α_T, and α_E) are shown in Table 4-1 (Refer to Chapter 7 for more details). These boundaries can be easily implemented in real-time using if-then conditions.

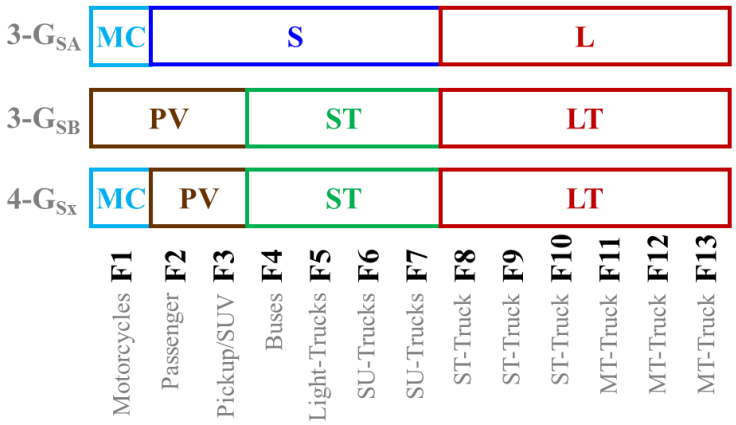


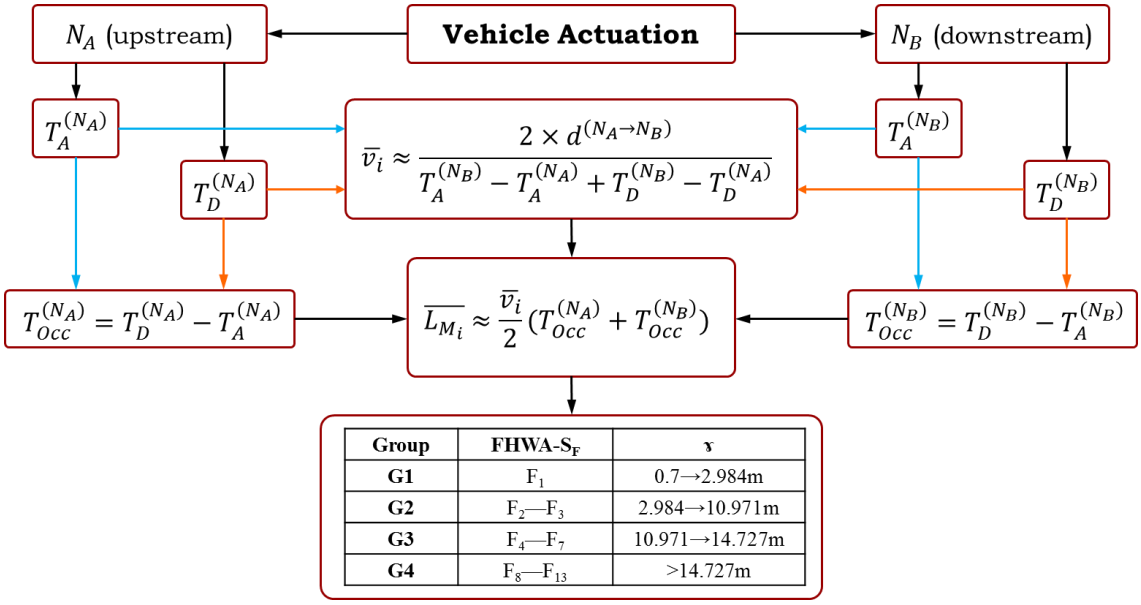
Figure 4-23 Proposed LBVC Schemes for MAG

Table 4-1 Length boundaries for 4-G_{SX} using different thresholding methods

		4G-S_x MAG		
Group	**FHWA-S_F**	**τ**	**α_T**	**α_E**
G1	F_1	0.7→2.984m	0.7→3.736m	0.7→2.9107m
G2	F_2—F_3	2.984→10.971m	3.736→7.7516m	2.912→7.427m
G3	F_4—F_7	10.971→14.727m	7.7516→14.95m	7.427→15.136m
G4	F_8—F_{13}	>14.727m	>14.95m	>15.136m

The implementation model for LBVC scheme using MAG is depicted in Figure 4-24. A vehicle actuation will trigger the detection algorithm at the upstream sensor node (N_A) and again at the downstream sensor node (N_B). Both nodes send arrival and

departure times to *i*AP, which computes speed and magnetic length. The vehicle is then classified by comparing computed length to decision boundaries in Table 4-1.



Group	FHWA-S_F	x
G1	F_1	0.7→2.984m
G2	F_2—F_3	2.984→10.971m
G3	F_4—F_7	10.971→14.727m
G4	F_8—F_{13}	>14.727m

Figure 4-24 Implementation model for LBVC Scheme using MAG

Chapter 5: FIELD TESTING & DATA COLLECTION

Several field studies and tests were conducted during this research—many of which were in parking lots at the *University of Oklahoma-Tulsa campus*. Additionally, eight major field tests were conducted on *highways* and *urban roads* throughout the state of Oklahoma. The objectives of these studies were to test sensor hardware, validate various developed algorithms, evaluate overall sensor real-time performance, and collect data for further analysis.

5.1 Data Collection Methodology

This section will report on major field studies conducted on the following Oklahoma highways and roadways:

- *Field Test 1* to *3—U.S. 412, Chouteau, OK 74337 USA*
- *Field Test 4—S. Yale Ave., Tulsa, OK 74135 USA*
- *Field Test 5 —Lake Hefner Pkwy, U.S. 74, OK 73120 USA*
- *Field Test 6—536 W State Hwy 152, Mustang, OK 73064 USA*
- *Field Test 7—Will Rogers Expy, OKC, OK 73108 USA*
- *Field Test 8—5959 Northwest Expy, OKC, OK 73132 USA*

5.1.1 Field Test 1

The first field study was conducted March 31st, 2015, from 10:55 to 13:15 at *U.S. 412, Chouteau, OK 74337 USA*, to evaluate the detection algorithm. *i*VCCS nodes were deployed in two setups: 1) *roadway surface* at lane center, and 2) *roadside surface* adjacent to rightmost and leftmost lanes. In both setups, MAG sensor *x-axis* was alongside traffic direction; *y-axis* was perpendicular to traffic lane; and *z-axis* was

pointing upward, perpendicular to the ground. Two *i*APs were installed by the roadside. The system was configured so that each *i*AP sent configuration and initialization commands to its *i*VCCS nodes cluster. In turn, *i*VCCS nodes sent vehicle counts in real time to their corresponding *i*AP. Two video cameras were used as ground-truth for data validation and performance evaluation. Vehicle classes and counts were manually extracted from video images by counting axel number per FHWA Scheme F with 13 classes. To reduce human error, the extraction process was validated by comparing extracted classes with collected data from a nearby WIM site. Video-based validation is considered the most accurate ground-truth, notwithstanding the fact that this method requires intensive labor.

Although only one *i*VCCS node is needed in each lane for vehicle detection, six nodes were deployed in each lane to study detection algorithm portability, as well as repeatability of vehicle magnetic signature. Cameras, *i*VCCS nodes, and *i*APs were synchronized using a GPS-based clock to aid in data analysis and validation. Deployment setup is depicted in Figure 5-1. Figure 5-2 shows the initial prototype enclosure for the *i*VCCS node, where *a* is top view, and *b* and *c* are bottom views. Enclosure size was 15.24(L)×15.24(W)×2.54(H) cm. The prototype was printed on a desktop 3D printer using PVC materials. Of interest is that many nodes were cracked during the test as a result of enormous dynamic load caused by heavily loaded trucks traveling at 70mph speed. Figure 5-3 shows the placement of *i*VCCS nodes, *i*AP, and cameras at the deployment site. The objectives of this field test were to:

- Evaluate hardware reliability and system performance in a real-life scenario
- Evaluate the detection algorithm

- Evaluate the initial enclosure prototype
- Collect vehicle signature data for further analysis

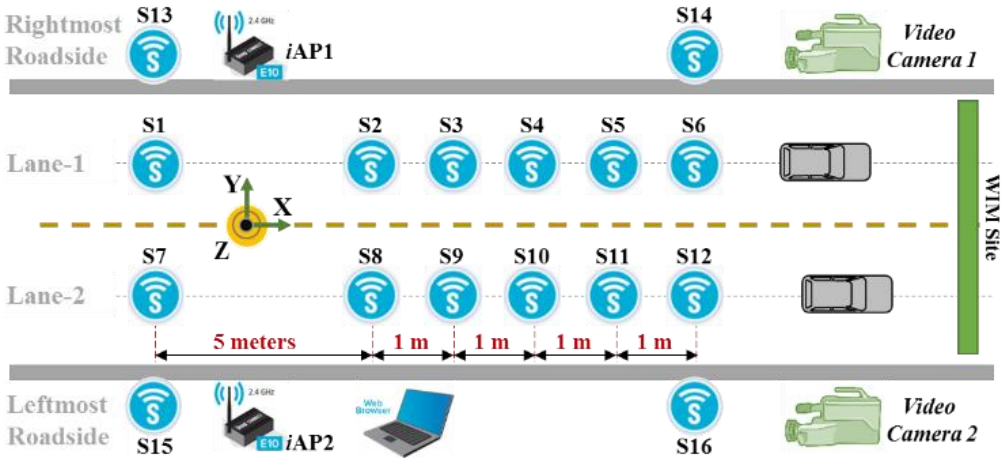


Figure 5-1 System setup layout on roadways (S1–S12) and roadsides (S13–S16)

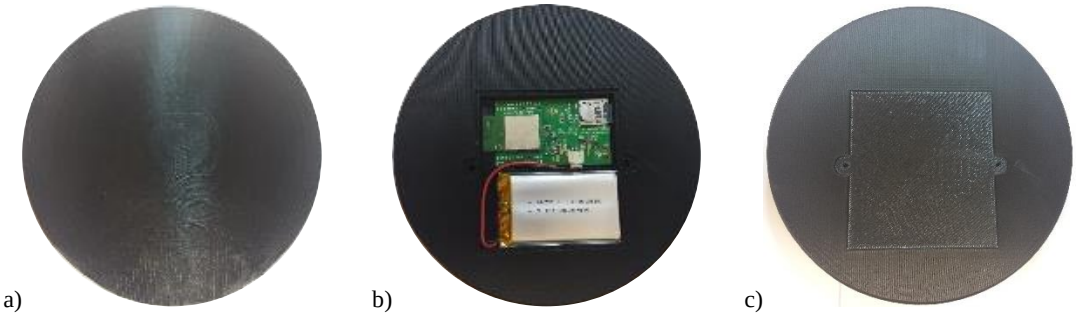


Figure 5-2 *i*VCCS enclosure—1st prototype



Figure 5-3 Field Test 1 deployment site

5.1.2 Field Test 2

A second field study was conducted August 3-, 2015, from 8:50 to 12:50 at *U.S. 412 near Chouteau, OK, 74337 USA*. The overall purpose was to evaluate detection, synchronization, and speed estimation algorithms in two scenarios. Several *i*VCC nodes were installed on the *roadway surface* of the left lane center and adjacent to the left lane. The right lane was blocked using a closure so that traffic was forced to travel only on the left lane. All nodes for MAG axis (i.e., *x*, *y*, and *z*) were positioned identical to those in Field Test 1. The system was configured so that *i*VCC nodes reported vehicle count and timestamp to a corresponding *i*AP in real-time. A video camera, as well as *Road Runner 3 Kit* [124] from Diamond Traffic, were used as ground-truth for data validation and performance evaluation. The *Road Runner kit* is a road tube-based vehicle counting and classification device. The kit reports 2-channel event timestamp data at a resolution of 30.5μs. Vehicles classes were manually extracted from video images by counting the number of axles for each vehicle. The effect of potential human error resulting from the extraction process was significantly reduced by comparing extracted classes from video with the number of axels counted by *Road Runner*. Estimated speed and length from the *Road Runner* device were used to validate estimated speed and length reported by *i*VCCS.

Cameras, along with the *Road Runner kit*, *i*VCCS nodes, and *i*APs, were synchronized using a GPS-based clock. The deployment setup is depicted in Figure 5-4. Figure 5-5 shows the second prototype enclosure for *i*VCCS node: again, *a* is the top view, and *b* and *c* are the bottom views. Enclosure size is 12.5(L)×12.5(W)×2.54(H) cm. Prototype shells were imported from China. A bucket for housing the sensor PCB

inside the shell was designed and printed on a desktop 3D printer. The shell was filled with epoxy after installing the battery and sensor bucket. Unfortunately, some nodes were cracked during the test, primarily because the epoxy material was not hard enough to withstand the dynamic load of heavy-loaded trucks. Figure 5-6 depicts the deployment site.

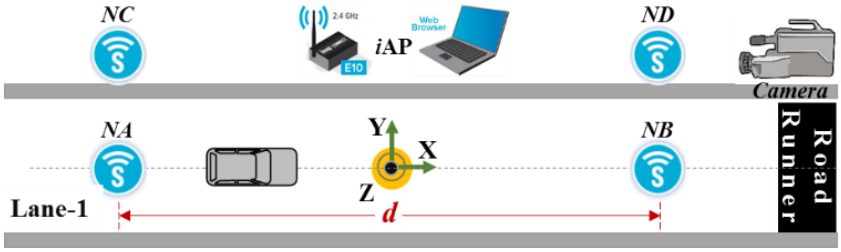
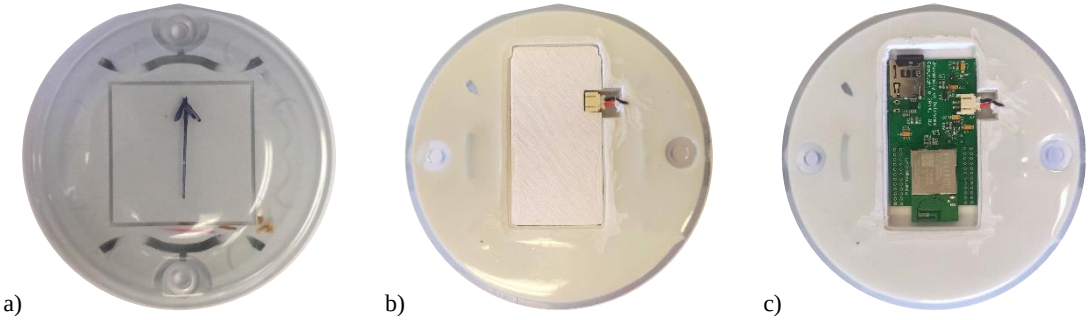


Figure 5-4 System setup layout on roadways (NA–NB) and roadsides (NC–ND)



a) b) c)

Figure 5-5 *i*VCCS node enclosure—2nd prototype



Figure 5-6 Field test 2 deployment site

The objective of field test 2 was to evaluate the following improvements:

- Holdover de-bounce time was based on the developed statistical modeling for detection error.
- An adaptive algorithm for geomagnetic baseline drift compensation was implemented to compensate for drift resulting from variations in temperature, vibrations, and aging.
- An algorithm for time synchronization using the on-board embedded GPS module and RTC unit was implemented to estimate speed.
- In this test, each sensor node maintained its own independent local clock that was globally synchronized to a PPS (pulse-per-second) signal generated by the on-board GPS module.

5.1.3 Field Test 3

The third field study was conducted October 8, 2015, from 8:22 to 14:00 at *U.S. 412, Chouteau, OK 74337, USA*. In this test, an incredibly hard epoxy-filling material was used for more durable enclosure. The left lane center was populated with six nodes (S_A, S_B, S_C, S_D, S_E, and S_F) installed on the *roadway surface* and separated by 2 meters. Six additional nodes (S_H, S_Q, S_L, S_G, S_I, and S_K) were installed on the roadway surface sides of the left lane. Two nodes (S_M, and S_N) were also installed between left lane center and the lane edge to accommodate a vehicle magnetic signature diversity study. The right lane was blocked using a closure so that traffic was forced to only use the left lane. A single node (S_O) was deployed in right lane center to study interference from the adjacent lane. All nodes were positioned the same as the MAG axis in the first field test.

Nodes were operated by three *i*AP installed on the road shoulder at a separation distance of 10 meters. Sensors were configured to report vehicle count and timestamp to a corresponding *i*AP in real-time. A video camera, speed radar, and *Road Runner 3 Kit* were used as ground-truth for data validation and performance evaluation. Vehicles class was manually extracted from video images by counting axel number for each vehicle. Estimated speeds and vehicle lengths reported from the *Road Runner Kit* were used to validate *i*VCCS data. The deployment setup layout is depicted in Figure 5-7. Figure 5-8 depicts the field test 3 deployment site, installed sensors, and equipment.

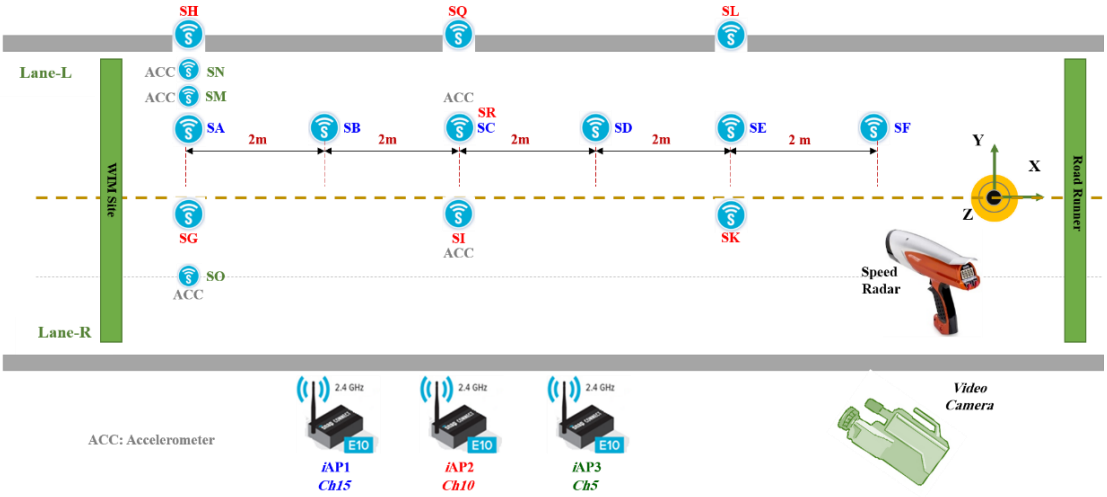


Figure 5-7 Field test 3 system setup layout



Figure 5-8 Field test 3 deployment site

The objective of field test 3 was to collect additional data about various classes for a vehicle classification analysis study and to evaluate the following improvements:

- An optimization programming was applied to improve detection algorithm performance at higher sampling rates (400Hz and 800Hz).
- An algorithm for adaptive compensation of RTC frequency drift resulting from temperature variations was developed and implemented.
- The T-synch algorithm was improved to correct residual errors.
- Arrival- and departure-detection time stamp procedures were optimized and improved for more accurate and consistent time-stamping.
- On-board ACCEL was activated to collect vehicle axle data for future vehicle classification and axle detection data analysis.

5.1.4 Field Test 4

Field study 4 was conducted October 15, 2015, from 9:30 to 17:30 on an urban road at *41st South Yale Ave, Tulsa, OK 74135 USA*. Eight *i*VCC nodes were installed—six nodes (S_A, S_E, S_F, S_G, S_H, and S_I) on the *roadway surface* center of each lane and two nodes (S_B, and S_K) on *roadsides surface* adjacent to the right lane. All nodes were operated using a single *i*AP. A video camera and *Road Runner Kit* were employed as ground truth for data validation and performance evaluation. Vehicle classes were manually extracted from video images by counting axel number for each vehicle. The same testing methodology was followed for this test as was for the first three tests. Deployment setup layout is depicted in Figure 5-9. Figure 5-10 pictures the field test 4 deployment site, as well as installed sensors and equipment. The objective of this test was to evaluate sensor performance and accuracy at traffic signals on an urban road.

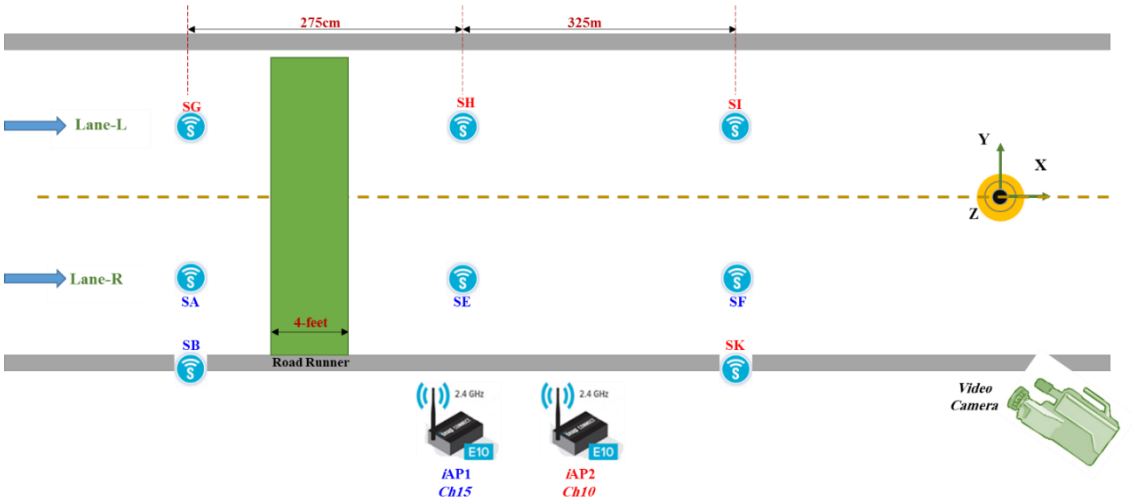


Figure 5-9 System setup layout on roadways and roadsides



Figure 5-10 Eight *i*VCCS nodes deployed on an urban road

5.1.5 Field Test 5

Field test 5 was conducted April 21, 2016, from 10:52 to 13:23 at *Britton Bridge* on *Lake Hefner Pkwy, U.S. 74, OK 73120*. Several *i*VCC nodes were deployed on the north side of the highway. A video camera was installed on the shoulder and employed as ground truth for data validation and performance evaluation (See Figure 5-11).

The primary objective of this study was to collect VMS sampled using MAG and IDL for a post-processing analysis aimed at identifying the differences between the two VMS sampled using MAG vs. IDL. The deployment location had been recently equipped by IDLs connected to a *Phoenix Traffic Classifier* from Diamond Traffic Products, Inc. This classifier device samples VMS from IDL at a sampling rate of 1KHz.

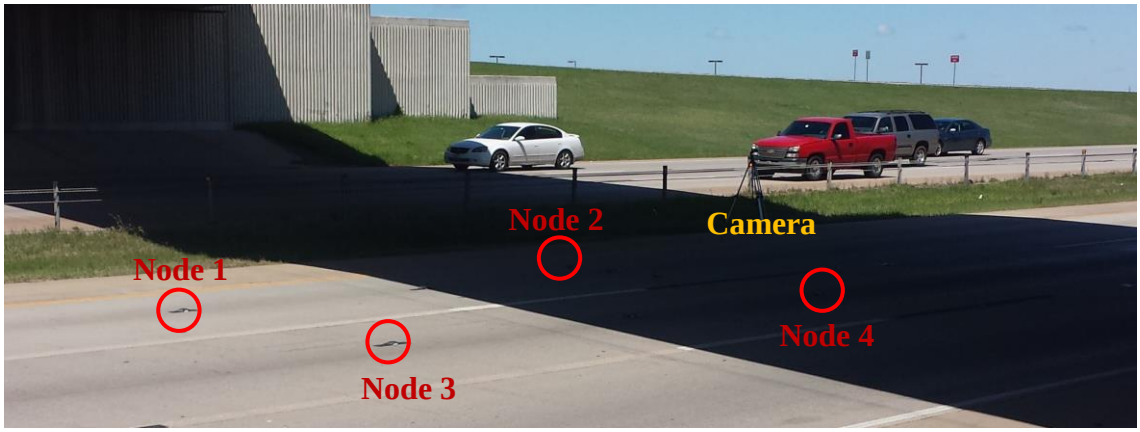


Figure 5-11 Field test 5 deployment site

5.1.6 Field Test 6

Field test 6 was conducted June 06, 2016, from 14:00 to 15:00 at *536 W State Hwy 152, Mustang, OK 73064 USA.* Several *i*VCC nodes were deployed to measure traffic traveling on the highway in both directions (See Figure 5-12). A tubes counter was also installed 20 feet from the sensors. A nearby AVC station was also employed in the study. ODOT personnel used a manual counter as ground truth for performance evaluation.

The objective of this study was comparing tube-count, AVC station-count, and *i*VCC-count performance with manual count. Initial data analysis was conducted by ODOT.

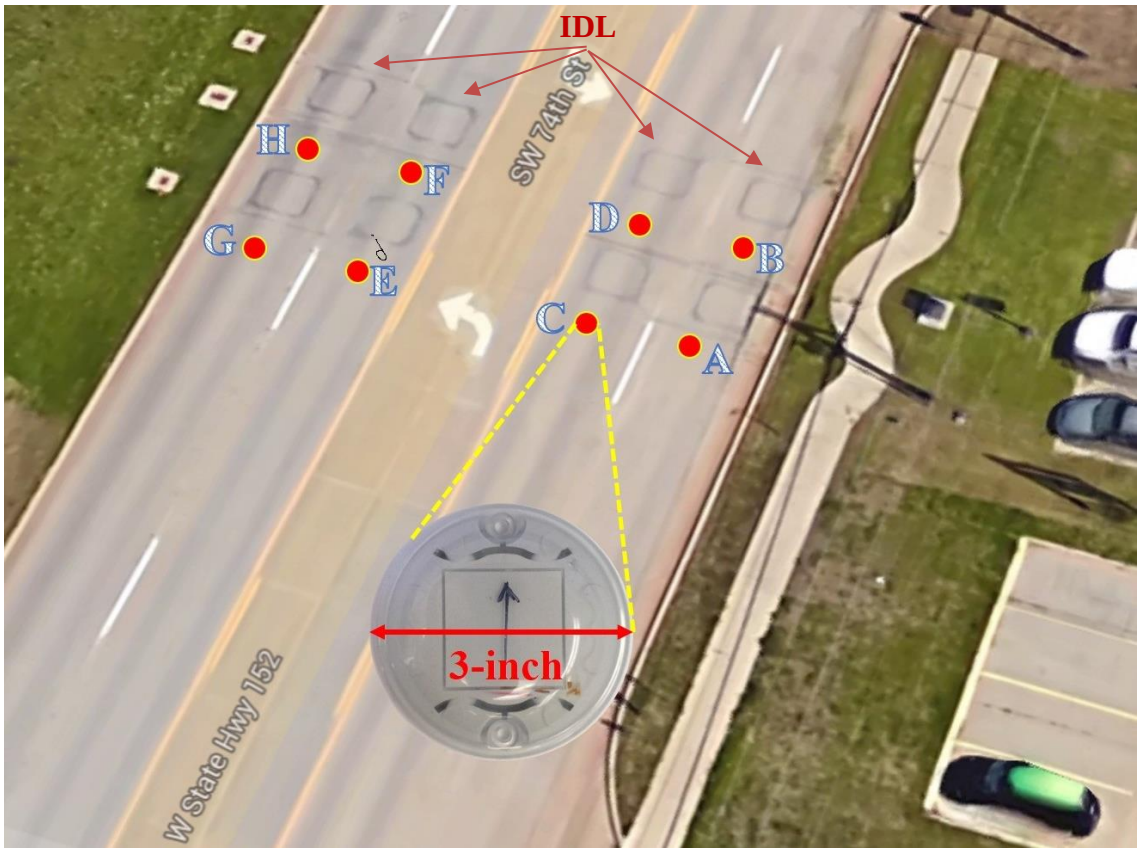


Figure 5-12 Field test 6 deployment site

5.1.7 Field Test 7

Field test 7 was conducted in June 06, 2016, from 09:00 to 10:00 at *Will Rogers Expy, OKC, OK 73108 USA*. A single *i*VCC node was placed on the far most left lane without traffic interruption (See Figure 5-13). A video camera deployed for an ODOT contractor was installed on the shoulder. A nearby AVC station was also employed in the study. ODOT personnel used a manual counter as ground truth for performance evaluation. The objective of this study was to compare performance between deployed technologies and manual count (i.e., ground truth data).

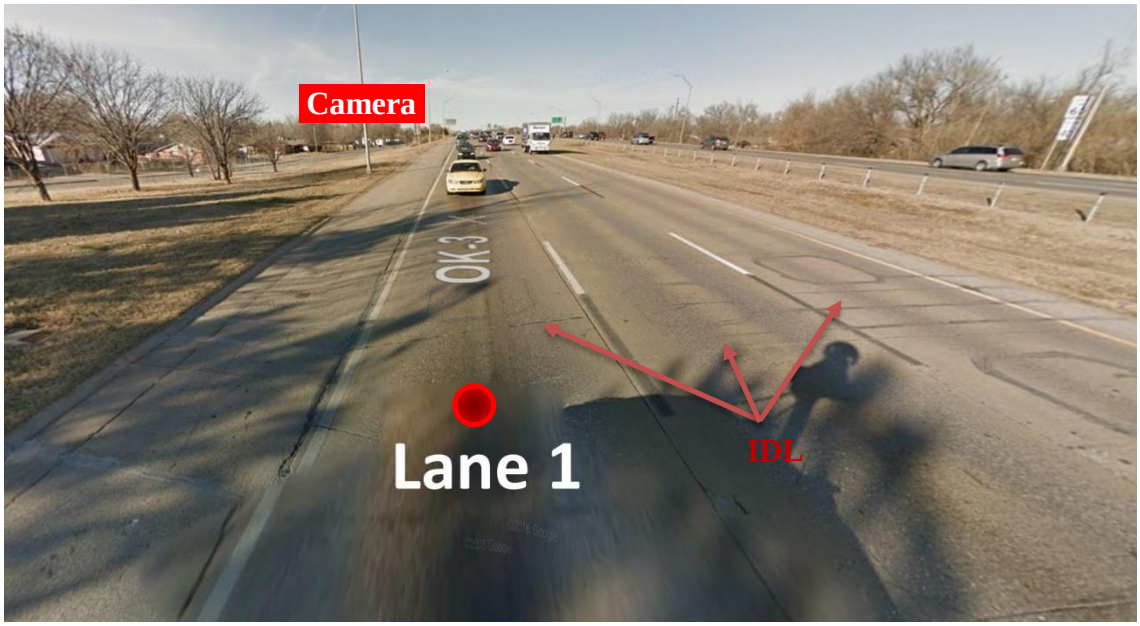


Figure 5-13 Field test 7 deployment site

5.1.8 Field Test 8

Field test 8 was conducted June 06, 2016, from 11:00 to 12:00 at *5959 Northwest Expy, OKC, OK 73132 USA*. Three *i*VCC nodes (A, B, C) were deployed at three points in the intersection (See Figure 5-14). A video camera for an ODOT contractor was installed on the shoulder, referenced to point A. A nearby AVC station was also employed in field test 8. A tube counter was installed 10 feet from the sensors at points B and C. ODOT personnel used a manual counter as ground truth for performance evaluation. The objective of this study was comparing the performance of employed technologies at intersection with the manual count of the ground truth.

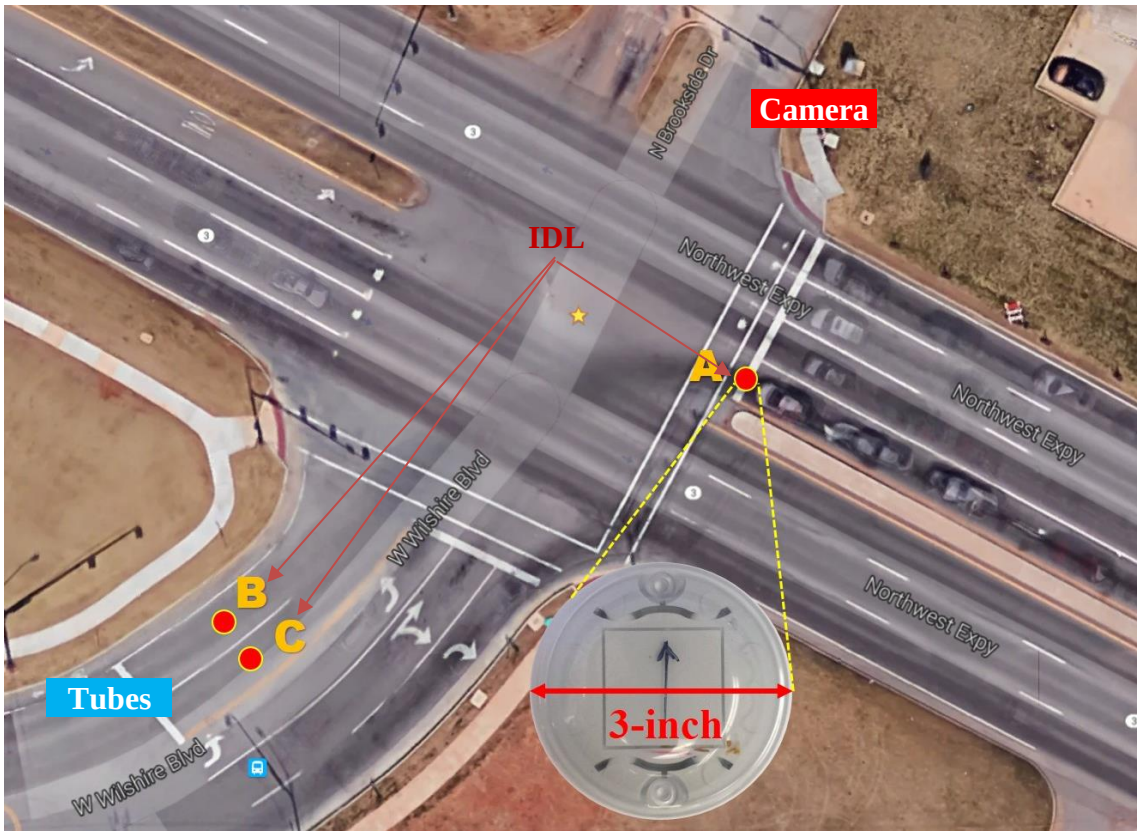


Figure 5-14 Field test 8 deployment site

5.2 Log Data File Format and Structure

The data-logging unit stored raw data on the microSD card using either an *ASCII* (American Standard Code for Information Interchange) or *Binary* format. *ASCII* format is a text-based representation of data, which is more intuitive and easy to read for humans. However, *ASCII* is a memory-consuming technique, as each single digit requires one byte in memory (e.g., the value 123 is represented in ASCII format using three bytes). Alternatively, binary format is a non-text file that might include any type of data encoded in a binary representation (e.g., the value 123 is represented in binary format using one byte). Besides efficient data storage, *binary* is energy conserving, permitting raw data transfer over the wireless link. One disadvantage of Binary format

is that data files require processing (i.e., format conversion) before humans can be read the data as text.

5.2.1 ASCII Log File Structure

An *ASCII* log file consists of a header, body, and an end of file (EOF) line. The header includes information about data log time and data, node ID, and sensor configuration settings. The body includes raw MAG (*Bx, By, Bz*) and ACCEL (*Ax, Ay, Az*) data, timestamps (i.e., vehicles arrival and departure times), instantaneous vehicle count, and reference timestamp, which is logged each minute.

Table 5-1 illustrates ASCII file fields and corresponding values range. The MAG/ACC setting field indicates which sensor is active—"1" MAG only, "2" ACCEL only, "3" MAG and ACCEL are active. Given MAG/ACC=1, only *Bx, By,* and *Bz* are logged. For MAG/ACC=2, only *Ax, Ay,* and *Az* will be logged. The ALL/VDT field indicates whether raw data are continually stored (i.e., ALL/VDT = 1) or only vehicle signature and/or acceleration data (i.e., vehicle detection) are stored (i.e., ALL/VDT=2). At midnight (i.e., 00:00:00), the current file will automatically close and a new file will be created. Figure 5-15 shows two examples of an ASCII data log file.

Table 5-1 Log file structure in ASCII format

	Field	*Format*	*Value*
Header	Open Log File Time-Data	[hh:mm:ss dd\mm\yy]	
	Senor's ID	[ID-Nx]	x≫ [A…Z]or[a…z]
	Settings	[ODR = xxxHz] [MAG/ACC = x] [ALL/VDT = x]	xxx≫ [12.5…800] x≫ [1,2,or 3] x≫ [1 or 2]
Body	MAG *Bx By Bz* ACCEL *Ax Ay Az*	sxxxx sxxxx sxxxx sxxxx sxxxx sxxxx	*Bx By Bz Ax Ay Az* s:±,xxxxx:0…16384
	Vehicle Arrival Time	[Nx_TA@secofday.RTCreg]	Secofday:0…86399 RTCreg: 0…32767
	Vehicle Departure Time	[Nx_TD@secofday.RTCreg]	
	Vehicle Number	[Nx_N#xxxxxxxxx]	[1…4294967295]
	Reference Timestamp	[t@hh:mm:ss]	
EOF	Close Log File Time-Data	[hh:mm:ss dd\mm\yy]	
	Total Number of Vehicles	[Nx_NT#xxxxxxxxx]	[1…4294967295]

```
[10:44:02  10\15\15]
ID-NK,      ODR=400Hz,      MAG/ACC=1,
ALL/VDT=1
-10 3 -1
   ⋮
NK_TA@38828.10391
   ⋮
30 -32 57
   ⋮
NK_TD@38828.21667
NK_N#1
-3 -6 -8
   ⋮
2 5 8
t@10:48:00
-1 8 -4
   ⋮
-3 9 -4
[17:33:00  10\15\15]
NK_VC#1352
```

```
[00:00:00  10\15\15]
ID-NK,      ODR=400Hz,      MAG/ACC=3,
ALL/VDT=1
-10 3 -1 -3 9 -4
   ⋮
NK_TA@107.581
   ⋮
30 -32 57 2 5 8
   ⋮
NK_TD@107.17633
NK_N#1
-3 -6 -8 7 5 -4
   ⋮
-9 5 -7 -2 -5 8
t@16:30:00
-8 7 -4 -3 9 -4
   ⋮
-3 9 -4 1 10 -9
[23:59:59  10\15\15]
NK_VC#18109
```

Figure 5-15 Example of ASCII data log file

5.2.2 Binary Log File Structure

In general, the binary file structure is similar to the ASCII file structure—both contain header, body and EOF sections. However, binary file format lacks control characters (e.g., CR) for separating data lines; thus, prefix [**P**] and suffix [**S**] binary values are used to differentiate between various data values. For data format of type *Word* or *Integer*, the order is always [MSB] then [LSB]. The sign is assigned as the last bit of the MSB byte; a '0' indicates positive number and '1' indicates negative number. The ODR is assigned a value from 1 to 7 as a reference to 25, 50, 100, 200, 400, 800, or 1600Hz, respectively. The header section starts with a prefix value [00] and ends with a suffix value [00]. The number of bytes in the header is fixed to 50 bytes; 40 bytes are reserved for future development purpose. Table 5-2 shows binary file format structure.

Table 5-2 Log file structure in Binary format

	Field	***Format***	***Value***	***bytes***
Header	*Open Log File Time-Data*	[00] **[-]**…**[-]**	hhmmssDDMMYY	06
	Senor's ID	**[-]**	ID≫(01…99)	01
	ODR	**[-]**	[01…06]	01
	MAG/ACC	**[-]**	[01,02, or 03]	01
	ALL/VDT	**[-]**[00]	[01 or 02]	01
	Reserved	**[-]**…**[-]**	R[255]	40
Body	*MAG Bx By Bz* *ACCEL Ax Ay Az*	**[-]**…**[-]** **[-]**…**[-]** [FF][FF]	$[MSB_x][LSB_x]…[MSB_z][LSB_z]$ $[sFFF]_{MSB}$≫ $s^{+}=0, s^{-}=1$	6/12
	Vehicle Arrival Time	[FA] **[-]**…**[-]** [FB][FF]	Secofday(0…86399)≫3-bytes RTCreg(0…32767)≫2-bytes	5
	Vehicle Departure Time	[FC] **[-]**…**[-]** [FD][FF]		
	Vehicle Number	[FE] **[-][-]** [FE][FF]	VN≫(1…65536)	2
	Reference Timestamp	[F8] **[-]**…**[-]** [F9][FF]	Secofday(0…86399)≫3-bytes	3
EOF	*Close Log File Time-Data*	[F6] **[-]**…**[-]** [F7][FF]	Secofday(0…86399)≫3-bytes	3
	Total Number of Vehicles	[F4] **[-][-]** [F5][FF]	TVN≫(1…65536)	2

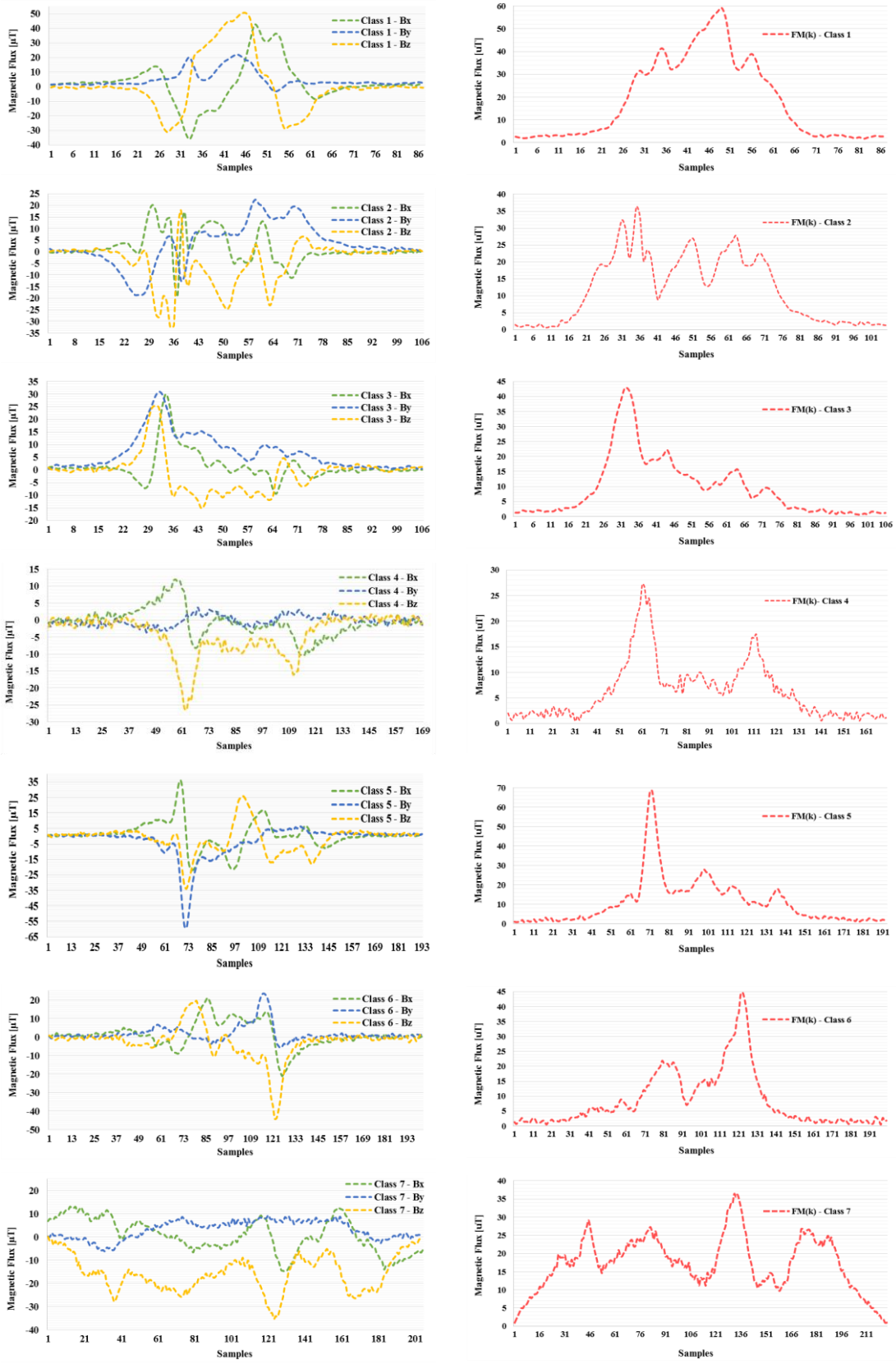
An example shows the order of data bytes in Binary format for MAG/ACC = **1** is as follows:

[0x00][hh][mm][ss][DD][MM][YY][ODR][MAG/ACC][ALL/VDT][0x00]
[40 reserved byte… 0xFF][MSB_x][LSB_x][MSB_y][LSB_y][MSB_z][LSB_z]
[0xFF][0xFF][MSB_x][LSB_x][MSB_y][LSB_y][MSB_z][LSB_z][0xFF][0xFF]
……[0xFA][$MSB^H{}_{Secofday}$][$MSB^L{}_{Secofday}$][$LSB_{Secofday}$][MSB_{RTCreg}][LSB_{RTCreg}]
[0xFB][0xFF][MSB_x][LSB_x][MSB_y][LSB_y][MSB_z][LSB_z][0xFF][0xFF]
……[0xFC][$MSB^H{}_{Secofday}$][$MSB^L{}_{Secofday}$][$LSB_{Secofday}$][MSB_{RTCreg}][LSB_{RTCreg}]
[0xFD][0xFF][xFE][MSB_{VN}][LSB_{VN}][0xFE][0xFF][MSB_x][LSB_x][MSB_y]
[LSB_y][MSB_z][LSB_z][0xFF][0xFF]……[0xF6][$MSB^H{}_{Secofday}$][$MSB^L{}_{Secofday}$]
[$LSB_{Secofday}$][MSB_{RTCreg}][LSB_{RTCreg}][0xF7][0xFF][0xF4][MSB_{TVN}][LSB_{TVN}
][0xF5][0xFF]

An example shows the order of data bytes in Binary format for MAG/ACC = **3** is as follows:

[0x00][hh][mm][ss][DD][MM][YY][ODR][MAG/ACC][ALL/VDT][0x00]
[40 reserved byte 0xFF][$MSB^M{}_x$][$LSB^M{}_x$][$MSB^M{}_y$][$LSB^M{}_y$][$MSB^M{}_z$]
[$LSB^M{}_z$][$MSB^A{}_x$][$LSB^A{}_x$][$MSB^A{}_y$][$LSB^A{}_y$][$MSB^A{}_z$][$LSB^A{}_z$][0xFF][0xFF][M
$SB^M{}_x$][$LSB^M{}_x$][$MSB^M{}_y$][$LSB^M{}_y$][$MSB^M{}_z$][$LSB^M{}_z$][$MSB^A{}_x$][$LSB^A{}_x$][$MSB^A{}_y$][LS
$B^A{}_y$][$MSB^A{}_z$][$LSB^A{}_z$][0xFF][0xFF]…[0xFA][$MSB^H{}_{Secofday}$][$MSB^L{}_{Secofday}$][
$LSB_{Secofday}$][MSB_{RTCreg}][LSB_{RTCreg}][0xFB][0xFF][$MSB^M{}_x$][$LSB^M{}_x$][$MSB^M{}_y$]
[$LSB^M{}_y$][$MSB^M{}_z$][$LSB^M{}_z$][$MSB^A{}_x$][$LSB^A{}_x$][$MSB^A{}_y$][$LSB^A{}_y$][$MSB^A{}_z$][$LSB^A{}_z$][
0xFF][0xFF]…[0xFC][$MSB^H{}_{Secofday}$][$MSB^L{}_{Secofday}$][$LSB_{Secofday}$][MSB_{RTCreg}
][LSB_{RTCreg}][0xFD][0xFF][xFE][MSB_{VN}][LSB_{VN}][0xFE][0xFF][MSB_x][
$MSB^M{}_x$][$LSB^M{}_x$][$MSB^M{}_y$][$LSB^M{}_y$][$MSB^M{}_z$][$LSB^M{}_z$][$MSB^A{}_x$][$LSB^A{}_x$][$MSB^A{}_y$][L
$SB^A{}_y$][$MSB^A{}_z$][$LSB^A{}_z$][0xFF][0xFF]……[0xF6][$MSB^H{}_{Secofday}$][$MSB^L{}_{Secofday}$]
[$LSB_{Secofday}$][MSB_{RTCreg}][LSB_{RTCreg}][0xF7][0xFF][0xF4][MSB_{TVN}][LSB_{TVN}
][0xF5][0xFF]

Figure 5-16 illustrates geomagnetic field components (B_X, B_Y, and B_Z) and corresponding flux magnitude (F_M) for vehicles of various classes and speeds that were collected by *i*VCCS in roadway setup.


Class 1 - Bx
Class 1 - By
Class 1 - Bz
FM(k) - Class 1
Class 2 - Bx
Class 2 - By
Class 2 - Bz
FM(k) - Class 2
Class 3 - Bx
Class 3 - By
Class 3 - Bz
FM(k) - Class 3
Class 4 - Bx
Class 4 - By
Class 4 - Bz
FM(k)- Class 4
Class 5 - Bx
Class 5 - By
Class 5 - Bz
FM(k) - Class 5
Class 6 - Bx
Class 6 - By
Class 6 - Bz
FM(k) - Class 6
Class 7 - Bx
Class 7 - By
Class 7 - Bz
FM(k) - Class 7
Magnetic Flux [μT]
Magnetic Flux [uT]
Samples

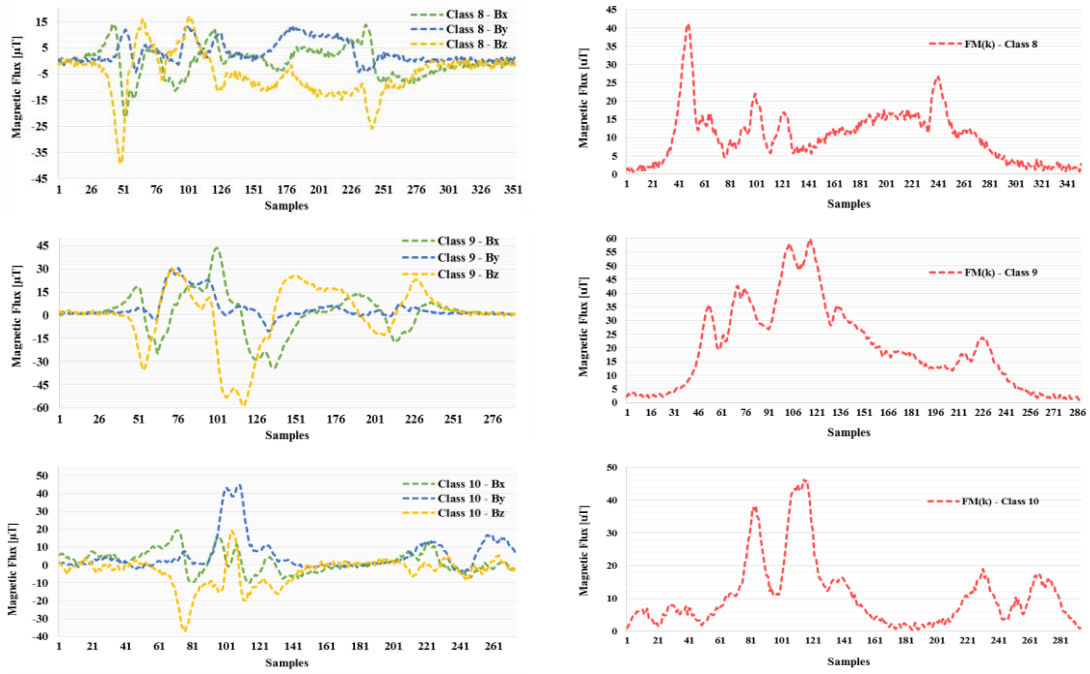


Figure 5-16 Vehicles signatures, *i*VCCS on roadway – $B^{(\gamma)}$ (left) and F_M (right)

Chapter 6: DATA ANALYSIS & PERFORMANCE EVALUATION

6.1 Overview

This chapter provides detailed information about various statistical data analysis studies applied on field test data reported in Chapter 5 that were collected using MAG sensors. Additionally, performance evaluation of developed algorithms—including field test results—are presented. Both data analysis and performance evaluation is illustrated in Figure 6-1.

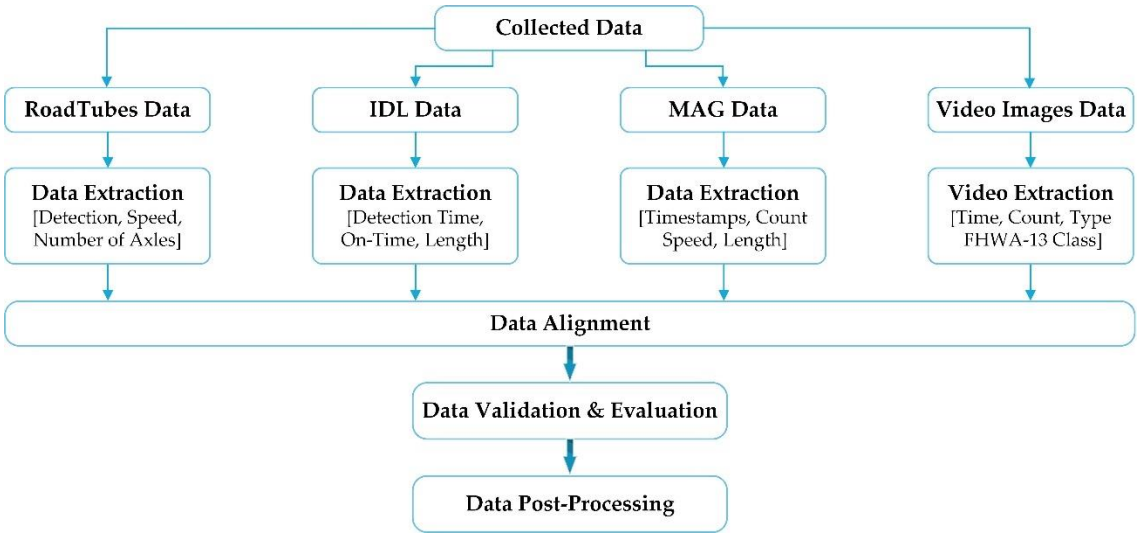


Figure 6-1 Flow diagram for data validation and performance evaluation

Data collected using MAG sensors, as well as ground truth data from *Road Runner Kit* and video cameras, was pre-processed to extract detection information (e.g., count, speed, length, detection time). This information had been extracted from video data and aligned—sample by sample—into a reference detection timestamp.

6.2 Magnetometer Sensor Characterization Analysis

6.2.1 Sampling Rate in Active Detection

Fixed sampling rates, ranging from 8Hz to 200Hz, for vehicle detection using MAG have been reported in literature [44], [47], [53], [125], [126]. Unlike other platforms, *i*VCCS, sampling rate can be configured on-the-fly within a range 0.781Hz~1.60KHz to best-fit application functionalities and power constraints. Increasing sampling rate will increase resolution of sampled VMS. Notably, sensor noise output and power consumption will also increase. FXOS8700CQ has an output noise range 0.3~1.5μT-rms@1.56~800Hz, while output noise range for KMX62 is 0.2~1.4 μT-rms@0.78~1600Hz. In terms of power consumption vs. sampling rate, FXOS8700CQ requires 40~575μA@12.5~400Hz, while KMX62 consumes 1.6~292μA@0.78~1600Hz (See Table 3-6).

6.2.2 MAG Output Noise Characterization

Knowledge about the distribution of MAG output noise at different sampling rates is important for setting MAG reference level and *Baseline threshold* (R_{TH}).

MAG noise characteristics defined in Table 3-6 do not reflect the effect of additional components on PCB. An experimental test was conducted to define noise characteristics and gain better understanding of MAG at various sampling rates in the presence of other active components on *i*VCCS board.

An *i*VCCS was tightly fixed on a wooden table in the absence of any ferrous objects. Eight sampling rates—from 1.56Hz to 800Hz—were tested. Each experiment had 50000 samples; each was a 3×16-bit. Flux magnitude (F_M) was calculated from geomagnetic field components to find histogram and standard deviation (STD) of F_M.

Table 6-1 and Figure 6-2 show that noise mean at 400Hz sampling rate was approximately 30, with peak noise at 55. Hence, if 400Hz was set, *Baseline threshold* (R_{TH}) should consider a value higher than noise peak.

Table 6-1 Field Magnitude STD for Different Sampling Rates

Sampling Rate	STD	Sampling Rate	STD
1.5625	2.58	**100**	5.57
6.25	3.39	**200**	7.46
12.5	3.51	**400**	9.88
50	4.63	**800**	13.04

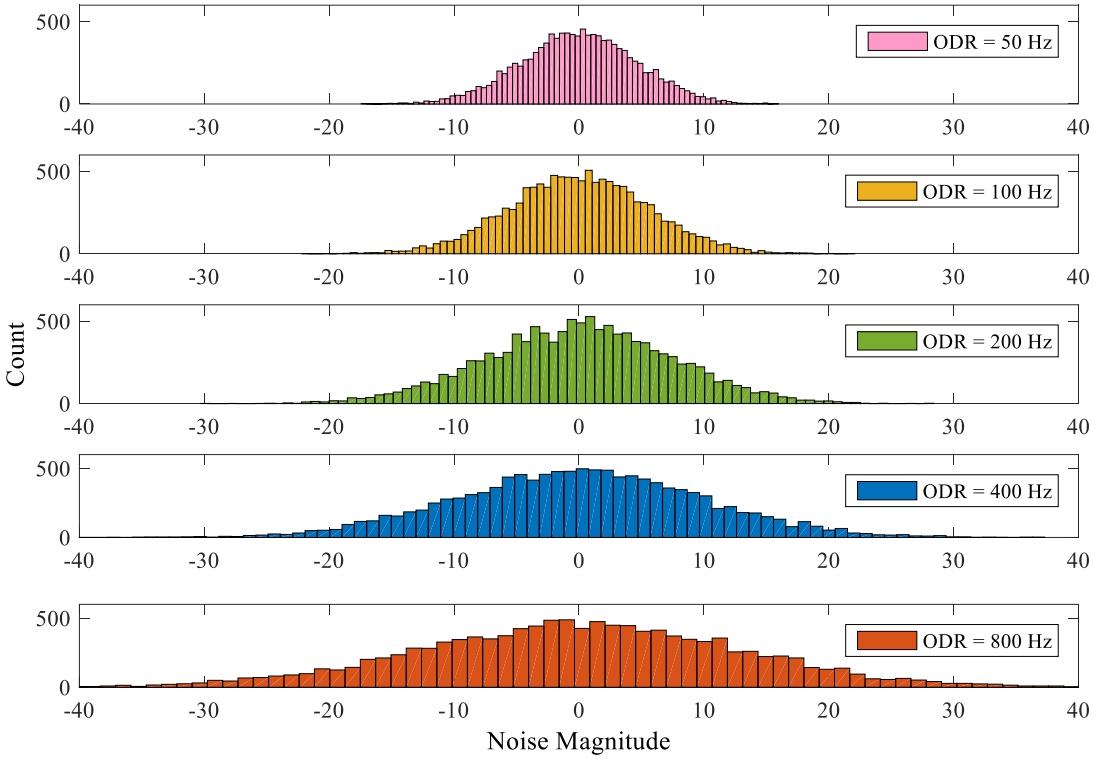


Figure 6-2 Field magnitude histogram at different sampling rates

6.2.3 MAG Sampling Rate Setting

To determine suitable sampling rate for a particular application, let's assume that a vehicle travels on a highway at a maximum speed of 140kmh and that the number of

samples represents the vehicle's magnetic signature S_{VMS} for a given sampling rate f_s and vehicle length l_V, as in Eq. 6-1.

$$S_{VMS} = 3.6 \times \left(\frac{l_{lde} + l_{tde} + l_V}{v} \right) \times f_s \times \alpha \qquad \textbf{Eq. 6-1}$$

VMS is subject not only to the disturbance in the Earth's magnetic field caused by a passing vehicle structure, but also to the sensor's detection zone. The leading and trailing detection edge of this zone is denoted as l_{lde} *and* l_{tde}, respectively. A correction factor is denoted by α. Assuming that l_V = 5 meters; f_s = 200Hz; l_{lde}=1.1 m; and l_{tde}= 1.1 m, by substituting in Eq. 6-1, S_{VSL} = 37 samples.

Although knowing minimum number of S_{VSL} and low f_s (e.g., 100Hz) might be sufficient for vehicle detection applications, a higher sampling rate is needed for accurate estimation, and a unique features extraction is needed for speed estimation, vehicle classification, or re-identification applications based on magnetic signature or magnetic length.

6.2.4 Effect of MAG Rotation Around z-axis

Vehicles can be modeled magnetically as an infinitely large number of magnetic dipoles, each with their own moment and direction in a three-dimensional space. MAG measures geometric sum of all dipoles on x, y, and z-axes. As a result, a vehicle can be considered a single dipole with a moment equal to the geometric sum of all dipoles. Hence, F_M will be the same regardless of sensor orientation. However, B_X, B_Y, and B_Z will be different for rotation angle θ. If θ is known, component values can be calculated before and after rotating sensor θ radians around z-axis using Eq. 6-2.

$$\begin{bmatrix} B_x' \\ B_y' \\ B_Z' \end{bmatrix} = \begin{bmatrix} \cos\theta & \sin\theta & 0 \\ \sin\theta & \cos\theta & 0 \\ 0 & 0 & 1 \end{bmatrix} \begin{bmatrix} B_x \\ B_y \\ B_z \end{bmatrix} \qquad \textbf{Eq. 6-2}$$

Figure 6-3 illustrates the test setup where nine *i*VCCS nodes were rotated around z-axis and the rotation of first node (θ=0°) components by 135°, compared to original node at 135°.

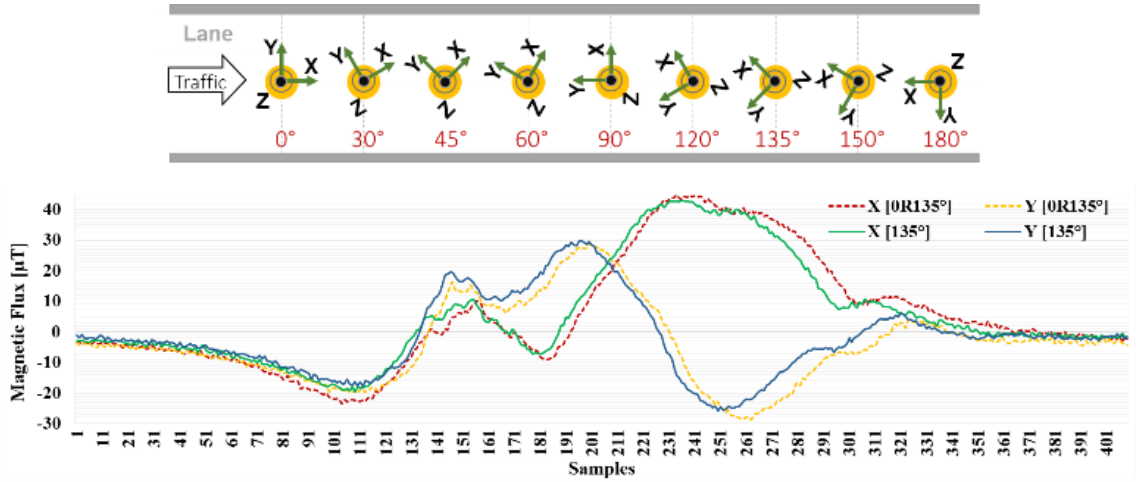


Figure 6-3 Orientation setup and *Bx* and *By* with *θ*=0° were rotated by 135°

6.2.5 Repeatability of VMS and MAG Sensors Output

The objective of this analysis was finding the degree of similarity of several magnetic signatures produced by multiple MAG sensors for the same vehicle under identical testing conditions.

Data collected in field test 3 was used to verify MAG output consistency. Data from only the first four sensor nodes, namely S_A, S_B, S_C, and S_D, each separated by 2m (See Figure 5-7), were used in this analysis. The dataset included 1655 vehicles, ranging from class 1 to 10. Cross-correlation data analysis was used to find the statistical relationship of generated signatures between four aligned sensors.

This method can be used to measure the similarity of two waveforms as a function of a time lag applied to either. Correlation between signals can be linear (e.g., impulses

signals) or circular (e.g., periodic signals). A correlation coefficient R was used to express correlation strength between signals. Pearson's correlation coefficient is the most common measure of linear dependency between two random variables, A and B, as in Eq. 6-3. A μ_A and σ_A are mean and STD of A, and μ_B and σ_B are mean and STD of B.

$$\rho(A,B) = \frac{cov(A,B)}{\sigma_A \sigma_B} = \frac{1}{N-1}\sum_{i=1}^{N}\frac{(A_i - \mu_A)(B_i - \mu_B)}{\sigma_A \sigma_B} \qquad \textbf{Eq. 6-3}$$

Given that our investigation had four sensors, R for pairwise signals was first found using Eq. 6-3, and then the correlation coefficient matrix for all signals was found by combining the Rs of all pairwise variable, as in Eq. 6-4. Diagonal entries are always equal to 1, as all signals are directly correlated to themselves.

$$R = \begin{pmatrix} \rho(N_A,N_A) & \rho(N_A,N_B) & \rho(N_A,N_C) & \rho(N_A,N_D) \\ \rho(N_B,N_A) & \rho(N_B,N_B) & \rho(N_B,N_C) & \rho(N_B,N_D) \\ \rho(N_C,N_A) & \rho(N_C,N_B) & \rho(N_C,N_C) & \rho(N_C,N_D) \\ \rho(N_D,N_A) & \rho(N_D,N_B) & \rho(N_D,N_C) & \rho(N_D,N_D) \end{pmatrix} \qquad \textbf{Eq. 6-4}$$

$$R = \begin{pmatrix} 1 & \rho(F_M^{(N_A)},F_M^{(N_B)}) & \rho(F_M^{(N_A)},F_M^{(N_C)}) & \rho(F_M^{(N_A)},F_M^{(N_D)}) \\ \rho(F_M^{(N_B)},F_M^{(N_A)}) & 1 & \rho(F_M^{(N_B)},F_M^{(N_C)}) & \rho(F_M^{(N_B)},F_M^{(N_D)}) \\ \rho(F_M^{(N_C)},F_M^{(N_A)}) & \rho(F_M^{(N_C)},F_M^{(N_B)}) & 1 & \rho(F_M^{(N_C)},F_M^{(N_D)}) \\ \rho(F_M^{(N_D)},F_M^{(N_A)}) & \rho(F_M^{(N_D)},F_M^{(N_B)}) & \rho(F_M^{(N_D)},F_M^{(N_C)}) & 1 \end{pmatrix} \qquad \textbf{Eq. 6-5}$$

Initially, correlation coefficient matrices of magnetic magnitudes F_M (See Eq. 4-5) obtained from the four sensor nodes were found, as in Eq. 6-5. Histograms for the first three pairwise signals, N_A-*vs*-N_B, N_A-*vs*-N_C, and N_B-*vs*-N_C, are shown in Figure 6-4, Figure 6-5, and Figure 6-6, respectively. The CDF for all pairwise combinations is shown in Figure 6-7. The histogram shows that most correlation coefficients range between 0.9 and 1 (i.e., 1462 out of 1655 values), indicating high similarity between sensor output across multiple nodes (See Figure 6-8). A p-values matrix was also found

for all pairwise combinations. The matrix returned noticeably small p-values (e.g., 2e-138), rejecting the null hypothesis and identifying significant correlations.

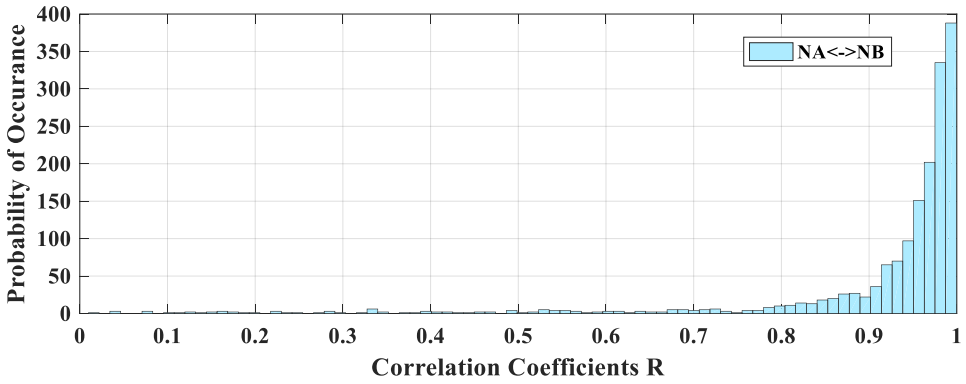


Figure 6-4 Histogram of R between magnetic magnitudes of Node-A and B

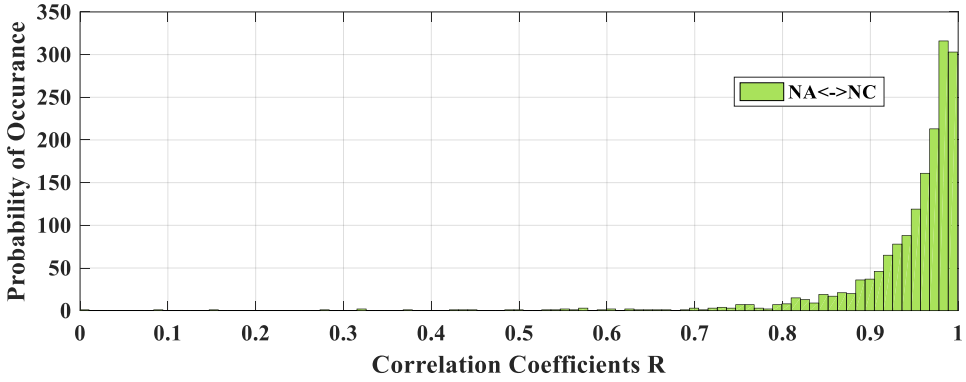


Figure 6-5 Histogram of R between magnetic magnitudes of Node-A and C

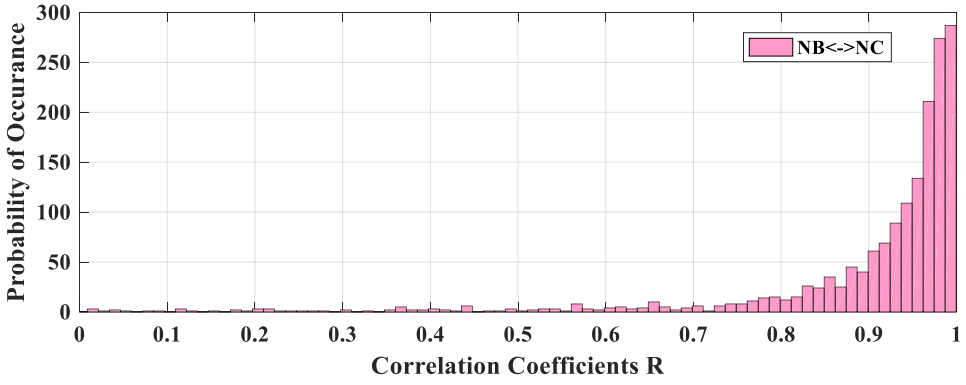


Figure 6-6 Histogram of R between magnetic magnitudes of Node-B and C

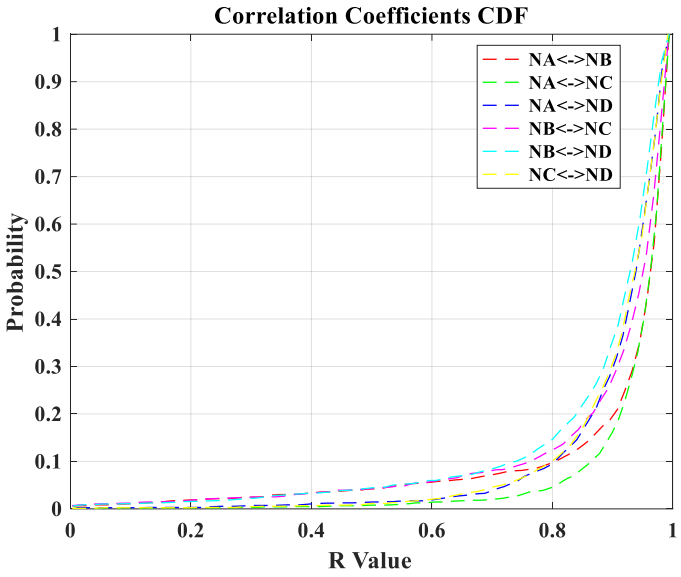


Figure 6-7 CDF of correlation coefficients for all pairwise signals

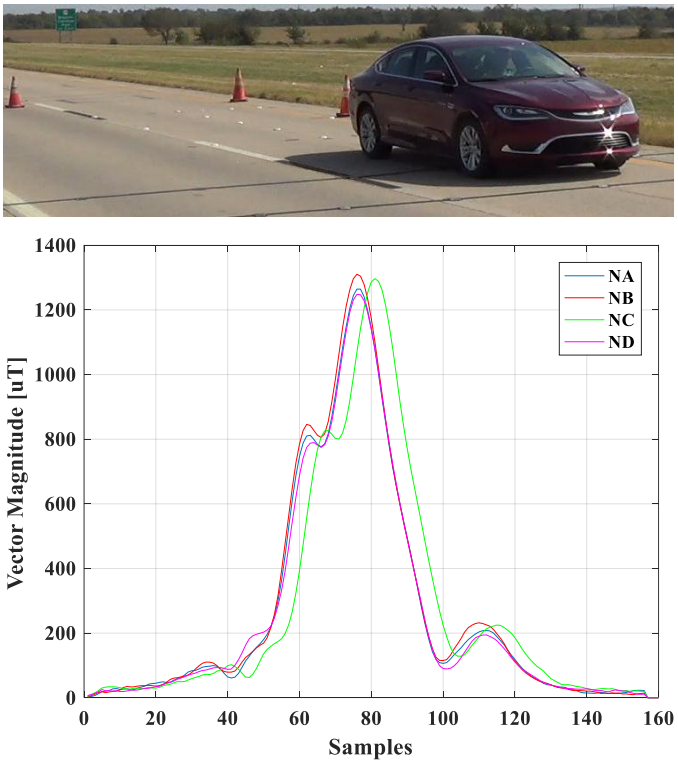


Figure 6-8 Magnetic magnitudes for class 2 vehicle obtained from all Nodes

Alternatively, approximately 11% (i.e., 193 out of 1655 values) of magnetic signatures had $R < 0.9$. In a real-world environment (e.g., highway), multiple factors could prevent repeatable results. Including pavement temperature, changes in vehicle

trajectory during passage, traffic interference from adjacent lanes, and data loss due to jittery sampling rate, are among the most significant factors. A sample set of vehicle signatures with low correlation coefficient value was visually inspected and compared to identify the cause for 11% degradation in sensor output similarity. Primary causes for sensor output variations proved to be either 1) running over the sensors, creating significant vibrations and, in some rare cases, data loss in sensors output or 2) changing vehicle trajectory during passage time. Figure 6-9 shows a class 3 vehicle traveling at 72mph driving over the edge of all four sensors. Data loss and noisy signal was observed in sensor N_B.

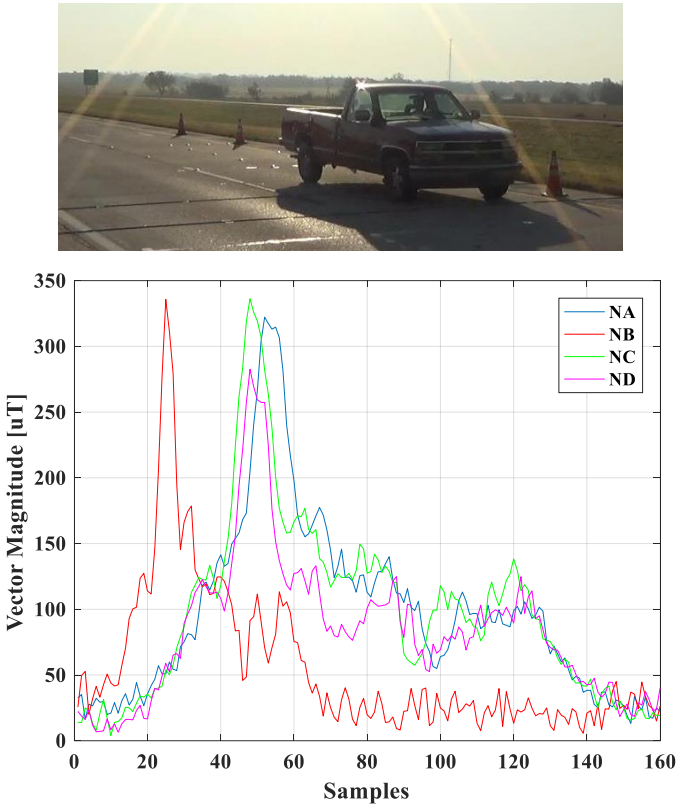


Figure 6-9 Magnetic magnitudes for class 3 vehicle driving over all sensors

Figure 6-10 depicts correlation coefficient CDFs for *X*, *Y*, and *Z-axis*, respectively. Clearly, the *Y* component (i.e., B_Y) demonstrates the highest consistency

among the three axis; X and Z components (i.e., B_X, B_Z) diverge and spread over many lower values. This phenomenon confirms that the major contributor for inconsistency is running over the sensor, which creates a huge vertical acceleration and random magnetic distortion on X and Z-axis. Higher correlation coefficients for F_M were observed, when compared with correlation coefficients for B_X, B_Y, and B_Z individually.

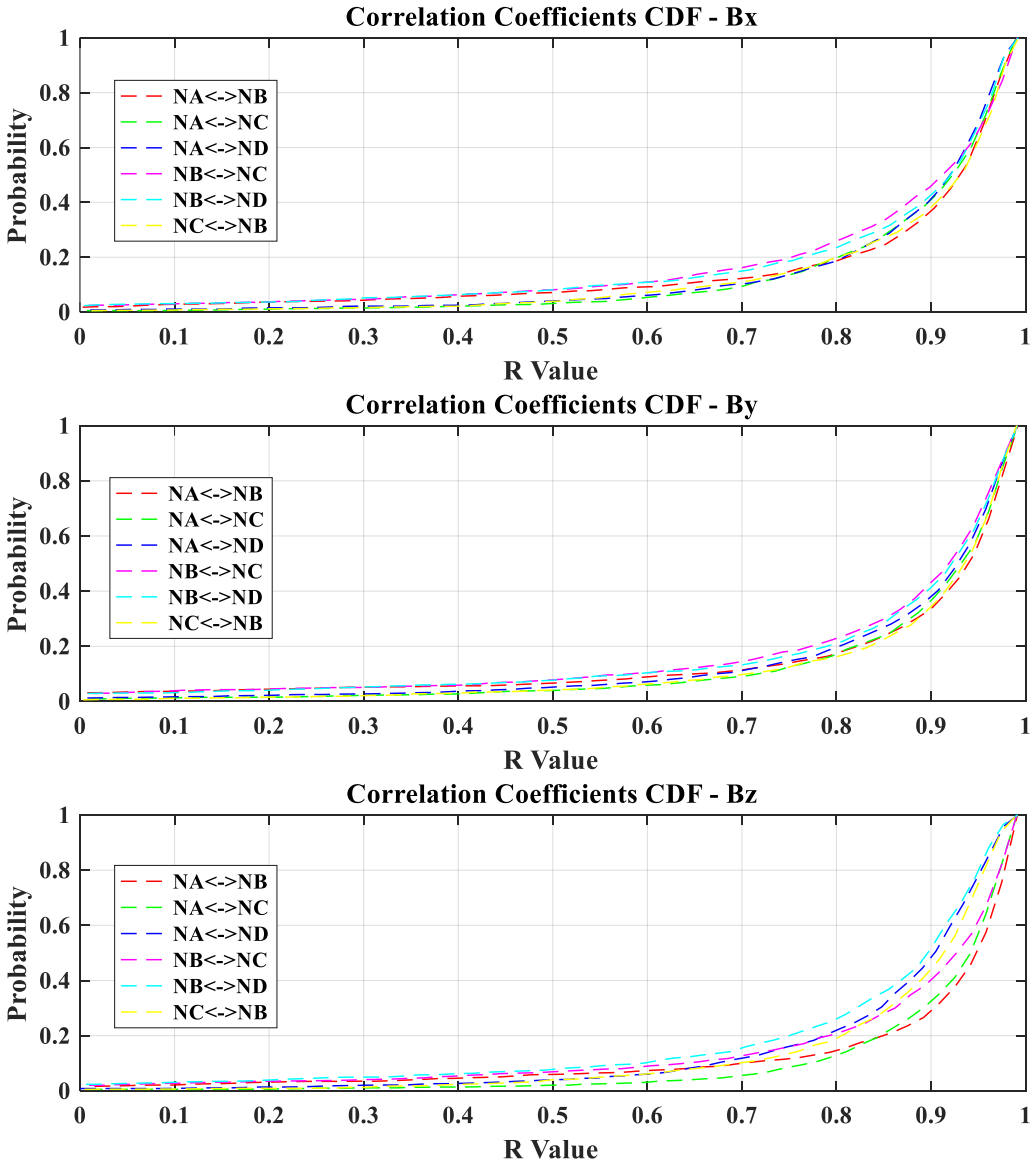


Figure 6-10 Correlation coefficients CDFs for all pairs on x, y, and z-axis

Small variations between different sensor outputs are considered a noise source with minimal effect on detection accuracy.

In conclusion, CDF for all pairwise combinations revealed that most *R* values are between 0.9 and 1, indicating high similarity in sensor output across multiple nodes. Furthermore, the p-value matrix returned insignificant p-values (i.e., 2e-138), which reject the null hypothesis and indicate significant correlations. Hence, each vehicle has a unique magnetic signature that can be utilized for vehicle re-identification applications.

6.3 Vehicle Detection

6.3.1 Optimal Detection Thresholds Analysis

F_M measurements for 12000 vehicles classified among various FHWA F scheme classes [13] via *i*VCCS on highway and urban roads were statistically analyzed to determine optimal O_{TH}, H_{TH}, and R_{TH} values—defined by Eq. 4-2, Eq. 4-3, and Eq. 4-4, thus guaranteeing optimal detection performance. Optimality was determined empirically.

F_M measurements are normally distributed with a mean μ and STD σ—$F_M \propto N(\mu, \sigma)$. F_M measurements can be represented as two Gaussians of a single dimension dataset—one representing noise and the other representing vehicle signatures. Since no information was provided with regard to which points belong to which distribution, a Gaussian Mixture Model (GMM) was used to separate the two distributions, assuming both are normally distributed.

GMM is a parametric probability density function (PDF) of continuous measurements represented as a weighted sum of *M* component Gaussian densities (CGD), as in Eq. 6-6, where *x* is a data vector of *d*-dimensional continuous measurements such that $x = [x^1, x^2, \dots, x^d]^T$; Σ is the covariance matrix of the Gaussian; *M* is the number of Gaussians; ω_i is the weight of Gaussian i such that

$\sum_i \omega_i = 1\,, \omega_i \geq 0,$ and $\mathcal{N}(x|\mu_i, \Sigma_i)$; and $i = 1 \ldots M$ is the CGD given by Eq. 6-7. GMM parameters are estimated from a training dataset by maximum likelihood using expectation-maximization (EM) algorithm or maximum a posteriori (MAP) estimation.

An iterative Expectation-Maximization (EM) algorithm was used to fit two GMMs to F_M components, which assumed to be normally distributed. Using initial values for covariance matrixes, components means, and mixing ratio, the EM algorithm iterates in two steps, namely Expectation step (E-Step) and Maximization step (M-Step). In E-Step, the algorithm computes posterior probabilities of component memberships for each observation. In M-Step the algorithm applies maximum likelihood to estimate covariance matrixes, components mean, and mixing ratio by using the component membership posterior probabilities found in the E-Step as weights. The new estimated parameters then become the initial parameters for the next iteration, and the process iterates until convergence. The initial condition parameter was set to random.

$$p(x|\lambda) = \sum_{i=1}^{M} \omega_i . \mathcal{N}(x|\mu_i, \Sigma_i) \qquad \textbf{Eq. 6-6}$$

$$\mathcal{N}(x|\mu_i, \Sigma_i) = \frac{1}{(2\pi)^{d/2}\sqrt{|\Sigma_i|}} e^{-\frac{1}{2}(x-\mu)^T \Sigma^{-1}(x-\mu)} \qquad \textbf{Eq. 6-7}$$

Since d=1 and M=2, Eq. 6-7 can be rewritten as given in Eq. 6-8 and Eq. 6-9, where x_i is a vector of F_M readings (32,905,300) and μ_n, σ_n^2 and μ_s, σ_s^2 are the mean and variance of noise and vehicle signature, respectively.

These equations can be solved using Bayesian's role by calculating the likelihood to which Gaussian each value of F_M belongs, using Eq. 6-10 and Eq. 6-11. The result is two distributions (as shown in Figure 6-11), where μ_n=18.6; σ_n=8.24; μ_s=153.5; and

σ_s=153.3. By substituting μ_n, σ_n in Eq. 4-2, Eq. 4-3, and Eq. 4-4, and by considering β=5 and α=6 (i.e., 6σ represents 99.999% confidence level), we find R_{TH}=35; O_{TH}=68; and H_{TH}=60 are the optimal thresholds.

$$\mathcal{N}(x_i|\mu_s,\sigma_s^2) = \frac{1}{\sqrt{2\pi\sigma_s^2}}\exp\left\{-\frac{(x_i-\mu_s)^2}{2\sigma_s^2}\right\} \quad \textbf{Eq. 6-8}$$

$$\mathcal{N}(x_i|\mu_n,\sigma_n^2) = \frac{1}{\sqrt{2\pi\sigma_n^2}}\exp\left\{-\frac{(x_i-\mu_n)^2}{2\sigma_n^2}\right\} \quad \textbf{Eq. 6-9}$$

$$p(\mu_s,\sigma_s^2|x_i) = \frac{p(x_i|\mu_s,\sigma_s^2)p(\mu_s,\sigma_s^2)}{p(x_i|\mu_s,\sigma_s^2)p(\mu_s,\sigma_s^2)+p(x_i|\mu_n,\sigma_n^2)p(\mu_n,\sigma_n^2)} \quad \textbf{Eq. 6-10}$$

$$p(\mu_n,\sigma_n^2|x_i) = 1 - p(\mu_s,\sigma_s^2|x_i) \quad \textbf{Eq. 6-11}$$

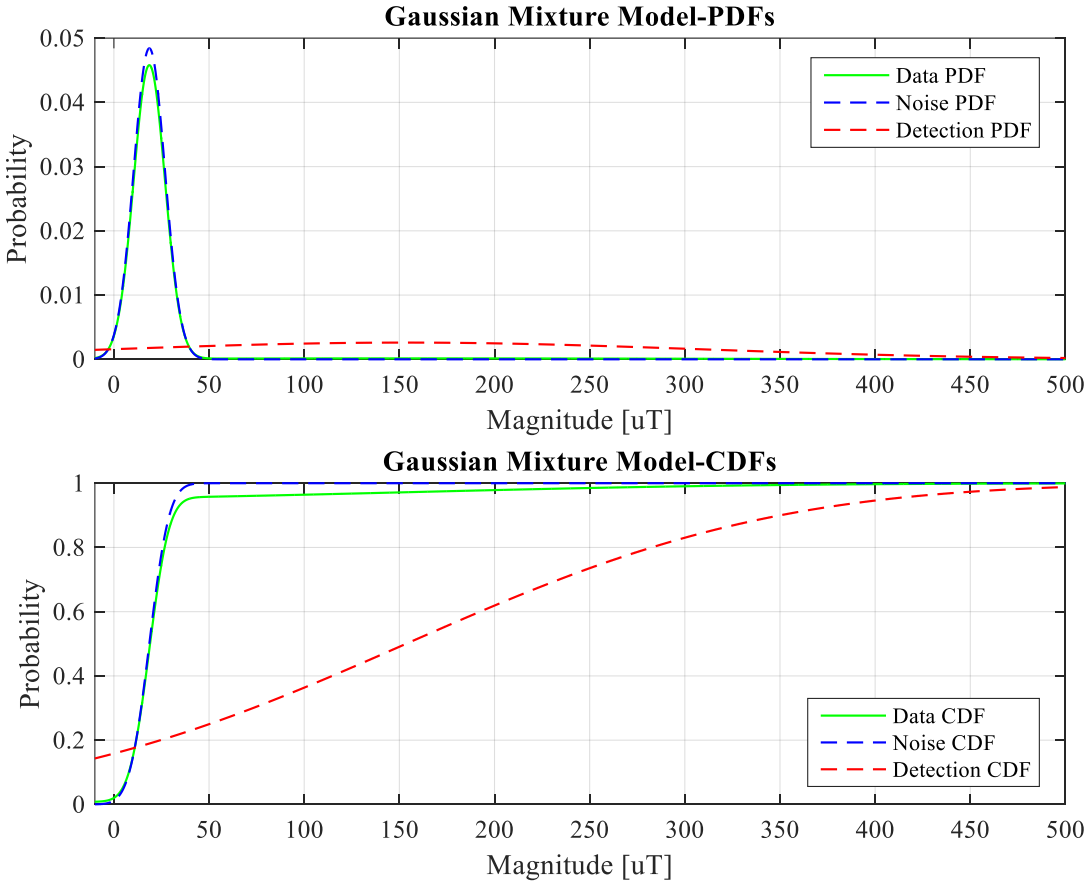


Figure 6-11 Distribution of magnetic noise and signature separated using GMM

6.3.2 Optimal Holdover Debounce-time Value

Three detection errors can be observed if MAG is used for vehicle detection:

a) *Misdetection*: Two successive vehicles at close proximity grouped as one

b) *Double detection*: Long vehicle has insignificant ferrous composition in center

c) *False detection*: Interfering from adjacent lanes caused by large trucks.

Mis-, double-, and false-detection errors are illustrated in Figure 6-12, Figure 6-15, and Figure 6-16, respectively. Both mis- and double-detection errors can be eliminated using Holdover debounce timer (H_{DT}).

Misdetection occurs when two vehicles driving at close proximity, bumper-to-bumper, are grouped as one when the condition $g_T < H_{DT}$ is true (See Figure 6-12), where g_T is the gap time between departure of vehicle *i* and arrival of vehicle *i+1* at a designated detection point *x*, as depicted in Figure 6-13; and where sensor detection zone, vehicle length, headway, gap, and clearance are denoted by $l_{DZ}^{(Ni)}$, $\overline{l_V}$, $\bar{h}$, $\bar{g}$, and $\bar{c}$, respectively.

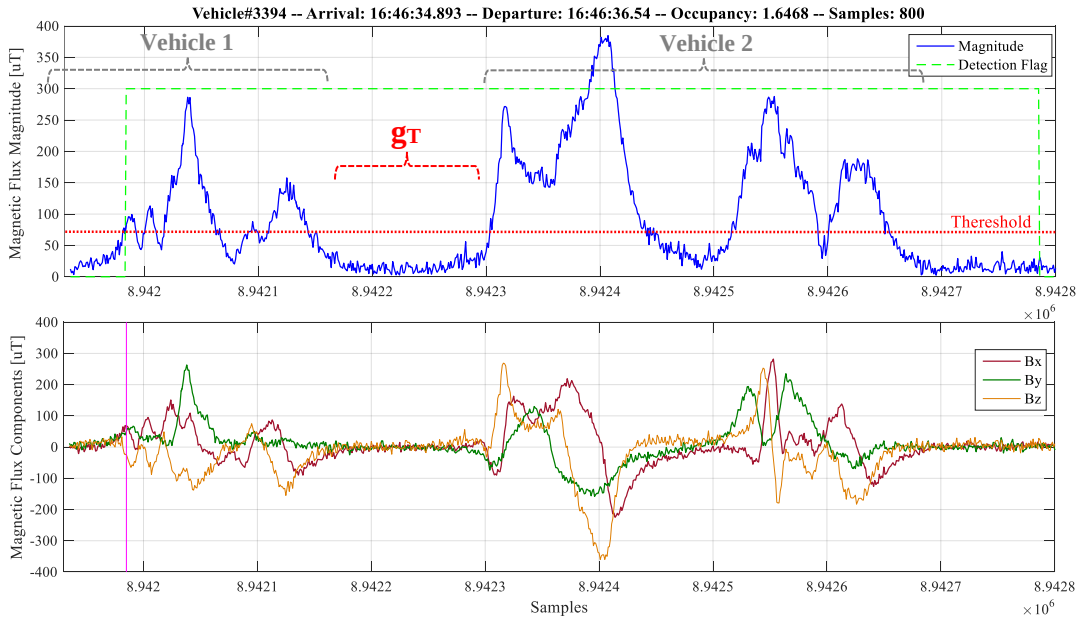


Figure 6-12 Miss-detection caused by two vehicle driving at close proximity

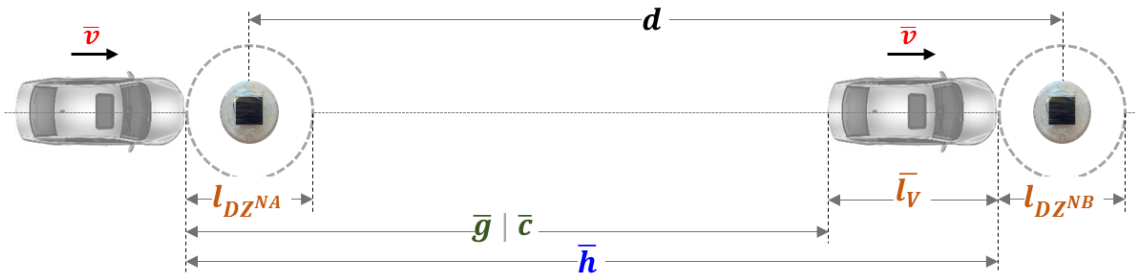


Figure 6-13 Speed estimation deployment setup

Double-detection error is observed with combination trucks (i.e., long trucks), as their structure can be magnetically divided into three sections: lead, center, and tail. Figure 6-14 illustrates the magnetic signature for a class 9 vehicle: lead section engine and first three axles, which contain the majority of the vehicle's ferromagnetic mass. The tail section includes two axles. The central section $S^{(2)}$ has a relatively small ferromagnetic mass, making $F_M(k) < H_{TH}$ true for duration $S^{(2)}_T > H_{DT}$, given truck speed is relatively slow so that the vehicle is double detected, as shown in Figure 6-15. This phenomenon is referred to in literature as *pulse break-up* [127]–[131].

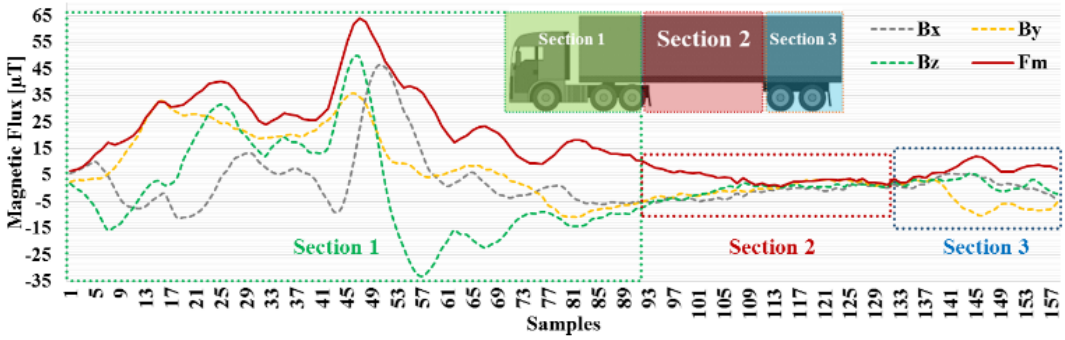


Figure 6-14 Magnetic Flux and Sections of a class 9 vehicle

During the early stages of developing the detection algorithm, Tafish [132], [133] developed an analytical model to describe detection error as function of debounce time T_d based on vehicle detection data collected using an inductive loop deployed on a highway. The probability of detection error was found as the weighted sum of the pulse break-up and tailgating probabilities. A Poisson processes was used to model vehicle

arrival and inter-arrival time. Vehicle inter-arrival time PDF, representing a Gamma distribution, was used to model waiting times between Poisson arrivals. To find pulse break-up probability, four assumptions were made: 1) magnitude signature of the central section of long truck will fall below detection threshold; 2) length of the central section is equivalent to the spacing between axle 3 and 4 of class 9 vehicles, thus assumed normally distributed; 3) radius r of detection zone is known; and 4) vehicle speed when passing over detection zone is constant. The probability of pulse break-up was found as the probability that passage time of a class 9 vehicle central section is more than the debounce time T_d. Optimal value of T_d that minimizes both pulse breakup and tailgating for data collected in field Test 1 and presented in Table 6-3 was found using the Golden Section Search algorithm. Simulation results showed that T_d = 385ms is the optimal debounce time value, given that speed mean is 70mph and vehicle arrival rate is 10 vehicles per minute.

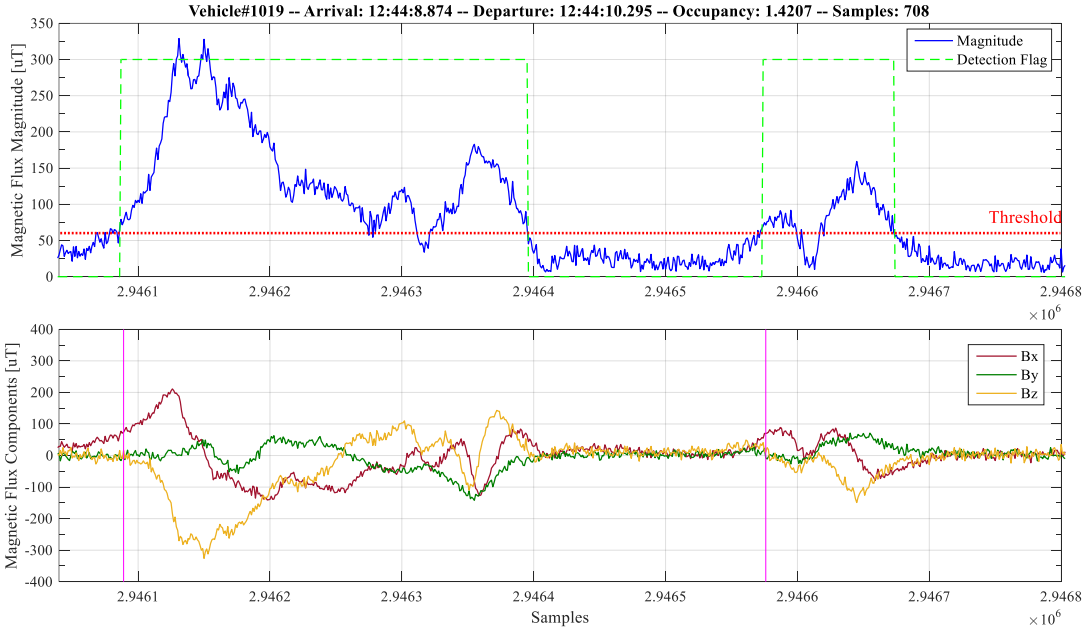


Figure 6-15 Double detection caused by class 9 vehicle

The developed model in [132] is valid for free flow traffic and IDL. The inter-arrival time distribution model was found to vary depending on traffic characteristics (i.e., low, medium, and high volume traffic) and location (e.g., on-ramp, off-ramp, intersection, stop-and-go, free flow) [134], [135]. Radius *r* for IDL is constant and equal to the loop radius. However, MAG *r* is characterized by the amount of furious materials in a vehicle structure because MAG, unlike IDL, are passive sensors.

The following sections introduce statistical data analysis applied on a dataset that included 30580 records collected on highways and urban roads under various traffic conditions in the state Oklahoma. The objective was to find H_{DT} values that satisfy the condition $g_T > H_{DT} > S^2_T$ (i.e., minimize mis- and double-detection errors). No assumptions where made in this analysis.

6.3.2.1 Minimizing misdetection error

Minimizing misdetection errors was achieved by statistically analyzing g_T, computed in Eq. 6-12. The objective was to determine optimal value of H_{DT}, thus minimizing misdetection error such that $g_T > H_{DT}$. The longer the gap time, the larger debounce time, and vice versa. g_T values were computed from historical data collected using *i*VCCS (See Chapter 5). Dataset included 13400 records collected on Oklahoma highways, in addition to 17180 records collected on urban roads in Tulsa. PDF and cumulative distribution function (CDF) were subsequently found (See Figure 6-17). CDF showed that setting H_{DT} to 370ms for the highway setup and 430ms for the urban road setup reduced misdetection error to 0.1865% and 0.5065%, respectively.

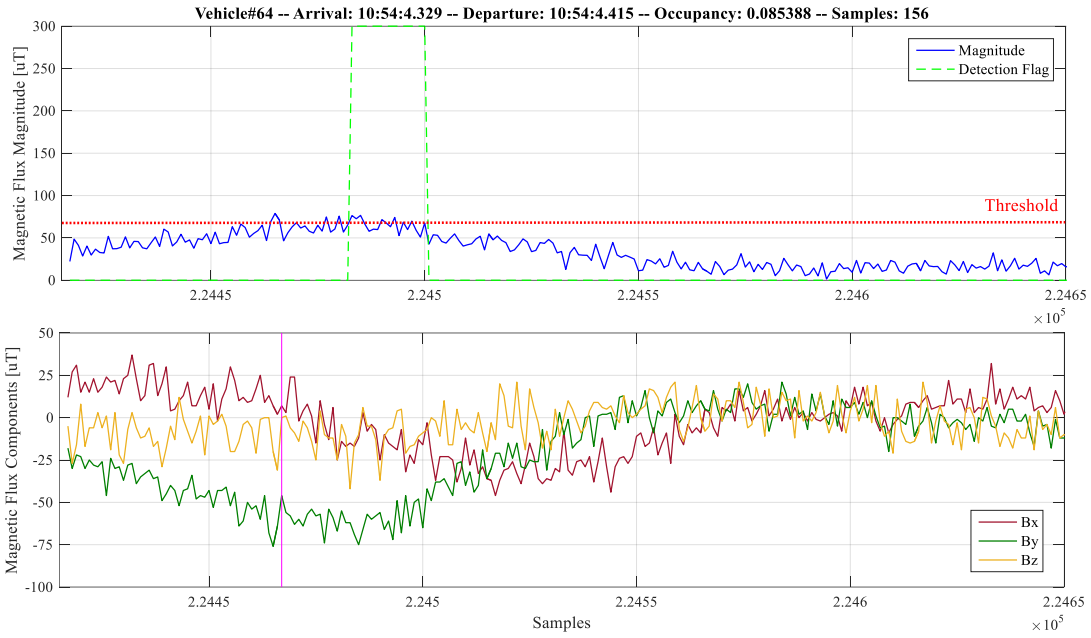


Figure 6-16 False detection caused by a vehicle passing in adjacent lane

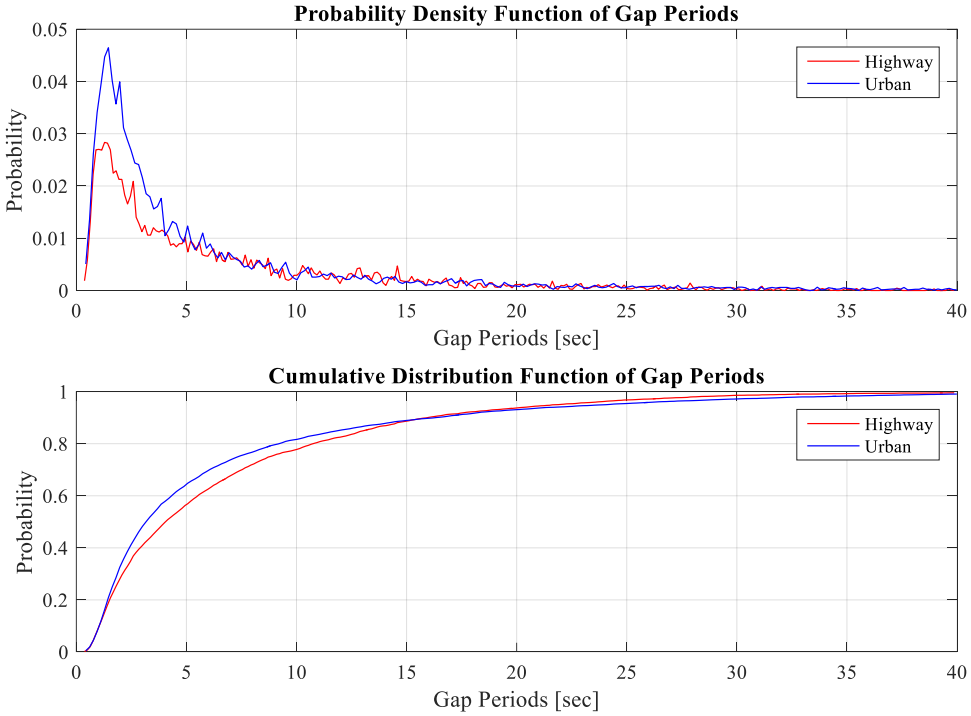


Figure 6-17 Probability distributions of Gap periods

$$g_T(k) = T_A(k+1) - T_d(k) \qquad \textbf{Eq. 6-12}$$

6.3.2.2 Minimizing double-detection error

To define optimal value of H_{DT} that minimizes double-detection error such that $H_{DT} > S^2_T$, PDF and CDF of $S^{(2)}_T$ for 1770 vehicle of class 8, 9, and 10 were found from data collected using *i*VCCS on highway and urban roads at a speed range between 25 and 88mph. The computation process for S^2_T is depicted in Figure 6-18. CDF in Figure 6-19 indicates that the longest S^2_T is 500ms. Error probability distribution showed 0.004% and 0.005% probability of double-detection error when setting $H_{DT} \geq 400$ms and $H_{DT} \geq 370$ms, respectively (See Figure 6-20).

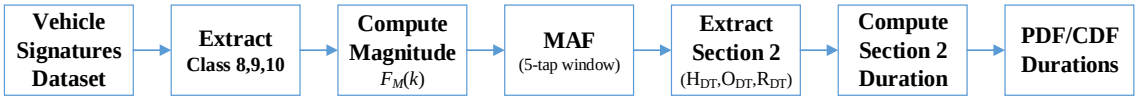


Figure 6-18 S^2_T computation process

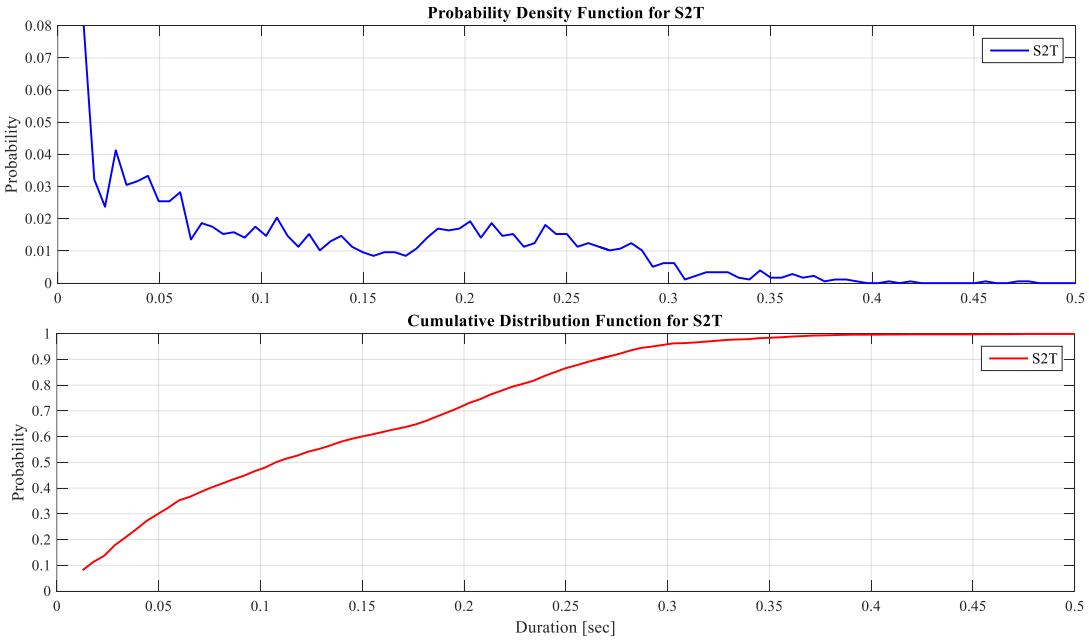


Figure 6-19 Probability distributions of Section 2 periods

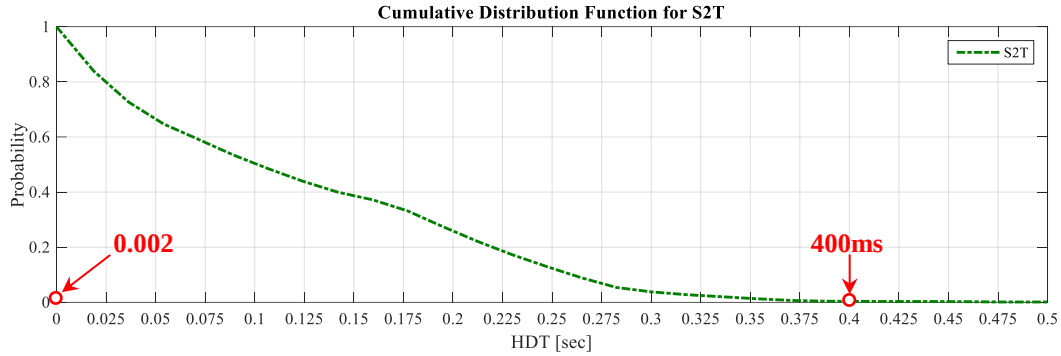


Figure 6-20 Probability of double detection for a given H_{DT}

6.3.2.3 Minimizing false-detection error

False-detection error is the result of a magnetic disturbance in the adjacent lane caused by a vehicle with high magnetic flux density traveling at the edge of lane. Such a disturbance will be detected by sensors in both lanes.

False-detection can initially be eliminated by defining sensor detection zone (*DZ*). In general, *DZ* can be defined at five detection edges (see Figure 6-21): 1) *leading*, 2) *trailing*, 3) *right-side*, 4) *left-side*, and 5) *elevation* edge. An empirical test was conducted to find the relationship between distance and magnetic disturbance magnitude. Results are illustrated in Table 6-2. Notably, leading edge has the highest magnetic disturbance because vehicles contain most ferromagnetic mass in the front section (e.g., engine).

Table 6-2 Detection zone characteristics based on Class 2 vehicle

Leading Edge		**Trailing Edge**		**Side sensitivity**	
Distance (m)	**F_M (μT)**	**Distance (m)**	**F_M (μT)**	**Distance (m)**	**F_M (μT)**
2.50	3	2.50	1	2.00	3
2.20	4	2.20	2	1.30	7
1.25	6	1.16	4	0.90	10
1.10	7	1.10	6	0.60	18
0.90	10	0.90	7	0.30	30
0	70	0	10	0.20	40

Detection zone can be controlled by either changing MAG sensor sensitivity or changing detection thresholds, O_{TH} and H_{TH}, where α and β (See Eq. 4-2, Eq. 4-3 and Eq. 4-4) can be calibrated to control detection zone and to eliminate interference outside the detection region.

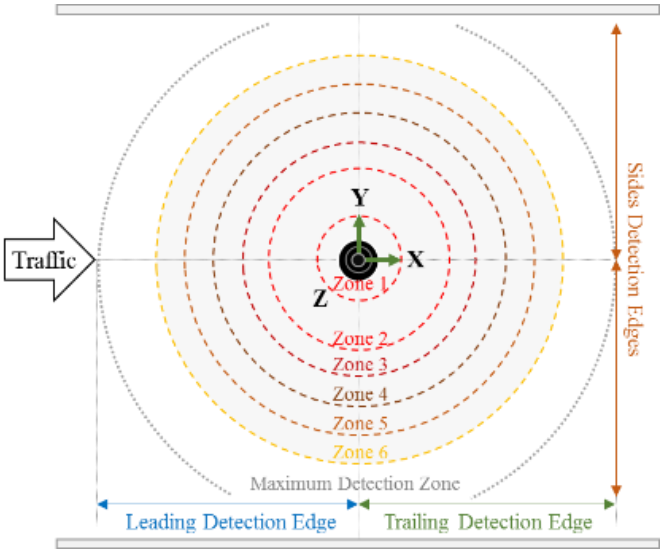


Figure 6-21 Detection zone edges was found to be symmetric

Analyzing the vehicle magnetic signatures dataset revealed that increasing O_{TH} to 9µT and H_{TH} to 6µT prevents false detection. However, increasing O_{TH} or H_{TH} results in the loss of a portion of the vehicle magnetic signature, hence, rendering an unreliable estimation of vehicle length and loss of important features for vehicle classification. Conversely, reducing sensitivity might cause motorcycle mis- and delayed-detection.

To solve this issue, variations in B_X, B_Y, and B_Z components were analyzed to measure the interference on each component from a vehicle traveling in an adjacent lane. Analysis showed insignificant interference effect on B_Z. Thus, by using 10-tap MAF, calculating $B_Z(k)$ mean—as in Eq. 6-13—and comparing μB_Z for each detected vehicle (V_n) with a threshold I_{TH}, a decision can be made as to whether V_n is a real detection or an interfering signal. I_{TH} =80 was statistically found from dataset. Figure

6-22 shows variations in $B^{(\gamma)}$, their magnitude ($B^{(\gamma)}m$), and after MAF ($B^{(\gamma)}m$a) for class-3 with trailer detected in the right lane and an interfering vehicle in adjacent lane.

$$\mu B_Z(V_n) = \frac{1}{\mathrm{N}}\sum_{k=1}^{N}\left(\frac{1}{M}\sum_{i=0}^{M-1} B_{Zm}(k-i)\right) \geq I_{TH};\ B_{Zm}(k) = \sqrt{\left(B_Z(k) - B_{Zref}\right)^2} \qquad \textbf{Eq. 6-13}$$

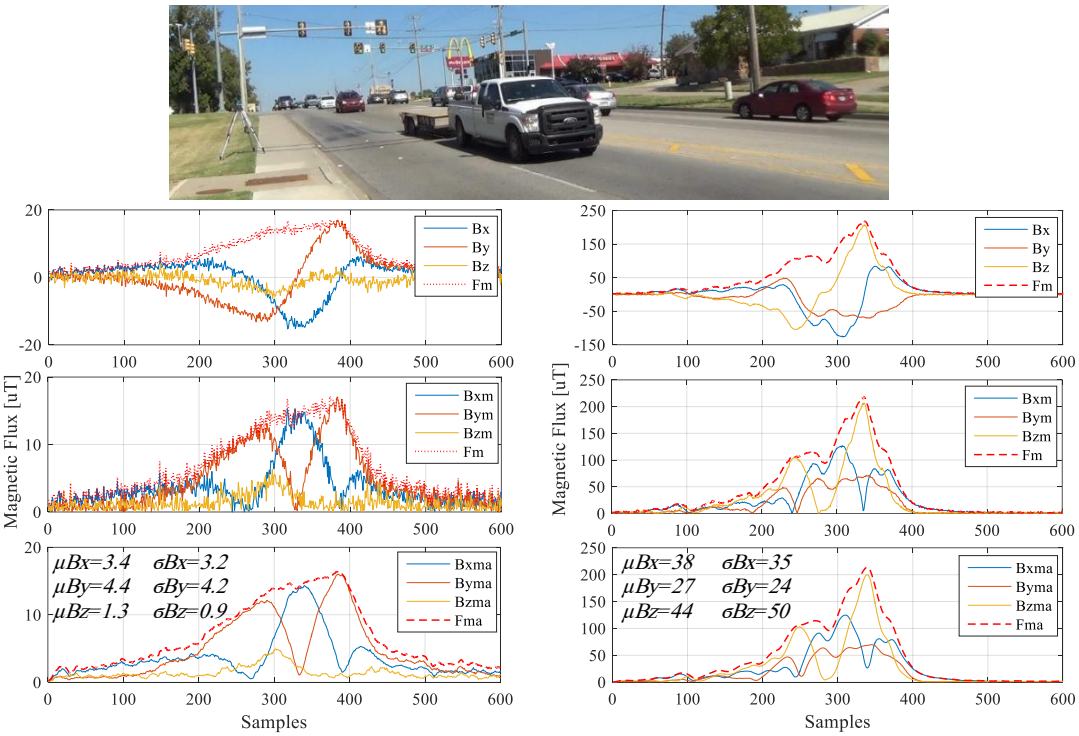


Figure 6-22 Variations in $B^{(\gamma)}$caused by interfering (left) and detection (right)

6.3.3 Adaptive Geomagnetic Baseline Drift Compensation Performance

To evaluate adaptive baseline drift compensation algorithm performance, a sensor node was deployed on pavement in the absence of ferrous materials over the course of the day. Notably, algorithm testing for one day when sensor is deployed on one site is not enough to reach a general conclusion about its worthiness. However, the developed algorithm repeatedly and indirectly was evaluated during many field testing campaigns throughout the study.

Distribution of noise was found with and without the use of the baseline drift compensation algorithm. Figure 6-23 shows drift in F_{Mref} over 240 minutes without

(yellow) and with (blue) the geomagnetic baseline compensation algorithm. Figure 6-24 shows vector magnitude normalized distributions without (yellow) and with (blue) compensation. Given no compensation is applied, mean is μ=7.67μT and STD is σ=1.6319μT. Given the application of compensation algorithm, mean and STD are μ=1.79μT and σ=0.7μT, respectively.

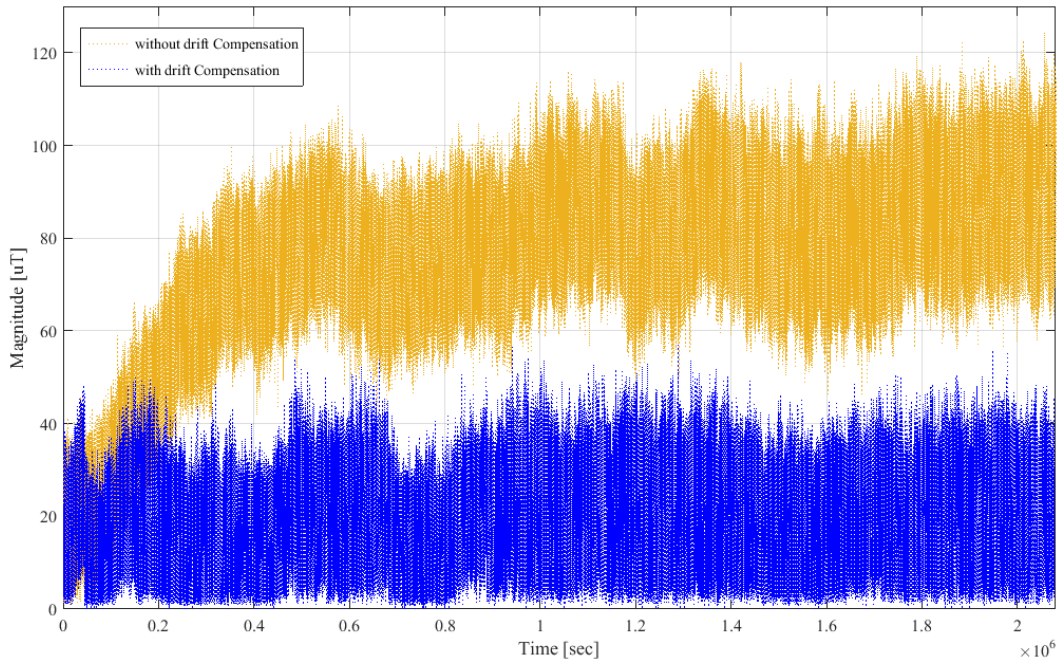


Figure 6-23 The drift in F_{Mref} with and without adaptive compensation

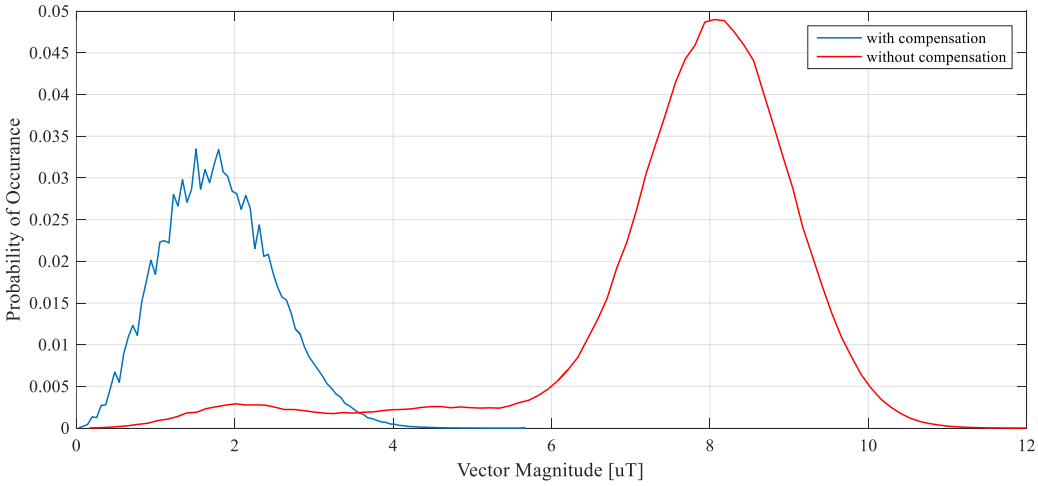


Figure 6-24 F_{Mref} distribution over 24-hour with and without compensation

6.3.4 Detection and Counting Accuracy

Counting accuracy was evaluated using the mean absolute percent error (MAPE), computed as in Eq. 6-14.

$$MAPE = \frac{1}{n}\sum_{1}^{n}\frac{|Count_{video} - Count_{iVCCS}|}{|Count_{video}|}\times 100 \qquad \textbf{Eq. 6-14}$$

Field Test 1 resulted in high detection ratio with overall 2% relative error. Dataset was limited to 463 vehicles. Classes 4, 7, 10, 11, 12, and 13 were not observed during this test. Remaining classes were correctly detected, with the exception of class 9, which was double detected with 9% error, as presented in Table 6-3.

Table 6-3 Detection MAPE for Roadway Setup—Field Test 1

Vehicle Class	Video Count	*i*VCCS Count	MAPE
F01	1	1	0.0%
F02	247	247	0.0%
F03	65	65	0.0%
F05	65	65	0.0%
F06	8	8	0.0%
F08	2	2	0.0%
F09	75	82	9.0%
Total	**463**	**470**	**2.0%**

Double-detection is one of three detection errors detailed in Section 6.3.2; these can be observed when using MAG for vehicle detection. As stated earlier, double detection occurs when signal magnitude drops below *Holdover Threshold* (H_{TH}) for duration $S^2_T > H_{DT}$ and crosses H_{TH} again while the same vehicle remains in the detection zone. Finding optimal H_{DT} value that satisfies the condition $H_{DT} > S^2_T$ would

solve this problem. Section 6.3.2 provides a detailed analysis for optimal H_{DT} value that minimizes double-detection error.

Field Test 2 had two deployment setups—roadway and roadside. *Roadway* setup resulted in 99.90% detection accuracy for dataset with 2007 vehicles. Class 1, 4, 11, 12, and 13 vehicles were not observed during this test (See Table 6-4). Unlike *Field Test 1*, all class 9 vehicles were correctly detected, primarily because a new H_{TH} value based on the analysis study in Section 6.3.2 was implemented for this test. However, a misdetection of two class 2 vehicles occurred when two successive vehicles located within close proximity of one another were grouped as one. This could occur given that $H_{DT} > g_T$. Hence, to reduce the probability of double-detection and mis-detection, optimal H_{DT} value for satisfying the condition $g_T > H_{DT} > S^2_T$ should be found This requirement is well-detailed in Section 6.3.2.

The *Roadside* setup in *Field Test 2* confirmed 99.95% detection accuracy (See Table 6-5). Flux magnitude variations in *roadside* setup were relatively uniform when compared to *roadway* setup, which accounts for slightly improved accuracy.

Table 6-4 Detection MAPE for Roadway Setup—Field Test 2

Vehicle Class	Video Count	iVCCS Count	MAPE
F02	624	622	0.32%
F03	1027	1027	0.00%
F05	97	97	0.00%
F06	32	32	0.00%
F07	1	1	0.00%
F08	8	8	0.00%
F09	213	213	0.00%
F10	5	5	0.00%
Total	2007	2005	0.099%

Table 6-5 Detection MAPE for Roadside Setup—Field Test 2

Video Count	iVCCS Count	Detection	MAPE
2044	2045	99.951%	**0.0489%**

Field Test 3 resulted in a high detection ratio with only 0.0363% MAPE. Dataset included 2754 vehicles. Class 11, 12, and 13 vehicles were absent. Detection results per class are shown in Table 6-6.

Table 6-6 Detection MAPE for Roadway Setup—Field Test 3

Vehicle Class	Video Count	Roadrunner	iVCCS Count	MAPE
1	10	10	8	10%
2	919	919	918	0.10881393%
3	1287	1287	1287	0
4	13	13	13	0
5	133	133	133	0
6	48	48	48	0
8	13	13	13	0
9	327	330	329	0.6116208%
10	4	4	4	0
Total	**2754**	**2757**	**2753**	**0.036311%**

Field Test 4 proved excellent *in-lane* detection. However, unlike the first three highway-based field tests, Field Test 4 was conducted on an urban road. Doing so introduced a new false-detection error resulting from interfering vehicles on an adjacent lane. This error was specifically caused due to the following scenarios:

1) Dissimilar lane widths: highway lanes measured at least 12 feet (3.7 m) wide and urban road lanes measured 9 feet (2.7 m) wide

2) Trucks traveling at the edge of a detection lane (See Figure 6-25, Figure 6-26, and Figure 6-27) or hybrid cars traveling on an adjacent lane (See Figure 6-28)

3) Vehicles with a significant amount of steel in their structure



Figure 6-25 Class 9 truck at the edge of lane 2, detected in both lanes



Figure 6-26 Class 6 truck on the edge of lane 2, detected in both lanes



Figure 6-27 Class 3 truck with huge trailer on edge of lane 2, detected in both lanes



Figure 6-28 Class 2 hybrid car on the edge of lane 2, detected in both lanes

Results for in-lane detection errors (i.e., errors resulting from adjacent lane interference are not considered) are illustrated in Table 6-7. All classes were detected correctly, with the exception of two class 9 vehicles and one class 8 vehicle that were double-detected when traveling at very low speeds (e.g., 10 mph). Mean Absolute Error (MAE) for per class detection is 0.25% for Lane 1 and 0% for Lane 2. MAPE is 0.058% for Lane 1 and 0% for Lane 2. Classes 7, 10, and 13 were not observed during this test.

Table 6-7 Number of detections In-Lane per-class—Field Test 4

Class	Video		*i*VCCS		MAPE	
	Lane 1	Lane 2	Lane 1	Lane 2	Lane 1	Lane 2
1	7	4	7	4	0	0
2	2607	2552	2607	2552	0	0
3	793	817	793	817	0	0
4	1	2	1	2	0	0
5	39	24	39	24	0	0
6	4	0	4	0	0	0
8	3	2	3	2	0	0
9	6	0	8	0	33.33%	0
Total	**3460**	**3401**	**3462**	**3401**	**0.058%**	**0%**

Table 6-8 shows overall detection error when vehicles detected from adjacent lanes are considered in the error analysis. Overall MAPE is 1.676%. Out of 6976 detected by *i*VCCS on both lanes, 115 vehicles (either trucks or hybrid cars) were falsely detected from an adjacent lane. False-detection caused by hybrid cars can be attributed to the large amount of metal located in the stack of battery elements, as well as a large magnet in the electric engine router.

Table 6-8 Total Detection Error—Field Test 4

Detection	iVCCS		Video		MAE		MARE	
	Lane 1	Lane 2	Lane 1	Lane 2	Lane 1	Lane 2	Lane 1	Lane 2
In-Lane	3462	3401	3460	3401	4.02%	6.45%	1.27%	2.088%
Adj-Lane Trucks	23	56	-	-				
Adj-Lane Hybrid	19	15	-	-				
Total	**6976**		**6861**		**5.24%**		**1.676%**	

False-detection error can be eliminated, as described in Section 6.3.2, by computing μB_Z using Eq. 6-13, and then comparing μB_Z for each detected vehicle (V_n)

with threshold I_{TH}. A decision can be made whether V_n is an actual in-lane vehicle or an interfering signal from an adjacent lane.

Field Test 5 results (See Table 6-9) demonstrated outstanding detection performance. Notably, several class 1 (i.e., motorcycles) were detected, albeit falsely from adjacent lane interference) by *i*VCCS, because they had an insignificant ferromagnetic mass and passed near detection zone (See Figure 6-29). Some class 2 and 3 vehicles were not detected because *i*VCCS was in calibration state when the vehicle passed over the nodes. Vehicles traveling between lanes were considered false-detection by *i*VCCS sensors in both lanes.

Table 6-9 Detection MAPE—Field Test 5

Class	Video		*i*VCCS		MAPE	
	Lane 1	Lane 2	Lane 1	Lane 2	Lane 1	Lane 2
1	3	9	2	7	33.3333	22.2222
2	2062	947	2059	943	0.1454	0.42234
3	582	289	581	287	0.17186	0.6922
4	6	0	6	0	0	0
5	40	11	40	11	0	0
6	14	4	14	4	0	0
7	1	1	1	1	0	0
8	2	0	2	0	0	0
9	15	6	15	6	0	0
10	1	1	1	1	0	0
12	3	0	3	0	0	0
Total	**2729**	**1268**	**2724**	**1260**	**0.1832%**	**0.6309%**



Figure 6-29 Motorcycle considered as False-detection

Field Test 6 and *7* results were evaluated by ODOT to determine the accuracy of the OU-developed wireless sensor. Real-time implementation and off-line detection accuracy were examined. ODOT used automatic vehicle count based on embedded inductive loops as ground truth. ODOT-reported results are listed in Table 6-10 and Table 6-11. In *Field Test 6*, *i*VCCS outperformed AVC and video-based counting methods with 0.639% MAPE. In *Field Test 7*, *i*VCCS achieved 98.5% detection accuracy.

Table 6-10 Detection MAPE—Field Test 6

Detection Method	Manual	Video	AVC23	*i*VCCS
Total Count	**1252**	**1227**	**1263**	**1260**

Table 6-11 Detection MAPE—Field Test 7

Detection Method	Manual	Tubes	AVC04	*i*VCCS
Total Count Lane 1	314	314	307	302
Total Count Lane 2	286	292	293	289
Total Count Lane 3	228	226	225	224
Total	**828**	**832**	**825**	**815**

6.3.5 Detection in Stationary-state and Stop-and-go Scenarios

Stationary state occurs when a vehicle stops completely (e.g., parking lots) or travels in stop-and-go traffic conditions (e.g., traffic signals and intersections). The

developed detection algorithm was tested for both scenarios. Achieved detection accuracy was 100% when the sensor was deployed in either a *roadside* or *roadway* setup. Figure 6-30 and Figure 6-31 show go-stop-go detections for Honda Accord 2004 in both roadside and roadway setups. *R1* represents vehicle arrival; *R2* represents steady state (stop); and *R3* represents departure. Figure 6-32 shows F_M for go-stop-go scenario in both roadside and roadway setups. G_A, S_S, and G_D represent vehicle arrival section (go-in), vehicle in steady state (stop); and vehicle departure section (go-out).

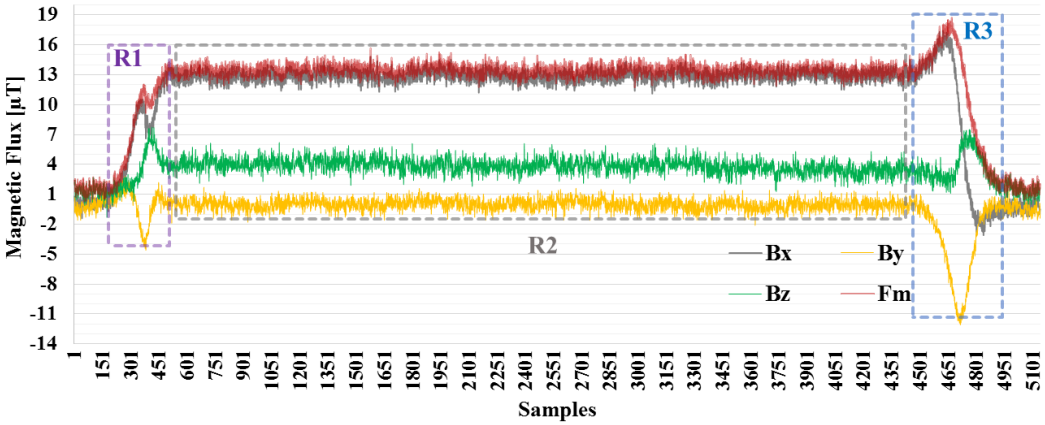


Figure 6-30 Go-Stop-Go detection using sensor in roadside setup

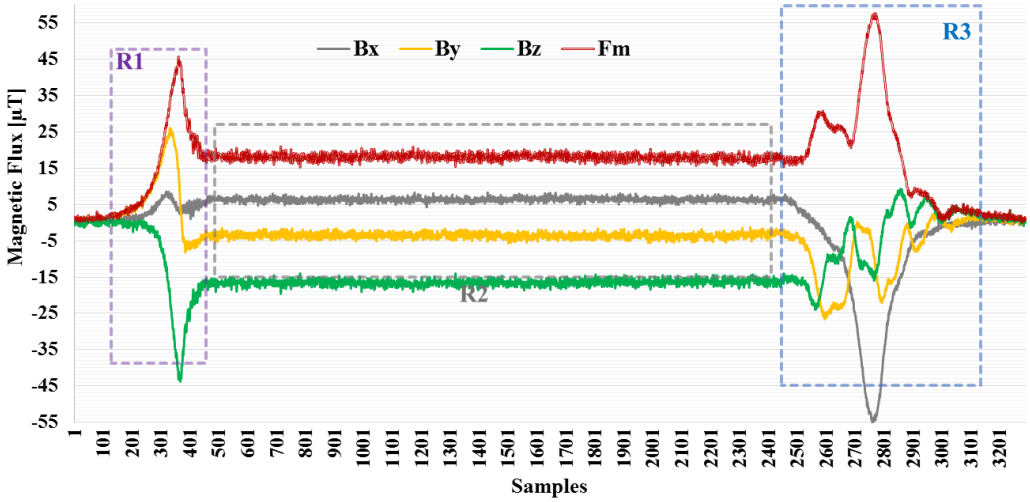


Figure 6-31 Go-Stop-Go detection using sensor in roadway setup

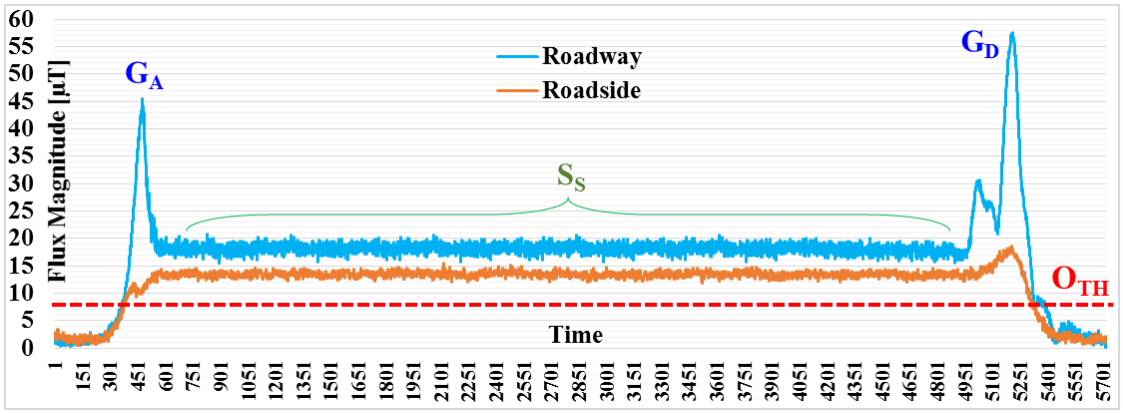


Figure 6-32 The FM and detection flag in Go-Stop-Go scenario

6.4 Assessment of Time Synchronization Algorithm

To assess T-Sync algorithm performance and evaluate drift error on each node, as well as over a network, the following test was conducted.

RTC-1Hz signal duration $T_{RTC}^{(MCU)} = 1/f_{RTC}^{(MCU)}$ was compared to GPS-PPS signal duration $T_{PPS}^{(GPS)} = 1/f_{PPS}^{(GPS)}$ over the course of 24 hours. Both clocks were sampled using the MCU's high frequency clock at $f_{TCLK}^{(MCU)} = 32MHz$. Measurement resolution is one-cycle of $f_{TCLK}^{(MCU)}$, which is equal to 31.25ns. $f_{TCLK}^{(MCU)}$has a tolerance ±5*ppm*; however, since both signals are measured instantaneously using the same clock, tolerance error is differentiated and canceled. Differences between measured durations were logged.

This particular test was implemented instantaneously on five different *i*VCCS nodes. RTC drift for each node was calculated separately and compared statistically with other node drift(s) to find over-network T-Sync error. Drift dataset included 86400 measurements from each sensor. Temperature measurements were also combined on a one-minute basis. Figure 6-33 shows a histogram for absolute error between RTC-1Hz and GPS-PPS signals over the course of day for three *i*VCCS Nodes—A, B, and C. Consistent drift between RTC-1Hz and GPS-PPS signals with mean 20~25µSec can be

observed for all nodes. Figure 6-34 shows distribution of T-Sync error between two nodes. Drift with a mean of 2~4µSec can be observed among Nodes A, B, and C.

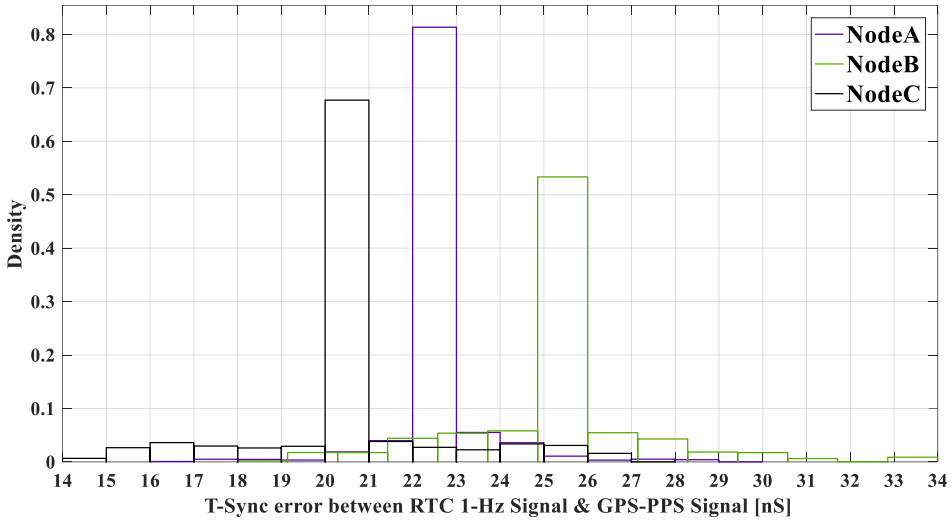


Figure 6-33 Histogram of T-Sync error between RTC and GPS

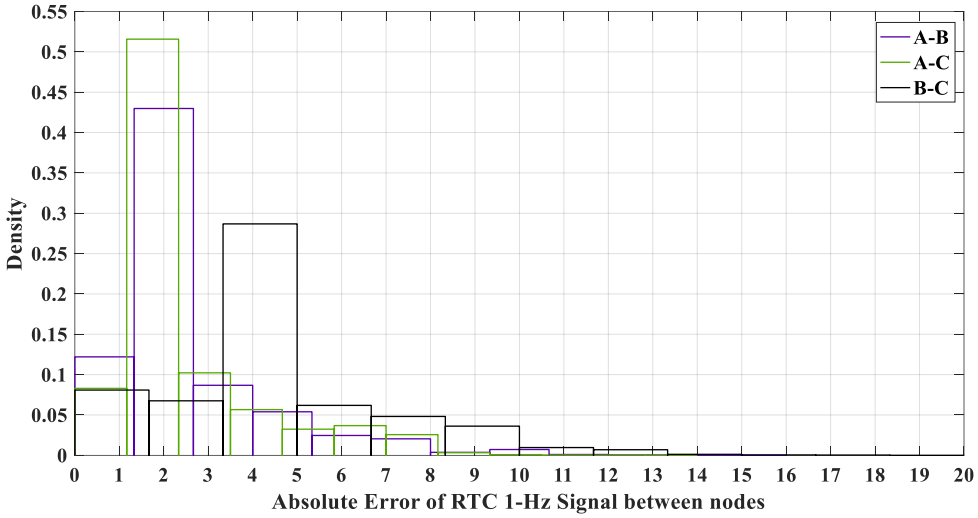


Figure 6-34 Histogram of absolute error of RTC between two nodes

6.4.1 Evaluation of Timestamps Consistency

GPS-PPS signal was used to synchronize spatially distributed sensor nodes that share a globally synchronized timestamp. However, error in arrival and departure timestamps might be driven by factors other than T-Synch error (e.g., delay in MCU's interrupt routine and instruction execution).

Delay in executing arrival and departure timestamps is nondeterministic. Rather, it is subject to frequency tolerance $f_{osc\text{-}tol}$ of MCU's oscillator and priority of task being executed by MCU at the moment of a timestamp event. Arrival timestamp event is triggered by MAG *Magnitude Interrupt* over the MC's external interrupt *INT0*.

To evaluate consistency and determine time-stamping delay while MCU is executing its typical cycles, a highly accurate signal generator was used to trigger *INT0* at consistent frequency $f_{Trigger}$. Trigger time was logged, and delay between each two consecutive triggers was calculated. The test was repeated for different $f_{Trigger}$, ranging 1~1600Hz, each with 10^8 samples. The test resulted in trivial delay (i.e., tens of nanosecond) at various $f_{Trigger}$ values.

6.5 Vehicle Speed Estimation

Speed estimation accuracy was evaluated against *Road Runner 3 kit* with 30.5μs event timestamp resolution. Two statistical measurements were used: 1) Mean Absolute Percentage Error (MAPE), which measures systematic bias to error such that estimated speed values are consistently high or low (Eq. 6-15) and 2) Root Mean Square Error (RMSE), which measures mean deviation of estimated speed values (Eq. 6-16). Speed analysis is shown in Table 6-12.

Three separations between the nodes, namely 6-, 8-, and 10-meters, were investigated. Better results occurred when 8 meters was used to separate two nodes. Notably, increasing separation distance between sensor nodes reduces the effect of MAG sampling rate tolerance between different nodes. *Roadside* setup demonstrated a higher speed estimation error when compared to *roadway* setup. This phenomenon can be attributed to lower SNR in the roadside scenario.

$$MAPE = \frac{1}{n}\sum_{i=1}^{n}\left|\frac{True\ Speed_{(i)} - Estimated\ Speed_{(i)}}{True\ Speed_{(i)}}\right| \quad \textbf{Eq. 6-15}$$

$$RMSE = \sqrt{\frac{1}{n}\sum_{i=1}^{n}\left(True\ Speed_{(i)} - Estimated\ Speed_{(i)}\right)^2} \quad \textbf{Eq. 6-16}$$

Table 6-12 Speed Estimation Accuracy

Setup	MAPE	RMSE	Speed Accuracy
Roadside (*d*=6m)	6.4603 mph	6.5001%	93.5012%
Roadway (*d*=6m)	3.2064 mph	2.6585%	97.3415%
Roadway (*d*=8m)	2.9281 mph	2.5773%	97.4227%
Roadway (*d*=10m)	2.9867 mph	2.5218%	97.4782%

Speed estimation using MAG is subject to several inaccurate factors (e.g., sensor sampling rate (f_S), T-Sync error, and defined vehicle detection zone, among others).

Nondeterministic error ξ_{Ts} could occur as the result of a delay in sampling the exact instant of vehicle arrival or departure. Maximum ξ_{Ts} is equal to the period of pre-defined sampling rate (e.g., if f_S=100Hz, then ξ_{Ts}=10ms). Assume a vehicle with 5-meter average length travels at 90mph (i.e., 40m/s). Occupancy time on each sensor $T_{Occ} = 5/40 = 125ms$. Hence, maximum error in T_A and T_A timestamps is $2\xi_{Ts}/T_{Occ}$ = 320μs, which accounts for 0.256% error in speed estimation.

Based on data observations and statistical analysis, the following issues must be considered for more accurate speed estimation.

1) The higher the sampling rate, the higher the speed estimation accuracy.
2) All sensor nodes should implement the same detection reference thresholds (O_{TH}, H_{TH}, and R_{TH}) and debounce timers (O_{DT}, H_{DT}, and P_{DT}); any difference in thresholding between nodes will add a detection timestamp error.

3) Tolerance error in sensors sensitivity—due to environmental factors—can be reduced by using higher sampling rates; however, this error can be neglected without need for compensation. The reason for this phenomenon is that the sensor has only 2% maximum sampling rate tolerance. Moreover, this error depends on the accuracy of MAG internal clock, and it might be practically infeasible to characterize this error over operating temperature range.

4) Changes in vehicle trajectory at detection point might result in a T_A and T_A timestamp error; however, this error is rare, trivial, and can be neglected.

6.6 Vehicle Magnetic Length Estimation

Vehicle magnetic length (VML) is estimated from the product of vehicle estimated speed and occupancy time using Eq. 4-27. The highway dataset includes 4178 VML measurements; urban road dataset includes 6856 VML measurements. Figure 6-35 and Figure 6-36 show the distribution of VML by FHWA F Scheme with 13 classes for tests conducted on highway and urban roads, respectively. Combined distribution is shown in Figure 6-37.

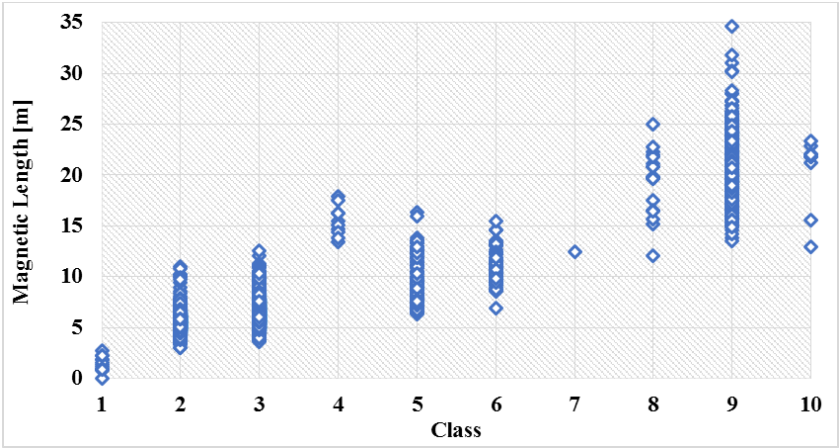


Figure 6-35 VML by FHWA F Scheme – Highway Data

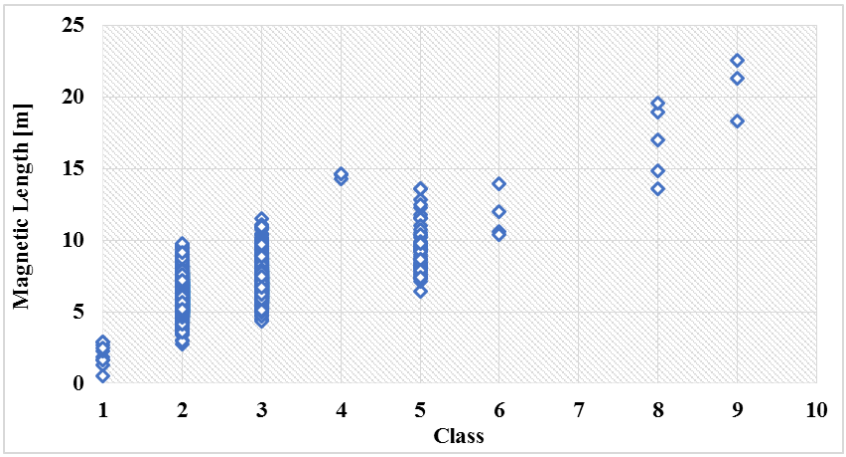


Figure 6-36 VML by FHWA F Scheme – Urban Data

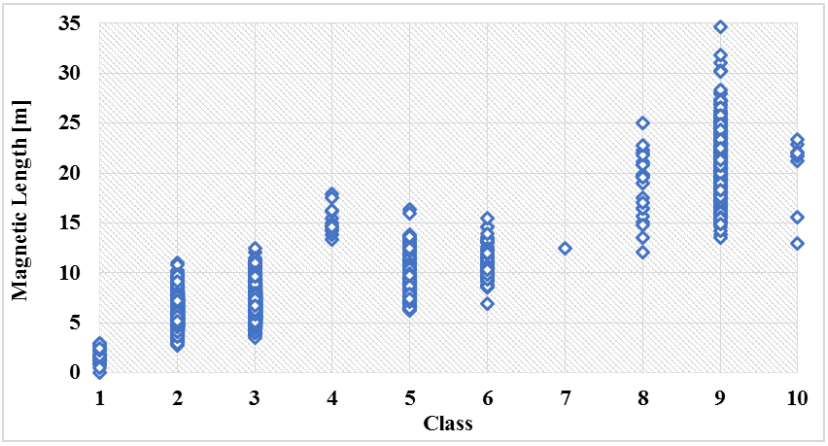


Figure 6-37 VML by FHWA F Scheme – Combined

Chapter 7: *i*VCCS APPLICATIONS IN TRAFFIC SURVEILLANCE

7.1 Overview

In addition to the applications presented in previous chapters, several traffic monitoring applications can be implemented using the developed platform, for example, in atypical situations for uneventful traffic management of an unplanned evacuation path using localized traffic management. Intelligent parking lot management is another application wherein the sensor can be used to manage traffic by reporting occupied/vacant parking spots and their locations. Other applications include automatic garage doors, automatic gates, drive thru vehicle detectors, ramp metering, travel time estimation, traffic data collection, intersection capacity, collision avoidance, and highway design.

This chapter provides a detailed study of two particular applications, including the development of vehicle classification schemes and re-identification models using *i*VCCS.

7.2 Introduction to Vehicle Classification Schemes

7.2.1 Axle-based Vehicle Classification Scheme

In general, vehicle class data is collected from WIM and AVC sites, which use inductive loops (IDL) and piezoelectric sensors to report vehicle class according to FHWA Scheme F with 13 classes, as depicted in Figure 7-1.

Scheme F was developed during the 1980s and is based on manual classification of visually identifiable vehicle characteristics. The scheme was later amended to provide computational classification based on number of axles and wheelbase axle spacing. Such axle-based vehicle classification (ABVC) systems require intrusive

sensors that are plagued with a number of drawbacks, chiefly their reliance on pavement geometry. This means that pavement deterioration will cause unreliable ABVC data. A study [136] conducted by WECAD center at the University of Oklahoma reported high classification inaccuracy rates resulting from sensor misconfiguration at Oklahoma AVC sites. ABVC schemes have proven problematic due to overlapping among vehicle classes, especially with regard to vehicles pulling one-, two-, or three-axle trailers [136]. For example, in one study, 43% of class 3 vehicles were falsely classified as class 2, and 45% of class 5 were falsely classified as class 3. In fact, three- or four-axle class 3 trucks often overlap with class 8 trucks, which—upon sensor overpass—causes class 3 to be classified as class 8. Class 6 trucks also overlap with class 4 three-axle buses. Significant overlap has been observed for three- or four-axle class 5 with trailers and classes 8 and 5, as well as buses [136].

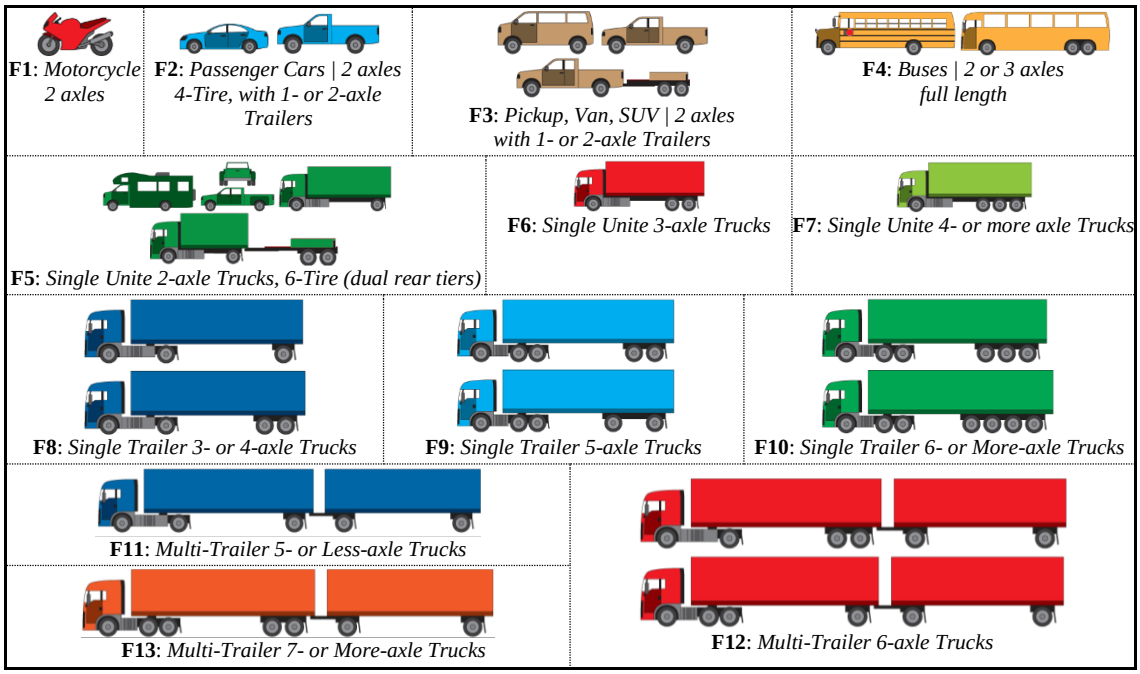


Figure 7-1 U.S. FHWA Classification Scheme F with 13 class

As stated earlier, high costs associated with ABVC scheme technologies, as well as high regular maintenance and calibration costs, limit spatial distribution of such systems. As such, they are often installed only at strategic points. Thus, the availability of ABVC data is limited. Additionally, the feasibility of collecting ABVC data in urban areas is significantly hindered by bumper-to-bumper congestion during peak hours. Vehicle acceleration/deceleration and stop-and-go scenarios at signals are factors contributing to erroneous data. ABVC using MAG remains challenging and warrants ongoing research.

7.2.2 Available Length-Based Vehicle Classification Schemes

Traffic flow characteristics are directly affected by long vehicles (i.e., trucks), which have a major impact on road service life [137]. Hence, it is crucial for U.S. DOT agencies to estimate percentage of roadway damage. Accordingly, the *FHWA Traffic Monitoring Guide* [13] provides a generic length-based vehicle classification (LBVC) scheme based on nationwide IDL data. Even so, it is practically impossible to define LBVC boundaries for FHWA F Scheme with 13 classes. Clearly, vehicle magnetic length (VML) overlapping occurs between a number of classes (e.g., class 2 through 5 and class 8 through 10). The proposed LBVC scheme [13] categorizes vehicles into four groups, namely passenger vehicles (PV), single-unit trucks (SU), combination-unit trucks (CU), and multi-unit trucks (MU). The scheme is inexpensive and works best with dual-IDL stations. Notably, the FHWA guide permits states to develop their own LBVC scheme and define length threshold boundaries that best fit vehicle characteristics that vary among states.

Since there is no generic definition for LBVC boundaries, several states have begun to adopt a LBVC scheme that replaces outdated ABVC and is based on local vehicular data collected from AVC and WIM sites located throughout a state's roadways [138], [139]. Many states have defined different length boundaries for their developed schemes. Some have adopted a four-group LBVC scheme; others use a three-group scheme by combining group 3 and 4. For example, the Ohio DOT has adapted a statewide three-group LBVC scheme that bins FHWA Scheme F vehicles into PV, SU, and MU [140], [141]. Florida, Illinois, Washington, and Idaho have also adopted three-group LBVC schemes that classify the same Scheme F vehicles into PV, short trucks (ST), and long trucks (LT) [142]. Minnesota's DOT (MDOT) proposed a four-group LBVC scheme (e.g., motorcycles [MC], short [S], medium [M], and long [L] vehicles) and recognizes a fifth-group, namely very long (VL), in areas with significant numbers of seven-or-more axle, multi-trailer trucks [138]. Table 7-1, Table 7-2, and Table 7-3 summarize LBVC schemes from a number of states and provide a list of boundaries. This information was identified from data collected using IDLs. Notably, very few efforts attempt to assess the feasibility of defining magnetic length boundaries based on data collected using wireless MAG.

Table 7-1 Three-group LBVC schemes boundaries for different states

Description	FHWA	Illinois	Washington	Idaho	Florida	Ohio	New York
Passenger Car(PV)	F1—F3	0→6.7m	0→6.1m	0→7m	0→6.52m	0→8.53m	0→6.7m
Short trucks (ST)	F4—F7	6.7→11.9m	6.1→12.8m	7→12.2m	6.52→12.9m	8.53→14m	6.7→11.9m
Long trucks (LT)	F8—F13	≥11.9m	≥12.8m	≥12.2m	≥12.9m	≥14m	≥11.9m

Table 7-2 Four-group FHWA-LBVC scheme boundaries

Description of Vehicles	FHWA-ABVC	FHWA-LBVC
Passenger vehicles (PV)	F1—F3	0→3.96m
Single unit trucks (SU)	F4—F7	3.96→10.67m
Combination trucks (CU)	F8—F10	10.67→18.59m
Multi-trailer trucks (MU)	F11—F13	18.59→36.58m

Table 7-3 MDOT-LBVC scheme boundaries

Description of Vehicles	FHWA-ABVC	Minnesota
Motorcycle (MC)	F1	0→1.98m
Short vehicle (S)	F2—F3	1.98→6.55m
Medium vehicle (M)	F4—F7	6.55→14.93m
Long vehicle (L)	F8—F13	14.93→36.58m

Unlike VMS produced by IDL, vehicle signatures sampled using MAG have less consistent peak magnitude due to several factors, such as differences in sensitivity, vehicle trajectory, and non-symmetry of detection zone. Moreover, IDLs are active magnetic sensors, meaning that they generate magnetic field in the IDL zone and resonate at a constant frequency that increases when the generated field is induced by a passing vehicle. When this occurs, a detection state is triggered. Unlike IDLs, MAG are passive sensors that rely on the disturbance of the Earth's magnetic field relative to the presence of a metallic object (i.e., vehicle). Hence, the amount of preamble ferrous materials in a vehicle structure plays a major role in the sensor's detection range [122], [123], [143]. A vehicle with a large amount of steel can be detected from quite a lengthy distance, creating significant variations in VML per class. These factors make using MAG for LBVC extremely challenging. The development and implementation of

computationally efficient, real-time LBVC schemes for wireless MAG will be introduced in the next section.

7.3 Development of Real-Time Length-Based Vehicle Classification

LBVC algorithm using two timely, synchronized MAG nodes was developed and implemented by means of machine learning (ML) and probabilistic modeling. Several classification schemes are proposed. The developed algorithm enables real-time, computationally efficient vehicle classification based on VML.

Classification based on VML requires precise vehicle detection and highly accurate speed estimation. Precise detection demands a consistent baseline (i.e., localized geomagnetic field) and coherent sampling rate. Speed estimation accuracy relies on the precision of time-stamping (i.e., vehicle arrival and departure time), which is dependent upon the accuracy of a time synchronization algorithm. All algorithms are well detailed in companion publications [122], [123], [143].

7.3.1.1 Vehicle Magnetic Length

Before developing any classification scheme that bins multiple classes, it is important to understand the underlying statistical distribution of each class, as well as the overlap among various classes. Classes that show significant overlapping should be grouped into the same bin. Significant overlap between two groups will result in a high misclassification rate.

In this study, the combined VML dataset (11034 sample) was considered for data analysis and classification study. Vehicles in classes 11, 12, and 13 were missing from dataset, as they were not observed during the field studies. Figure 7-2 shows VML scatter plots for the dataset used to develop the LBVC schemes. Table 7-4 presents five

essential statistical measurements for each class, namely mean, standard deviation (STD), and variance (Var), as well as maximum and minimum values. Notably, a significant overlap is observed among classes 2 and 3, classes 5 through 7, and classes 8 through 13. Additionally, significant variations in VML per class are attributed to differences in the amount of permeable ferrous materials in each vehicle structure. Vehicles with a large amount of steel in their structure can be detected from a longer distance; hence, their magnetic length will be longer. There is no way to find a general dipole model for all vehicles, even for those within the same class. Figure 7-3 illustrates the histograms of VML by FHWA Scheme F with 13 classes.

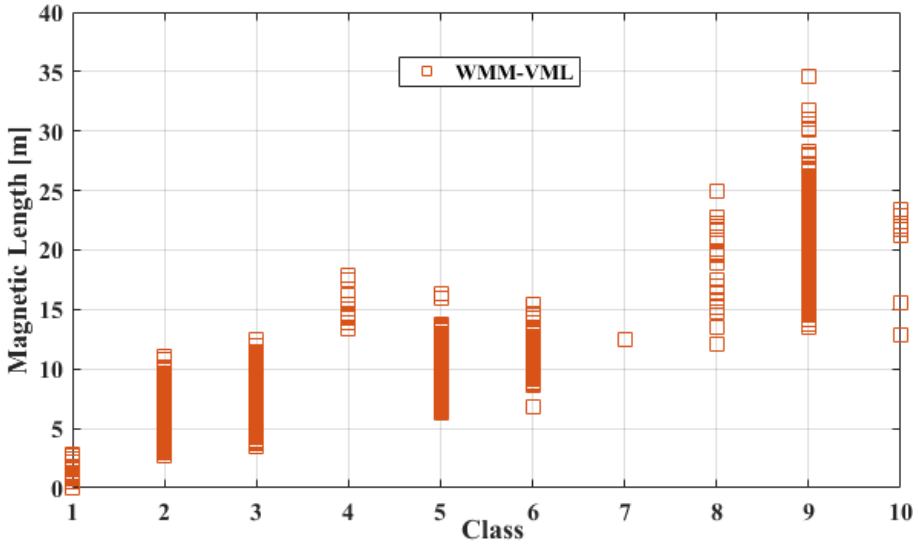


Figure 7-2 VML scatter plots for dataset that used to develop LBVC schemes

Table 7-4 VML statistical measurements

FHWA Class	Mean Length (m)	Standard Deviation	Variance	Minimum Length (m)	Maximum Length (m)
F01	1.7629	0.7156	0.5120	0.5370	2.9106
F02	5.9383	0.8190	0.6708	2.7606	11.0377
F03	6.6140	1.0713	1.1477	3.5516	12.5161
F04	15.2446	1.3782	1.8996	13.3784	17.9241
F05	9.2552	1.9270	3.7132	6.2894	16.3884

F06	10.9073	1.6149	2.6078	6.8855	15.4366
F07	12.4458	NA	NA	12.4458	12.4458
F08	18.8185	3.2396	10.4950	12.0606	25.0102
F09	21.3425	2.9298	8.5840	13.5164	34.6607
F10	20.3949	3.5930	12.9097	12.9307	23.3700

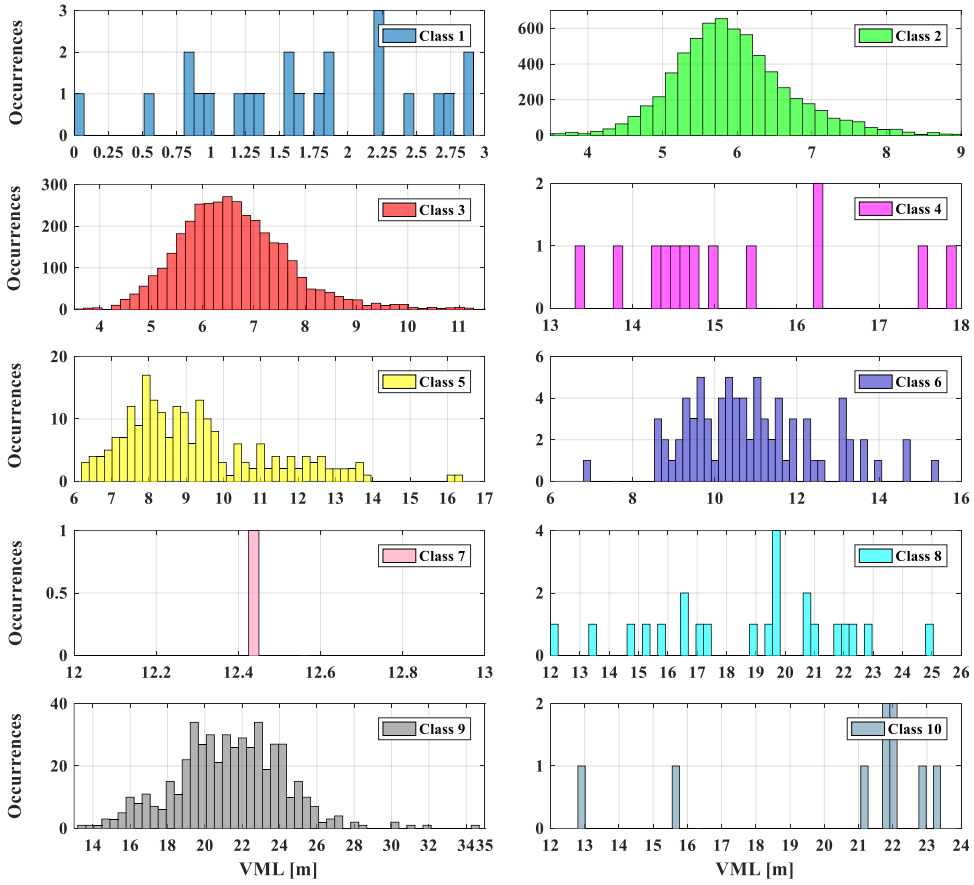


Figure 7-3 Histograms of VML by FHWA F Scheme Classes

7.3.1.2 Proposed Classification Schemes

According to the FHWA's traffic monitoring guide, "*If length-based classification is used, it should accommodate motorcycle identification as one of the groups*" [13]. Based on a) visual observation of VML data shown in Figure 7-2 and Figure 7-3, b) statistical measurements presented in Table 7-4, as well as c) structural similarity of vehicles, three distinctive LBVC schemes are proposed, as in Figure 7-4.

MC group includes only motorcycles. PV group includes passenger cars, pickups, and SUVs. Short-trailer group (ST) includes buses, light-trucks, and single-unit-trucks. Long vehicles (L/LT) group includes single-trailer and multi-trailer trucks.

The main objective of the *Three Groups LBVC Scheme A* (3-G_{SA}) is providing a general distinction of long and heavy commercial vehicles, which includes buses, semi-trailer (ST) trucks, and multi-trailer (MT) trucks. The 3-G_{SB} and 4-G_{SX} provide further distinction between Passenger Vehicles (PV) and Single-Unit Trucks (SU).

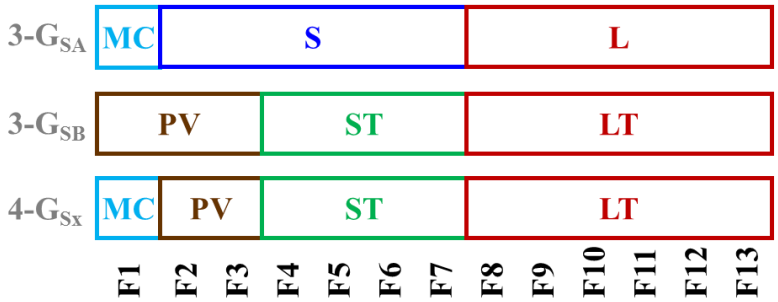


Figure 7-4 Recommended Classification Schemes

Scatter plots for datasets based on proposed LBVC schemes are shown in Figure 7-5. A histogram and statistical measurements for 3-G_{SA} are illustrated in Figure 7-6 and Table 7-5, respectively. Statistical measurements for 3-G_{SB} are illustrated in Table 7-6. A histogram and statistical measurements for 4-G_{Sx} are illustrated in Figure 7-7 and Table 7-7, respectively.

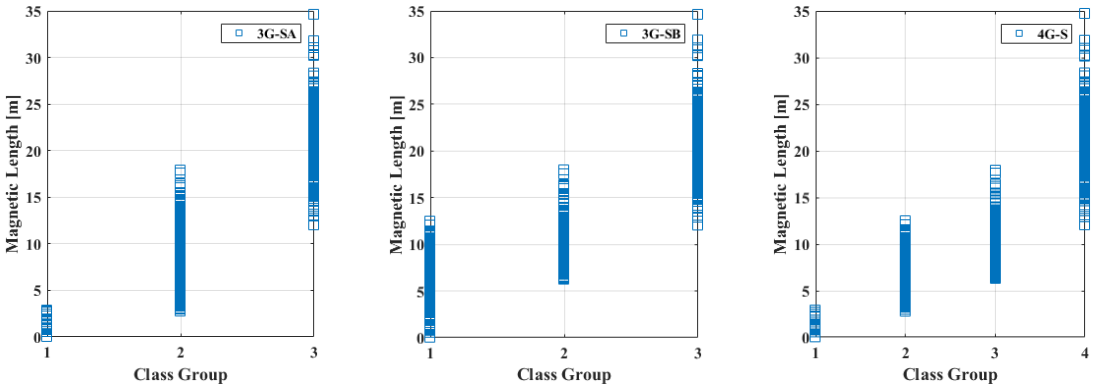


Figure 7-5 Dataset scatter plots for 3-G_{SA}; 3-G_{SB}; and 4-G_{Sx}

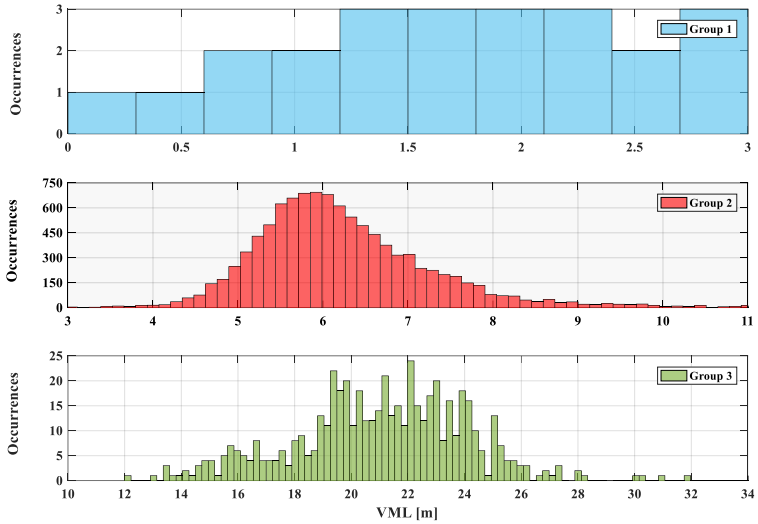


Figure 7-6 Histograms of VML by 3-G_{SA}

Table 7-5 VML statistical measurements for 3-G_{SA}

Group Number	Mean Length (m)	Standard Deviation	Variance	Minimum Length (m)	Maximum Length (m)
G1	1.6863	0.7899	0.6239	0.8112	2.9106
G2	6.2912	1.2165	1.4799	2.7606	17.9241
G3	21.2157	2.9961	8.9765	12.0606	34.6607

Table 7-6 VML statistical measurements for 3-G_{SB}

Group Number	Mean Length (m)	Standard Deviation	Variance	Minimum Length (m)	Maximum Length (m)
G1	6.1681	0.9949	0.9898	0.8112	12.5161
G2	9.9333	2.2571	5.0944	6.2894	17.9241
G3	21.2157	2.9961	8.9765	12.0606	34.6607

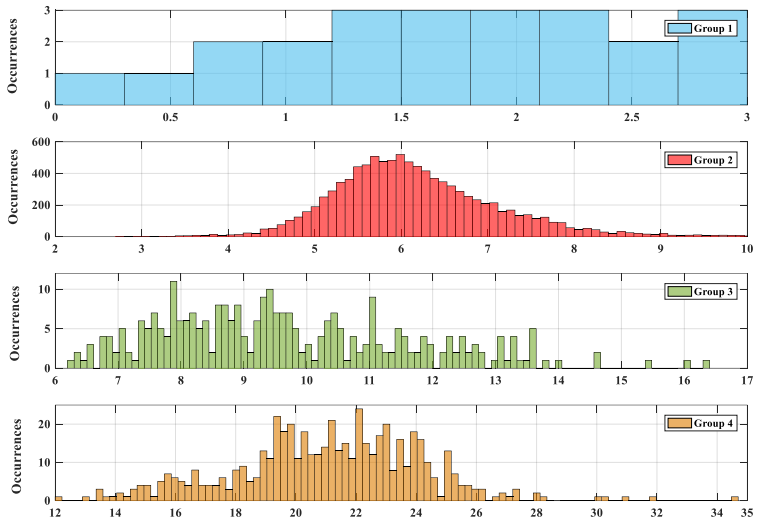


Figure 7-7 Histograms of VML by 4-G_{Sx}

Table 7-7 VML statistical measurements for 4-G_{Sx}

Group Number	Mean Length (m)	Standard Deviation	Variance	Minimum Length (m)	Maximum Length (m)
G1	1.6863	0.7899	0.6239	0.8112	2.9106
G2	6.1783	0.9720	0.9447	2.7606	12.5161
G3	9.9333	2.2571	5.0944	6.2894	17.9241
G4	21.2157	2.9961	8.9765	12.0606	34.6607

7.3.1.3 LBVC Model using Machine Learning

Intelligent classification algorithms learn to classify vehicles into predefined classes by statistically modeling the relationship between vehicle class and probabilistic distribution of features set (or predictors) extracted from VMS. Several ML classification methods (e.g., Decision Trees [DT], Support Vector Machine [SVM], *k*-Nearest Neighbor [*k*NN], and Naïve Bayes Classifier [NBC]) were evaluated, investigating best practices to build a system classification model and to infer optimal length boundaries of a real-time LBVC using MAG or IDL. Optimality was determined empirically.

VML dataset was divided into two subsets—training and testing. The first was used for training the intelligent classifier and the other for assessing its performance. Predictive accuracy of fitted models was examined using 10-fold cross-validation. This method builds *k*-different test sets from the same training set; trains all models based on the remaining training dataset; and utilizes best performing hypothesis on average to avoid over-fitting.

All classification methods attempt to maximize total classification accuracy. However, each method implements different techniques. ML methods and their techniques are not the focus of this dissertation; interested readers can review details in [144]. Greatly important is that Radial Basis Function (RBF) kernel SVM outperformed other kernel types. Since SVM is a binary classifier, a one-vs.-all approach was used. This means that *m-class* models are fitted to the training data—one model for every class. When fitting the model for the *mth* class, training dataset labels are changed. Thus, the model is fitted to distinguish among two classes at once. During validation with the test dataset, *m*-individual scores are estimated—one for each model. The class with the highest score is chosen as the predicted class. For DT, a J84 version was implemented. This algorithm optimizes the tree size using "pruning" (i.e., cease splitting if the number of objects in a branch is smaller than a predefined value). Optimal values for other parameters (e.g., *k*-value in *k*NN; size of the tree and number of leaves in DT; C and gamma in SVM) were found using hyper-parameter optimization algorithms.

Classifier performance was assisted using 10 commonly-used metrics (See Table 7-8), namely, classification rate (C_R), MAPE, RMSE, root relative squared error

(*RRSE*), true positive rate (*TPR*), false positive rate (*FPR*), F-measure (*F1*), Matthews's correlation coefficient (*MCC*), area under receiver operating characteristic (*ROC*) curve (*AUC*), and confusion matrix (*CM*), denoting the *True Class* as c^* and *Predicted Class* as $\hat{c}$. C_R indicates the efficacy of classifier to assign a correct vehicle class, where N is the number of classified vehicles and $\delta_n(\hat{c}_n)$ is a binary indicator function. *MAE* is a linear average of classification error magnitude. *RMSE* measures the distance from $\hat{c}$ to c^*. *RRSE* reports the relative amount a predicted class differs from itself. *TPR* indicates the number of vehicles correctly classified. *FPR* is an indicator of how many vehicles were classified incorrectly. *F1* measures harmonic mean of the precision or positive prediction value (*PPV*) and *FPR*. *MCC* is an important balanced measure of classification quality even if classes are imbalanced. *AUC* measures overall classifier quality. *CM* includes *True Classes* in rows and *Predicted Classes* in columns. *CM* diagonal shows the match between *true class* and *predicted class*; values outside the diagonal indicate a misclassification. *TPR*, *FPR*, *F1*, *MCC*, and *AUC* will be reported from this point as a weighted average score instead of per-class score.

Table 7-8 Performance metrics used to evaluate built classification models

Metric	Formula	
C_R	$C_R = \frac{1}{N}\sum_{n=1}^{N}\delta_n(\hat{c}_n)\,; \quad \delta_n(\hat{c}_n) = \begin{cases} 1, & \hat{c}_n = c_n^* \\ 0, & \hat{c}_n \neq c_n^* \end{cases}$	**Eq. 7-1**
MAPE	$MAE = \frac{1}{N}\sum_{n=1}^{N}\lvert\hat{c}_n - c_n^*\rvert$	**Eq. 7-2**
RMSE	$MSE = \sqrt{\frac{1}{N}\sum_{n=1}^{N}(\hat{c}_n - c_n^*)^2}$	**Eq. 7-3**

RRSE	$RSE = \sqrt{\frac{\sum_{n=1}^{N}(\hat{c}_n - c_n^*)^2}{\sum_{n=1}^{N}(\bar{c}_n - c_n^*)^2}}$	**Eq. 7-4**
TPR	$TPR = \frac{TP}{TP + FN}$	**Eq. 7-5**
FPR	$FPR = \frac{FP}{FP + TN}$	**Eq. 7-6**
F1	$F1 = 2\frac{\text{PPV}\times FPR}{\text{PPV} + FPR}; \quad PPV = \frac{TP}{TP + FP}$	**Eq. 7-7**
MCC	$MCC = \frac{(TP\times TN) - (FP\times FN)}{\sqrt{(TP + FP)(TP\times FN)(TN + FP)(TN\times FN)}}$	**Eq. 7-8**

Table 7-9 presents performance results of all classification methods applied on the proposed LBVC schemes using the MAG dataset. Notably, all classification methods showed comparable accuracy when correctly assigning vehicle to a class. Results can be attributed to parameter optimization (i.e., hyper-parameter optimization), which was conducted for each ML classification method. DT models were adopted primarily to identify length boundaries using a generated decision tree, primarily because it is quite easy to implement and it is very memory efficient. 3G-S_A slightly outperformed 3G-S_B, as the later had more overlap between group 1 and group 2. 3G-S_A provides a general distinction of long- and heavy-commercial vehicles from other small and medium vehicles. 3G-S_B, on the other hand, provides further distinction between PV, pickups, and SUVs in one group, and SU trucks and buses in another group. 4G-S_x provides an important distinction for motorcycles and outperforms 3G-S_B due to the fact that there is no overlap between group 1 and group 2.

Table 7-9 LBVC Schemes performance results for MAG Dataset

Criteria		Classification Method & Classification Scheme											
		DT			***k*-NN**			**C-SVM**			**NBC**		
		3G-S_A	**3G-S_B**	**4G-S_x**	**3G-S_A**	**3G-S_B**	**4G-S_x**	**3G-S_A**	**3G-S_B**	**4G-S_x**	**3G-S_A**	**3G-S_B**	**4G-S_x**
Average	**C_R**	99.82%	97.70%	97.69%	99.82%	97.80%	97.79%	99.83%	97.83%	97.78%	99.83%	97.59%	97.75%
	MAE	0.0022	0.0274	0.022	0.0021	0.0226	0.0171	0.0012	0.0145	0.0111	0.0025	0.022	0.0173
	RMSE	0.0342	0.1185	0.1057	0.0338	0.1082	0.0963	0.034	0.1202	0.1054	0.0323	0.117	0.0932
	RRSE	19.19%	54.07%	54.94%	18.94%	49.35%	50.08%	19.08%	54.84%	54.80%	18.12%	53.35%	48.47%
Weighted Average	**TPR**	0.998	0.977	0.977	0.998	0.978	0.978	0.998	0.978	0.978	0.998	0.976	0.977
	FPR	0.016	0.220	0.238	0.017	0.199	0.195	0.016	0.209	0.206	0.012	0.144	0.204
	PPV	0.998	0.973	0.974	0.998	0.975	0.975	0.998	0.975	0.974	0.998	0.975	0.974
	F1	0.998	0.973	0.971	0.998	0.975	0.975	0.998	0.975	0.974	0.998	0.975	0.974
	MCC	0.981	0.841	0.838	0.981	0.846	0.849	0.982	0.847	0.848	0.983	0.838	0.846
	AUC	0.997	0.912	0.864	0.999	0.967	0.963	0.991	0.885	0.886	0.999	0.987	0.987

Length boundaries (ɤ) found by DT models for all LBVC schemes are presented in Table 7-10 relative to corresponding FHWA Scheme F classes.

Table 7-10 Decision boundaries for proposed LBVC Schemes—unites are in meter

Group	3G-S_A		3G-S_B		4G-S_x	
	FHWA	**ɤ-MAG**	**FHWA**	**ɤ-MAG**	**FHWA**	**ɤ-MAG**
G1	F_1	0.7→2.984	F_1—F_3	0.7→10.971	F_1	0.7→2.984
G2	F_2—F_7	2.984→14.727	F_4—F_7	10.971→14.727	F_2—F_3	2.984→10.971
G3	F_8—F_{13}	>14.727	F_8—F_{13}	>14.727	F_4—F_7	10.971→14.727
G4	—	—	—	—	F_8—F_{13}	>14.727

One important observation from Table 6-18 is that MCC for 3G-S_B and 4G-S_x was slightly degraded in all classifiers. As stated earlier, MCC is a balance measure of statistical correlation between a true class and predicted class. A correlation coefficient of '+1' represents perfect agreement between prediction and observation; a '0' indicates nothing but random prediction; and '−1' indicates total disagreement between prediction and observation. Declining MCC value, notwithstanding extremely high classification rate, is attributed to class imbalance in the training set. CM for 3G-S_B illustrates 32.7% classification accuracy for group 2 compared to 99.75% classification accuracy for group 1 and 97.15% for group 3. The same can be seen in 4G-Sx CM. The primary problem with ML algorithms is that researchers try to maximize total classification accuracy while imbalanced class distributions increase sensitivity of ML algorithms towards overrepresented class [145].

Imbalanced data is very common in data analysis using machine learning. A powerful method to accommodate strongly imbalanced data is leveraging algorithms that combine boosting and data sampling, such as RUSBoost and SMOTEBoost [145]. SMOTEBoost (Synthetic Minority Oversampling Technique) works in direct contrast to

RUSBoost (Random Under-sampling). However, both techniques implement multiple learners to produce a more intelligent classifier. In this study, RUSBoost was investigated. This iterative method creates a model, examines instances misclassified, assigns more weight, under-samples the overrepresented class, and produces a revised model. After all iterations are complete, trained models vote on which class each observation should belong, and predicted outputs are based on a weighted majority.

Ninety-one percent classification accuracy was obtained when using the RUSBoost technique with 4G-S, as opposed to 97.7% classification accuracy using DT. MCC for RUSBoost was 0.93, showing a more balanced measure when compared to 0.83 with DT. A 0.9119 TPR and 0.0322 FPR were observed using RUSBoost. Figure 7-8 presents CM for RUSBoost using 4G-Sx dataset. Class 1 was correctly classified with 100% TPR. Although 91% of observations in class 2 where correctly classified, 30 observations were misclassified as class 1 and 894 observations where misclassified as class 3.

4GS/WMM RUSBoost		Predicted Class								
		C1	**C2**	**C3**	**C4**	**FNR**	**TPR**	**Total**	**FNR**	**TPR**
Ture Class	**C1**	**23**	0	0	0	0	**23**	23	**0%**	**100%**
	C2	30	**9149**	894	0	879	**9149**	10073	**9%**	**91%**
	C3	0	46	**248**	5	51	**165**	299	**17%**	**83%**
	C4	0	0	7	**531**	7	**531**	538	**1%**	**99%**

Figure 7-8 Confusion Matrix for RUSBoost using 4G-S/MAG dataset

Classification error for class 3 dropped to 17% compared to 74% using DT, indicating a classification balance between groups. However, this method is computationally inefficient, requiring10 learners, each composed of a decision tree with 11 split to implement the intelligent classifier. Thus, probabilistic modeling is proposed to empirically achieve optimal solutions, as presented in the next section.

The fact that vehicle class distributions are imbalanced is not unique to Oklahoma, where more than 97% of vehicles belong to classes 2, 3, 5, 6, 8, and 9, as seen in our vehicle data collection (See Figure 7-9) and in another dataset collected over three months from IDL. Similar results can be found in [12], [43], [53], [59], [146]–[150], although none considers this fact and most studies reported classification rate only as an overall measure of classifier performance.

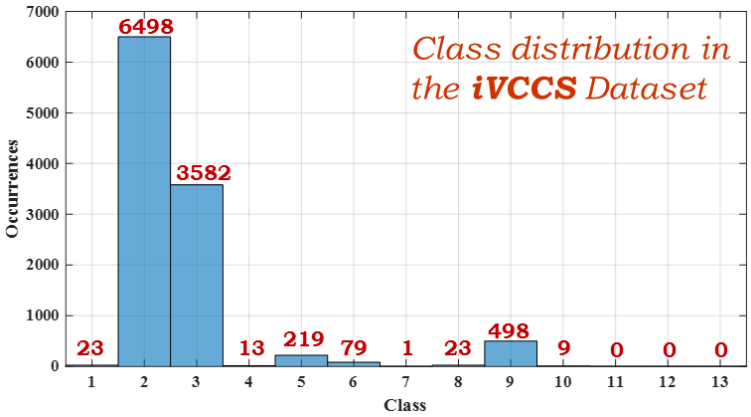


Figure 7-9 Class distribution in Dataset collected using MAG

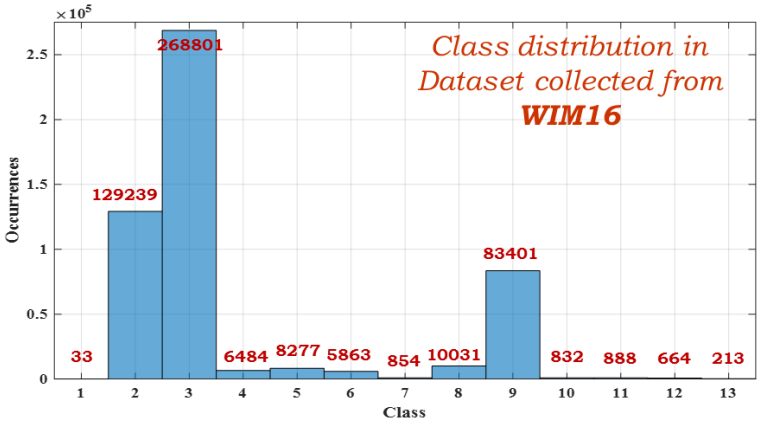


Figure 7-10 Class distribution in Dataset collected from IDL

7.3.1.4 LBVC Model using Probabilistic Modeling

Separating two neighboring classes from each other can be treated as a binary problem. As such, probabilistic models can be employed to empirically determine optimal boundary decisions to separate neighboring classes whose vehicles have

overlapping lengths [151]. These methods can be implemented in real-time, require no training sets, and improve classification accuracy by minimizing classification errors. This section describes the implementation of probabilistic models and optimization theory.

Let x be the vehicle magnetic length, and C_1 and C_2 represent two vehicle classes. The probability of error between two distributions, as shown in Figure 7-11, include $P(C_1|C_2)$ and $P(C_2|C_1)$, given in Eq. 7-9 and representing probability of error for classifying C_2 as C_1 and C_1 as C_2.

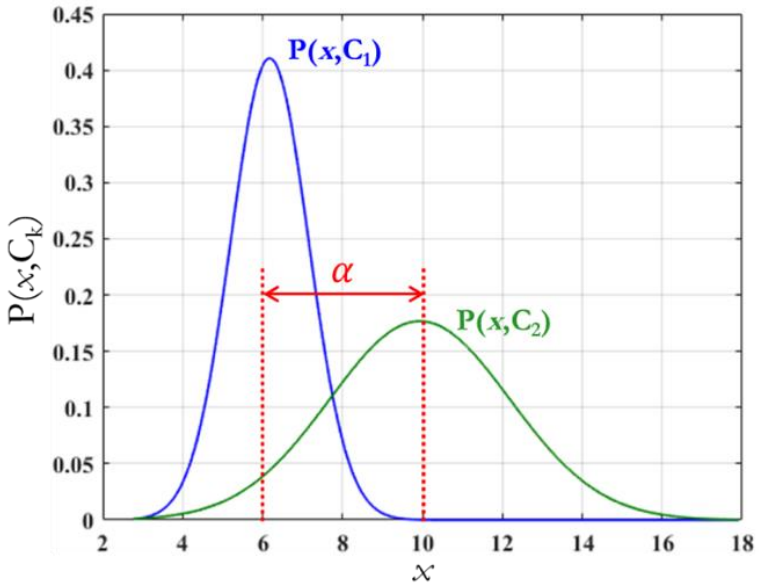


Figure 7-11 Two overlapped Gaussian distributions with an unknown decision threshold α

$$P(error) = \int_{-\infty}^{\alpha} P(x|C_2)P(C_1)dx + \int_{\alpha}^{+\infty} P(x|C_1)P(C_2)dx \qquad \textbf{Eq. 7-9}$$

Distributions $P(x, C_1)$ and $P(x, C_2)$, shown in Figure 7-11, statistically describe random variable, x, corresponding to VML for vehicles traveling on Oklahoma roadways. In accordance with central limit theorem and law of large numbers, these

distributions can be approximated as Gaussian distribution models, per Eq. 7-10, Eq. 7-11, and Eq. 7-12, where *k* is the class number.

$$X_k \propto \mathcal{N}\left(\mu_{C_k}, \sigma_{C_k}\right) \rightarrow \; p\left(x|\mu_{C_k}, \sigma_{C_k}\right) = \frac{1}{\sigma_{C_k}\sqrt{2\pi}} e^{-\frac{\left(x-\mu_{C_k}\right)^2}{2\sigma_{C_k}^2}} \qquad \textbf{Eq. 7-10}$$

$$\mu_{C_k} = \frac{1}{n}\sum_{i=1}^{n} x_i \;\; , \;\; \sigma_{C_k} = \sqrt{\frac{1}{n}\sum\nolimits_{i=1}^{n}\left(x_i - \mu_{C_k}\right)^2} \qquad \textbf{Eq. 7-11}$$

$$P(error) = P(C_1)\int_{-\infty}^{\alpha_T} \frac{1}{\sigma_{C2}\sqrt{2\pi}} e^{-\frac{(x-\mu_{C2})^2}{2\sigma_{C2}^2}}.dx + P(C_2)\int_{\alpha_T}^{+\infty} \frac{1}{\sigma_{C1}\sqrt{2\pi}} e^{-\frac{(x-\mu_{C1})^2}{2\sigma_{C1}^2}}.dx \qquad \textbf{Eq. 7-12}$$

The integration of a probability distribution function (PDF) is a cumulative distribution function (CDF) represented by the error function *erf*, as given in Eq. 7-13.

$$P(error) = P(C_1)\frac{1}{2}\left[1 + erf\left\{\frac{\alpha_T - \mu_{C2}}{\sigma_{C2}\sqrt{2}}\right\}\right] + P(C_2)\left(1 - \left(\frac{1}{2}\left[1 + erf\left\{\frac{\alpha_T - \mu_{C1}}{\sigma_{C1}\sqrt{2}}\right\}\right]\right)\right) \qquad \textbf{Eq. 7-13}$$

Optimal threshold α_T can be empirically found by taking the derivative of Eq. 7-13 and equating the outcome to 0, as presented in Eq. 7-14.

To ensure classification error will not change at various times when new values are added to either group—as not all groups have the same number of vehicle instances per unit of time—weights, $P(C_1)$ and $P(C_2)$, that are proportional to the number of instances in each class group are calculated, as in Eq. 7-15. It is worth mentioning that

optimal threshold found empirically by solving Eq. 7-14 is global minima, which can be verified using the second derivative test, as in Eq. 7-16, such that $\alpha_T > 0$.

$$\frac{dP(error)}{d\alpha_T} = 0 \rightarrow \frac{P(C_1)}{\sigma_{C2}\sqrt{2\pi}} e^{-\frac{(\alpha_T-\mu_{C2})^2}{2\sigma_{C2}^2}} - \frac{P(C_2)}{\sigma_{C1}\sqrt{2\pi}} e^{-\frac{(\alpha_T-\mu_{C1})^2}{2\sigma_{C1}^2}} = 0 \qquad \textbf{Eq. 7-14}$$

$$P(C_1) = \frac{Length(C_1)}{Length(C_1 + C_2)} \quad ; \quad P(C_2) = \frac{Length(C_2)}{Length(C_1 + C_2)} \qquad \textbf{Eq. 7-15}$$

$$\frac{d2P(error)}{d\alpha_T^2} = 0$$

$$\rightarrow P(C_1)\frac{(\mu_{C2} - \alpha_T)}{\sigma_{C2}^3\sqrt{2\pi}} e^{-\frac{(\alpha_T-\mu_{C2})^2}{2\sigma_{C2}^2}} \qquad \textbf{Eq. 7-16}$$

$$- P(C_2)\frac{(\mu_{C1} - \alpha_T)}{\sigma_{C1}^3\sqrt{2\pi}} e^{-\frac{(\alpha_T-\mu_{C1})^2}{2\sigma_{C1}^2}} = 0$$

The α_E uses equal weights ($P(C_1) = P(C_2)$) but implements a classification error minimization algorithm among groups. In other words, α_E is found by solving Eq. 7-17 such that probability of error for C_1 classified as C_2 is equal to probability of error for C_2 classified as C_1; ε is a precision value (e.g., 0.001). Equating classification errors would result in a decreased classification error for one particular group (i.e., the one with fewer instances), but will increase classification error for the second group (i.e., the one with more instances), and, hence, increase overall system classification error.

$$P(\alpha_E, C_1) - P(\alpha_E, C_2) \leq \varepsilon \qquad \textbf{Eq. 7-17}$$

Developed models can now be applied on all overlapping problematic LBVC schemes (e.g., 4G-S_x and 3G-S_B) that have imbalanced data, as well as high overlap ratio among neighboring groups.

1) Decision Boundaries for 3G-S_B:

Figure 7-12 shows the fitted Gaussian distribution models and found decision thresholds for MAG 3G-S_B dataset. Misclassification occurs between problematic groups G1 and G2, as high overlapping is observed.

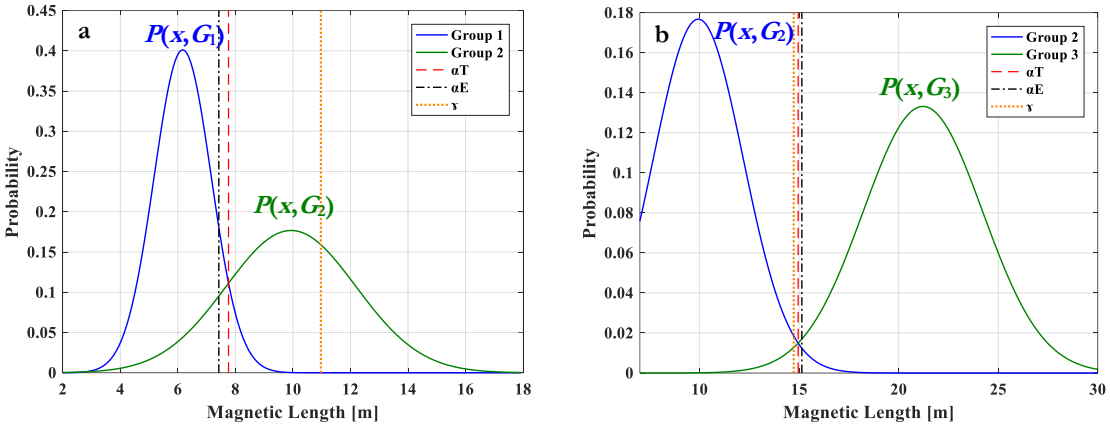


Figure 7-12 Gaussian distribution models and decision thresholds for the MAG *3G-S_B* dataset

Table 7-11 presents a comparison between decision boundaries found by various proposed thresholding methods for *3G-S_B* dataset. Corresponding classification rates in each group (i.e., how many where correctly classified as G_X out of the total number of instances in G_X) and classification errors between groups (i.e., how many were incorrectly classified out of the total number of instances in both groups) for pairwise overlapped groups are shown in Table 7-12. Table 7-13 presents a comparison between classification rates for different thresholding schemes applied onto the 3G-S_B dataset.

Decision threshold γ, found using ML methods, was 10.97m, which maximizes total classification accuracy at the expense of misclassifying more instances in G2. Optimal threshold for achieving balance among groups—regardless of instances in each group, α_T—was set at 7.76m, which significantly reduces G2 misclassification error at the expense of decreasing accurate classification rate for G1. See Table 11 ($C_{R\text{-}G1\text{-}vs\text{-}G2}$). Because the number of instances in G_1 is considerably larger than G_2 (See Figure 7-2),

overall classification accuracy was decreased (See Table 7-13). Optimal threshold for equal error among overlapping groups' scenario α_E was 7.43m, which rendered an equal classification rate $C_{R\text{-}G1\text{-}vs\text{-}G2}$ at the expense of reducing overall classification accuracy to 90.2314%, compared to 99.70% and 93.8077% for γ and α_T, respectively. For classification rates between G2 and G3 ($C_{R\text{-}G2\text{-}vs\text{-}G3}$), all scenarios achieved comparable performance primarily because a minimum overlapping could be observed.

Table 7-11 Decision boundaries found by different thresholding methods for 3G-S_B

		3G-S_B MAG		
Group	**FHWA-S_F**	γ	α_T	α_E
G1	F_1—F_3	0.81→10.971m	0.81→7.761m	0.81→7.4286m
G2	F_4—F_7	10.971→14.727m	7.761→14.9504m	7.427→15.136m
G3	F_8—F_{13}	>14.727m	>14.9504m	>15.136m

Table 7-12 Pairwise classification rates and errors for different decision boundaries applied on 3G-S_B dataset

	3G-S_B MAG	
Threshold	**$C_{R\text{-}G1\text{-}vs\text{-}G2}$ /C_{Err} (%)**	**$C_{R\text{-}G2\text{-}vs\text{-}G3}$ /C_{Err} (%)**
γ	99.9109 vs. 29.8077 / 2.1906	96.7949 vs. 98.6667 / 2.0311
α_T	93.9778 vs. 83.9744 / 6.3221	97.1154 vs. 98.0952 / 2.2700
α_E	89.9366 vs. 90.0641 / 10.059	97.4359 vs. 97.5238 / 2.5090

Table 7-13 Comparison between classification rates by different thresholding methods for 3G-S_B LBVC

		3G-S_B MAG		
Group	**FHWA-S_F**	γ	α_T	α_E
G1	F_1—F_3	99.70%	93.9778%	89.9366%
G2	F_4—F_7	32.70%	81.0897%	87.5000%
G3	F_8—F_{13}	97.10%	98.0952%	97.5238%
Overall C_R		**97.70%**	**93.8077%**	**90.2314%**

2) Decision Boundaries for 4G-Sx:

Figure 7-13 illustrates fitted Gaussian distribution models and decision thresholds for MAG 4G-S_x dataset.

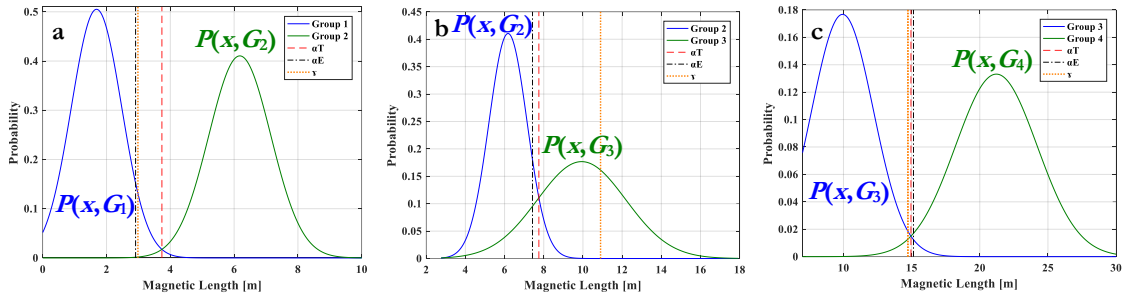


Figure 7-13 Gaussian distribution models and decision thresholds for the MAG *4G-S_x* dataset

Problematic groups in *4G-S_x* are G2 and G3, which have more significant overlap in MAG dataset when compared to IDL dataset, as seen in Figure 7-13/b. Table 7-14 presents a comparison between decision boundaries determined by various proposed thresholding methods for MAG and IDL *4G-S_x* datasets.

Table 7-15 presents the corresponding classification rates and errors for pairwise overlapping groups. A comparison between classification rates for various thresholding methods applied on the 4G-S_x dataset is presented in Table 7-16.

Table 7-14 Decision boundaries found by different thresholding methods for 4G-S_x

		4G-S_x MAG		
Group	**FHWA-S_F**	**γ**	**α_T**	**α_E**
G1	F_1	0.7→2.984m	0.7→3.736m	0.7→2.9107m
G2	F_2—F_3	2.984→10.971m	3.736→7.7516m	2.912→7.427m
G3	F_4—F_7	10.971→14.727m	7.7516→14.95m	7.427→15.136m
G4	F_8—F_{13}	>14.727m	>14.95m	>15.136m

Table 7-15 Pairwise classification rates and errors for different decision boundaries applied on 4G-S_x

	4G-S_x MAG		
Threshold	**$C_{R\text{-}G1\text{-}vs\text{-}G2}$ /C_{Err} (%)**	**$C_{R\text{-}G2\text{-}vs\text{-}G3}$ /C_{Err} (%)**	**$C_{R\text{-}G3\text{-}vs\text{-}G4}$ /C_{Err} (%)**
γ	100 vs. 99.98 / 0.0198	99.91 vs. 29.81 / 2.196	96.79 vs. 98.67 / 2.031
α_T	100 vs. 99.69 / 0.307	93.86 vs. 84.29 / 6.423	97.115 vs. 98.09 / 2.27
α_E	100 vs. 99.99 / 0.0099	89.90 vs. 90.06 / 10.09	97.44 vs. 97.52 / 2.509

Table 7-16 Comparison between classification rates by different thresholding methods for 4G-S_x

		4G-S_x MAG		
Group	**FHWA-S_F**	γ	α_T	α_E
G1	F_1	91.30%	100%	100%
G2	F_2—F_3	99.90%	93.557%	89.8938%
G3	F_4—F_7	26.30%	81.4103%	87.5%
G4	F_8—F_{13}	98.70%	98.0952%	97.5238%
Overall C_R		**97.6951%**	**93.4419%**	**90.2131%**

For G1 and G2, an insignificant overlapping rendered comparable high rates for all thresholding methods. However, G2 and G3 demonstrated a significant overlap, as G3 included SU (e.g., class 5), which are highly overlapped in length with class 3 included in G2. ML methods set γ at a value that maximizes total classification accuracy at the expense of misclassifying most instances in the other groups (G3 classification error 73.7%) because the number of instances in G_2 is considerably larger than G_3. Classification error for G3 was significantly reduced to 18.5897% when using α_T. However, overall classification accuracy was decreased. Classification rate for G3 improved when using α_E to achieve balanced classification rates among all groups (See

Table 7-15) at the expense of reducing overall classification accuracy to 90.2131% when compared with 97.6951% and 93.4419% for γ and α_T, respectively. All scenarios achieved comparable classification performance for G3 and G4, as a minimum overlapping can be observed. Also, number of data points in both groups is relatively comparable.

7.3.1.5 Discussion on LBVC Models

A comparison between LBVC scheme boundaries developed for MAG in this study and in alternative schemes based on IDL data developed by various states throughout the U.S. can be seen in Figure 7-14 and Figure 7-15. Observations include the following:

- → Vehicle length boundaries detected in a number of states throughout the U.S. vary because vehicle and traffic characteristics differ per road type, region, state, and other factors; hence, LBVC boundaries developed in one state might require adjustment to remain applicable in another.
- → Boundaries defined for MAG detectors are longer in length than those detected by IDL detectors; this is primarily due to the fact that MAG estimate VML, which is longer than the physical length (See Figure 7-14 and Figure 7-15).
- → Defining an accurate detection zone for MAG is challenging, as disturbance to the Earth's magnetic field depends upon detection; this is proportional to vehicle length, height of vehicle chasse above ground, and vehicle structure composition of ferrous materials.
- → Analyses demonstrated the importance of investigating not only the classification rate for evaluating classification models, but also other

performance metrics (e.g., CM and MCC) for identifying bias in the model as a result of imbalanced class distributions; this increases sensitivity of ML algorithms toward overrepresented classes.

→ Three algorithms developed for identifying length boundaries for LBVC schemes resulted in three very different sets of thresholds (γ, α_T, and α_E): 1) γ maximizes classification accuracy at the expense of minority classes; 2) α_T achieves balance among overlapped groups regardless of number of instances in each group; and 3) α_E tries to equate classification error between two overlapped groups despite group population size. The question remains as to which algorithm is suitable. The answer depends exclusively on the objective of the LBVC system. If traffic engineers are more concerned with vehicles in higher classes (i.e., trucks that are generally highly underrepresented), then it is important to utilize a method that achieves balance among classes (i.e., α_T). However, if classification accuracy is paramount regardless of classification rate per group, then γ method would be suitable. For balanced classification error among groups, α_E should be implemented.

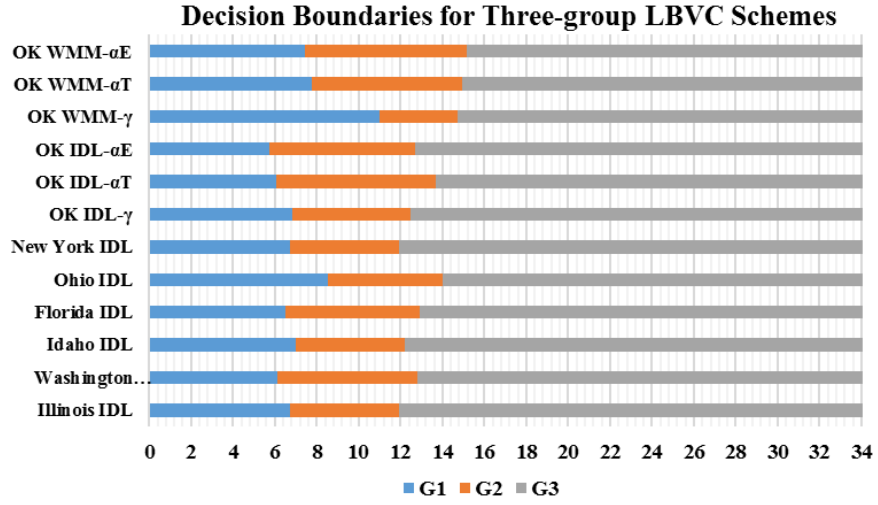


Figure 7-14 Decision boundaries for *3G-S_B* LBVC for several states

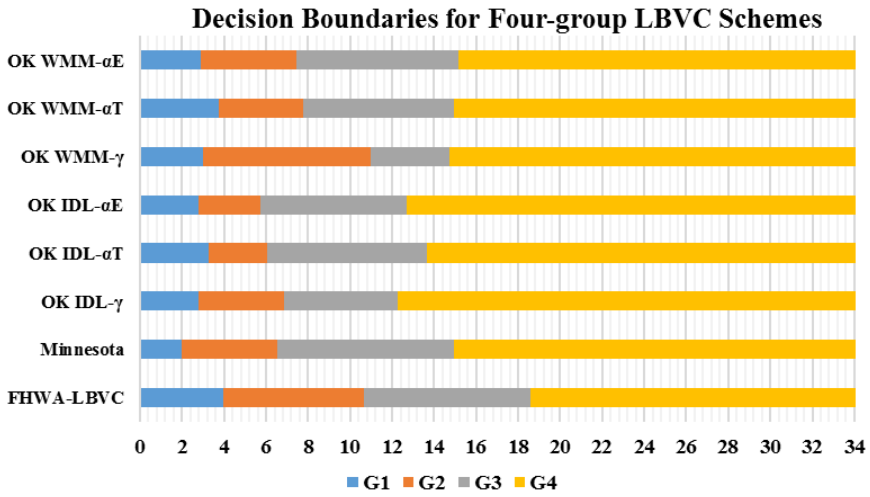


Figure 7-15 Decision boundaries for *4G-S_x* LBVC for several states

7.4 Introduction to Vehicle Re-Identification and Travel Time Estimation

Vehicle re-identification provides important information about link Travel Time (TT) distribution between two detection points (i.e., origin and destination) of an individual path. TT is a reciprocal of average speed and can be defined as a measure of traffic congestion between two points on a road segment. TT has been identified as a time-based performance measure of transportation quality and level of service. This information is highly beneficial for travelers, operations, and Traffic Management Centers (TMC). TMC uses TT for traffic prediction and analyses. Accurate and reliable TT information can aid in reducing congestion, improving safety, and enhancing traffic flow (e.g., informing commuters to avoid congested roadways, assisting transportation agencies to optimize traffic planning).

Measuring TT requires speed estimation and vehicle re-identification. Several technologies have been used by transportation agencies to estimate TT. These include Bluetooth and Wi-Fi identification detection, toll tag reader, in-pavement magnetic detectors, automatic license plate reader, machine vision, radar equipment, inductive

loops, crowdsourcing, and cell phone signal monitoring. A detailed description of these technologies and best practices for TT implementation and data collection can be found in [152][153]. A comprehensive study for evaluating various TT estimation technologies was reported in [154]. The study showed that TT estimation accuracy depends heavily on the average penetration rate. Each TT technology was shown to have advantages and disadvantages (e.g. accuracy, coverage, cost, portability, and other factors) that should be considered when designing a scheme to evaluate technology reliability. Final conclusions indicated that the most overall reliable TT estimation can be achieved by employing multi-sensor technologies.

A limited number of publications focus on vehicle re-identification using MAG. Most investigations implement re-identification algorithms based on multi-sensor array. This technology is used to overcome the degradation in re-identification rate due to change of vehicle orientation or speed between the two detection points. The most notable work centered on TT was proposed by the University of California, Berkeley [155], [156] Researchers matched vehicle magnetic signatures obtained from an array of seven wireless magnetic sensors positioned perpendicular to the road lane. A dynamic-time warping algorithm (DTW) was used to calculate the distance between VMS obtained from the sensor array at upstream point with another sensor array downstream. Minimum distance was selected and compared to a threshold statistically determined individually for each location (i.e., mean and standard deviation serve as functions of algorithm parameters that must be determined beforehand for each site, primarily because traffic characteristics vary from place to place). The test was conducted on a road with a 0.9-mile distance between the two points. A 64~74% matching rate, 15%

mismatching rate in free flow, and 20~60% mismatching rate during congestion was found. A vehicle re-identification algorithm based on multi-sensor correlation was also proposed in [157]. The correlation of signatures from multiple sensor nodes was calculated, and a maximum likelihood estimation was applied to fuse data from multiple sensors to correct errors due to vehicle trajectory or speed change. A 77.6% to 92.8% re-identification rate was reported. In [158], Euclidean distances between VMS collected using several three-axis magnetic sensors at a sampling rate of 200Hz was implemented from vehicle re-identification. Ten sensors were fixed on a 0.6m wide plastic plate in the lane center. The algorithm was tested on only 25 vehicles. A 90~100% re-identification rate was reported.

7.5 Development of Vehicle Re-Identification Algorithm using MAG

Vehicle re-identification provides realization on the link TT distribution, $TT_{link} = \{TT_1, TT_2, \dots, TT_n\}$, between two detection points (i.e., original and destination) of an individual path. TT of a vehicle *i* between two detection points, namely Upstream (u) and Downstream (d), can be simply found using Eq. 7-18, where T_A and T_D are the time of arrival and departure, respectively. Total and average TT for *n* vehicles traveled over link segment *s* within time window W_t is given by Eq. 7-19 and Eq. 7-20, respectively.

$$TT_{(i)} = T_A^d(i) - T_A^u(i) = T_D^d(i) - T_A^u(i) \quad \textbf{Eq. 7-18}$$

$$TT_{total} = \sum_{k=1}^{n} \left(T_A^d(k) - T_A^u(k)\right) \quad \textbf{Eq. 7-19}$$

$$TT_{avg} = \frac{\sum_{k=1}^{n} \left(T_A^d(k) - T_A^u(k)\right)}{n} \quad \textbf{Eq. 7-20}$$

Vehicle re-identification using MAG is dependent upon matching an individual vehicle signature at two detection points. In this work, two models were developed, namely, *Thresholding* and *Majority Voting*, for vehicle re-identification based on matching VMS from a single MAG.

Vehicle re-identification in both models involves three high-level steps, each consisting of several low-level steps. The first high-level step is VMS processing, which includes time coding, signal smoothing, magnitude computation, signal windowing, and amplitude normalization. The second step includes unique features extraction. The third step is the matching process, where unique features being extracted from a VMS at the downstream node is compared to a buffer of unique features for vehicles detected at the upstream node. Both upstream and downstream nodes are globally synchronized to the same reference clock (i.e., GPS).

7.5.1 Vehicle Magnetic Signature Processing

Vehicle Magnetic Signature Processing will apply on VMS collected at both detection points. The magnetic signature for each vehicle $S_{V_n}^{(B^\gamma)} : \{ k_{T_A^{(N_i)}}, \dots, k_{T_D^{(N_i)}} \}$ is simply extracted by means of arrival and departure times at each detection point, where V_n is vehicle number; B^γ is geomagnetic flux magnitude sampled using MAG in three axles—$\gamma = \{x, y, z\} \in \mathbb{R}^3$; and k is number of samples in VMS at detection node N_i.

Observing vehicle signatures revealed that moments of vehicle arrival and departure create transient state in the signal, which appear as small peaks that cause a larger feature set and could possibly degrade re-identification algorithm performance. A windowing is applied to remove transient state samples from the right and left tails of the signal, which represents 10msec of the signal at each tail.

MAG was configured to run at 400Hz sampling rate, resulting in a significant fluctuation in VMS. For a more consistent signal, it is highly recommended to apply a smoothing algorithm on the signal using MAF, as in Eq. 7-21, to filter out fast signal fluctuations that are not necessary for vehicle re-identification processes. *M* is the total number of samples in a VMS. Using eight-point MAF was empirically found to be the suitable setting for signal sampled at 400Hz. The smoothing algorithm has a significant impact on feature extraction algorithm performance, hence, re-identification accuracy. Once the signal is smoothed, signal magnitude F_M is computed using Eq. 4-5.

$$S_{V_nFiltered}^{(B^\gamma)} = \frac{1}{M}\sum_{i=0}^{M-1} S_{V_N}^{(B^\gamma)}(k-i)\,; \quad \gamma = \{x, y, z\} \in \mathbb{R}^3 \qquad \textbf{Eq. 7-21}$$

Because vehicle trajectory might not be identical at the two detection points, the summation ($\boldsymbol{H}_{V_n}$), difference ($\boldsymbol{I}_{V_n}$), and ratio ($\boldsymbol{R}_{V_n}$) of $S_{V_n}^{(B^x)}, as\ well\ as\ S_{V_n}^{(B^y)}$ were also calculated in this step (See Eq. 7-22). As stated in Chapter 5, MAG sensor *x-axis* was alongside traffic direction; *y-axis* was perpendicular to traffic lane; and *z-axis* was perpendicular to the ground pointing upward in all field test setups. Recalling "*1.5.1 Magnetometer Sensor Theory of Operation*" in Chapter 1, $\boldsymbol{B}_\gamma$ vector is described using seven components in the field coordinate plane (See Figure 1-2). Horizontal intensity ***H*** is the magnitude of B^x and B^y. The ratio of B^x and B^yrepresents magnetic variation between Geographic North and horizontal intensity. Considering these components can solve the problem of changing vehicle trajectory between points to a certain level (e.g., relatively small change and MAG is not captured near the wheels).

$$\begin{aligned} \boldsymbol{H}_{V_nFiltered} &= S_{V_n}^{(B^x)} + S_{V_n}^{(B^y)} \\ \boldsymbol{L}_{V_nFiltered} &= S_{V_n}^{(B^x)} - S_{V_n}^{(B^y)} \end{aligned} \qquad \textbf{Eq. 7-22}$$

$$\boldsymbol{R}_{V_nFiltered} = S_{V_n}^{(B^y)} / S_{V_n}^{(B^x)}$$

Next, amplitude normalization is performed to individually rescale each signal, including the magnitude F_M, by the range of its elements prior to further calculations. $S_{V_n}^{(F_M)}$ was rescaled between [0, 1], as in Eq. 7-23, and signals $S_{V_n}^{(B^x)}$, $S_{V_n}^{(B^x)}$, $S_{V_n}^{(B^x)}$, H_{V_n}, L_{V_n}, and R_{V_n} were rescaled between [-1, +1], as in Eq. 7-24.

$$S_{V_nNormalized}^{(F_M)} = \frac{S_{V_nFiltered}^{(F_M)} - \min\left(S_{V_nFiltered}^{(F_M)}\right)}{\max\left(S_{V_nFiltered}^{(F_M)}\right) - \min\left(S_{V_nFiltered}^{(F_M)}\right)} \qquad \textbf{Eq. 7-23}$$

$$S_{V_nNormalized}^{(B^Y)} = -1 + 2\frac{S_{V_nFiltered}^{(B^Y)} - min\left(S_{V_nFiltered}^{(B^Y)}\right)}{max\left(S_{V_nFiltered}^{(B^Y)}\right) - min\left(S_{V_nFiltered}^{(B^Y)}\right)} \qquad \textbf{Eq. 7-24}$$

The result is seven normalized signals for each vehicle at each detection point (P), as in Eq. 7-25, where (N) is either the upstream (u) or downstream (d) detection node; X_{V_n}, Y_{V_n}, and Z_{V_n} is the normalized vector of measurements for a vehicle *Vn* on *x*-axis, *y*-axis, and *z*-axis, respectively; and $F_{M_{V_n}}$ is the normalized vector of magnitude values. $S_{V_n}^{(B^Y)}$ and $S_{V_n}^{(F_M)}$ are illustrated in Figure 7-16 and Figure 7-17, respectively; (a) raw signal, (b) signals after smoothing, and (c) signals after normalization. $H_{V_n}^{(N)}$, $L_{V_n}^{(N)}$, and $R_{V_n}^{(N)}$ are depicted in Figure 7-18.

$$\begin{aligned} X_{V_n}^{(N)} &= \{x_i\}_{i=1}^{k} \\ Y_{V_n}^{(N)} &= \{y_i\}_{i=1}^{k} \\ Z_{V_n}^{(N)} &= \{z_i\}_{i=1}^{k} \\ H_{V_n}^{(N)} &= \{h_i\}_{i=1}^{k} \\ L_{V_n}^{(N)} &= \{l_i\}_{i=1}^{k} \\ R_{V_n}^{(N)} &= \{r_i\}_{i=1}^{k} \end{aligned} \qquad \textbf{Eq. 7-25}$$

$$F_{M_{V_n}}^{(N)} = \{F_{Mi}\}_{i=1}^{k}$$

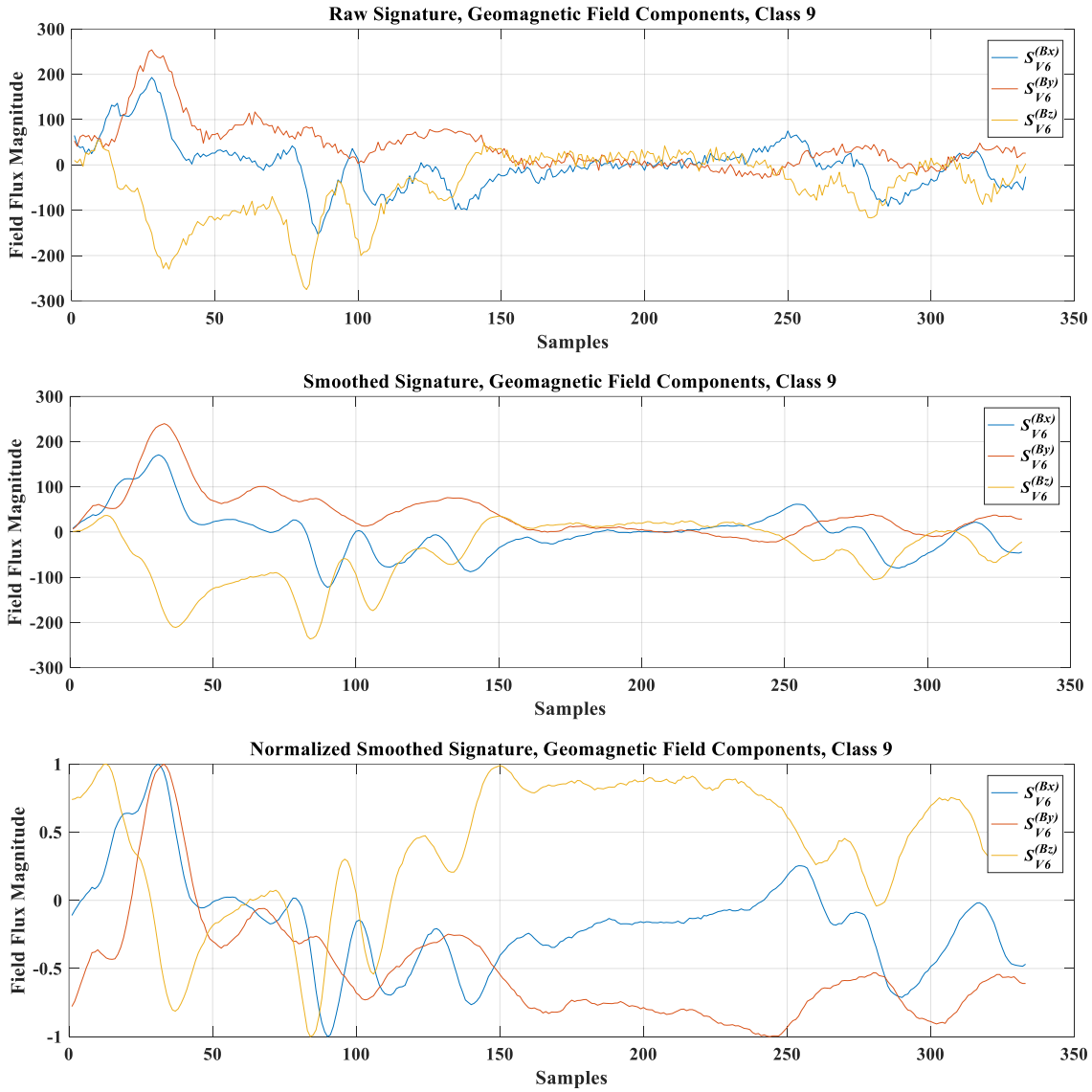
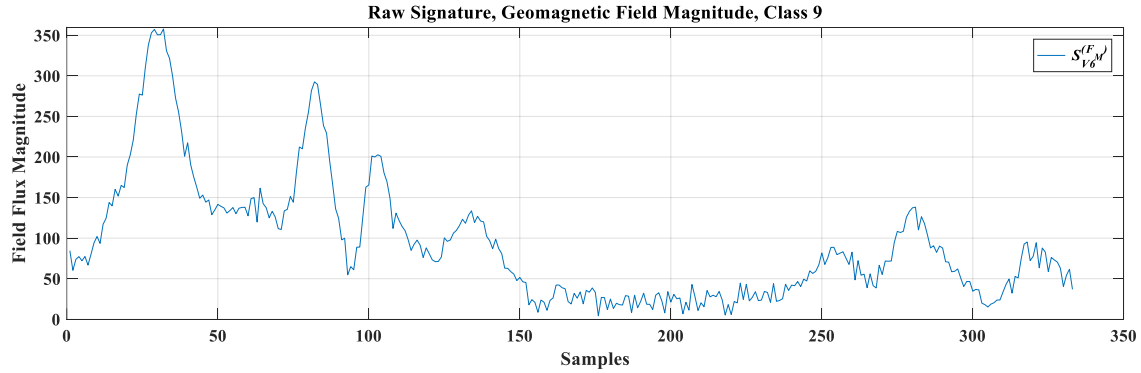


Figure 7-16 VMS components before and after smoothing and normalization



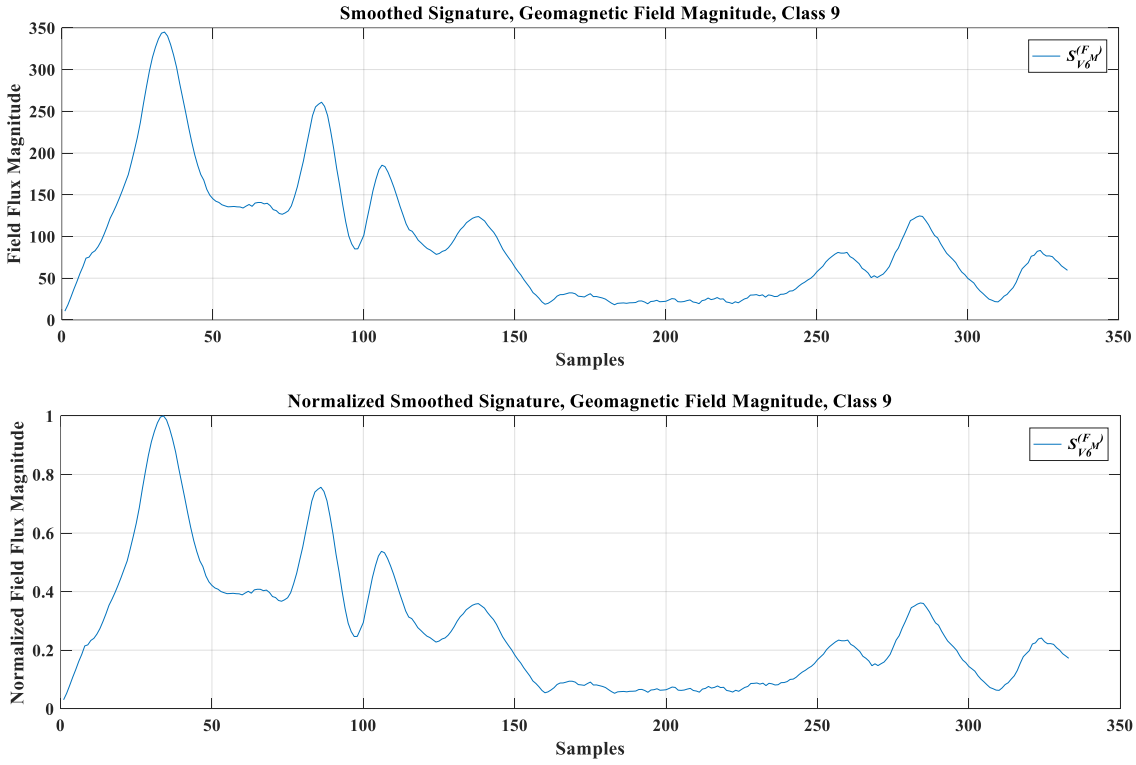


Figure 7-17 VMS magnitude before and after smoothing and normalization

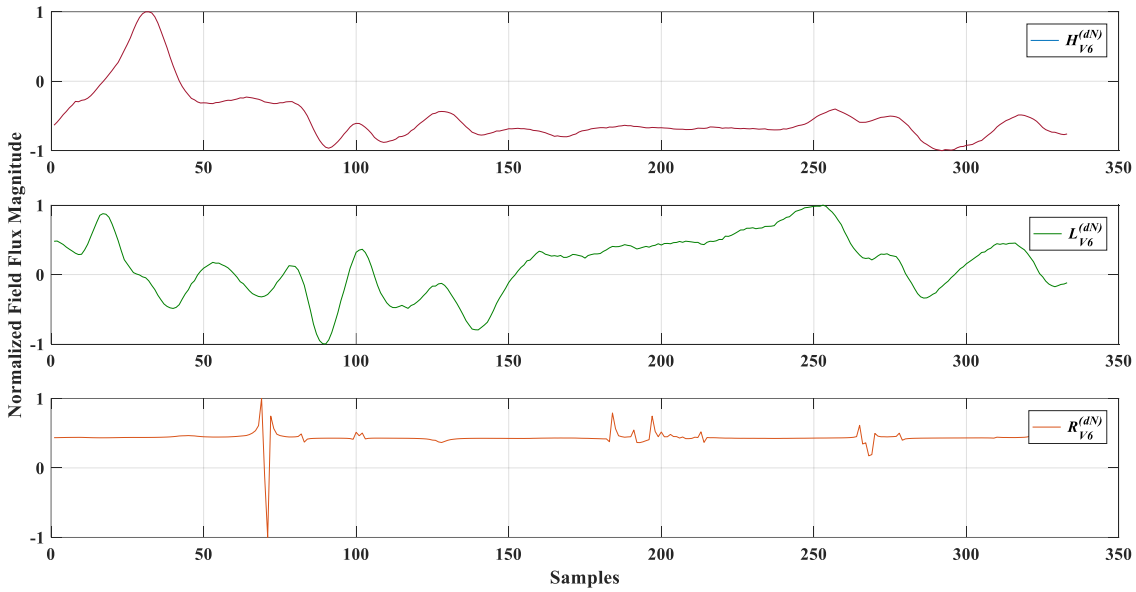


Figure 7-18 VMS different combinations of B^x and B^y.

7.5.2 Features Extraction & Data Transformation

Vehicle magnetic signature (VMS) can be represented as a time series. Over the last decades, a variety of algorithms have been proposed in literature for time series

segmentation or representation. For example, authors in [159] used Perceptually Important Points (PIP) to dynamically segment the price time series into subsequences and then identify similar historical subsequences using Dynamic Time Warping (DTW). The PIP process was first introduced and used for pattern matching of in financial applications [160]. Piecewise Linear Representation (PLR) is another technique that is widely used as an approximation of a time series (e.g., Electrocardiogram time series). An extensive review and empirical comparison of several techniques for segmenting time series can be reviewed in [160], [161].

In this work, PIP was used as data transformation to reduce the dimension of VMS by preserving the salient points for each signal in Eq. 7-25. The extracted salient points maintain the unique characteristics of signal while reducing the amount of data to be processed or transferred from the sensor node to *i*AP.

To find PIP for a VMS, each point is compared with neighboring points. Given a normalized signal $S_{V_n}^{(N)}$, which includes *k* sample point, we can say that $S_{V_n}^{(N)}[k]$ is a peak if its neighboring points within a moving window *w* at y-axle are smaller than its value. $S_{V_n}^{(N)}[k]$ is a valley if its neighboring points are larger than its value. The algorithm also includes the first and last points of the VMS. The generated features vector $EV[i]$ includes the value of each PIP point (*i*), which represents variations in *y* coordinate. The *w* value can be calculated using Eq. 7-27, where *a* is a coefficient that was found experimentally.

$$EV = \begin{cases} peak, & S_{V_n}^{(N)}[k-w] < S_{V_n}^{(N)}[k] > S_{V_n}^{(N)}[k+w] \\ valley, & S_{V_n}^{(N)}[k-w] > S_{V_n}^{(N)}[k] < S_{V_n}^{(N)}[k+w] \end{cases} \quad \textbf{Eq. 7-26}$$

$$w = \frac{a}{\max\left(S_{V_n}^{(N)}\right) - \min\left(S_{V_n}^{(N)}\right)}; \qquad a = 6 \qquad \textbf{Eq. 7-27}$$

The difference between consecutive PIP points, which represents variations in *x* coordinate, was also taken into consideration to improve vehicle re-identification accuracy in the event that signal amplitude is different at the two detection points (i.e., vehicle trajectory changed). Doing so eliminates the need for deploying more sensors laterally, as proposed [155], [157], [158]. Spacing difference vector (*TS*) between PIP points was calculated by taking the difference between PIP point indices.

Finally, Piecewise Linear Representation (PL) of the PIP points was found. PL consists of slope values in [0, 1], which represent the linear relationship between amplitude and spacing between PIP points.

The result of this step is three sets of features (i.e., $EV[i]$, $TS[i]$, and $PL[i]$), each consisting of seven vectors (See Eq. 7-25), as in Eq. 7-28. The sets are computed for each vehicle (V_n) at each detection point (N). Figure 7-19 and Figure 7-20 depict the PIP points, spacing, and PL extracted from magnitude and geomagnetic field components for a class 9 vehicle.

$$\begin{aligned} EV_{V_n}^{(N)} &= \left\{EV\left(X_{V_n}^{(N)}\right), EV\left(Y_{V_n}^{(N)}\right), EV\left(Z_{V_n}^{(N)}\right), EV\left(F_{V_n}^{(N)}\right), EV\left(H_{V_n}^{(N)}\right), EV\left(L_{V_n}^{(N)}\right), EV\left(R_{V_n}^{(N)}\right)\right\} \\ TS_{V_n}^{(N)} &= \left\{TS\left(X_{V_n}^{(N)}\right), TS\left(Y_{V_n}^{(N)}\right), TS\left(Z_{V_n}^{(N)}\right), TS\left(F_{V_n}^{(N)}\right), TS\left(H_{V_n}^{(N)}\right), TS\left(L_{V_n}^{(N)}\right), TS\left(R_{V_n}^{(N)}\right)\right\} \\ PL_{V_n}^{(N)} &= \left\{PL\left(X_{V_n}^{(N)}\right), PL\left(Y_{V_n}^{(N)}\right), PL\left(Z_{V_n}^{(N)}\right), PL\left(F_{V_n}^{(N)}\right), PL\left(H_{V_n}^{(N)}\right), PL\left(L_{V_n}^{(N)}\right), PL\left(R_{V_n}^{(N)}\right)\right\} \end{aligned} \qquad \textbf{Eq. 7-28}$$

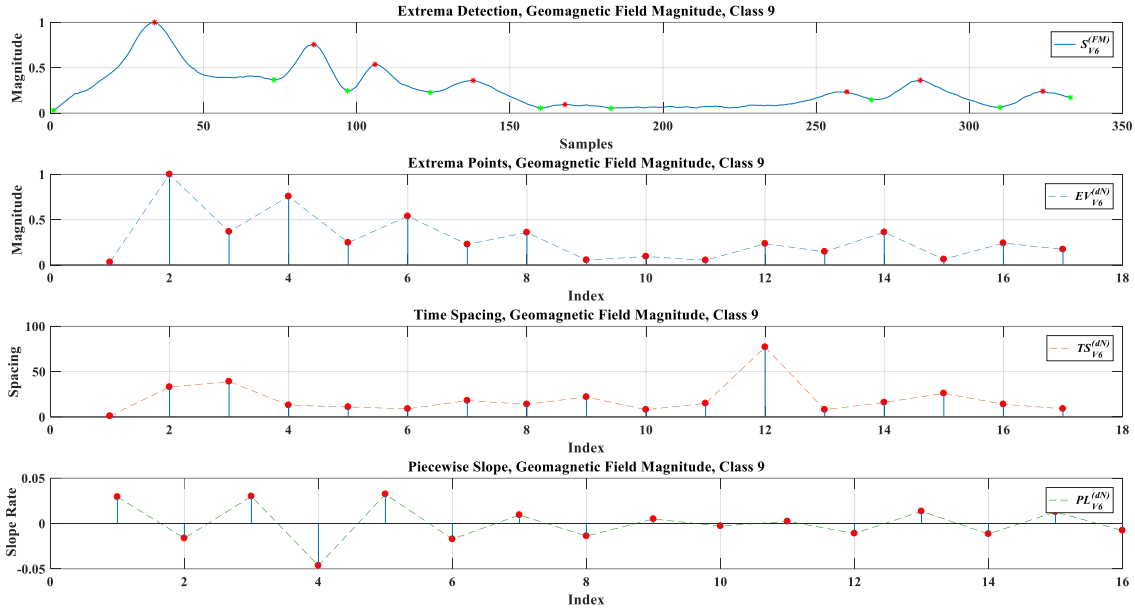


Figure 7-19 The PIP, spacing, and PL features for Class 9 VMS

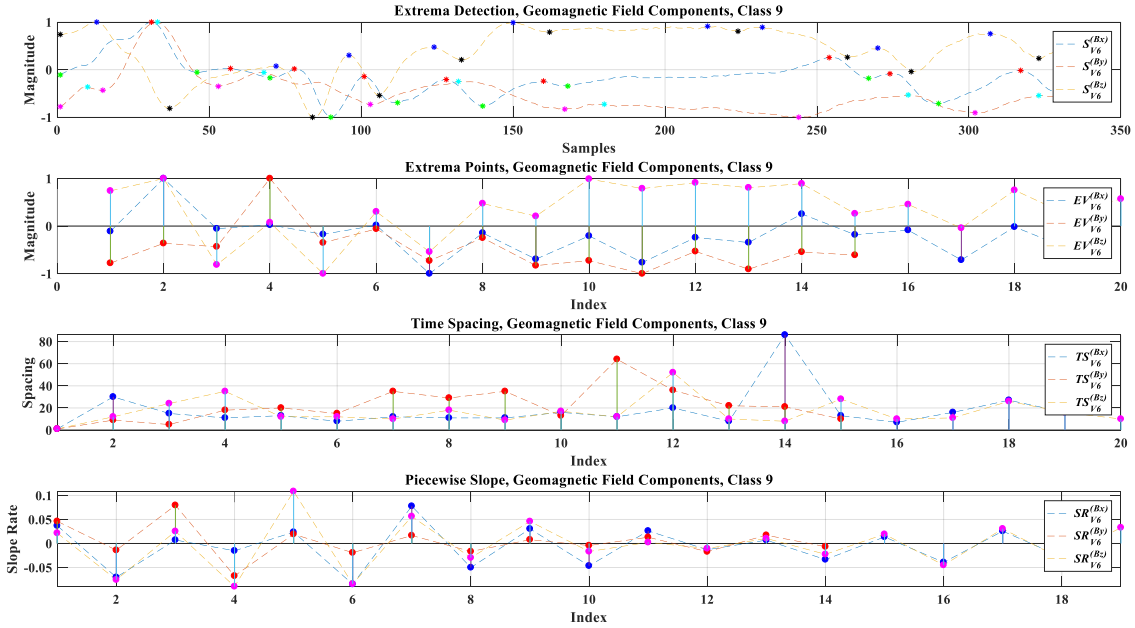


Figure 7-20 Field components PIP, spacing, and PL

7.5.3 Matching Process

A large number of methods for calculating distance between two time series signals $X = [x_1, x_2, \dots, x_n]$ and $Y = [y_1, y_2, \dots, y_n]$ in an n-dimensional space are detailed in [160], [162]. Euclidean distance (See Eq. 7-29), Manhattan distance,

Minkowski distance, Chebyshev distance, and Cross-correlation are among the most common methods for calculating the distance between two signals. All methods align the *i*-th point on a time series signal with the *i*-th point on the other signal. However, they require compared signals X and Y of the same length (i.e., time normalization). Moreover, the methods are sensitive to any change in trajectory and/or acceleration of a vehicle overpassing sensors in a detection zone, primarily because disturbance to the earth's magnetic field is dependent upon the relative position of the vehicle to the sensor's detection zone, where any change in vehicle lateral position will cause variations in VMS amplitude, hence, the number of points. This effect can be clearly observed on the z-axis.

$$dist(X,Y) = \|X - Y\| = \sqrt{(x_1 - y_1)^2 + (x_2 - y_2)^2 + \cdots + (x_n - y_n)^2} \qquad \textbf{Eq. 7-29}$$

Dynamic time warping (DTW) [163] is a non-linear alignment method measuring similarity between two temporal time series sequences that might vary in speed (i.e., sequences are out of phase in the time axis). The DTW algorithm compresses or expands in time to find optimal mapping between two signals so that their difference is minimized.

To align two time series, C and Q, of lengths m and n, using DTW, an $m \times n$ matrix is first constructed, where the i^{th} and j^{th} element of the matrix contains the distance $dist(q_i, c_j)$ between the two points q_i and c_j. The Euclidean distance corresponds both to the alignment between points q_i and c_j (i.e., $dist(q_i, c_j) = (q_i - c_j)^2$).

Warping path $W = \{w_1, \dots, w_k\}$. k^{th} element is defined as $w_k = (i_k, j_k)$, and $max(m,n) \leq K < m + n - 1$ defines mapping between C and Q, such that the distance between them is minimized (See Eq. 7-30).

$$DTW(Q,C) = \min_{w}\left[\sum_{k=1}^{K} dist(w_k)\right]; \qquad \textbf{Eq. 7-30}$$

$$dist(w_k) = dist\left(q_{i_k}, c_{i_k}\right) = \left(q_{i_k} - c_{i_k}\right)^2$$

In reality, the signature matching process is performed within a time window that matches vehicle signature detection at a downstream point with a number of signatures in a candidate vehicle set detected by the upstream point. The matching process is always one (in current time)-vs.-all (past time). The number of vehicles in a matching window depends on traffic flow, distance, and segment low speed limit between upstream and downstream points (See Table 7-17). The longer the distance, the larger the number of vehicles in the window buffer and the less the re-identification rate. In general, TT is estimated based on 0.5-mile spacing between detectors on urban roads and 5- to 10-mile spacing between detectors on highways.

Table 7-17 Matching window size for different distances between detection points

Flow (VPH)	**1200**							
Distance (mile)	0.50		1.00		5.00		10.00	
Avg. Speed (mph)	20	40	30	50	40	70	50	80
Time Interval (Min)	**1.5**	**0.75**	**2**	**1.2**	**7.5**	**4.3**	**12**	**7.5**
Window Size (Vehicle)	**30**	**15**	**40**	**24**	**150**	**86**	**240**	**150**

In this work, the matching process implements *DTW* algorithm for calculating distance (i.e., similarity) between corresponding extracted features at upstream and downstream detection points. DTW is applied in a single-dimension manner, such that

DTW distance is calculated for PIP feature vectors corresponding to *x*-axis at both detectors (i.e., $dist = DTW\left[EV\left(X_{V_n}^{(dN)}\right), EV\left(X_{V_n}^{(uN)}\right)\right]$). The same applies for other axles and feature vectors. The smaller the $dist(q_i, c_j)$, the more likely Q_i and C_j belong to the same vehicle. Figure 7-21 illustrates extracted features and calculated distances between upstream and downstream detection points for vehicle sample number 8.

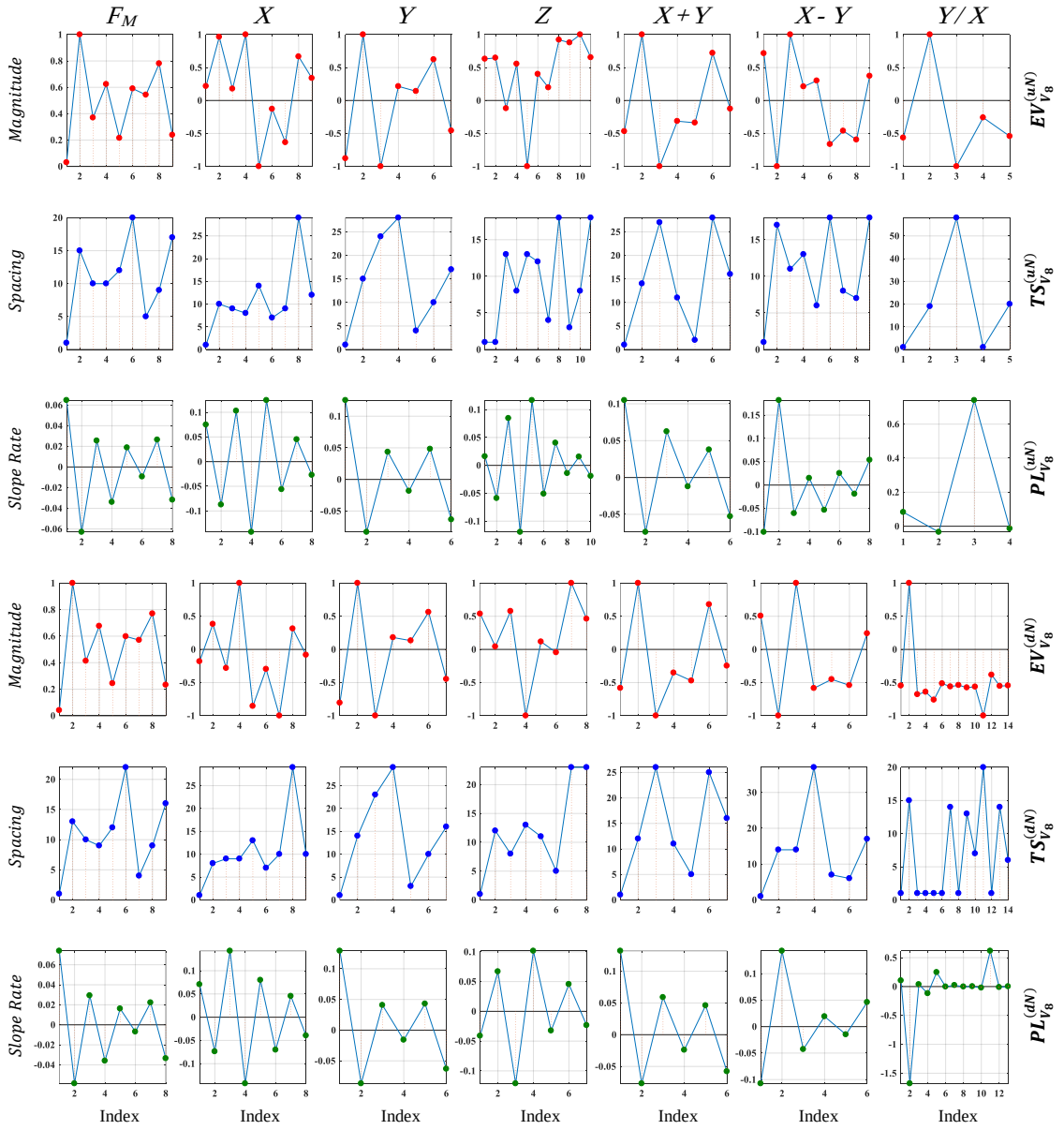


Figure 7-21 Extracted features at upstream and downstream for V_8

The decision whether a calculated $dist(q_i, c_j)$ value can be classified as "*Identical*" or "*Different*" can be made using one of two methods, namely Threshold-based and Majority Voting-based re-identification. Figure 7-22 illustrates the re-identification process for both methods.

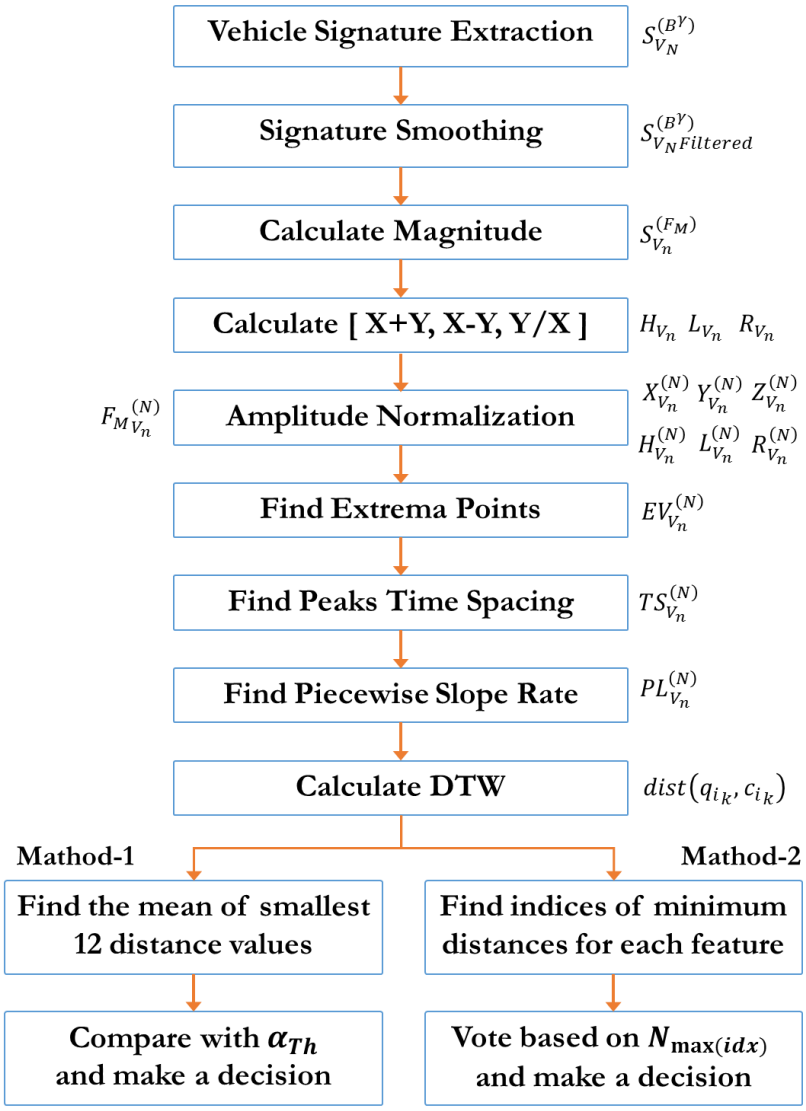


Figure 7-22 Re-identification algorithm block diagram

The first eight steps are applied for both methods; the only difference between Threshold-based and Majority Voting-based algorithms is that the first implements a decision threshold α_{Th} to compare VMS distances and classify them into one of two

classes, "*Identical*" or "*Different.*" The Majority Voting-based algorithm makes a decision based on maximum number of minimum distances for 21 features, requiring more processing when compared to the Threshold-based method. Notably, re-identification accuracy is much higher when using Majority Voting-based algorithm.

7.5.3.1 Threshold-based Vehicle Matching

The objective of *Threshold-based Vehicle Match* is finding an efficient matching function δ for classifying a calculated distance $dist(q_i, c_j)$ between upstream and downstream points into "Identical" (i.e., $\delta(i) = 1$) or "Different" (i.e., $\delta(i) = 0$), as in *Eq. 7-31*. A statistical model of distance matrix between upstream and downstream detection points is proposed in this study to find a decision threshold α_{Th}.

$$\delta(i) = \begin{cases} 1 \ ; & dist(q_i, c_j) \leq \alpha_{Th} \\ 0 \ ; & dist(q_i, c_j) > \alpha_{Th} \end{cases} \quad \textbf{Eq. 7-31}$$

To do so, a distance matrix A_{dist} is constructed of all pairwise signature distances $dist(q_i, c_j)$ calculated between upstream and downstream detection points (See Eq. 7-32). *M* is the number of vehicles at upstream point; *N* is the number of vehicles at downstream point; and *O* is the number of features. The dataset used in this study at upstream and downstream included 5154 VMS matched using video images as a ground truth. The dataset was collected from a highway during peak (congested) and free flow hours. A feature wise rescaling step was performed to normalize A_{dist} values calculated for each feature between [0,1], as in Eq. 7-23. Next, arithmetic mean of smallest 12 distance values of 21 features for each $dist(q_i, c_j)$ was found. Doing so reduced A_{dist} dimension into $M \times N$, where $dist(q_i, c_j)$ has become the mean of the smallest 12 distance values found in Eq. 7-28. This number was experimentally found based on a

grid search (i.e., exhaustive search) approach. Figure 7-23 illustrates distance matrixes for $EV\left(F_{V_n}^{(N)}\right)$, $TS\left(F_{V_n}^{(N)}\right)$, and $PL\left(F_{V_n}^{(N)}\right)$. The distance matrix for the mean of the lowest 12 first features is illustrated in Figure 7-24.

$$A_{dist} = \begin{Bmatrix} dist\left(q_i, c_j\right)_l & ; & 1 \le M \le i \\ & & 1 \le N \le j \\ & & 1 \le O \le l \end{Bmatrix} \qquad \textbf{Eq. 7-32}$$

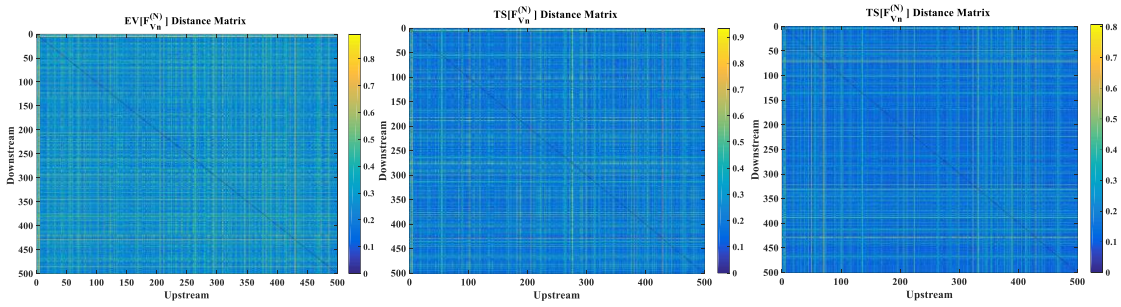


Figure 7-23 Distance matrixes for $EV\left(F_{V_n}^{(N)}\right)$, $TS\left(F_{V_n}^{(N)}\right)$, and $PL\left(F_{V_n}^{(N)}\right)$

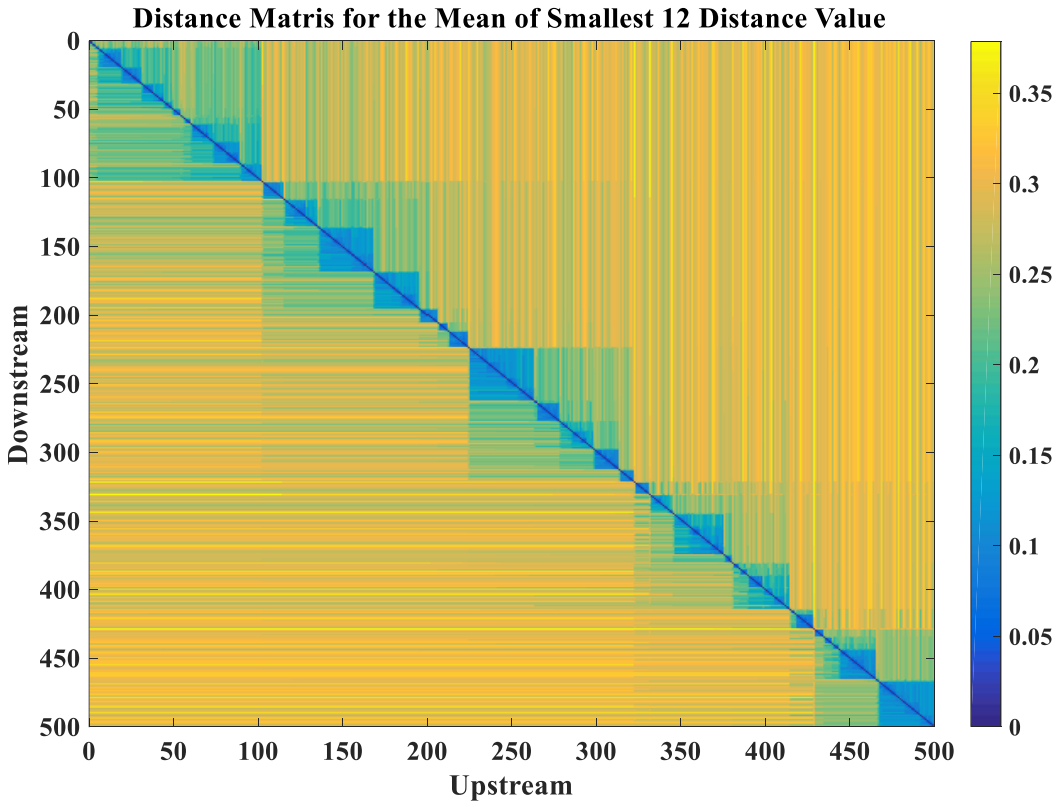


Figure 7-24 Distance matrix for the mean of lowest twelve first features

A_{dist} is a 2577×2577 matrix. A_{dist} diagonal, such that $dist(q_i, c_j)$ and $\forall\, i = j$, consists of all pairwise matched vehicles (i.e., "*Identical*"). The lower and higher triangular parts of A_{dist}, such that $dist(q_i, c_j)$ and $\forall\, i \neq j$, consist of all pairwise "*Different*" vehicles.

Next, two histograms were extracted for "*Identical*" and "*Different*" values of A_{dist}, as depicted in Figure 7-25. In accordance with central limit theorem and law of large numbers, distributions of "*Identical*," denoted by *f*, and "*Different*," denoted by *g*, statistically describe random variable corresponding to $dist(q_i, c_j)$. Hence, these can be approximated using Gaussian distribution models. Clearly, g consists of two distributions, which can be attributed to the fact that the dataset includes a significant number of trucks (e.g., classes 6, 7, 8, 9, and 10), where $dist(q_i, c_j)$ is larger between VMS for class 2 or class 3 and VMS for trucks, compared to $dist(q_i, c_j)$ between two vehicles of the same class. To find an accurate and realistic approximation, GMM was used to separate g into two distributions, g_1 and g_2, assuming both are normally distributed, as depicted in Figure 7-25.

Statistically, there is no overlap between *f* and g_2, as shown in in Figure 7-25 and Table 7-18. These statistics were estimated based on a distribution *f* of 2577 "*Identical*" pairs and distribution g of 6,638,352 "*Different*" pairs (See Eq. 7-33). Therefore, g_2 is not of interest for the developed model. Only f and g_1 are used to characterize the distance matrix and find α_{Th}; g_1 will be denoted hereafter as g.

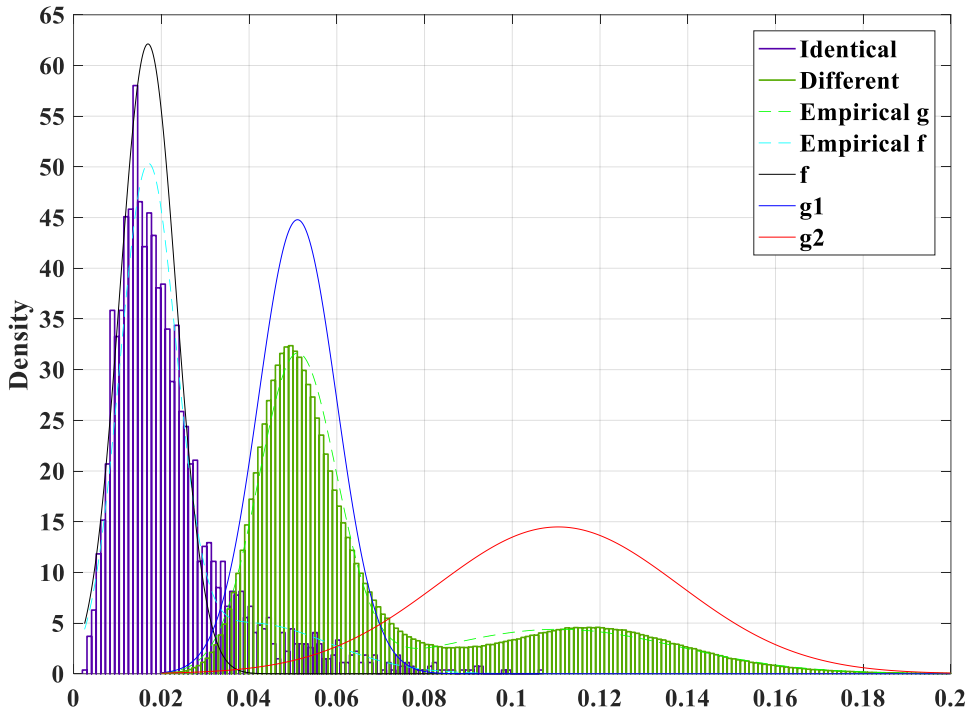


Figure 7-25 The empirical distributions and their Gaussian approximations

Table 7-18 Statistical characteristics of fitted distributions

	f	g_1	g_2
μ	0.0169	0.0510	0.1105
$\boldsymbol{\sigma}$	0.0064	0.0089	0.0275

$$A_{dist|\mu(\min(l1:l12))} = \begin{pmatrix} dist(q_1,c_1) & dist(q_1,c_2) & \cdots & dist(q_1,c_{2577}) \\ dist(q_2,c_1) & dist(q_2,c_2) & \cdots & dist(q_2,c_{2577}) \\ \vdots & \vdots & \ddots & \vdots \\ dist(q_{2577},c_1) & dist(q_{2577},c_2) & \cdots & dist(q_{2577},c_{2577}) \end{pmatrix} \quad \textbf{Eq. 7-33}$$

The objective was finding α_{Th} that maximizes probability of correct matching and minimizes probability of incorrect matching. In other words, α_{Th} should not compromise between correct and incorrect re-identification; rather it should minimize *false negative rate* (FNR) (i.e., incorrect matching). FNR has significant impact on TT reliability. The proposed algorithm estimates TT in real-time. A 50% re-identification rate was found sufficient to accurately estimate a distribution of TT for a given route.

To minimize FNR, α_{Th} must be computed such that the probability of Type II error is zero (See Figure 7-26). Optimal threshold α_{Th} is empirically found by taking the derivative of Eq. 7-34 and equating the outcome to 0.

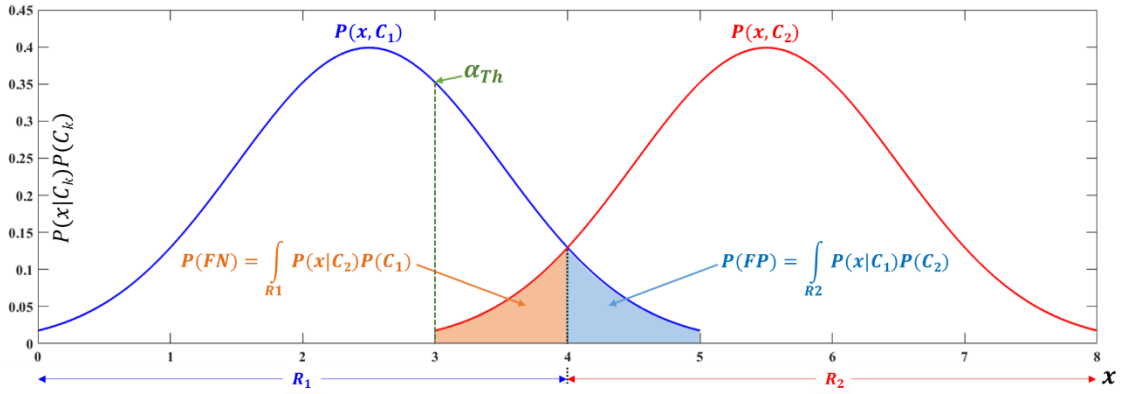


Figure 7-26 Illustration of different Errors for two overlapped distributions

$$P(FN) = \int_0^{\alpha_{Th}} P(x|C_2)P(C_1)dx = \int_0^{\alpha_{Th}} \left(dist(q_i, c_j)|C_2\right)P(C_1)dx$$

$$= P(C_1)\int_0^{\alpha_{Th}} \frac{1}{\sigma_{C2}\sqrt{2\pi}} \exp\left[-\frac{\left(dist(q_i, c_j) - \mu_{C2}\right)^2}{2\sigma_{C2}^2}\right].dx \qquad \textbf{Eq. 7-34}$$

$$= P(C_1)\frac{1}{2}\left(1 + erf\left[\frac{\alpha_{Th} - \mu_{C2}}{\sigma_{C2}\sqrt{2}}\right]\right)$$

Based on the statistical model in Eq. 7-34, which was estimated from distributions of 2577 "*Identical*" pairs and 6,638,352 "*Deferent*" pairs. Subsequently, determining "*Identical*" or "*Different*" can simply be made using Eq. 7-31.

Estimated value of α_{Th} was found to accurately model signature distances for both urban roads and highways, as shown in Table 7-19. This is true for two reasons: 1) statistical characteristics of fitted distributions are obtained from the mean of smallest distance values for 21 unique features, which was empirically found to have less overlap between "*Identical*" and "*Different*" distributions; and 2) α_{Th} was chosen to identify "*Identical*" classes at the cost of having unmatched vehicles, rather than

compromising between correct and incorrect re-identification, which is highly dependent upon traffic characteristics. Unmatched signatures in this case will be considered "*Different*" or will be discarded after matching window time (e.g., $W_t \geq TT_{max}$) is elapsed.

Re-identification performance was evaluated using six metrics, namely, 1) *true positive rate* ($TPR = TP/(TP + FN)$): "*Identical*" correctly identified as "*Identical*"; 2) *false positive rate* ($FPR = FP/(FP + TN)$): "*Different*" incorrectly identified as "*Identical*"; 3) *true negative rate* ($TNR = TN/(TN + FP)$): "*Different*" correctly identified as "*Different*"; 4) *false negative rate* ($FNR = FN/(TP + FN)$): "*Identical*" incorrectly identified as "*Different*"; 5) *positive predictive value* ($PPV = TP/(TP + FP)$): the probability that "*Identical*" was truly identified as "*Identical*"; and 6) *negative predictive value* ($NPV = TN/(TN + FN)$): the probability that "*Different*" was truly identified as "*Different.*" Table 7-19 presents Threshold-based re-identification results for various window sizes. Narrowing the search window reduces FPR impact. When search window includes 25 vehicles, an "*Identical*" decision is made when distance between feature sets for a vehicle detected at downstream point and any vehicle in the window meet the condition $dist(q_i, c_j) \leq \alpha_{Th}$. In this case the probability that FN occurs is less compared to a window size equal to 100 vehicles where probability of having vehicles that have high similarity is much higher. Notably, vehicles in the window will be discarded if no matching was found within the window specified time.

Table 7-19 Threshold-based re-identification evaluation results

Evaluation Metric	Window Size (Vehicle)			
	25	**50**	**100**	**500**
TP/FP	21/1	43/2	80/3	321/9
TPR	100.0%	86.00%	80.00%	65.25%
TNR	84.00%	99.84%	99.92%	99.99%
FPR	0.330%	0.160%	0.080%	0.010%
FNR	16.00%	14.00%	21.00%	34.76%
PPV	95.45%	95.56%	95.18%	97.27%
NPV	98.68%	70.59%	99.58%	99.86%

7.5.3.2 Majority Voting-based Vehicle Matching

Unlike the Threshold-based algorithm described in the previous section, Voting-based algorithms do not implement a decision threshold; rather the algorithms make a decision as to which VMS in a window buffer should a current VMS be matched based on maximum number of minimum distances calculated for the 21 features.

The algorithm simply compares the distance for M upstream VMS (q_i) in a window to a downstream VMS (c_j) just detected; stores the indices of minimum distance values for each feature (l) of the 21 ($O = 21$) in $M\times2$ matrix A_{vote} (See Eq. 7-35); and then votes for a matching decision based on maximum number of similar indices. Figure 7-27 depicts indices of minimum distance of 21 features for 25 vehicles.

$$A_{vote}(val_j, idx_j) = \min_{O}\left(dist(q_i, c_j)_l\right); \forall\, j \in [1{:}M], \forall\, l \in [1{:}O], i = 1 \qquad \textbf{Eq. 7-35}$$

If maximum number of similar indices $N_{\max(idx)} < \varepsilon$, then the vehicle will be considered unmatched. If more than one VMS share the same $N_{\max(idx)}$, which is a rare case, then a decision is based on which VMS with the same $N_{\max(idx)}$ has the smallest val_j mean in A_{vote}.

Indices of minimum distance - Upstream vs. Downstream	Features																				Votes
	8	1	1	1	24	1	1	1	11	1	1	1	1	1	5	1	1	10	14	24	1	14
	15	24	17	24	22	16	2	3	2	16	1	2	2	18	17	14	25	17	24	1	25	4
	16	3	3	3	3	3	3	3	20	24	3	3	3	3	16	3	3	16	3	3	20	15
	4	8	4	4	4	4	4	4	1	19	8	15	4	4	24	4	4	5	7	12	2	11
	5	5	5	22	5	5	5	5	20	22	24	16	5	5	18	5	25	23	5	23	23	11
	6	18	6	15	6	6	6	6	6	6	6	25	6	6	2	6	6	12	6	4	6	15
	7	7	24	7	7	7	7	7	19	7	4	19	7	7	7	7	7	19	4	7	7	15
	8	20	8	8	8	8	8	8	8	8	8	13	8	8	16	8	8	18	8	18	18	15
	9	11	9	9	9	9	9	9	2	1	9	9	9	9	19	9	9	13	9	19	9	15
	10	10	10	12	10	10	10	10	10	10	10	10	10	10	16	10	10	17	10	10	25	17
	1	11	11	24	11	11	11	9	11	11	11	12	11	11	11	11	11	19	11	11	11	16
	12	12	12	12	12	12	12	12	11	12	12	12	22	12	17	11	12	19	14	12	12	15
	13	13	13	13	13	13	13	13	13	13	13	13	23	13	12	13	13	20	23	13	16	16
	14	9	14	14	14	14	14	14	2	14	23	2	14	14	23	14	14	15	14	14	12	14
	22	15	15	3	15	15	15	15	14	15	15	15	15	15	16	15	15	15	2	15	15	16
	16	16	16	16	16	16	16	16	16	16	16	16	16	16	16	16	16	16	16	16	16	21
	17	17	17	17	17	17	17	17	17	17	23	17	17	19	20	17	17	11	24	3	3	14
	15	15	18	13	23	15	25	18	18	15	18	23	18	18	15	18	18	20	3	18	20	9
	19	19	19	19	19	19	19	19	14	24	19	19	19	19	17	19	19	17	24	3	19	15
	20	20	20	22	17	20	14	20	23	1	3	20	20	20	16	20	9	16	16	14	17	9
	21	21	21	21	21	21	21	21	21	21	21	20	21	21	5	21	21	17	21	21	21	18
	22	22	15	22	22	22	22	10	22	22	13	20	22	22	16	22	22	9	22	22	22	15
	22	23	3	23	9	23	5	23	24	15	9	15	5	23	16	14	23	23	24	23	14	8
	24	24	15	24	24	24	24	24	2	24	18	24	24	24	3	24	24	23	24	24	2	15
	14	25	25	25	16	25	25	13	25	25	3	13	12	25	15	12	25	19	25	25	12	11

Figure 7-27 Indices of minimum distance of 21 features for 25 vehicles

Table 7-20 details evaluation results for various window sizes. Clearly, re-identification accuracy was improved using Majority Voting-based algorithm. It is worth mentioning that this method requires more processing power when compared to a Threshold-based method. However, processing is not a concern if it occurs on the server side, while dynamic programming can be used to optimize computation speed.

Table 7-20 Voting-based re-identification evaluation results

Evaluation Metric	Window Size (Vehicle)				
	25	**50**	**100**	**250**	**500**
Matched	25	50	97	239	451
Mismatched	0	0	0	1	3
Unmatched	0	0	3	10	46
Re-identification Rate	100%	100%	97%	95.6%	90.2%
Mismatching Rate	0%	0%	0%	0.4%	0.6%
Unmatching Rate	0%	0%	3%	4%	9.2%

Chapter 8: CONCLUSION

8.1 Research Outcomes

With the approaching era of IoT (Internet of Things) and smart cities, market demand will likely drive innovation toward more autonomous and self-powered wireless sensors. Combining advancements in state-of-the-art ultra-low-power embedded systems, smart physical sensors, WSN, and EH will enable fully autonomous IoT devices that remain operational—ideally without battery replacement—for decades. This technological breakthrough is the key enabler for smart cities, smart homes, and smart energy, among many other perspective innovations.

Real-time traffic monitoring systems play a major role in the transition toward smart cities and more efficient ITS. Autonomous traffic sensing is at the heart of smart cities infrastructure, wherein smart wireless sensors are used to measure traffic flow, predict congestion, and adaptively control traffic routes. Such information enables a more efficient use of resources and infrastructure.

This dissertation introduces the design, development, and implementation of a novel, fully-autonomous, self-powered, intelligent wireless sensor for various traffic surveillance applications. The sensor integrates state-of-the-art, embedded components, featuring ultralow power, high-performance 32-bit embedded microcontroller, energy-efficient wireless transceiver, smart embedded sensors (i.e., 3D MAG and ACCEL), highly-accurate low-power embedded Global Positioning System (GPS) receiver, dual data storage units, an ultralow power EH power management unit (PMU) with maximum power point tracking (MPPT) and charge management controllers, battery fuel gauge, wireless power charging receiver, and atmospheric sensors. All components

are managed by distinctive algorithms designed for implementation in various traffic monitoring applications.

The developed sensor is portable, self-powered (e.g., primary battery and solar cell), inexpensive (e.g., $30 per node), easy-to-install into highway surfaces, roadways, or even roadsides without intrusive roadwork, and able to accurately detect, count, estimate speed and length, classify, and re-identify vehicles in real-time. The sensor can be used for short-term deployment (e.g., work zone safety, temporary roadway design studies, traffic management in atypical situations such as evacuations) and long-term deployment (e.g., traffic management, turn movement, collision avoidance).

A reliable and distinctive computationally efficient algorithm for real-time traffic monitoring was developed, integrated, and validated. Optimization programming tasks were applied to improve detection algorithm performance at higher sampling rates and compensate for drift in the geomagnetic reference field. An algorithm for adaptive compensation of RTC Frequency Drift resulting from variations in temperature was implemented. Each sensor node relies on an onboard GPS module and RTC unit to maintain an independent local clock that is globally synchronized to the GPS pulse-per-second (PPS) signal. Wireless connectivity is not necessary for accurate *i*VCCS node functioning. Time stamping, timekeeping, and failure recovery functions are enabled by the MCU's internal RTC unit, which is calibrated and aligned using the PPS signal. A time-synchronization algorithm based on GPS-PPS signal was developed and evaluated. Results indicated 2~4μSec consistent T-Sync accuracy among the internal RTC of several nodes.

Several field studies and evaluation tests were conducted during this research, many of which were conducted in parking lots at the *University of Oklahoma-Tulsa* campus. Eight additional field tests were conducted on *highways* and *urban roads* under various traffic conditions throughout the state of Oklahoma. System performance evaluation was conducted using real-time data, offline data, video images, and reports from the highly accurate *Roadrunner Kit 3*.

Repeatability of VMS and consistency of MAG sensor output were investigated. The objective was to find degree of similarity of several magnetic signatures produced by multiple MAG sensors for the same vehicle under like-testing conditions. Cross-correlation was used to measure the similarity of two VMS as a function of a time lag applied to one or the other. A correlation coefficients matrix of VMS magnitudes obtained from four sensor nodes was constructed. CDF for all pairwise combinations revealed that most correlation coefficients range between 0.9 and 1, indicating high similarity between sensor outputs across multiple nodes. Furthermore, the p-value matrix returned insignificant p-values (i.e., 2e-138), which rejects the null hypothesis and identifies significant correlations. Hence, each vehicle has a unique magnetic signature that can be used for vehicle re-identification applications.

Three detection errors were observed during this study: 1) *Misdetection error*, in which two successive vehicles at close proximity are grouped as one; 2) *Double-detection error*, in which a long vehicle with insignificant ferrous composition in its center is detected as two vehicles; and 3) *False-detection error* caused by an interference from large trucks traveling in adjacent lanes. Both misdetection and double-detection errors were reduced by using statistical analysis to find an optimal

holdover debounce timer (H_{DT}). Optimality was determined empirically. False-detection error analysis showed insignificant interference effect on the *z-axis*. This observation was used to reduce false detection by comparing the mean of vertical components to a statistically determined threshold.

Vehicle detection and counting accuracy was evaluated using MAPE. Validation studies showed MAPE between 0.4% and 0.7% for detection of all vehicle classes at various traffic conditions and speeds in both roadside and roadway setups.

Speed estimation was evaluated using MAPE and RMSE, indicating 97.4782% speed estimation accuracy with 2.9867mph MAPE and 2.5218% RMSE.

Two methods for vehicle classification using MAG are proposed, namely length-based (LBVC) and magnetic signature-based vehicle classification (SBVC). Several LBVC schemes were developed, implemented, and evaluated via machine learning algorithms and probabilistic modeling of VML. A case study of Oklahoma classification stations using wireless MAG sensors was performed. This study serves as the first LBVC scheme for the state of Oklahoma; the intended purpose is supplementing or replacing axle-based data collection methods. The developed LBVC models are computationally efficient and can provide real-time data. The methodology and work process proved to be adaptable, thus, can be of a great benefit for other states and territories interested in developing LBVC schemes. This work can be extended for gathering LBVC data using non-intrusive technologies, such as vision systems and microwave radars. An LBVC evaluation study resulted in 97.6951% classification rate when vehicles are binned into four groups based on their magnetic length.

Two vehicle re-identification models based on matching VMS from a single MAG were also developed. Features extraction was performed on each sensor node to determine three sets of features for each normalized signal. These included Perceptually Important Points (PIP), Time Spacing between consecutive PIP, and Piecewise Linear Representation (PLR). Notably, the objective of data transformation is reducing the dimensionality of the data while maintaining the unique characteristics of signal, thus, reducing the amount of data processing or transfer from the sensor node to *i*AP. The matching process implemented a *DTW* algorithm to calculate distance (i.e., similarity) between corresponding extracted features at upstream and downstream detection points. The decision whether a calculated distance value can be classified as "*Identical*" or "*Different*" was made using one of two methods, namely *Threshold-based* and *Majority Voting-based* re-identification. A statistical model of distance matrix between upstream and downstream detection points was proposed to determine a decision threshold that maximizes the probability of correct matching and minimizes the probability of incorrect matching. A majority voting-based algorithm makes a decision based on the maximum number of minimum distances for 21 features, which requires more processing when compared to a threshold-based method. Re-identification accuracy depends on window size (i.e., the number of vehicles compared to one another). Threshold-based re-identification evaluation results revealed 65.25%~100% identification rate for the 25~500 vehicle window size. Voting-based re-identification evaluation results showed 90~100% identification rate for 25~500 vehicle window size.

System functionality testing revealed consistent behavior and accurate performance that can be exploited for more advanced applications. System cost was

estimated at less than $1000 for eight sensor nodes and an access point, meaning that the system could be promoted as a replacement for expensive and invasive traditional traffic surveillance systems that depend on piezoelectric sensors, magnetic loops, and pneumatic tubes.

8.2 Future Work Plan

Currently, vehicle classification based on VMS collected using MAG is not feasible for more than 5classes. The reasoning behind this conclusion centers on the fact that each vehicle has a unique composition of furious materials causing a unique VMS. Characteristics of VMS for vehicles of the same class are quite different. During this research, several methods where exhausted, including neural networks and deep learning. It is nearly impossible to cluster vehicles based on their classes by only analyzing VMS. Hence, two approaches are proposed for more accurate vehicle classification. The first takes advantage of the highly sensitive, low noise 3D accelerometer sensor in *i*VCSS$_{G2}$ design and investigates sophisticated signal processing and data analysis methods for fusing accelerometer and MAG data toward achieving axle-based classification. In a late stage of this research work, measuring road surface vertical acceleration using accelerometer for data collected from a sensor node placed adjacent to the road demonstrated a clear indication of vehicle axle positions. Exploiting this phenomenon to detect and count axles improves classification accuracy and allows the measurement of several vehicle dynamics (e.g., axle spacing), given that vehicle speed is known. The second approach proposes taking advantage of VMS uniqueness for implementing a classification model based on encoding an enormous

number of labeled VMS and storing them into a database. Euclidian distance measure can be used to compare a real-time VMS with database and identify a class of vehicles.

Additionally, two areas of interest relative to this research are presented. These include enabling a scalable implementation of the system's wireless sensors network through self-configuration; optimizing sensor node power consumption while maximizing network lifetime by analyzing power consumption characteristics of a sensor node; and then incorporating an energy-awareness algorithm to maintain high performance and operation fidelity.

REFERENCES

[1] "FHWA Forecasts of Vehicle Miles Traveled (VMT): May 2014," *Office of Highway Policy Information*, 2014. [Online]. Available: http://www.fhwa.dot.gov/policyinformation/tables/vmt/vmt_forecast_sum.cfm. [Accessed: 17-Apr-2015].

[2] "WHO | Global status report on road safety 2015."

[3] "National Highway Traffic Safety Administration (NHTSA), 2013 Traffic Safety Facts FARS/GES Annual Report." [Online]. Available: http://www-nrd.nhtsa.dot.gov/Pubs/812139.pdf. [Accessed: 14-Feb-2016].

[4] National Highway Traffic Safety Adminstriation, "The Economic and Societal Impact Of Motor Vehicle Crashes, 2010," Washington, DC, 2014.

[5] "2015 Urban Mobility Scorecard and Appendices — Urban Mobility Information." [Online]. Available: http://mobility.tamu.edu/ums/report/. [Accessed: 14-Feb-2016].

[6] C. C. D. US EPA, "Carbon Dioxide Emissions." [Online]. Available: http://www.epa.gov/climatechange/ghgemissions/gases/co2.html. [Accessed: 16-Apr-2015].

[7] "Truck Safety – Advocates for Highway and Auto Safety." [Online]. Available: http://saferoads.org/issues/truck-safety/. [Accessed: 10-Jan-2016].

[8] L. E. Y. Mimbela and L. a Klein, "A Summary of Vehicle Detection and Surveillance Technologies used in Intelligent Transportation Systems."

[9] G. Orosz, R. E. Wilson, and G. Stépán, "Traffic jams: dynamics and control.," *Philos. Trans. A. Math. Phys. Eng. Sci.*, vol. 368, no. 1928, pp. 4455–79, Oct. 2010.

[10] S. (Shawn) Jang, B. Bai, G.-S. Hong, and J. T. O'Leary, "Understanding travel expenditure patterns: a study of Japanese pleasure travelers to the United States by income level," *Tour. Manag.*, vol. 25, no. 3, pp. 331–341, Jun. 2004.

[11] "Industrial electronics Internet of Things opportunity | VentureOutsource.com." [Online]. Available: https://www.ventureoutsource.com/contract-manufacturing/industrial-electronics-internet-of-things-opportunity/.

[12] S. Cheung, "Traffic Surveillance by Wireless Sensor Networks : Final Report," 2007.

[13] F. H. Administration, "Traffic Monitoring Guide," 2013.

[14] I. Khan, F. Belqasmi, R. Glitho, N. Crespi, M. Morrow, and P. Polakos, "Wireless Sensor Network Virtualization: A Survey," *IEEE Commun. Surv. Tutorials*, pp. 1–1, 2015.

[15] F. Losilla, A.-J. Garcia-Sanchez, F. Garcia-Sanchez, J. Garcia-Haro, and Z. J. Haas, "A Comprehensive approach to WSN-based ITS applications: a survey.," *Sensors (Basel).*, vol. 11, no. 11, pp. 10220–65, Jan. 2011.

[16] D. Tacconi, D. Miorandi, I. Carreras, F. Chiti, and R. Fantacci, "Using wireless sensor networks to support intelligent transportation systems," *Ad Hoc Networks*, vol. 8, no. 5, pp. 462–473, Jul. 2010.

[17] A. Haoui, R. Kavaler, and P. Varaiya, "Wireless magnetic sensors for traffic surveillance," *Transp. Res. Part C Emerg. Technol.*, vol. 16, no. 3, pp. 294–306, Jun. 2008.

[18] N. G. D. Center, "NGDC Geomagnetic Calculators."

[19] N. Administrator, "2012: Magnetic Pole Reversal Happens All The (Geologic) Time," Apr. 2015.

[20] N. Wahlstrom and F. Gustafsson, "Magnetometer Modeling and Validation for Tracking Metallic Targets," *IEEE Trans. Signal Process.*, vol. 62, no. 3, pp. 545–556, Feb. 2014.

[21] J. Jackson, *Classical electrodynamics*. New York: Wiley, 1999.

[22] S. M. and A. T. Chulliat, A., S. Macmillan, P. Alken, C. Beggan, M. Nair, B. Hamilton, A. Woods, V. Ridley, "The US/UK World Magnetic Model for 2015-2020: Technical Report, National Geophysical Data Center, NOAA.," 2015. [Online]. Available: https://www.ngdc.noaa.gov/geomag/WMM/DoDWMM.shtml. [Accessed: 17-Dec-2015].

[23] Q. Liu, A. P. Roberts, J. C. Larrasoaña, S. K. Banerjee, Y. Guyodo, L. Tauxe, and F. Oldfield, "Environmental magnetism: Principles and applications," *Rev. Geophys.*, vol. 50, no. 4, p. RG4002, Nov. 2012.

[24] M. T. Report, "Evaluating Detection and Estimation Capabilities of Magnetometer-Based Vehicle Sensors," 2012.

[25] N. Wahlstrom and F. Gustafsson, "Magnetometer Modeling and Validation for Tracking Metallic Targets," *IEEE Trans. Signal Process.*, vol. 62, no. 3, pp. 545–556, Feb. 2014.

[26] I. Buchmann, *Batteries in a Portable World: A Handbook on Rechargeable Batteries for Non-Engineers*, 4th editio. Cadex Electronics Inc., 2016.

[27] T. Coughlin and I. C. E. S. Future Directions Committee, "A Moore's Law for Mobile Energy: Improving upon conventional batteries and energy sources for mobile devices," *IEEE Consum. Electron. Mag.*, vol. 4, no. 1, pp. 74–82, Jan. 2015.

[28] F. K. Shaikh and S. Zeadally, "Energy harvesting in wireless sensor networks: A comprehensive review," *Renew. Sustain. Energy Rev.*, vol. 55, pp. 1041–1054, 2016.

[29] A. S. M. Zahid Kausar, A. W. Reza, M. U. Saleh, and H. Ramiah, "Energizing wireless sensor networks by energy harvesting systems: Scopes, challenges and approaches," *Renew. Sustain. Energy Rev.*, vol. 38, pp. 973–989, 2014.

[30] C. P. and D. S. S. Basagni, M.Y. Naderi, *Wireless Sensor Networks With Energy Harvesting; in Mobile ad hoc networking: the cutting edge directions*, 2nd ed. Hoboken, NJ: John Wiley & Sons Inc., 2013.

[31] S. Rajab, "ACCURATE VEHICLE CLASSIFICATION INCLUDING MOTORCYCLES USING PIEZOELECTRIC SENSORS," University of Oklahoma, 2012.

[32] S. V. Marshall, "Vehicle detection using a magnetic field sensor," *IEEE Trans. Veh. Technol.*, vol. 27, no. 2, pp. 65–68, 1978.

[33] N. Wahlstrom, R. Hostettler, F. Gustafsson, W. Birk, N. Wahlström, S. Member, R. Hostettler, F. Gustafsson, W. Birk, N. Wahlstrom, R. Hostettler, F. Gustafsson, and W. Birk, "Classification of driving direction in traffic surveillance using magnetometers," *IEEE Trans. Intell. Transp. Syst.*, vol. 15, no. 4, pp. 1405–1418, 2014.

[34] K. Liu, H. Xiong, and H. He, "New method for detecting traffic information based on anisotropic magnetoresistive technology," in *Proc. SPIE 8783, Fifth International Conference on Machine Vision (ICMV 2012): Computer Vision, Image Analysis and Processing*, 2013, p. 87830S.

[35] L. Yalong, L. Bin, and W. Zhiqiang, "A novel method of automatic vehicle detection based on active magnetic theory," in *2010 International Conference on Information, Networking and Automation (ICINA)*, 2010, vol. 2, pp. V2-382-V2-385.

[36] J. L. J. Lan and Y. S. Y. Shi, "Vehicle detection and recognition based on a MEMS magnetic sensor," *2009 4th IEEE Int. Conf. Nano/Micro Eng. Mol. Syst.*, pp. 404–408, 2009.

[37] A. Kaadan and H. H. Refai, "iICAS: Intelligent intersection collision avoidance system," in *2012 15th International IEEE Conference on Intelligent Transportation Systems*, 2012, pp. 1184–1190.

[38] A. Daubaras and M. Zilys, "Vehicle Detection based on Magneto-Resistive Magnetic Field Sensor," *Electron. Electr. Eng.*, vol. 118, no. 2, pp. 27–32, Feb. 2012.

[39] Z. Zhang, X. Li, H. Yuan, and F. Yu, "A Street Parking System Using Wireless Sensor Networks," vol. 2013, no. c, 2013.

[40] H. Zhu and F. Yu, “A Vehicle Parking Detection Method Based on Correlation of Magnetic Signals,” vol. 2015, 2015.

[41] D. Liu, X. Xu, C. Fei, W. Zhu, X. Liu, G. Yu, and G. Fang, “Direction identification of a moving ferromagnetic object by magnetic anomaly,” *Sensors Actuators A Phys.*, vol. 229, pp. 147–153, 2015.

[42] R. D. Komguem, R. Stanica, M. Tchuente, F. Valois, R. Domga Komguem, R. Stanica, M. Tchuente, and F. Valois, “WARIM: Wireless Sensor Networks Architecture for a Reliable Intersection Monitoring,” in *17th International IEEE Conference on Intelligent Transportation Systems (ITSC)*, 2014, pp. 1226–1231.

[43] S. Taghvaeeyan and R. Rajamani, “Portable roadside sensors for vehicle counting, classification, and speed measurement,” *IEEE Trans. Intell. Transp. Syst.*, vol. 15, no. 1, pp. 73–83, 2014.

[44] B. Koszteczky and G. Simon, “Magnetic-based vehicle detection with sensor networks,” in *2013 IEEE International Instrumentation and Measurement Technology Conference (I2MTC)*, 2013, pp. 265–270.

[45] W. Zhang, G. Tan, and N. Ding, “Vehicle Speed Estimation Based on Sensor Networks and Signal Correlation Measurement,” pp. 1–12, 2014.

[46] D.-H. Kim, K.-H. Choi, K.-J. Li, and Y.-S. Lee, “Performance of vehicle speed estimation using wireless sensor networks: a region-based approach,” *J. Supercomput.*, vol. 71, no. 6, pp. 2101–2120, 2015.

[47] D. Obertov, V. Bardov, and B. Andrievsky, “Vehicle speed estimation using roadside sensors,” in *2014 6th International Congress on Ultra Modern Telecommunications and Control Systems and Workshops (ICUMT)*, 2014, pp. 111–117.

[48] D. Nan, T. Guozhen, M. Honglian, L. Mingwen, and S. Yao, “Low-power Vehicle Speed Estimation Algorithm based on WSN,” in *2008 11th International IEEE Conference on Intelligent Transportation Systems*, 2008, pp. 1015–1020.

[49] L. Zhang, R. Wang, and L. Cui, “Real-time traffic monitoring with magnetic sensor networks,” *J. Inf. Sci. Eng.*, vol. 27, no. 4, pp. 1473–1486, 2011.

[50] X. DENG, Z. HU, P. ZHANG, and J. GUO, “Vehicle Class Composition Identification Based Mean Speed Estimation Algorithm Using Single Magnetic Sensor,” *J. Transp. Syst. Eng. Inf. Technol.*, vol. 10, no. 5, pp. 35–39, Oct. 2010.

[51] H. Li, H. Dong, L. Jia, D. Xu, and Y. Qin, “Some practical vehicle speed estimation methods by a single traffic magnetic sensor,” in *2011 14th International IEEE Conference on Intelligent Transportation Systems (ITSC)*, 2011, pp. 1566–1573.

[52] J. Lan, Y. Xiang, L. Wang, and Y. Shi, “Vehicle detection and classification by measuring and processing magnetic signal,” *Measurement*, vol. 44, no. 1, pp. 174–180, Jan. 2011.

[53] B. Yang and Y. Lei, “Vehicle Detection and Classification for Low-Speed Congested Traffic With Anisotropic Magnetoresistive Sensor,” *IEEE Sens. J.*, vol. 15, no. 2, 2015.

[54] D. Kleyko, R. Hostettler, W. Birk, and E. Osipov, “Comparison of Machine Learning Techniques for Vehicle Classification Using Road Side Sensors,” *2015 IEEE 18th Int. Conf. Intell. Transp. Syst.*, pp. 572–577, 2015.

[55] W. Ma, D. Xing, A. McKee, R. Bajwa, C. Flores, S. Member, B. Fuller, P. Varaiya, S. Member, B. Fuller, P. Varaiya, C. Author, D. Xing, A. McKee, R. Bajwa, C. Flores, and B. Fuller, “A wireless accelerometer-based automatic vehicle classification prototype system,” *IEEE Trans. Intell. Transp. Syst.*, vol. 15, no. 1, pp. 1–8, 2014.

[56] Y. He, Y. Du, L. Sun, and Y. Wang, “Improved waveform-feature-based vehicle classification using a single-point magnetic sensor,” *J. Adv. Transp.*, vol. 49, no. 5, pp. 663–682, Aug. 2015.

[57] W. Zhang, G. Z. Tan, H. M. Shi, and M. W. Lin, “A distributed threshold algorithm for vehicle

classification based on binary proximity sensors and intelligent neuron classifier," *J. Inf. Sci. Eng.*, vol. 26, no. 3, pp. 769–783, 2010.

[58] E.-H. N. E.-H. Ng, S.-L. T. S.-L. Tan, and J. G. Guzman, "Road traffic monitoring using a wireless vehicle sensor network," *2008 Int. Symp. Intell. Signal Process. Commun. Syst.*, 2009.

[59] B. Coifman and S. Kim, "Speed estimation and length based vehicle classification from freeway single-loop detectors," *Transp. Res. Part C Emerg. Technol.*, vol. 17, no. 4, pp. 349–364, Aug. 2009.

[60] C. H. Wu, J. M. Ho, and D. T. Lee, "Travel-time prediction with support vector regression," *IEEE Trans. Intell. Transp. Syst.*, vol. 5, no. 4, pp. 276–281, 2004.

[61] X. Sun and R. Horowitz, "Set of New Traffic-Responsive Ramp-Metering Algorithms and Microscopic Simulation Results," *Transp. Res. Rec. J. Transp. Res. Board*, vol. 1959, pp. 9–18, Jan. 2006.

[62] C. B. Winkler, "Work Zone Safety ITS Smart Barrel for an Adaptive Queue-Warning System," no. February, 2005.

[63] C. Monsere, C. Nolan, R. Bertini, E. Anderson, and T. El-Seoud, "Measuring the Impacts of Speed Reduction Technologies: Evaluation of Dynamic Advanced Curve Warning System," *Transp. Res. Rec.*, vol. 1918, no. 1, pp. 98–107, 2005.

[64] A. J. Kean, R. a Harley, and G. R. Kendall, "Effects of Vehicle Speed and Engine Load on Motor Vehicle Emissions," *Environ. Sci. Technol.*, vol. 37, no. 17, pp. 3739–3746, 2003.

[65] D. Kleyko, R. Hostettler, W. Birk, and E. Osipov, "Comparison of Machine Learning Techniques for Vehicle Classification Using Road Side Sensors," *2015 IEEE 18th Int. Conf. Intell. Transp. Syst.*, pp. 572–577, 2015.

[66] H. Zhu and F. Yu, "A Cross-Correlation Technique for Vehicle Detections in Wireless Magnetic Sensor Network," vol. 16, no. 11, pp. 4484–4494, 2016.

[67] "Sensor | Sensys Networks." [Online]. Available: http://www.sensysnetworks.com/products/sensor/. [Accessed: 20-Apr-2015].

[68] "Vehicle Detector WD-300 | Sensebit." [Online]. Available: http://www.sensebit.se/products/traffic-measurement/vehicle-detector-wd-300/. [Accessed: 20-Apr-2015].

[69] "M100 Wireless Vehicle Detection System." [Online]. Available: http://www.clearviewtraffic.com/golden-river/products-golden-river/art/44/m100-wireless-vehicle-detection-system.htm. [Accessed: 20-Apr-2015].

[70] D. L. Mills, "Computer Network Time Synchronization: The Network Time Protocol on Earth and in Space, Second Edition," Nov. 2010.

[71] J. Elson, L. Girod, and D. Estrin, "Fine-grained network time synchronization using reference broadcasts," *ACM SIGOPS Oper. Syst. Rev.*, vol. 36, no. SI, p. 147, Dec. 2002.

[72] S. Ganeriwal, R. Kumar, and M. B. Srivastava, "Timing-sync protocol for sensor networks," in *Proceedings of the first international conference on Embedded networked sensor systems - SenSys '03*, 2003, p. 138.

[73] K. Shahzad, A. Ali, and N. D. Gohar, "ETSP: An Energy-Efficient Time Synchronization Protocol for Wireless Sensor Networks," in *22nd International Conference on Advanced Information Networking and Applications - Workshops (aina workshops 2008)*, 2008, pp. 971–976.

[74] H. Xiao, C. Lu, and H. Ogai, "A Multi-hop Low Cost Time Synchronization Algorithm for Wireless Sensor Network in Bridge Health Diagnosis System," in *2012 IEEE International Conference on Embedded and Real-Time Computing Systems and Applications*, 2012, pp. 392–395.

[75] M. Mar□ti, B. Kusy, G. Simon, and □kos L□deczi, “The flooding time synchronization protocol,” in *Proceedings of the 2nd international conference on Embedded networked sensor systems - SenSys ’04*, 2004, p. 39.

[76] P. Sommer and R. Wattenhofer, “Gradient clock synchronization in wireless sensor networks,” pp. 37–48.

[77] J. van Greunen and J. Rabaey, “Lightweight time synchronization for sensor networks,” in *Proceedings of the 2nd ACM international conference on Wireless sensor networks and applications - WSNA ’03*, 2003, p. 11.

[78] S. Youn, “A Comparison of Clock Synchronization in Wireless Sensor Networks,” *Int. J. Distrib. Sens. Networks*, vol. 2013, p. 10, 2013.

[79] I. F. Akyildiz, W. Su, Y. Sankarasubramaniam, and E. Cayirci, “Wireless sensor networks: a survey,” *Comput. Networks*, vol. 38, no. 4, pp. 393–422, Mar. 2002.

[80] R. Kim, T. Nagayama, H. Jo, and J. Spencer, “Preliminary study of low-cost GPS receivers for time synchronization of wireless sensors,” *Proc. SPIE Sensors Smart Struct. Technol. Civ. Mech. Aerosp. Syst.*, vol. 8345, no. 1, p. 83451A--83451A--9, 2012.

[81] Z. Li, T. Braun, and D. C. Dimitrova, “Methodology for GPS Synchronization Evaluation with High Accuracy,” in *2015 IEEE 81st Vehicular Technology Conference (VTC Spring)*, 2015, pp. 1–6.

[82] E. Sazonov, V. Krishnamurthy, and R. Schilling, “Wireless Intelligent Sensor and Actuator Network - A Scalable Platform for Time-synchronous Applications of Structural Health Monitoring,” *Struct. Heal. Monit.*, vol. 9, no. 5, pp. 465–476, Apr. 2010.

[83] D. R. Fuhrmann, J. Stomberg, S. Nooshabadi, D. McIntire, and W. Merill, “Node Synchronization in a Wireless Sensor Network Using Unreliable GPS Signals,” in *2014 IEEE Military Communications Conference*, 2014, pp. 630–636.

[84] J. Bae and B. Moon, “Time Synchronization in Wireless Sensor Networks,” in *Smart Wireless Sensor Networks*, H. D. Chinh and Y. K. Tan, Eds. InTech, 2010, pp. 253–280.

[85] “ATMEL XMEGA MCU - ATxmega128A4U.” [Online]. Available: http://www.atmel.com/devices/atxmega128a4u.aspx. [Accessed: 21-Apr-2015].

[86] “Freescale Digital Sensor - FXOS8700CQ.” [Online]. Available: http://www.freescale.com/webapp/sps/site/prod_summary.jsp?code=FXOS8700CQ. [Accessed: 21-Apr-2015].

[87] “MEMS-Based Sensor Technology | Freescale.” [Online]. Available: http://www.freescale.com/webapp/sps/site/overview.jsp?code=SNSMEMSOVERVIEW. [Accessed: 22-Apr-2015].

[88] “Synapse SM200P81 RF Engine.” [Online]. Available: https://www.synapse-wireless.com/documents/products/Synapse-SM200P81-Engine-Product-Brief.pdf. [Accessed: 22-Apr-2015].

[89] “Synapse‘s SNAP Network Operating System,” *David Ewing*. [Online]. Available: http://synapse-wireless.com/documents/white_paper/Synapse-SNAP-OS-White-Paper.pdf. [Accessed: 22-Apr-2015].

[90] “Maxim Integrated - DS3231M Real-Time Clock.” [Online]. Available: http://www.maximintegrated.com/en/products/digital/real-time-clocks/DS3231M.html. [Accessed: 22-Apr-2015].

[91] “GlobalTop Technology Inc. - Titan 2 (GMS-G6).” [Online]. Available: http://www.gtop-tech.com/en/product/Titan-2-GMS-G6/GPS_Modules_Gms-g6.html. [Accessed: 22-Apr-2015].

[92] “Maxim Integrated - MAX17043 Compact, Low-Cost 1S/2S Fuel Gauges with Low-Battery Alert.” [Online]. Available: http://www.maximintegrated.com/en/products/power/battery-

management/MAX17043.html. [Accessed: 22-Apr-2015].

[93] R. Yan, H. Sun, and Y. Qian, “Energy-Aware Sensor Node Design With Its Application in Wireless Sensor Networks,” *IEEE Trans. Instrum. Meas.*, vol. 62, no. 5, pp. 1183–1191, May 2013.

[94] “STM32L071KB - Ultra-low-power ARM Cortex-M0+ MCU with 128-Kbytes Flash, 32 MHz CPU - STMicroelectronics.” [Online]. Available: http://www.st.com/content/st_com/en/products/microcontrollers/stm32-32-bit-arm-cortex-mcus/stm32l0-series/stm32l0x1/stm32l071kb.html.

[95] “Wireless Technologies Flood the IoT Landscape | Systems content from Microwaves & RF.” [Online]. Available: http://mwrf.com/systems/wireless-technologies-flood-iot-landscape.

[96] “AW516x Nano Type ZigBee Wireless Module.” [Online]. Available: http://www.zlg.com/wireless/wireless/product/id/136.html.

[97] “SiT1552 Ultra-Small, Precision 32 kHz TCXO.” [Online]. Available: https://www.sitime.com/products/32-khz-temperature-compensated-oscillators-tcxo/sit1552.

[98] “GNSS L76 - Quectel Wireless Solutions.” [Online]. Available: http://quectel.com/product/prodetail.aspx?id=30.

[99] “SanDisk Industrial Cards.” [Online]. Available: https://www.sandisk.com/oem-design/industrial/industrial-cards.

[100] “TPD8F003 | 8-Channel EMI Filter.” [Online]. Available: http://www.ti.com/product/tpd8f003/description.

[101] “Ultra Low Power Flash Memories.” [Online]. Available: http://www.macronix.com/en-us/Product/NORFlash/pages/UltraLowPowerFlash.aspx.

[102] “ADP165 | Very Low Quiescent Current, 150 mA, with Output Discharge LDO Regulator.” [Online]. Available: http://www.analog.com/en/products/power-management/linear-regulators/adp165.html.

[103] “How to Prolong Lithium-based Batteries - Battery University.” [Online]. Available: http://batteryuniversity.com/learn/article/how_to_prolong_lithium_based_batteries.

[104] “BQ27621-G1 | System-Side Fuel Gauge with Dynamic Voltage Correlation, Battery Gas Gauge.” [Online]. Available: http://www.ti.com/product/BQ27621-G1/description.

[105] “ADP165 | Very Low Quiescent Current, 150 mA, with Output Discharge LDO Regulator.” .

[106] “TPS22860 | Ultra-low leakage load switch.” [Online]. Available: http://www.ti.com/product/TPS22860.

[107] X. Lu, P. Wang, D. Niyato, D. I. Kim, and Z. Han, “Wireless Charging Technologies: Fundamentals, Standards, and Network Applications,” Sep. 2015.

[108] “BQ51051B | Integrated Wireless Power Li-Ion Charger Receiver.” [Online]. Available: http://www.ti.com/product/bq51051b/description.

[109] “Vishay - IWAS-4832FE-50 - Wireless Charging Receiving Coil/Shield.” [Online]. Available: http://www.vishay.com/ppg?34376.

[110] “Semitec’s NT-4 Glass NTC Thermistors.” [Online]. Available: http://www.atcsemitec.co.uk/nt-glass-thermistors.html.

[111] “TMJ S1gma™ Series – AVX.” [Online]. Available: http://www.avx.com/products/tantalum/automotive/tmj-s1gma-series/.

[112] “Macronix - MX25R6435F.” [Online]. Available: http://www.macronix.com/en-us/products/NOR-Flash/Serial-NOR-Flash/Pages/spec.aspx?p=MX25R6435F. [Accessed: 16-Dec-2016].

[113] “Tri-Axis Magnetometer/Tri-Axis Accelerometer - KMX62.” [Online]. Available: http://www.kionix.com/product/KMX62.

[114] “TI TPS3839A09 | Supervisor and Reset IC.” [Online]. Available: http://www.ti.com/product/TPS3839A09. [Accessed: 16-Dec-2016].

[115] “TPS782 | Single Channel LDO.” [Online]. Available: http://www.ti.com/product/TPS782. [Accessed: 16-Dec-2016].

[116] “ADP5091 | Ultralow Power Energy Harvesting PMU with MPPT, Charge Management.” [Online]. Available: http://www.analog.com/en/products/power-management/battery-management/battery-charger-ic/adp5091.html.

[117] IXYS, “SLMD121H04, IXOLAR High Efficiency SolarMD.” [Online]. Available: http://ixapps.ixys.com/Datasheet/20110107-SLMD121H04-DATA-SHEET.pdf.

[118] “Industrial External GPRS Wireless Data Transmission Unit.” [Online]. Available: http://www.zlg.com/wireless/wireless/product/id/16.html.

[119] M. Ramezani, J. Haddad, and N. Geroliminis, “Dynamics of heterogeneity in urban networks: aggregated traffic modeling and hierarchical control,” *Transp. Res. Part B Methodol.*, vol. 74, pp. 1–19, Apr. 2015.

[120] “Econolite :: Wireless In-Ground.” [Online]. Available: http://www.econolite.com/index.php/products/detection/wireless/. [Accessed: 20-Dec-2015].

[121] B. Coifman and S. Kim, “Speed estimation and length based vehicle classification from freeway single-loop detectors,” *Transp. Res. Part C Emerg. Technol.*, vol. 17, no. 4, pp. 349–364, Aug. 2009.

[122] W. Balid, H. Tafish, and H. H. Refai, “Development of Portable Wireless Sensor Network System For Real-time Traffic Surveillance,” in *18th IEEE International Conference on Intelligent Transportation Systems, IEEE - ITSC 2015, September 15-18, 2015*, 2015.

[123] W. Balid, H. Tafish, and H. H. Refai, “Versatile Real-Time Traffic Monitoring System Using Wireless Smart Sensors Networks,” in *IEEE Wireless Communications and Networking Conference (WCNC), Track 4 - Services, Applications, and Business,*.

[124] “Road Runner 3 Counter and Classifier Kit | Diamond Traffic.” [Online]. Available: http://diamondtraffic.com/product/RoadRunner3Kit. [Accessed: 05-Sep-2015].

[125] M. Isaksson, “Vehicle Detection using Anisotropic Magnetoresistors,” CHALMERS UNIVERSITY OF TECHNOLOGY, Goteborg, Sweden, 2008.

[126] F. Palhinha, D. Carona, A. Serrador, and T. Canas, “Wireless Magnetic Based Sensor System for Vehicles Classification,” *Procedia Technol.*, vol. 17, pp. 632–639, 2014.

[127] H. Lee and B. Coifman, “Identifying and Correcting Pulse-Breakup Errors from Freeway Loop Detectors,” *Transp. Res. Rec. J. Transp. Res. Board*, vol. 2256, pp. 68–78, 2011.

[128] L. Chen and A. D. May, “Traffic Detector Errors and Diagnostics,” *Transp. Res. BOARD*, no. 1132, pp. 82–93, 1987.

[129] B. Coifman, “Using Dual Loop Speed Traps To Identify Detector Errors,” *Transp. Res. Rec.*, vol. 1683, no. 1, pp. 47–58, 1999.

[130] B. Coifman and H. Lee, “A Single Loop Detector Diagnostic: Mode On-Time Test,” *Appl. Adv. Technol. Transp. Proc. Ninth Int. Conf. ASCE*, pp. 623–628, 2006.

[131] P. Cheevarunothai, Y. Wang, and N. Nihan, “Using Dual-Loop Event Data to Enhance Truck Data Accuracy,” *Transp. Res. Rec.*, vol. 1993, no. 1, pp. 131–137, 2007.

[132] H. Tafish, “A LOW-COST VEHICLE DETECTION AND CLASSIFICATION SYSTEM USING MAGNETOMETERS,” University of Oklahoma, 2015.

[133] H. Tafish, W. Balid, and H. H. Refai, “Cost effective Vehicle Classification using a single wireless magnetometer,” in *2016 International Wireless Communications and Mobile Computing Conference (IWCMC)*, 2016, pp. 194–199.

[134] E. Öner, “Cumulative Interarrival Time Distributions of Freeway Entrance Ramp Traffic for Traffic Simulations,” *PROMET - Traffic&Transportation*, vol. 25, no. 1, Feb. 2013.

[135] A. K. Pandey, “Transportation System Engineering - Vehicle Arrival Models : Headway - Chapter 12,” pp. 1–18, 2015.

[136] H. Refai, N. Bitar, J. Schettler, and O. Al Kalaa, “The Study of Vehicle Classification Equipment with Solutions to Improve Accuracy in Oklahoma.”

[137] “Aligning Oversize/Overweight Fees with Agency Costs: Critical Issues.” [Online]. Available: http://www.trb.org/Main/Blurbs/169473.aspx. [Accessed: 28-Jan-2016].

[138] “Loop- and Length-Based Vehicle Classi cation , Federal Highway Administration – Pooled Fund Program,” vol. 5, no. November, 2012.

[139] “Loop and Length Based Classification Pooled Fund.” [Online]. Available: http://www.pooledfund.org/details/study/416. [Accessed: 03-Sep-2015].

[140] H. Wei, Q. Ai, D. Eustace, and B. Coifman, “Length-based Vehicle Classification Models using Dual-loop Data against Stop-and-Go Traffic Flow,” in *Transportation Research Board 90th Annual Meeting*, 2011.

[141] B. Coifman, “Vehicle Classification from Single Loop Detectors,” Mar. 2007.

[142] T. Mauga, “Development of Florida Length Based Vehicle Classification Scheme Using Support Vector Machines,” Florida State University, 2016.

[143] W. Balid, H. Tafish, and H. H. Refai, “Intelligent Vehicle Counting and Classification Sensor for Real-Time Traffic Surveillance,” *IEEE Trans. Intell. Transp. Syst.*, no. Under Review, 2016.

[144] C. M. Bishop, “Pattern Recognition and Machine Learning (Information Science and Statistics),” Aug. 2006.

[145] C. Seiffert, T. M. Khoshgoftaar, J. Van Hulse, and A. Napolitano, “RUSBoost: A Hybrid Approach to Alleviating Class Imbalance,” *IEEE Trans. Syst. Man, Cybern. - Part A Syst. Humans*, vol. 40, no. 1, pp. 185–197, Jan. 2010.

[146] S. Kaewkamnerd, J. Chinrungrueng, R. Pongthornseri, and S. Dumnin, “Vehicle classification based on magnetic sensor signal,” *2010 IEEE Int. Conf. Inf. Autom.*, pp. 935–939, 2010.

[147] R. Wang, L. Zhang, K. Xiao, R. Sun, and L. Cui, “EasiSee: Real-Time Vehicle Classification and Counting via Low-Cost Collaborative Sensing,” *IEEE Trans. Intell. Transp. Syst.*, vol. 15, no. 1, pp. 414–424, 2014.

[148] H. X. Liu and J. Sun, “Length-based vehicle classification using event-based loop detector data,” *Transp. Res. Part C Emerg. Technol.*, vol. 38, pp. 156–166, Jan. 2014.

[149] L. Wu and B. Coifman, “Improved vehicle classification from dual-loop detectors in congested traffic,” *Transp. Res. Part C Emerg. Technol.*, vol. 46, pp. 222–234, Sep. 2014.

[150] S.-T. (Cindy) Jeng and S. G. Ritchie, “Real-Time Vehicle Classification Using Inductive Loop Signature Data,” *Transp. Res. Rec. J. Transp. Res. Board*, vol. 2086, no. 1, pp. 8–22, 2009.

[151] N. Bitar and H. H. Refai, “A Probabilistic Approach to Improve the Accuracy of Axle-Based Automatic Vehicle Classifiers,” *IEEE Trans. Intell. Transp. Syst.*, pp. 1–8, 2016.

[152] J. Singer, A. E. Robinson, J. Krueger, J. E. Atkinson, and M. C. Myers, “Travel Time on Arterials and Rural Highways: State-of-the-Practice Synthesis on Arterial Data Collection Technology, FHWA-HOP-13-028,” Washington, DC 20590, 2013.

[153] S. Ishak, O. Osman, R. Thapa, and S. Jenkins, “Real Time Driver Information for Congestion

Management, Final Report 543," Baton Rouge, Louisiana, 2015.

[154] Y. Wang, B. N. Araghi, Y. Malinovskiy, J. Corey, and T. Cheng, "Error Assessment for Emerging Traffic Data Collection Devices: WSDOT Research Report," Seattle, Washington, 2014.

[155] R. O. Sanchez, C. Flores, R. Horowitz, R. Rajagopal, and P. Varaiya, "Vehicle re-identification using wireless magnetic sensors: Algorithm revision, modifications and performance analysis," in *Proceedings of 2011 IEEE International Conference on Vehicular Electronics and Safety*, 2011, pp. 226–231.

[156] K. Kwong, R. Kavaler, R. Rajagopal, and P. Varaiya, "Arterial travel time estimation based on vehicle re-identification using wireless magnetic sensors," *Transp. Res. Part C Emerg. Technol.*, vol. 17, no. 6, pp. 586–606, Dec. 2009.

[157] Y. Tian, H. Dong, L. Jia, and S. Li, "A vehicle re-identification algorithm based on multi-sensor correlation," *J. Zhejiang Univ. Sci. C*, vol. 15, no. 5, pp. 372–382, May 2014.

[158] A. C. Pitton, A. Vassilev, and S. Charbonnier, "Vehicle re-identification with several magnetic sensors," in *Advanced Microsystems for Automotive Applications 2012: Smart Systems for Safe, Sustainable and Networked Vehicles*, 2012, pp. 281–290.

[159] P. E. Tsinaslanidis and D. Kugiumtzis, "A prediction scheme using perceptually important points and dynamic time warping," *Expert Syst. Appl.*, vol. 41, no. 15, pp. 6848–6860, 2014.

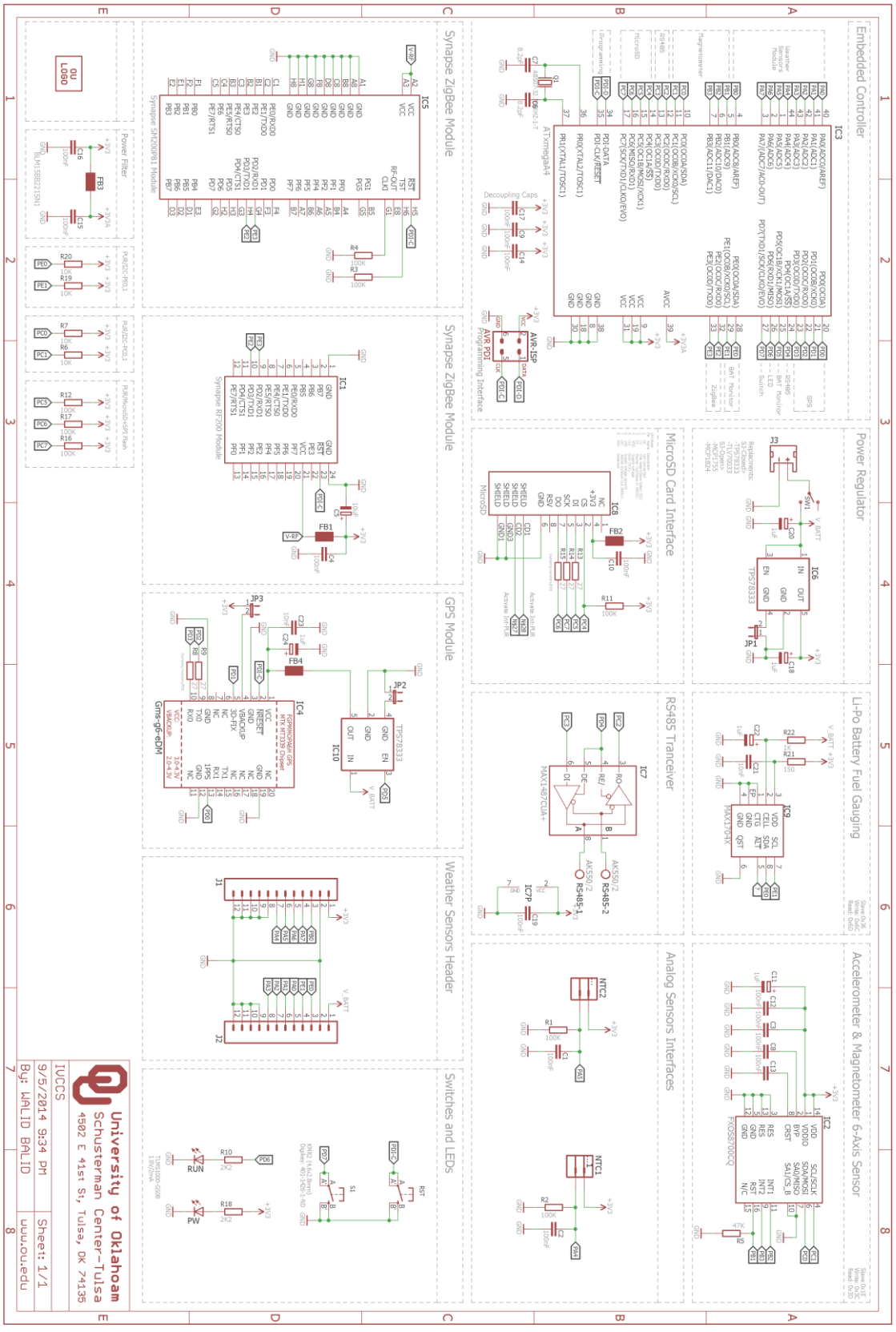
[160] T. Fu, "A review on time series data mining," *Eng. Appl. Artif. Intell.*, vol. 24, no. 1, pp. 164–181, 2011.

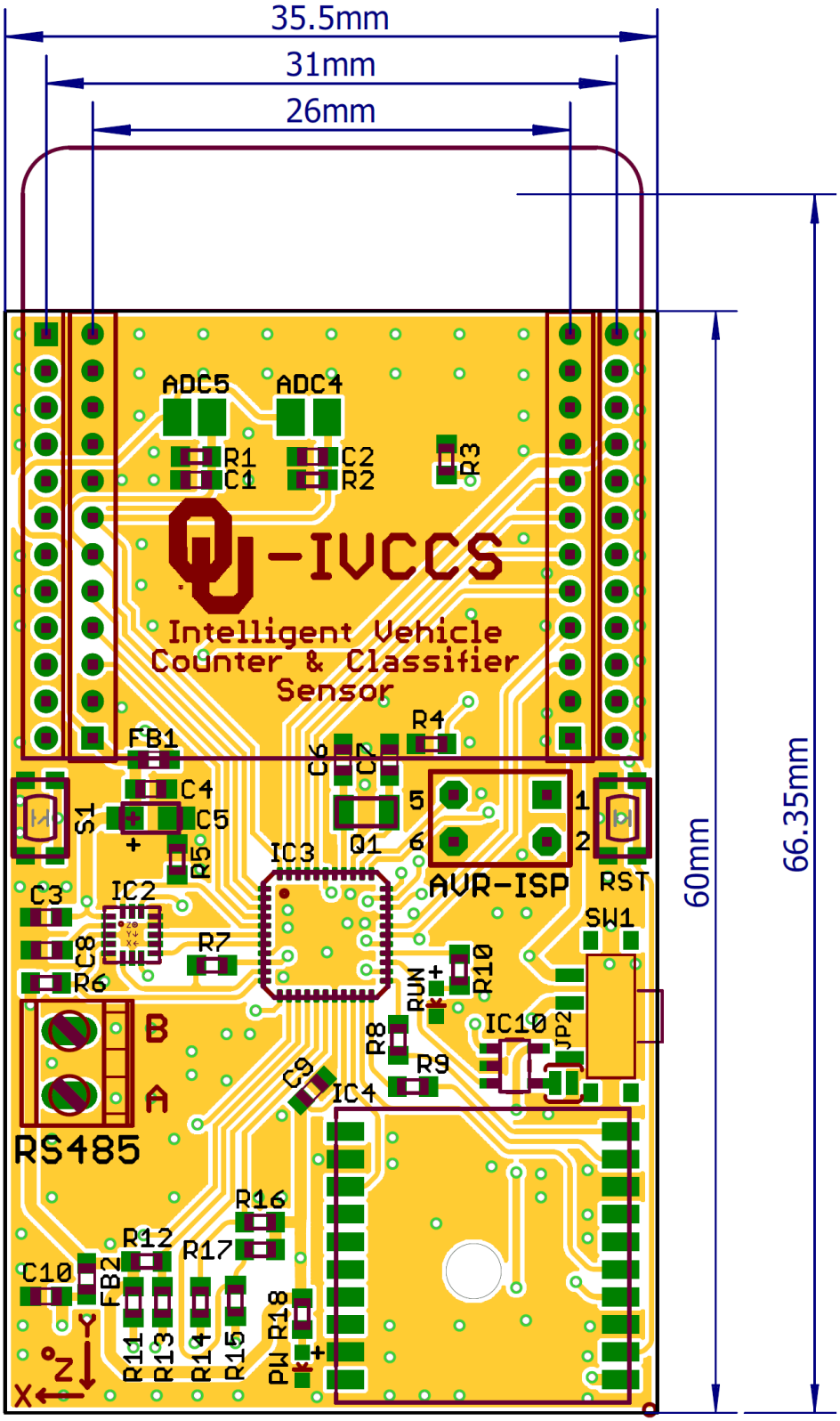
[161] E. Keogh, E. Keogh, S. Chu, D. Hart, and M. Pazzani, "Segmenting Time Series: A Survey and Novel Approach," *AN Ed. Vol. DATA Min. TIME Ser. DATABASES. Publ. BY WORLD Sci.*, pp. 1--22, 1993.

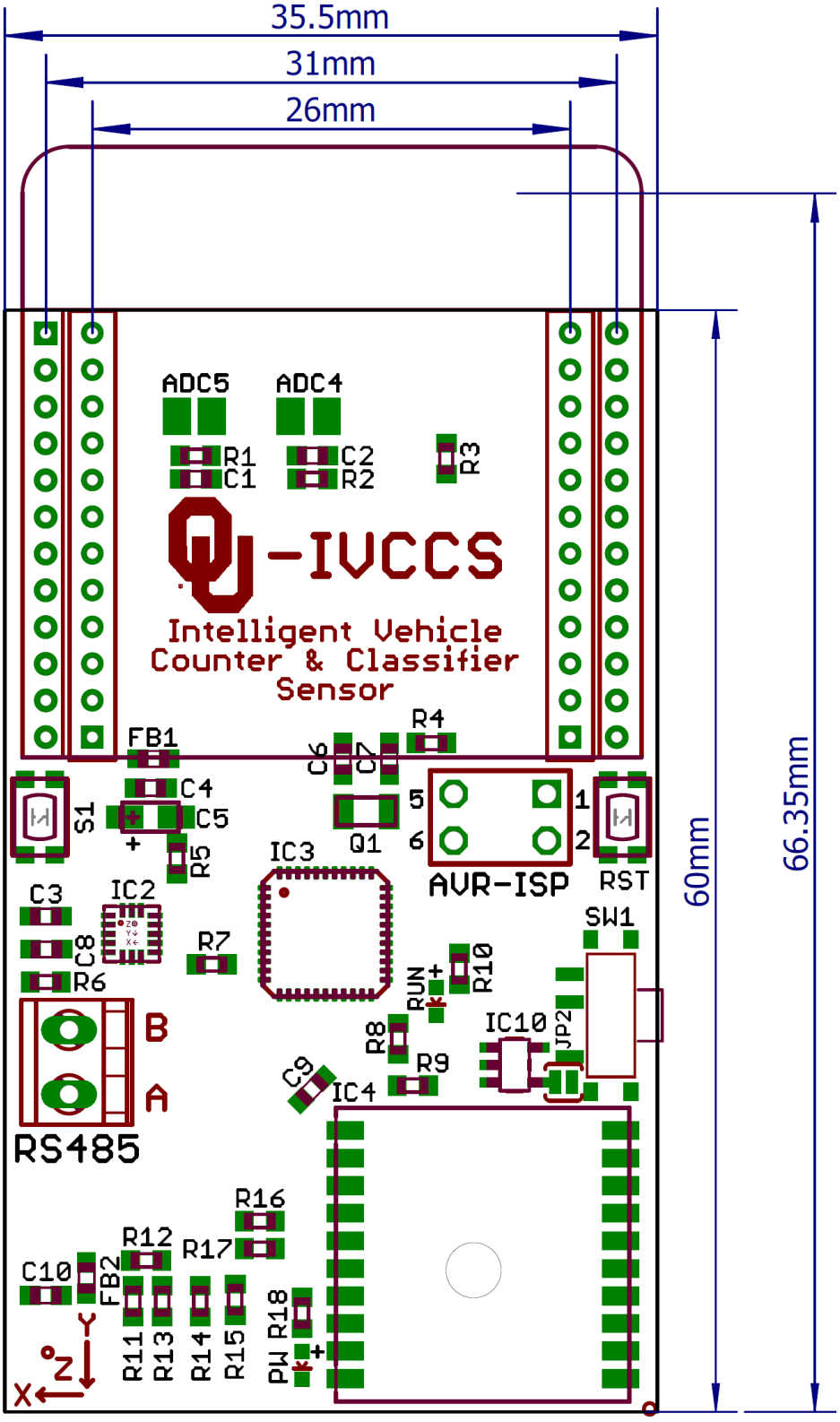
[162] T. Warren Liao, "Clustering of time series data—a survey," *Pattern Recognit.*, vol. 38, no. 11, pp. 1857–1874, 2005.

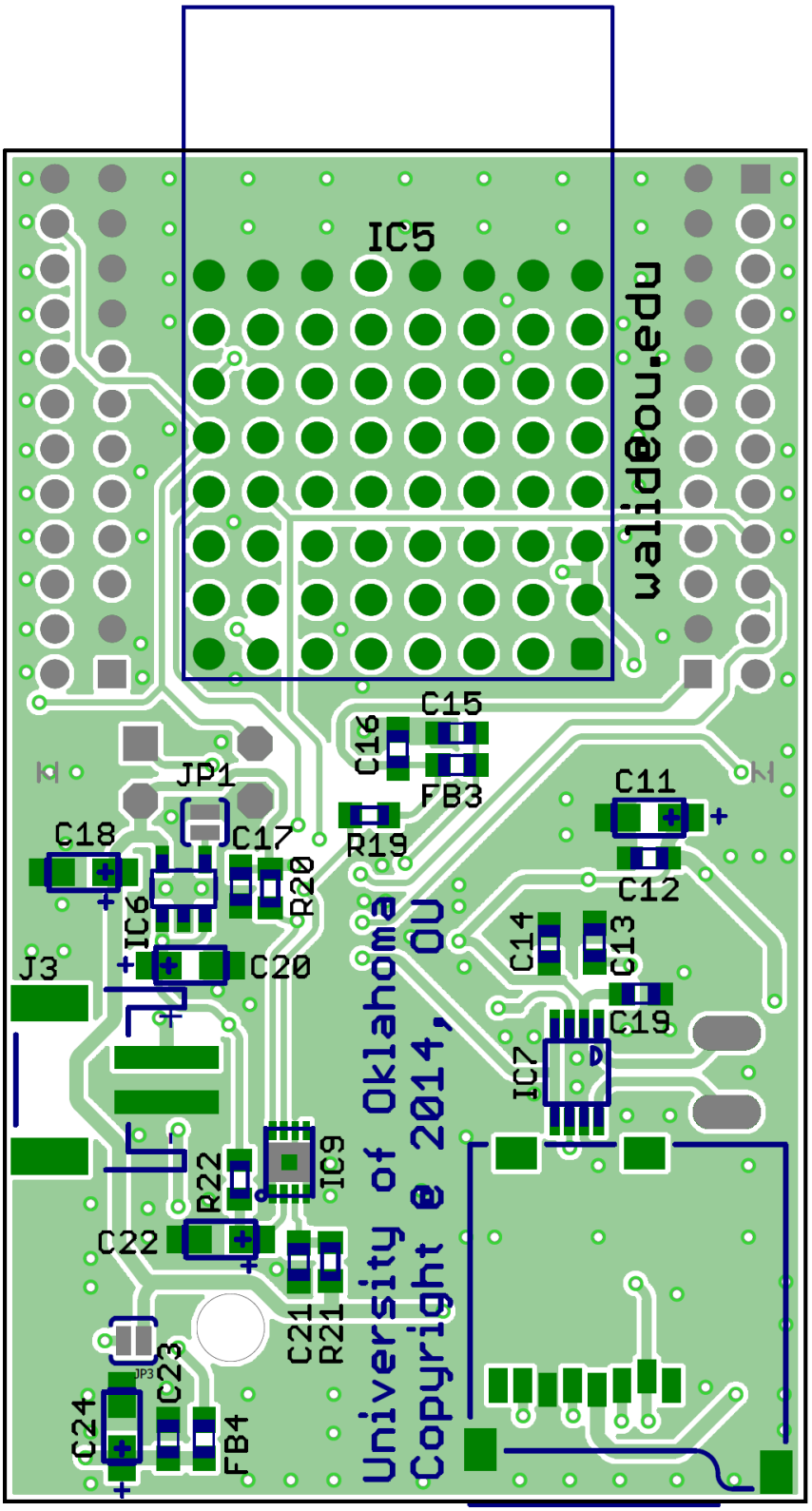
[163] D. J. Berndt and J. Clifford, "Using dynamic time warping to find patterns in time series," *Proceedings of the 3rd International Conference on Knowledge Discovery and Data Mining*. AAAI Press, pp. 359–370, 1994.

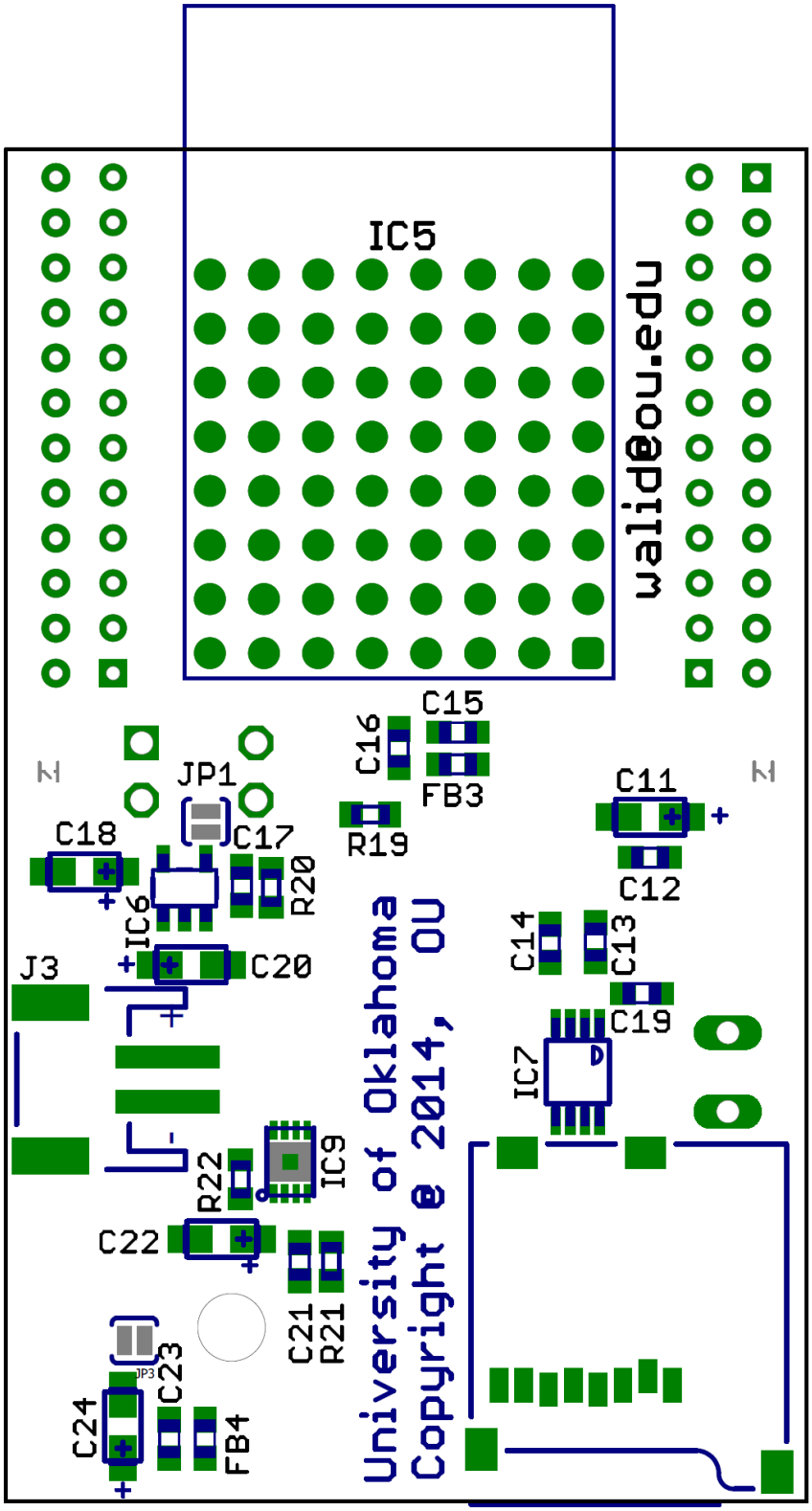
APPENDIX A: *i*VCCS$_{G1}$ SCHEMATIC, LAYOUT, BOM

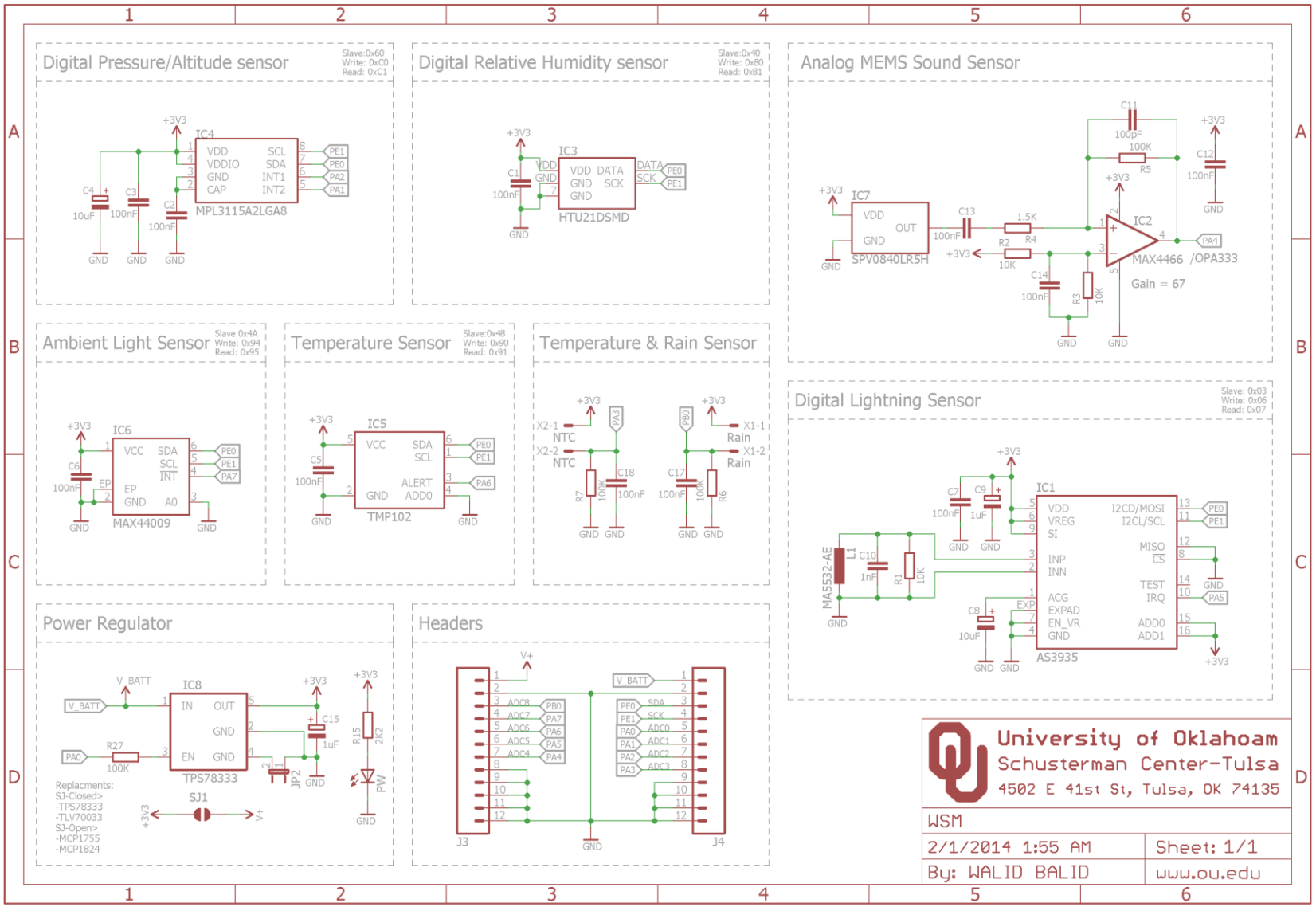


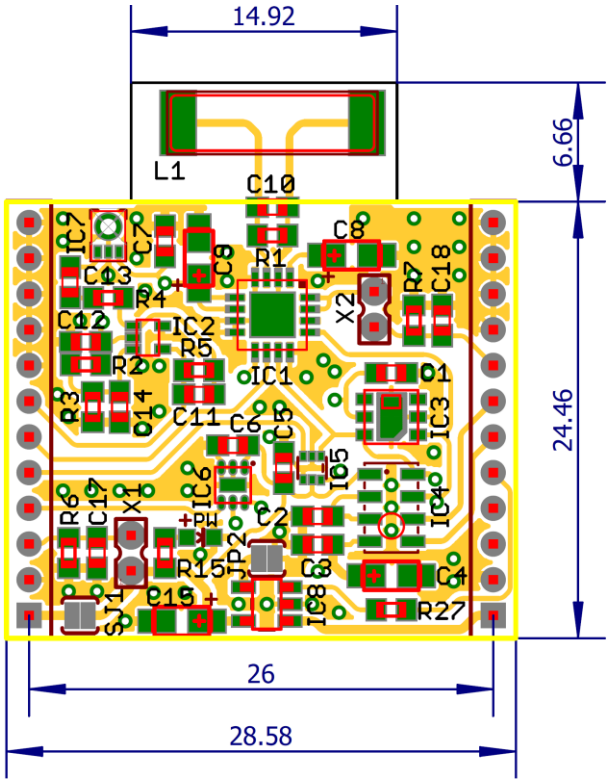

35.5mm
31mm
26mm
66.35mm
60mm
ADC5
ADC4
R1
C1
C2
R2
R3
OU-IVCCS
Intelligent Vehicle
Counter & Classifier
Sensor
R4
FB1
C6
C7
C4
C5
S1
Q1
5
6
1
2
AVR-ISP
RST
IC3
IC2
C3
C8
R6
R7
R5
SW1
RUN
R10
IC10
JP2
R8
R9
C9
IC4
B
A
RS485
R16
R12
R17
C10
FB2
R11
R13
R14
R15
PW
R18
Y
Z
X

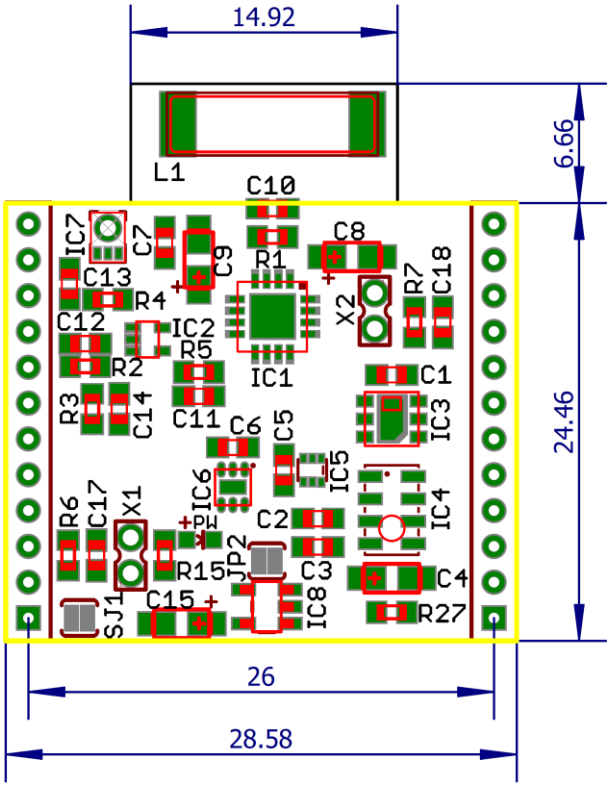

35.5mm
31mm
26mm
60mm
66.35mm
ADC5
ADC4
R1
C1
C2
R2
R3
-IVCCS
Intelligent Vehicle
Counter & Classifier
Sensor
FB1
R4
C6
C7
C4
C5
S1
Q1
5
6
1
2
AVR-ISP
RST
R5
IC3
C3
IC2
C8
R6
R7
SW1
RUN
R10
R8
R9
IC10
JP2
C9
IC4
B
A
RS485
R16
R12
R17
C10
FB2
R11
R13
R14
R15
PW
R18
Y
Z
X

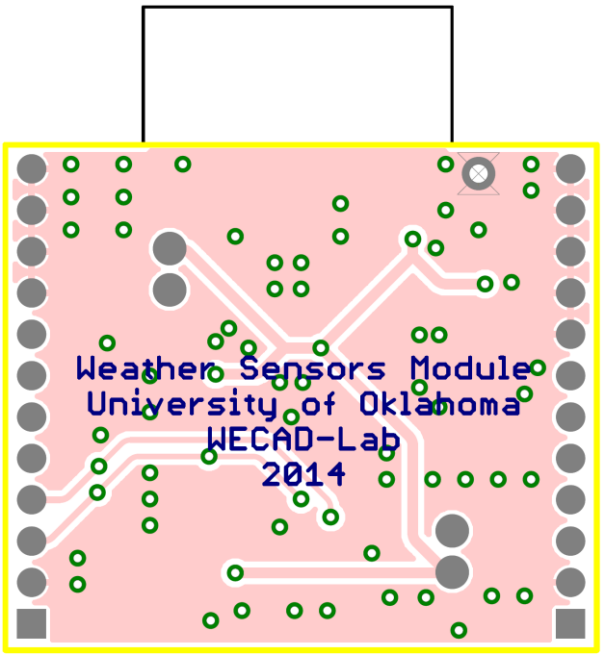

IC5
walid@ou.edu
C15
C16
FB3
JP1
C18
C17
R19
C11
R20
IC6
C12
C14
C13
J3
C20
C19
IC7
R22
IC9
C22
C21
R21
C23
JP3
C24
FB4
University of Oklahoma
Copyright @ 2014, OU

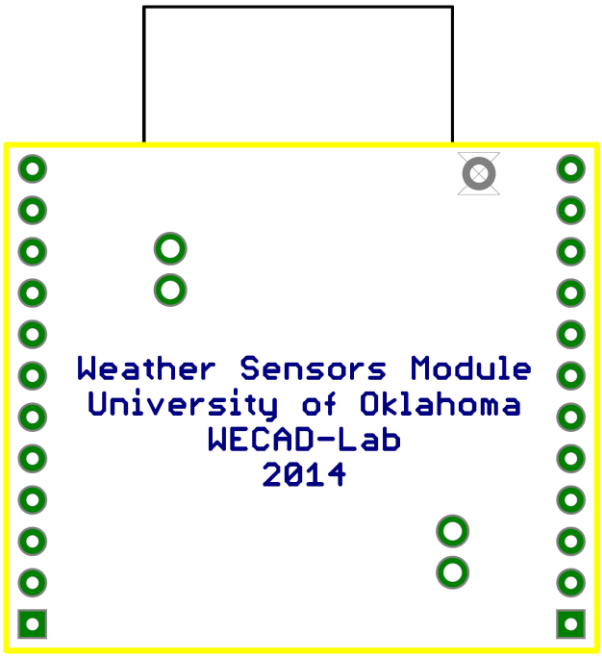

IC5
walid@ou.edu
C15
C16
FB3
JP1
C11
C18
C17
R19
C12
R20
IC6
C14
C13
J3
C20
C19
IC7
IC9
R22
C22
C21
R21
C23
C24
FB4
University of Oklahoma
Copyright @ 2014, OU


Digital Pressure/Altitude sensor
Slave:0x60
Write: 0xC0
Read: 0xC1
IC4
MPL3115A2LGA8
Digital Relative Humidity sensor
Slave:0x40
Write: 0x80
Read: 0x81
IC3
HTU21DSMD
Analog MEMS Sound Sensor
IC7
SPV0840LR5H
IC2
MAX4466 /OPA333
Gain = 67
Ambient Light Sensor
Slave:0x4A
Write: 0x94
Read: 0x95
IC6
MAX44009
Temperature Sensor
Slave:0x48
Write: 0x90
Read: 0x91
IC5
TMP102
Temperature & Rain Sensor
NTC
Rain
Digital Lightning Sensor
Slave: 0x03
Write: 0x06
Read: 0x07
IC1
AS3935
MA5532-AE
Power Regulator
IC8
TPS78333
Replacments:
SJ-Closed>
-TPS78333
-TLV70033
SJ-Open>
-MCP1755
-MCP1824
Headers
J3
J4
University of Oklahoam
Schusterman Center-Tulsa
4502 E 41st St, Tulsa, OK 74135
WSM
2/1/2014 1:55 AM
Sheet: 1/1
By: WALID BALID
www.ou.edu


14.92
6.66
L1
C10
IC7
C7
C9
C8
R1
C13
R4
C12
IC2
R5
R2
IC1
R7
C18
X2
C1
IC3
R3
C14
C11
C6
C5
IC5
IC4
R6
C17
X1
IC6
C2
JP2
R15
C3
C4
SJ1
C15
IC8
R27
24.46
26
28.58


14.92
6.66
L1
C10
IC7
C7
C9
C8
R1
C13
R4
C12
IC2
R5
R2
IC1
R7
C18
X2
C1
IC3
R3
C14
C11
C6
C5
IC5
IC4
R6
C17
X1
IC6
C2
JP2
R15
C3
C4
SJ1
C15
IC8
R27
24.46
26
28.58


Weather Sensors Module
University of Oklahoma
WECAD-Lab
2014

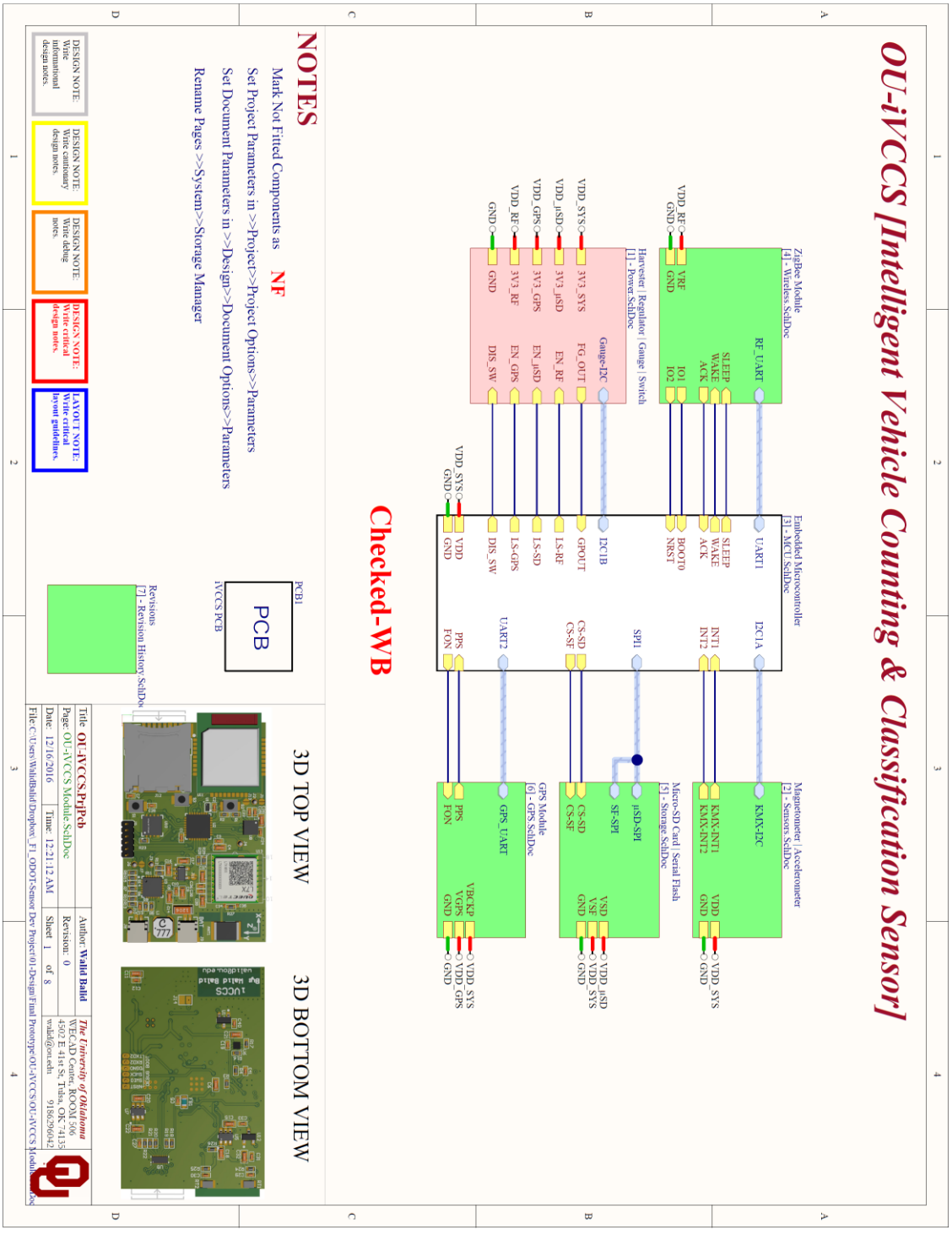

Weather Sensors Module
University of Oklahoma
WECAD-Lab
2014

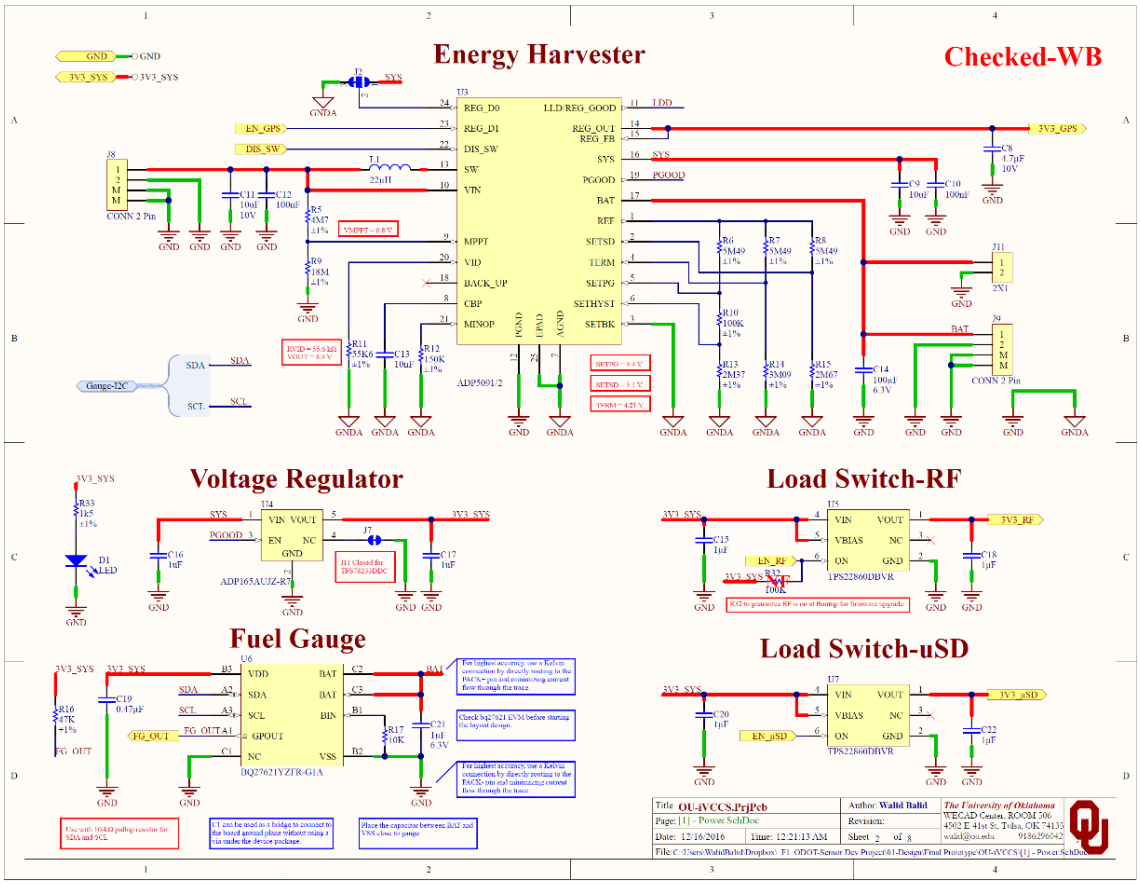
*i*VCCS$_{G1}$ BOM								
Qty	**Value**	**Device**	**Package**	**Identifier**	**Description**	**Supplier**	**Price**	**Part number**
1	NA	AVR-PDIVERT	AVR-ISP-6	J1	CONN HEADER .100" DUAL STR 6POS	digikey	$0.20	S2011EC-40-ND
4	NA	FB	603	FB1, FB2, FB3, FB4	Chip Ferrite Bead	digikey	$0.10	490-5985-1-ND
1	NA	GPS_FGPMMOPA6H	FGPMMOPA6H	IC8	GPS Module - MTK MT3	G.Top	$15.00	From OK Repr.
1	NA	JST_2MM_MALE	JST-2-SMD	J2	Mates to single-cell	digikey	$0.56	455-1749-1-ND
2	NA	LED0603	LED-0603	LED1, PW	LEDs	digikey	$0.17	475-2506-1-ND
2	100K OHM 1% @ 25C	NTC Thermistors	*	NTC1, NTC2	THERMO STRNG 100K OHM 1% NTC	digikey	$0.90	490-5631-ND
2	NA	M12-2MM	1X12-2MM	J3, J4	CONN 2MM VERT SGL ROW 12POS	digikey	$1.00	S5751-12-ND
1	NA	RF200P81	RF200P81	IC7	RF Engine® Model SM2	digikey	$0.00	51765
1	NA	SM200P81	SM200P81	IC9	RF Engine® Model SM2	robot	$15.00	746-1031-1-ND
1	NA	SWITCH_SPDT	KPS-1290	SW1	Side-actuated SPDT s	digikey	$0.82	401-2016-1-ND
3	NA	SW_TACT_SMT4.6X2.8	BTN_KMR2_4.6X2.8	RST, S3, S4	SMT Tact Switches	digikey	$0.58	401-1426-1-ND
12	100K	R-EU 100K	R0603	R3, R6, R7, R8, R10, R11, R16, R21, R22, R25, R26, R27	RESISTOR	digikey	$0.10	311-100KHRCT-ND
14	100nF	C-EUC603 100nF	C0603	C1, C6, C7, C8, C9, C10, C11, C13, C14, C15, C16, C22, C23, C24	CAPACITOR	digikey	$0.50	399-1096-1-ND
4	10K	R-EU 10K	R0603	R1, R2, R12, R13	RESISTOR	digikey	$0.10	311-10.0KHRCT-ND
2	10nF	C-EUC603 10nF	C0603	C5, C21	CAPACITOR	digikey	$0.10	399-7841-1-ND
1	10uF	CPOL-USCT3216T 10uF	CT3216	C19	POLARIZED CAPACITOR	mouser	$0.10	74-TL3A106K016C1700
1	150	R-EU 150R	R0603	R5	RESISTOR	digikey	$0.10	311-150HRCT-ND
1	1K	R-EU 1K	R0603	R4	RESISTOR	digikey	$0.10	311-1.00KHRCT-ND
5	1uF	CPOL-USCT3216T 1uF	CT3216	C2, C3, C4, C12, C20	POLARIZED CAPACITOR	mouser	$0.10	74-TL3A105K035C6000
5	27	R-EU 27R	R0603	R9, R19, R20, R23, R24	RESISTOR	digikey	$0.10	311-27.0HRCT-ND
2	2K2	R-EU 2K2	R0603	R15, R17	RESISTOR	digikey	$0.10	311-2.20KHRCT-ND
1	47K	R-EU 47K	R0603	R14	RESISTOR	digikey	$0.10	311-47.0KHRCT-ND
2	8.2pF	C-EUC603 8.2pF	C0603	C17, C18	CAPACITOR	digikey	$0.10	399-9130-1-ND
1	ABS07-32.768KHZ-1-T	Q_FC135	FC135	Q1	CRYSTAL 32.768KHZ 12.5PF SMD	digikey	$1.28	535-9808-1-ND
1	ATxmegaA4	ATXMEGA64A4U-MH	QFN44	IC1	Atmel XMega A4 serie	digikey	$3.00	ATXMEGA128A4U-MHRCT-ND
1	FXOS8700CQ	FXOS8700CQ	QFN-16_0.5MM	IC6	FXOS8700CQ 6-Axis Se	digikey	$1.80	FXOS8700CQR1CT-ND
1	MAX1704X	MAX17043	TDFN-8	IC4	MAX17043/MAX17044: B	digikey	$1.20	MAX17043G+T-ND
1	MicroSD	USD-SOCKETNEW	MICRO-SD-SOCKET-PP	IC2	microSD Socket	digikey	$1.84	101-00581-59-1-ND
1	TPS78333	TPS783XXSOT23-5	SOT23-5	IC3	Voltage Regulator	digikey	$0.92	296-27178-1-ND
1	W25Q256FV	W25QXXXSO8-208	SO08-208	IC5	SpiFlashR Memories w	digikey	$2.76	W25Q128FVSIG-ND
1	BAT	BAT	NA	BAT	3.7V/2000mA Li-Po Battery	China	$5.00	NA
1	NA	Shell	NA	NA	Enclosure	China	$2.00	NA
1	FR4	PCB Fabrication	NA	NA	Printed Circuit Board	China	$0.25	NA
1	Lead-Free	PCB Assembly	NA	NA	Assembly	China	$1.50	NA
						TOTAL	$57.48	

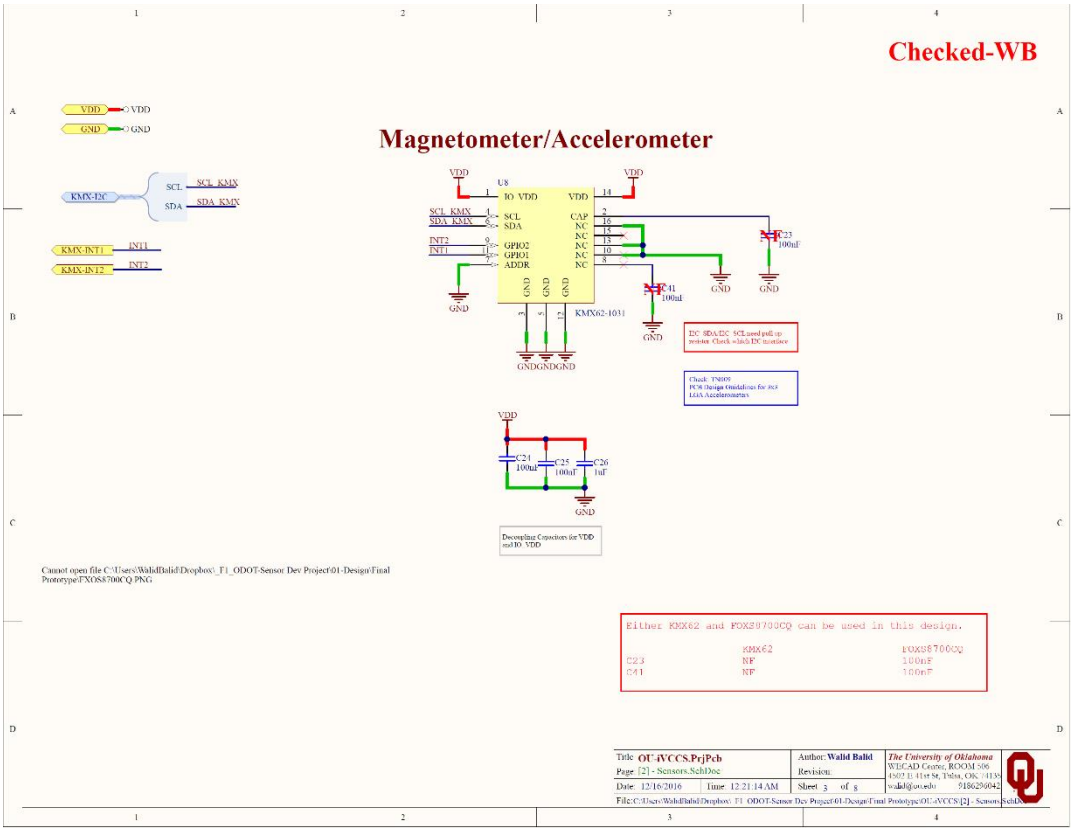
Weather Sensing Module BOM

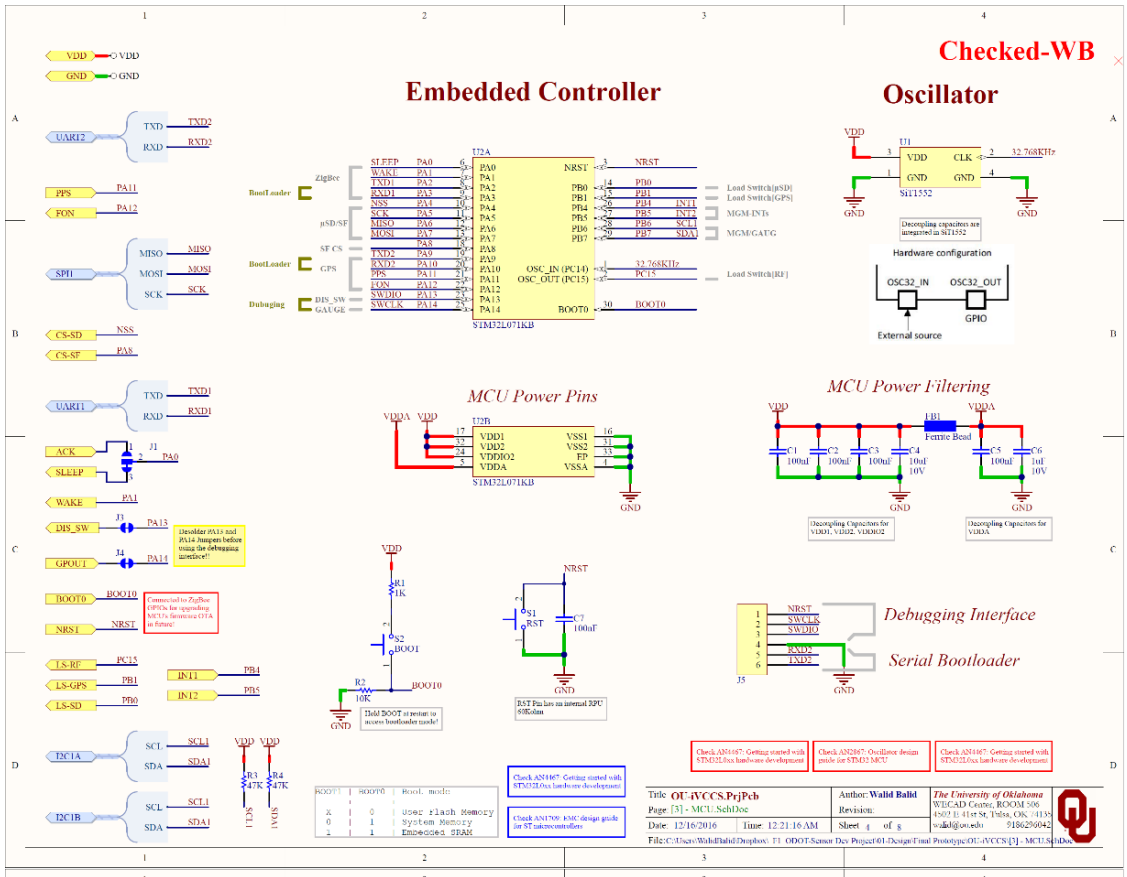
Qty	Value	Device	Package	Identifier	Description	Supplier	Price	Part number
1	NA	LED0603	LED-0603	PW	LEDs	digikey	$0.17	475-2506-1-ND
2	NA	M12-2MM	1X12-2MM	J3, J4	Male Header 2mm	digikey	$0.77	3M9330-ND
1	1.5K	R-EU	R0603	R4	RESISTOR, European s	digikey	$0.01	311-1.50KHRCT-ND
4	100K	R-EU	R0603	R5, R6, R7, R27	RESISTOR, European s	digikey	$0.04	311-100KHRCT-ND
11	100nF	C-EUC603	C0603	C1, C2, C3, C5, C6, C7, C12, C13, C14, C17, C18	CAPACITOR, European	digikey	$0.50	399-1096-1-ND
1	100pF	C-EUC603	C0603	C11	CAPACITOR, European	digikey	$0.10	399-8926-1-ND
3	10K	R-EU	R0603	R1, R2, R3	RESISTOR, European s	digikey	$0.10	311-10.0KHRCT-ND
2	10uF	CPOL-EUCT3216	CT3216	C4, C8	POLARIZED CAPACITOR,	mouser	$0.10	74-TL3A106K016C1700
1	1nF	C-EUC603	C0603	C10	CAPACITOR, European	digikey	$0.10	399-7835-1-ND
2	1uF	CPOL-EUCT3216	CT3216	C9, C15	POLARIZED CAPACITOR,	mouser	$0.10	74-TL3A105K035C6000
1	2K2	R-EU	R0603	R15	RESISTOR, European s	digikey	$0.10	311-2.20KHRCT-ND
1	AS3935	AS3935	16LDMLPQ	IC1	IC SENSOR LIGHTNING	digikey	$8.12	AS3935-BQFTCT-ND
1	HTU21D	HPP828E031	HTU21D	IC3	Digital Relative Hum	digikey	$8.31	223-1144-1-ND
1	MA5532-AE	MA5532-AE	COILCRAFT	L1	MA5532-AE; RFID Tran	coilcraft	$1.50	MA5532-AEB
1	MAX44009	MAX44009	6-UTDFN	IC6	Ambient Light Sensor	digikey	$3.57	MAX44009EDT+TCT-ND
1	MAX4466	MAX4466SC70	SC70	IC2	Single gate rail-to-	mouser	$0.69	700-MAX4466EXKT
1	MPL3115A2LGA8	MPL3115A2LGA8	LGA8	IC4	Altimeter/Pressure S	digikey	$2.88	MPL3115A2-ND
1	100K OHM 1% @ 25C	NTC Thermistors	*	NTC	NTC Thermistors	digikey	$0.90	490-5631-ND
1	SPV0840LR5H	SPV0840LR5H	SPV0840LR5H	IC7	Omnidirection bottom	mouser	$1.82	721-SPV0840LR5H-B
1	TMP102	TMP102	SOT563	IC5	I2C degC temp sensor	digikey	$1.72	296-26834-1-ND
1	TPS78333	TPS783XXSOT23-5	SOT23-5	IC8	Voltage Regulator	digikey	$0.92	296-27178-1-ND
1	FR4	PCB Fabrication	NA	NA	Printed Circuit Board	China	$0.25	NA
1	Lead-Free	PCB Assembly	NA	NA	Assembly	China	$1.00	NA
						TOTAL	**33.77**	

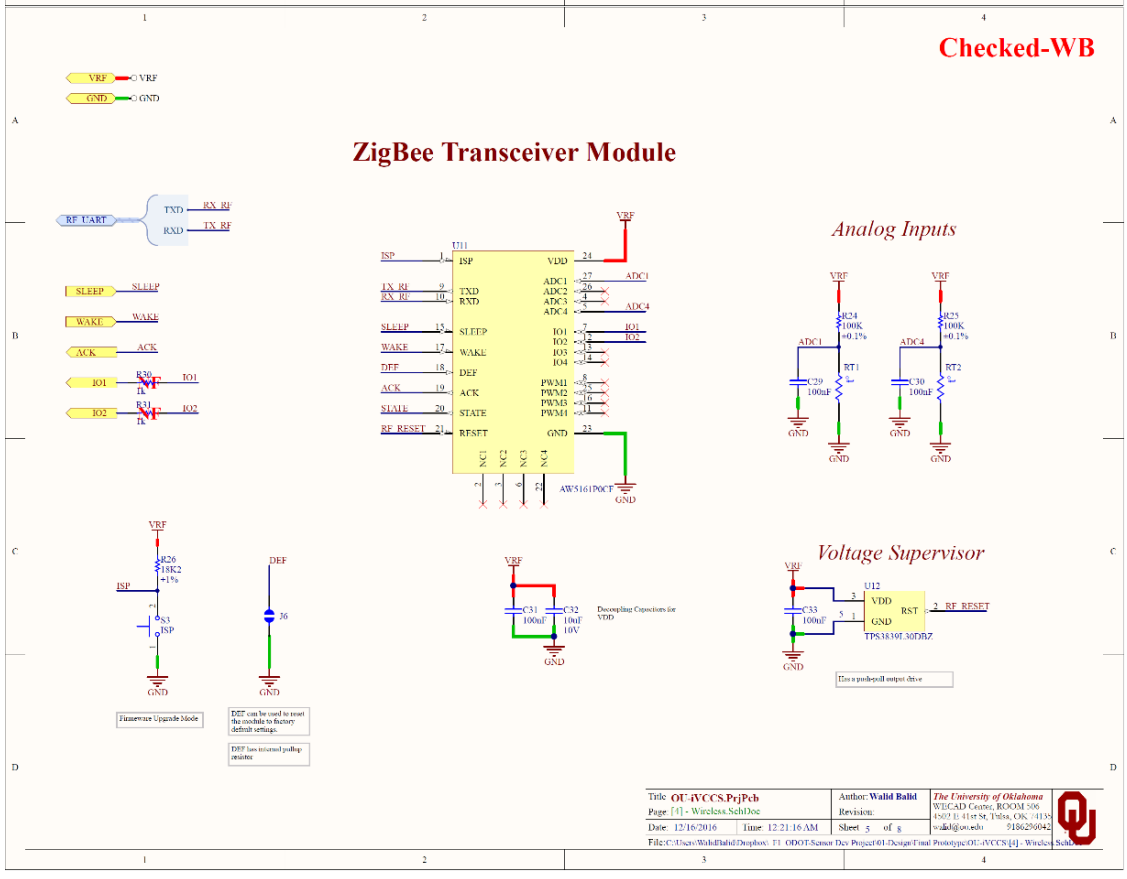
APPENDIX B: *i*VCCS$_{G2}$ SCHEMATIC, LAYOUT, BOM

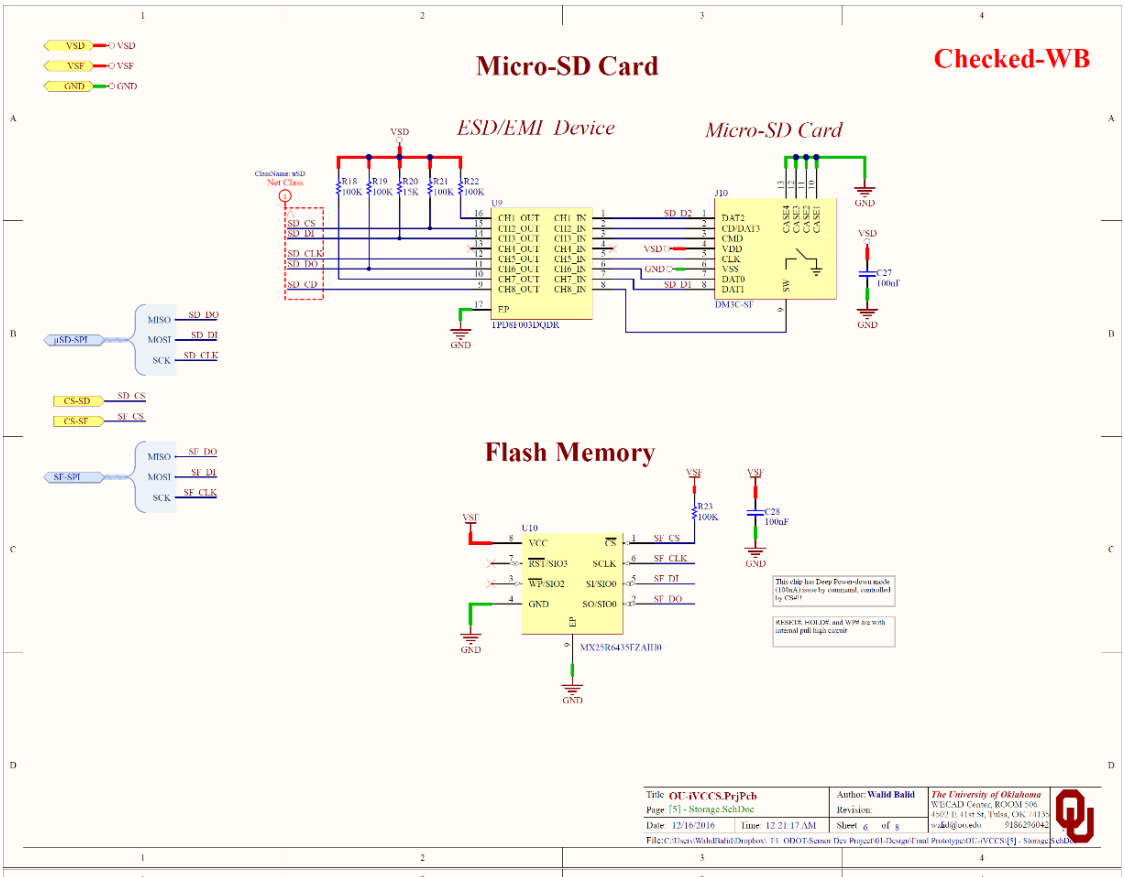


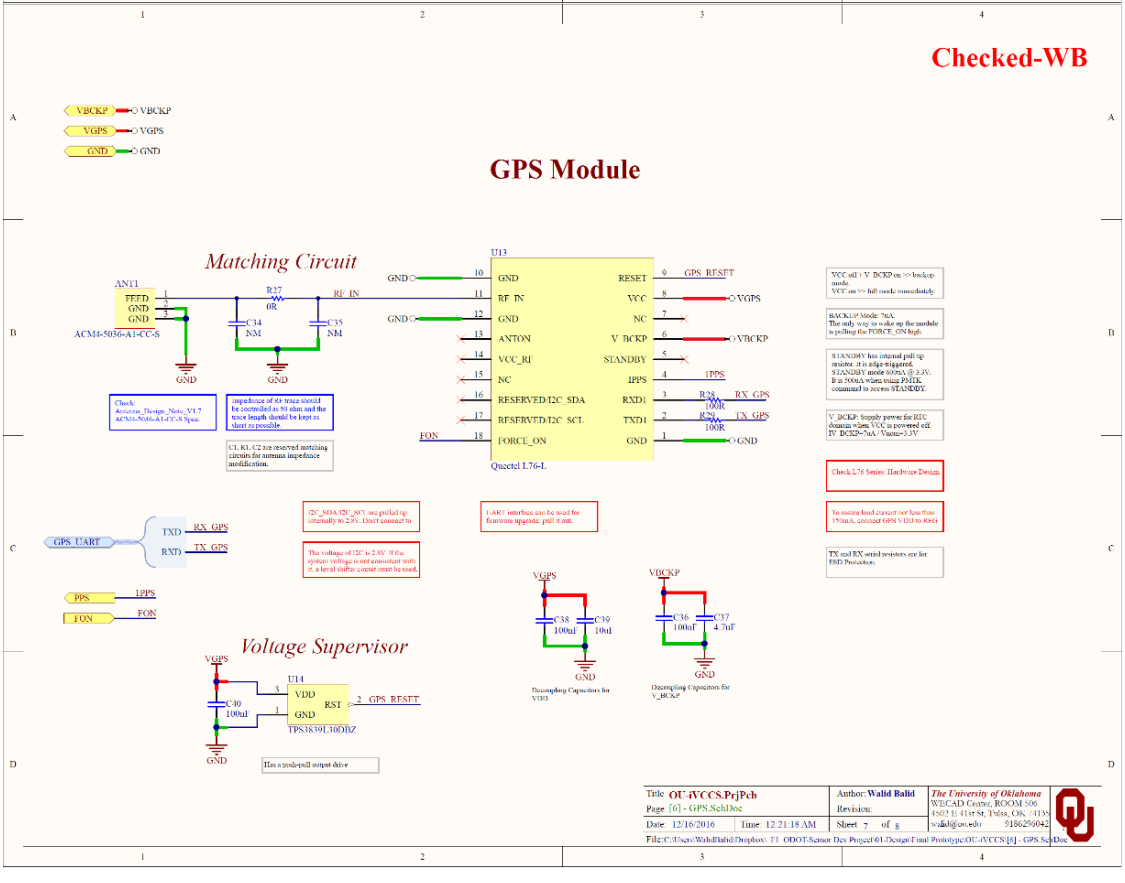

Energy Harvester
Checked-WB
Voltage Regulator
Load Switch-RF
Fuel Gauge
Load Switch-uSD
Title OU-iVCCS.PrjPcb
Author: Walid Balid
The University of Oklahoma
Page: [1] - Power SchDoc
Revision:
Date: 12/16/2016
Time: 12:21:13 AM
Sheet 2 of 8


Checked-WB
Magnetometer/Accelerometer
Either KMX62 and FOX87000CQ can be used in this design.
KMX62
FOX87000CQ
C23
NF
100nF
C41
NF
100nF
Title OU-iVCCS.PrjPcb
Author: Walid Balid
The University of Oklahoma
Page [2] - Sensors.SchDoc
Revision:
Date: 12/16/2016
Time: 12:21:14 AM
Sheet 3 of 8


Checked-WB
Embedded Controller
Oscillator
MCU Power Pins
MCU Power Filtering
Debugging Interface
Serial Bootloader
Hardware configuration
External source
Title: OU-iVCCS.PrjPcb
Page: [3] - MCU.SchDoc
Author: Walid Balid
The University of Oklahoma
WECAD Center, ROOM 506

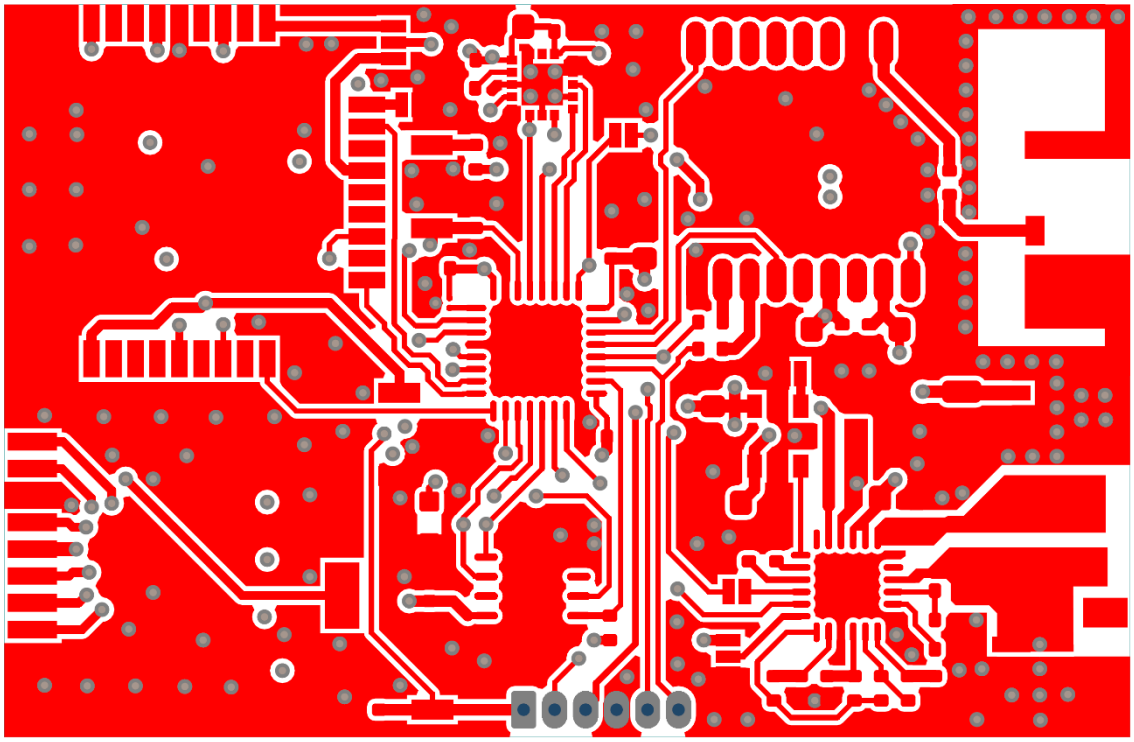

Checked-WB
ZigBee Transceiver Module
Analog Inputs
Voltage Supervisor
Title: OU-iVCCS.PrjPcb
Page: [4] - Wireless.SchDoc
Author: Walid Balid
The University of Oklahoma
WECAD Center, ROOM 506


Micro-SD Card
Checked-WB
ESD/EMI Device
Micro-SD Card
Flash Memory
VSD
VSF
GND
SD_DO
SD_DI
SD_CLK
SD_CS
SF_CS
SF_DO
SF_DI
SF_CLK
TPD8E003DQDR
DM3C-SF
MX25R6435FZAIL0
Title: OU-iVCCS.PrjPcb
Page: [5] - Storage.SchDoc
Author: Walid Balid
Date: 12/16/2016
Time: 12:21:17 AM
Sheet 6 of 8
The University of Oklahoma
WEAD Center, ROOM 506
4502 E 41st St, Tulsa, OK 74135
walid@ou.edu 9186290042

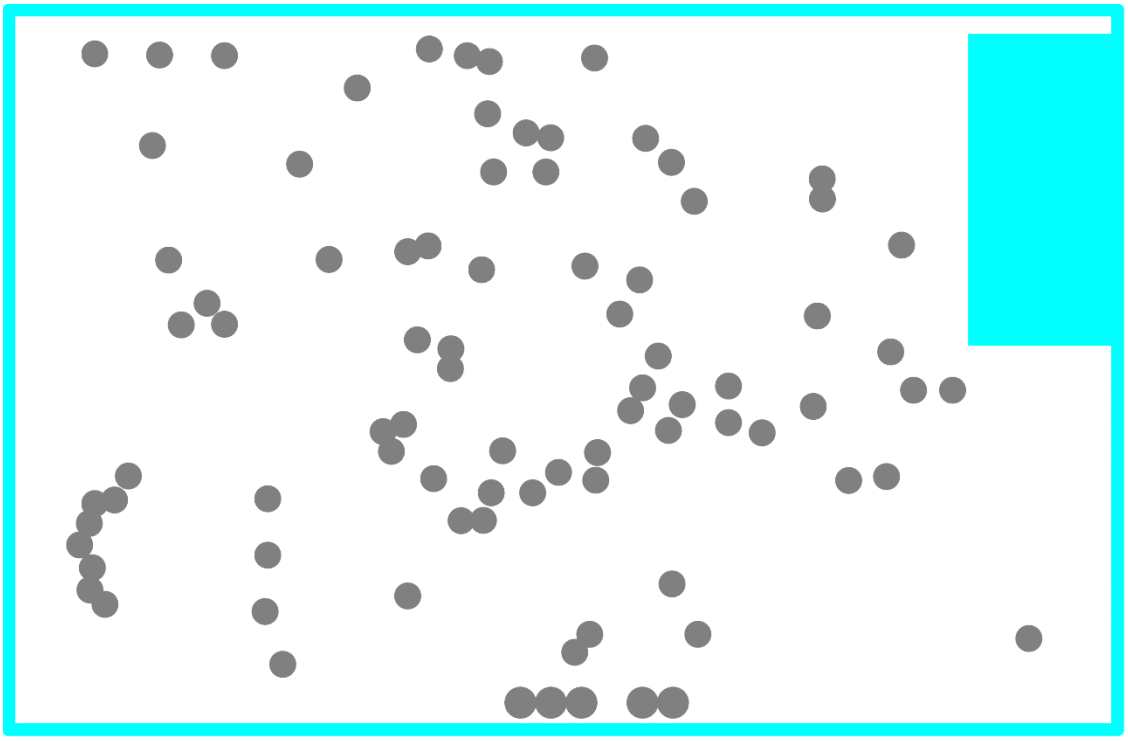

Checked-WB
GPS Module
Matching Circuit
Voltage Supervisor
VBCKP
VGPS
GND
GPS_RESET
RX_GPS
TX_GPS
PPS
FON
Quectel L76-L
TPS3839L30DBZ
Title: OU-iVCCS.PrjPcb
Page: [6] - GPS.SchDoc
Author: Walid Balid
Date: 12/16/2016
Time: 12:21:18 AM
Sheet 7 of 8
The University of Oklahoma
WEAD Center, ROOM 506
4502 E 41st St, Tulsa, OK 74135
walid@ou.edu 9186290042

*i*VCCS$_{G2}$

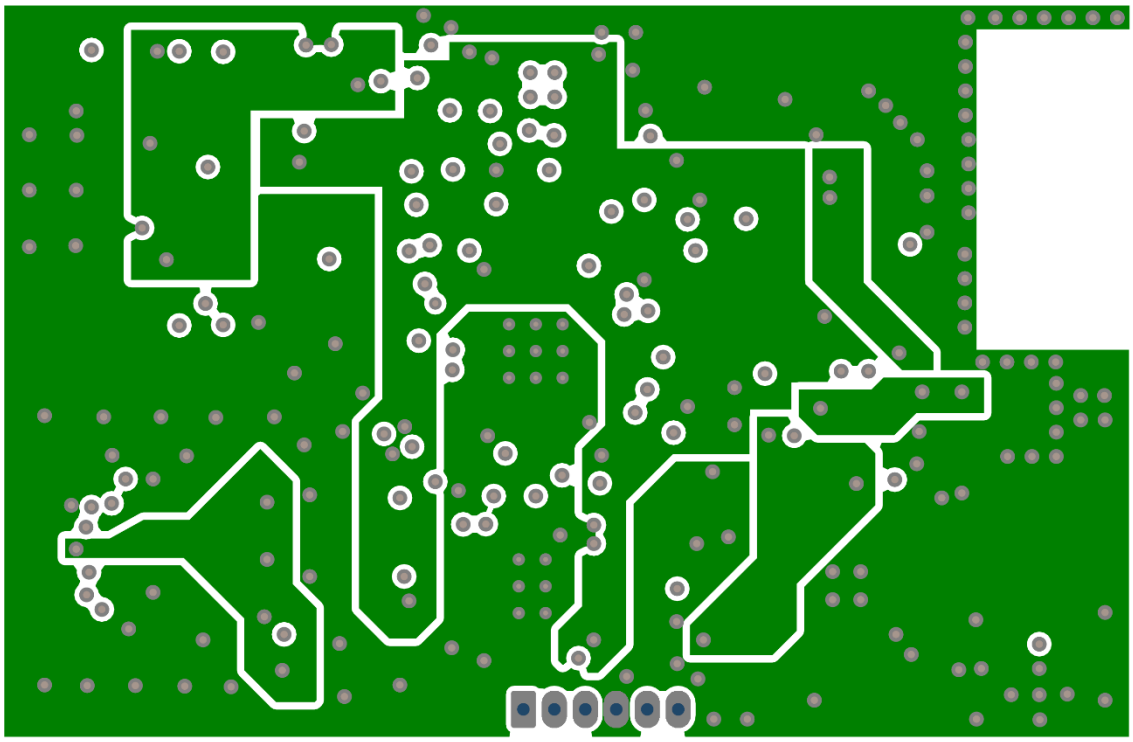
Description	QTY/PCB	Ref Des	Manufacturer	Mfg P/N #	Distributor	Distributor P/N #
GPS+Glonass Ceramic Chip Antenna	1	ANT1	INPAQ Technology	ACM4-5036-A1-CC-S	x	ACM4-5036-A1-CC-S
CAP CER 0.1UF 16V X7R 0402	18	C1, C2, C3, C5, C7, C10, C12, C24, C25, C27, C28, C29, C30, C31, C33, C36, C38, C40	Murata Electronics	GRM155R71C104KA88J	digikey	490-6328-6-ND
CAP CER 10UF 10V X5R 0603	5	C4, C9, C11, C32, C39	Murata Electronics	GRM188R61A106ME69D	digikey	490-10475-6-ND
CAP CER 4.7UF 10V X7S 0603	2	C8, C37	Murata Electronics	GRM188C71A475KE11D	digikey	490-11992-6-ND
CAP CER 10nF 10V X5R 0402	1	C13	Murata Electronics	GRM155R61A103KA01D	digikey	490-6296-6-ND
CAP CER 100UF 6.3V X6T 1206	1	C14	Murata Electronics	GRM31CD80J107ME39L	digikey	490-10525-6-ND
CAP CER 1UF 10V X7R 0603	9	C15, C18, C20, C22, C6, C16, C17, C26, C21	Murata Electronics	GRM188R71A105KA61D	digikey	490-3899-6-ND
CAP CER 0.47UF 10V X7R 0603	1	C19	Murata Electronics	GRM188R71A474KA61D	digikey	490-6420-6-ND
Ferrite Bead	1	FB1	Murata Electronics	BLM18KG331BH1D	digikey	490-14030-2-ND
CONN HEADER .050" 6POS PCB GOLD	1	J5	Sullins Connector Solutions	GRPB061VWVN-RC	digikey	S9014E-06-ND
2 Positions Header, Shrouded Connector 0.039" (1.00mm) Surface Mount, Right Angle Tin	2	J8, J9	JST	SM02B-SRSS-TB(LF)(SN)	digikey	455-1802-6-ND
10 (8 + 2) Position Card Connector Secure Digital - microSD™ Surface Mount, Right Angle Gold	1	J12	Hirose Electric	DM3C-SF	digikey	HR1940CT-ND
Green 570nm LED Indication - Discrete 1.7V/2mA 0603	1	PW	OSRAM Opto Semiconductors	LG L29K-F2J1-24-Z	Digi-Key	475-3118-1-ND
Inductor LPS4018-223MR	1	L1	coilcraft	LPS4018-223MRC	coilcraft	LPS4018-223MRC
RES SMD 1K OHM 1% 1/16W 0402	3	R1, R30, R31, R33	Yageo	RC0402FR-071KL	digikey	311-1.00KLRDKR-ND
RES SMD 10K OHM 1% 1/16W 0402	2	R2, R17	Yageo	RC0402FR-0710KL	digikey	311-10.0KLRCT-ND
RES SMD 47K OHM 1% 1/16W 0402	3	R3, R4, R16	Yageo	RC0402FR-0747KL	digikey	311-47.0KLRCT-ND
RES SMD 4.7M OHM 1% 1/16W 0402	1	R5	Yageo	CRCW04024M70FKED	digikey	541-4.70MLCT-ND
RES SMD 5.49M OHM 1% 1/16W 0402	3	R6, R7, R8	Vishay	541-5.49MLDKR-ND	digikey	CRCW04025M49FKED
RES SMD 18M OHM 1% 1/16W 0402	1	R9	Yageo	RC0402JR-0718ML-ND	digikey	RC0402JR-0718ML
RES SMD 100K OHM 1% 1/16W 0402	8	R10, R18, R19, R21, R22, R23, R24, R25	Yageo	RC0402FR-07100KL	digikey	311-100KLRDKR-ND
RES SMD 55.6K OHM 1% 1/16W 0402	1	R11	Yageo	311-56.0KLRDKR-ND	digikey	RC0402FR-0756KL
RES SMD 150K OHM 1% 1/16W 0402	1	R12	Yageo	RC0402FR-07150KL	digikey	311-150KLRDKR-ND
RES SMD 2.37M OHM 1% 1/16W 0402	1	R13	Vishay	541-2.37MLDKR-ND	digikey	CRCW04022M37FKED
RES SMD 3.09M OHM 1% 1/16W 0402	1	R14	Vishay	541-3.09MLDKR-ND	digikey	CRCW04023M09FKED
RES SMD 2.67M OHM 1% 1/16W 0402	1	R15	Vishay	541-2.67MLDKR-ND	digikey	CRCW04022M67FKED
RES SMD 15K OHM 1% 1/16W 0402	1	R20	Yageo	RC0402FR-0715KL	digikey	311-15.0KLRDKR-ND
RES SMD 18.2KOHM 0.5% 1/16W 0402	1	R26	Yageo	RT0402DRE0718K2L	digikey	311-2235-6-ND
RES SMD 0.0OHM JUMPER 1/16W 0402	1	R27	Yageo	RC0402JR-070RL	digikey	311-0.0JRDKR-ND
RES SMD 100 OHM 1% 1/16W 0402	2	R28, R29	Yageo	RC0402FR-07100RL	digikey	311-100LRDKR-ND
SWITCH TACTILE SPST-NO 0.05A 12V	3	S1, S2, S3	Omron Electronics	B3U-1000P	digikey	SW1020CT-ND
SiT1552AI-JE-DCC-32.768	1	U1	SiTIME	SiT1552AI-JE-DCC-32.768	digikey	1473-1318-1-ND
MCU 32-bit STM32 ARM Cortex M0+ RISC 128KB Flash 2.5V/3.3V 32-Pin UFQFPN, -40 to 125 degC	1	U2	STMicroelectronics	STM32L071KBU6	arrow	STM32L071KBU6
Ultralow Power Energy Harvesting PMU with MPPT, Charge Management and Input Power Monitor	1	U3	Analog Devices	ADP5092ACPZ-1-R7	digikey	ADP5092ACPZ-1-R7CT-ND
Very Low Quiescent Current, 150 mA, LDO Regulator, Industrial, 5-pin SOT23 (UJ-5), Reel	1	U4	Analog Devices/TI	TPS78233DDCT	digikey	296-24120-1-ND
Ultra-Low Leakage Load Switch, TPS22860DBVR	2	U5, U7	Texas Instruments	TPS22860DBVR	digikey	296-43982-1-ND
ULTRA LOW POWER, System-Side Fuel Gauge with Dynamic Voltage Correlation, Battery Gas Gauge	1	U6	Texas Instruments	BQ27621YZFR-G1A	digikey	296-37460-1-ND
Digital Tri-axis Magnetometer/ Tri-axis Accelerometer	1	U8	Kionix	KMX62-1031	x	KMX62-1031
EMI Filter for Display Interface, 8 Channels, -40 to +85 degC, 16-pin WSON (DQD)	1	U9	Texas Instruments	TPD8F003DQDR	digikey	296-25803-1-ND
ULTRA LOW POWER, 64M-BIT [x 1/x 2/x 4] CMOS MXSMIO® (SERIAL MULTI I/O) FLASH MEMORY	1	U10	Macronix	MX25R6435FZAIH0	digikey	1092-1173-ND
ZigBee Wireless Module	1	U11	ZLG	AW5161P0CF	x	AW5161P0CF
Ultra-Low 150nA, Ultra-Small Voltage Supervisor	2	U12, U14	Texas Instruments	TPS3839L30DBZR	digikey	296-35473-1-ND
Quectel L70 Compact GPS Module	1	U13	Quectel	L76L-M33	x	L76L-M33



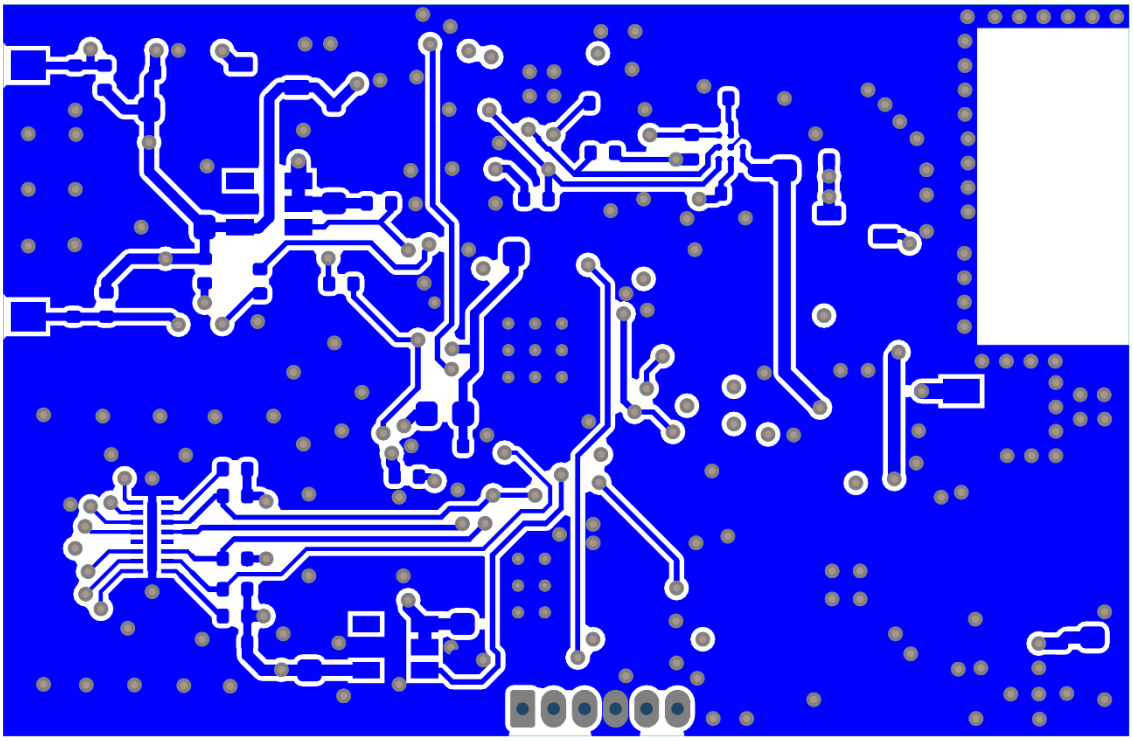
***i*VCCS$_{G2}$ PCB Top Layer**



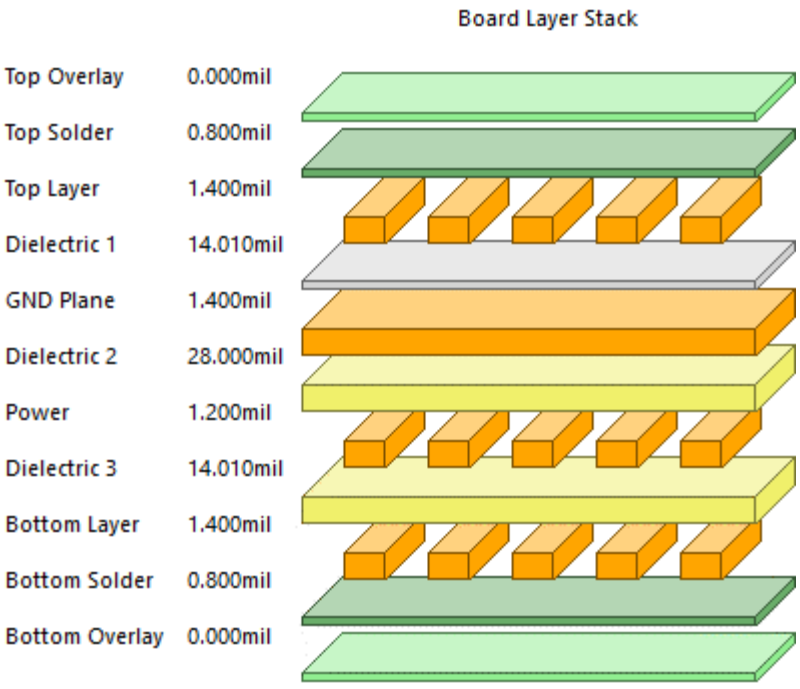
***i*VCCS$_{G2}$ PCB Ground Plan**



***i*VCCS$_{G2}$ PCB Power Plan**



***i*VCCS$_{G2}$ PCB Bottom Layer**

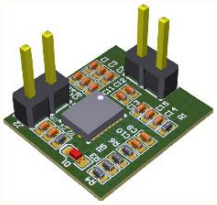


***i*VCCS$_{G2}$ Board Layer Stack Design**

WCR [Wireless Charging Receiver]

Designator
[1] WCR.SchDoc

Designator
[2] Revision History.SchDoc



NOTES

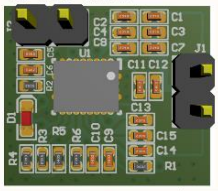
Mark Not Fitted Components as **NF**

Set Project Parameters in >>Project>>Project Options>>Parameters

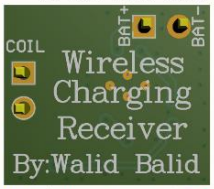
Set Document Parameters in >>Design>>Document Options>>Parameters

Rename Pages >>System>>Storage Manager

3D TOP VIEW



3D BOTTOM VIEW



DESIGN NOTE: Write informational design notes.

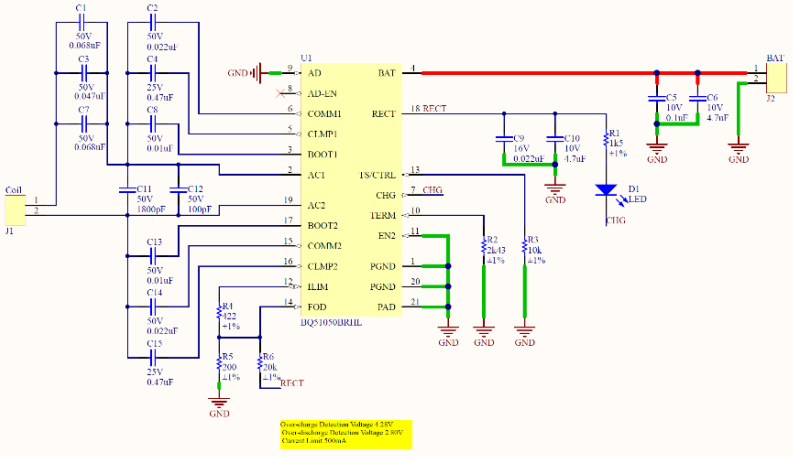
DESIGN NOTE: Write cautionary design notes.

DESIGN NOTE: Write debug notes.

DESIGN NOTE: Write critical design notes.

LAYOUT NOTE: Write critical layout guidelines.

Title: *Wireless Charging Receiver*	Author: Walid Balid	The University of Oklahoma
Page: WirelessChargerRx.SchDoc	Revision: 0	WECAID Center, ROOM 506
Date: 11/17/2016	Time: 10:52:02 AM	Sheet 1 of 3
File: C:\Users\WalidBalid\Dropbox_F1_ODOT-Seanor Dev Project\01-Design\WCR\WirelessChargerRx.SchDoc		



Title: *Wireless Charging Receiver*	Author: Walid Balid	The University of Oklahoma
Page: [1] WCR.SchDoc	Revision: 0	WECAID Center, ROOM 506
Date: 11/17/2016	Time: 10:52:02 AM	Sheet 2 of 3
File: C:\Users\WalidBalid\Dropbox_F1_ODOT-Seanor Dev Project\01-Design\WCR\[1] WCR.SchDoc		

Wireless Charging Receiver

Description	QTY/PCB	Ref Des	Manufacturer	Mfg P/N #	Distributor	Distributor P/N #
0.068µF ±10% 50V Ceramic Capacitor X7R 0402	2	C1, C7	Murata Electronics	GRM155R71H683KE14D	Digi-Key	490-12709-6-ND
0.022µF ±10% 16V Ceramic Capacitor X7R 0402	1	C9	Murata Electronics	GRM155R71C223KA01D	Digi-Key	490-3256-6-ND
0.022µF ±10% 50V Ceramic Capacitor X7R 0402	2	C2, C14	Murata Electronics	GRM155R71H223KA12D	Digi-Key	490-3884-1-ND
0.047µF ±10% 50V Ceramic Capacitor X7R 0402	1	C3	Murata Electronics	GRM155R71H473KE14D	Digi-Key	490-10702-6-ND
0.47µF ±10% 25V Ceramic Capacitor X5R 0402	2	C4, C15	Murata Electronics	GRT155R61E474KE01D	Digi-Key	490-12269-6-ND
0.10µF ±10% 10V Ceramic Capacitor X7R 0402	1	C5	Murata Electronics	GRM155R71A104KA01D	Digi-Key	490-6321-2-ND
4.7µF ±10% 10V Ceramic Capacitor X5R 0402	2	C6, C10	Murata Electronics	ZRB15XR61A475KE01D	Digi-Key	490-13252-6-ND
10000pF ±5% 50V Ceramic Capacitor X7R 0402	2	C8, C13	Murata Electronics	GRM155R71H103JA88D	Digi-Key	490-7763-6-ND
1800pF ±5% 50V Ceramic Capacitor X7R 0402	1	C11	Murata Electronics	GRM155R71H182JA01D	Digi-Key	490-12535-6-ND
100pF ±5% 50V Ceramic Capacitor C0G, NP0 0402	1	C12	Murata Electronics	GRM1555C1H101JA01D	Digi-Key	490-5922-6-ND
Green 569nm LED Indication - Discrete 2.1V 0603	1	D1	Lite-On	LTST-C190GKT	Digi-Key	160-1183-1-ND
RES SMD 1.5K OHM 1% 1/16W 0402	1	R1	Yageo	RC0402FR-071K5L	Digi-Key	311-1.50KLRDKR-ND
RES SMD 2.43K OHM 1% 1/16W 0402	1	R2	Yageo	RC0402FR-072K43L	Digi-Key	YAG3101DKR-ND
RES SMD 10K OHM 1% 1/16W 0402	1	R3	Yageo	311-10.0KLRDKR-ND	Digi-Key	RC0402FR-0710KL
RES SMD 422 OHM 1% 1/16W 0402	1	R4	Yageo	RC0402FR-07422RL	Digi-Key	YAG3158DKR-ND
RES SMD 200 OHM 1% 1/16W 0402	1	R5	Yageo	RC0402FR-07200RL	Digi-Key	311-200LRDKR-ND
RES SMD 20K OHM 1% 1/16W 0402	1	R6	Yageo	RC0402FR-0720KL	Digi-Key	311-20.0KLRDKR-ND
Wireless Power Receiver PMIC 20-VQFN	1	U1	Texas Instruments	BQ51050BRHLR	Digi-Key	296-35066-2-ND

APPENDIX C: *i*VCCS$_{G2}$ DESIGN PROCESS

